THESE DE DOCTORAT
DE
L'Universite Paris-Saclay
PREPAREE A
L'ECOLE POLYTECHNIQUE

Ecole Doctorale n°573 : interfaces
Approches interdisciplinaires : fondements, applications et innovation

Spécialité : Chimie des matériaux

Par

M. Fabien Lebreton

Silicon surface passivation properties of aluminium oxide
grown by atomic layer deposition for low temperature solar cells processes

Thèse présentée et soutenue à Palaiseau, le 20 décembre 2017 :

Composition du Jury :

Dr.	Kleider, Jean-Paul	GeePs	Président du jury
Prof.	Glunz, Stefan	Fraunhofer ISE	Rapporteur
Dr.	Blanc-Pelissier, Danièle	INL	Rapporteur
Dr.	Broussillou, Cédric	EDF	Examinateur
Dr.	Betremieux, Isabelle	TOTAL	Examinatrice
Dr.	Filonovich, Sergej	TOTAL	Encadrant
Dr.	Silva, François	LPICM	Directeur de thèse

"Discovery consists of seeing what everybody else has seen,
and thinking what nobody else has thought."
Albert Szent-Gyorgyi

À Stéphanie

ii

Remerciements

Ces trois courtes et intenses années de thèse se sont déroulées entre Total et le Laboratoire de Physique des Interfaces et Couches Minces (LPICM) via une convention CIFRE. Je tiens donc à remercier en premier lieu *Fabrice Devaux* et *Lars Oberbeck* pour m'avoir permis d'intégrer l'équipe R&D de Total, mais également, *Pere Roca i Cabarrocas* pour m'avoir ouvert son laboratoire et fait bénéficier de son expertise sur tous les pans de ce que peut être la Recherche.

Il est important pour moi de témoigner ma sincère gratitude à *François Silva* qui fut un directeur de thèse hors pair. Ses conseils avisés, sa disponibilité, son soutien et son exceptionnelle capacité à voir la tasse de Nespresso à moitié pleine ont été d'une grande aide tout au long de ces trois années. En ce sens, je suis également reconnaissant envers *Sergej Filonovich* de m'avoir épaulé au sein de Total et d'avoir su garder le sens de l'humour en toutes circonstances.

Par ailleurs, pour l'honneur qu'ils m'ont fait en acceptant de siéger au jury de cette thèse je remercie, *Isabelle Betremieux, Danièle -BlancPelissier, Cédric Broussillou, Stefan Glunz* et *Jean-Paul Kleider.*

Mes travaux ayant été principalement rattachés aux projets de l'Institut Photovoltaïque d'Ile de France (IPVF), je souhaite en remercier les membres avec lesquels j'ai eu l'opportunité de collaborer : *Thomas Blévin, Coralie Charpentier, François Cœuret, Jean-Yves Letellier, Yves Marot, Sylvain Pouliquen* et *Andy Zauner* côté Air Liquide ; *Philippe Baranek, Julien Couderc, Julien Dupuis, Pierre-Philippe Grand* et *Vanessa Riffet* côté EDF.

Ce travail doctoral n'aurait pu être mené à bien sans les discussions, la disponibilité et la collaboration de nombreux collègues du laboratoire. Je remercie donc chaleureusement, *Pavel Bulkin* (une ligne pilote à lui seul), *Wanghua Chen, Dmitri Daineka, Alice Defresne, Ileana Florea, Martin Foldyna, Enric Garcia-Caurel, Erik Johnson* (pour m'avoir fait découvrir les réalisateurs originaires de Winnipeg entre 1972 et 1973), *Rasha Khoury, Jean-Luc Maurice, Jean-Luc Moncel, Karim Ouaras, Denis Tondelier, Jacqueline Tran, Sandrine Tusseau-Nenez, Junkang Wang*. Merci également à l'équipe administrative ; *Laurence Corbel, Gabriela Medina* et *Fabienne Pandolfe.* De plus, je ne saurais oublier ceux qui maintiennent notre environnement en état et réparent quand une pompe primaire brûle ou quand un ordinateur crashe, c'est-à-dire l'équipe du BEER & WINE : *Nacib Benmammar* (♪ mets de l'huile petit homme dans la vie il faut que ça pompe ♪), *Jérôme Charliac, Frédéric Farci, Cyril Jadaud, Frédéric Liège* et *Eric Paillassa* et *Jean-Charles Vanel.*

Mes remerciements vont également à l'équipe de Total qui animait la vie de l'annexe du 404 à Palaiseau, à savoir *Ahmed Ben Slimane, Jean-François Besnier, Amjad Deyine, Jara Fernandez, Nada Habka, Ludovic Hudanski, Vincent Maillard, Julien Penaud* (de temps à autres), *Gilles Poulain, Patricia Prod'homme, Céline Richard,* et *Martin Sander* . Je n'oublie pas les Belges régulièrement de passage : *Guillaume Courtois* et *Patricia De Coux.*

iv

Contents

List of Figures

List of Tables

List of acronym and symbols

	Unit	Definition
α	cm^{-1}	Absorption coefficient
Al$_2$O$_3$		Aluminium oxide
Al-BSF		Aluminium back surface field
ALD		Atomic Layer Deposition
AM1.5		Solar spectrum at an air mass of 1.5
APCVD		Atmospheric Pressure Chemical Vapour Deposition
ARC		Anti-reflection coating
a-Si:H		Hydrogenated amorphous silicon
a-SiN$_X$:H		Hydrogenated amorphous silicon nitride
c-Si		Monocrystalline Silicon
CB		Conduction Band
CBM		Conduction Band Minimum
COCOS		Corona oxide characterisation of semiconductors
CSNSM		Centre de Sciences Nucléaires et de Sciences de la Matière
CVD		Chemical Vapour Deposition
Cz		Czochralski
D$_{it}$	eV^{-1}.cm^{-2}	Interfacial trap density
E$_{04}$	eV	optical bandgap energy
ε		Material emissivity
η	%	Efficiency
ERDA		Elastic recoil detection analysis
FF	%	Fill factor
FTIR		Fourier transform infrared spectroscopy
FZ		Float zone
σ$_n$	cm^2	Electron capture cross
σ$_p$	cm^2	Hole capture cross
G	cm^{-3}	Generation rate
GPC	Å/cycle	Growth per cycle
HF		Hydrofluoric acid
IPVF		Institut Photovoltaïque d'Île-de-France
Isc	mA	Short-circuit current
k		Extinction coefficient

λ	nm	Wavelength
LIBI		Low Intensity Bifacial Illuminator
LIFE$_2$		Light Induced Field Effect Enhancement
LPICM		Laboratoire de Physique des Interfaces et des Couches Minces
n		Refractive index
NRA		Nuclear Reaction Analysis
PA-ALD		Plasma Assisted Atomic Layer Deposition
PCD		Photoconductance decay
PECVD		Plasma Enhanced Chemical Vapour Deposition
PERC		Passivated emitter and rear cell
PL		Photoluminescence
PV		Photovoltaic(s)
Q_f	cm^{-2}	Fixed charge density
Ra	(AU)	Acoustic reflection coefficient
RBS		Rutherford backscattering spectrometry
R_{eff}	%	Effective reflectance
RF		Radio Frequency
RH	%	Relative humidity
sccm		Standard cubic centimetres per minute
S_{eff}	cm.s^{-1}	Effective Surface recombination velocity
SE		Spectroscopic Ellipsometry
SEM		Scanning electron microscopy
SIMS		Secondary Ion Mass Spectrometry
S_{eff}	cm^2.s^{-1}	Effective surface recombination velocity
SQL		Shockley–Queisser limit
SRH		Shockley–Read–Hall
SRV		Surface recombination velocity
τ_{eff}	µs	Effective lifetime
θ_c	°	critical angle
TDS		Thermal desorption spectroscopy
TD-ALD		Thermal Drift Atomic Layer Deposition
Th-ALD		Thermal Atomic Layer Deposition
TMA		Trimethylaluminium
U	cm^{-3}	Recombination rate
UV		Ultraviolet
VB		Valence Band
VBM		Valence Band Maximum
V$_{DC}$	V	Self-bias voltage
V$_{PL}$	V	plasma potential
V$_{RF}$	V	Potential at the RF electrode
V$_{sb}$	eV	Surface barrier potential
V$_{oc}$	mV	Open-circuit voltage
XRR		X-ray Reflectometry

Introduction

Solar energy outlook

In the 21st century, the energy access remains a major source of inequality around the world, leaving billions of people without electricity or without access to clean cooking facilities (Figure 0.1) [13]. Among all the continents, Africa is the one that requires the most intensive energy deployment because contrary to Asia, its demographic transition just begun. African people were 1.26 billion in 2015, representing only 17 % of the world population while in 2100 they will rise to 4.47 billion, representing 40 % of the world population and so a proportional energy demand [41]. The African continent is plenty of fossil resources that used to be extracted from their soil for centuries, but it also benefits from the largest solar power reaching the ground (Figure 0.1). It has to be reminded that the solar energy reaching earth can yearly cover more than 1000 times the world needs in energy [42].
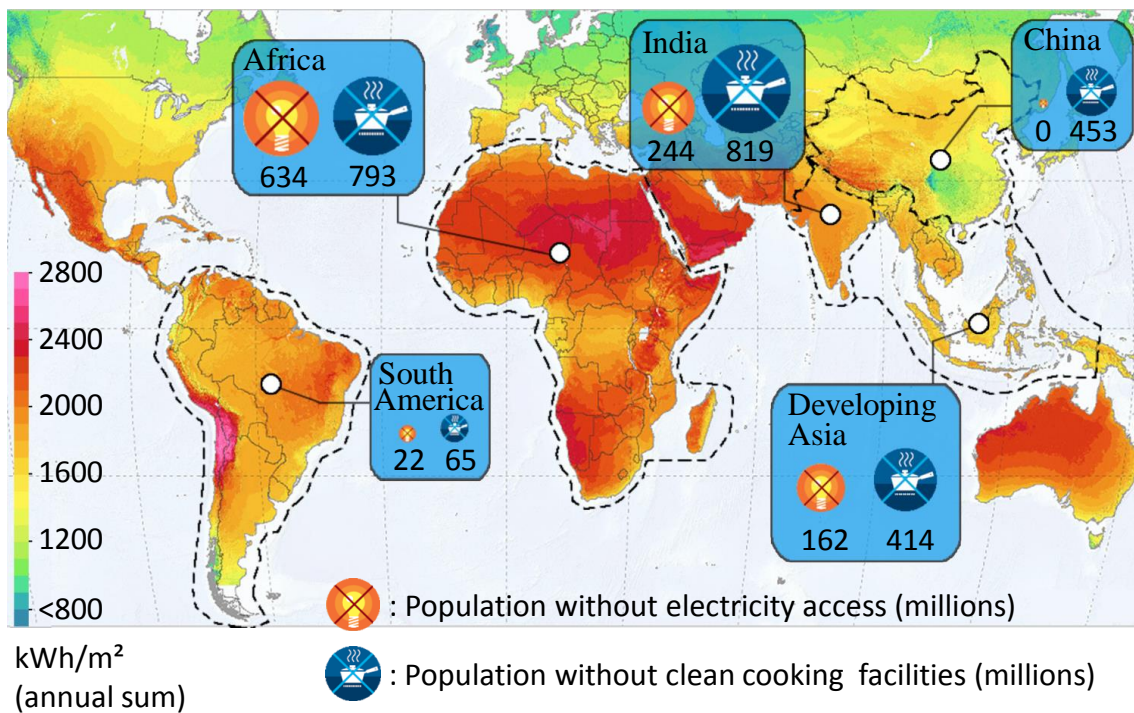
Figure 0.1: Number of people without access to electricity or to proper cooking facilities around the world [13]. Data are reported on the world solar resource map (Global Horizontal Irradiation) [36].

The solar energy has been used for its heat for millennia, from the ignition of the Olympic flame in the 3rd century B.C. to the vapour generation that powers electrical turbines nowadays [43]. However, the direct conversion of the sunlight into electricity, named the photovoltaic (PV) effect, has been reported only in 1839 by the French scientist Alexandre-Edmond Becquerel [44]. It took another century to create reliable devices that can be commercialised, but at prices that were not competitive for the mass production of electricity at that time (Figure 0.2.a). The reduction of the *$/W* ratio made the PV deployment possible in the late '90s. Thanks to technology's advances and mass production, the price per watt has been divided by ~320 in 40 years, allowing a world total installed capacity of about 388 GW by the end of 2017 (Figure 0.2.a). Despite this exceptional growth rate of the PV market, PV electricity represents only 1.5 % of the world electrical generation at the end of 2016 [45]. Further cost reduction and technological improvement are required to support the fast growth of PV.
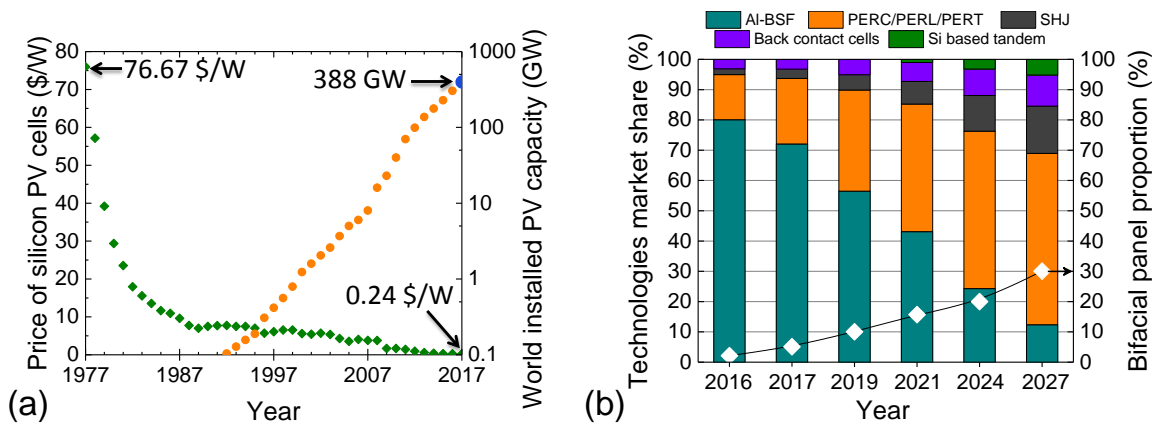
Figure 0.2: (a) Price of the c-Si photovoltaic cells (left axis) and World installed PV capacity (right axis) [32, 33]. (b) Market share forecasts for the main solar cells architectures and proportion of bifacial solar modules [38].

Many different types of photovoltaic solar cells have been developed over time, but these based on crystalline silicon (c-Si) have supplanted all the others, representing more than 93 % of the market at the end of 2016 [46]. Inside this market there is still a wide variety of technologies adopting different architectures. The 'Aluminium-Back Surface Field' (Al-BSF) is the mainstream one (Figure 0.2.b) because it is the simplest and the cheapest to manufacture.
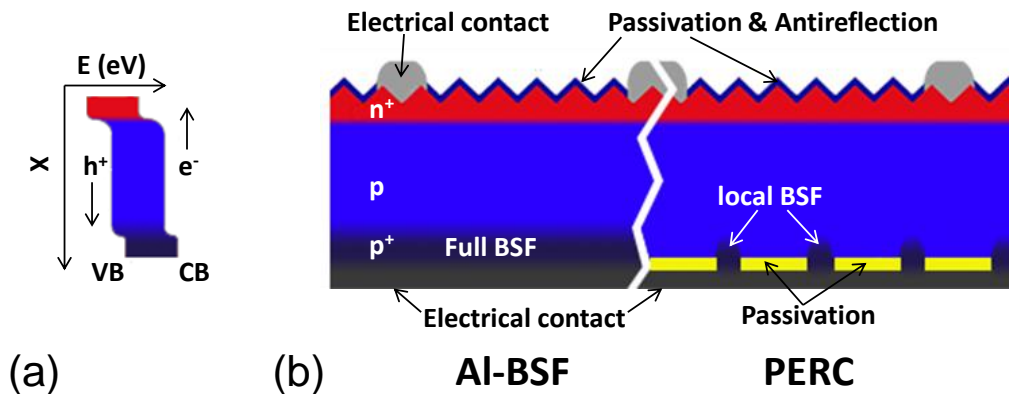
Figure 0.3: (a) Band structure of Al-BSF where VB stands for valence band and CB for conduction band (b) Schematic cross section of Al-BSF and PERC solar cells.

The Al-BSF maximum conversion efficiency seems to be around 20 % while its upgraded architecture PERC (Passivated Emitter and Rear Cell) is already promising 24 % [47-49]. Naturally the Al-BSF should give way to the PERC architecture and its variants in the next decade. In addition, these architectures are also compatible with the second market trend which is the adoption of bifacial architectures. The light collection on the back surface of the solar cells takes advantage of the albedo, increasing the system relative efficiency up to 30 % [50, 51].

The Al-BSF architecture consists in a p-type absorber with a bipolar p-n$^+$ junction on top and a unipolar p-p$^+$ junction below. These junctions result in the band structure shown on Figure 0.3.a that allows carrier separation and diffusion to the electrical contacts located on the top for electrons and at the bottoms for holes. The unipolar junction at the bottom is formed by alloying aluminium to the lowly doped absorber and gives its name to the architecture: Aluminium Back-Surface Field [52]. On the front surface there is an antireflection coating (ARC) on a textured surface to maximise photon collection. This layer also serves as surface passivation, which is a technological key element to master in order to continue the photovoltaic development. Its implementation on the back surface of solar cells such as in the PERC architecture (Figure 0.3.b) opened the route to higher conversion efficiency.

Thesis aim and outline

This doctoral work is dedicated to the fundamental understanding and improvement of c-Si surface passivation by aluminium oxide (Al$_2$O$_3$) and its related derivative stacks. It is part of the 'advanced silicon technologies' project conducted by the 'Institut Photovoltaïque d'Île-de-France' (IPVF). This project aims to develop a c-Si solar cell architecture fully processed at low temperature, *i.e.* lower than 400 °C, and that has a conversion efficiency higher than 20 %.

- The first chapter reminds the physics key points of passivation and its link with the solar cell efficiency. Then, a brief description of the mainstream characterisation techniques used in this work is done.

- The second chapter deals with the deposition technique and the material properties of Al$_2$O$_3$ films. The atomic layer deposition is described and the impacts of process conditions on film properties are investigated. The sensitivity of the passivation properties to post-deposition illumination is addressed in this chapter.

- The third chapter is dedicated to the passivation properties of Al$_2$O$_3$ films embedded in a stack with hydrogenated amorphous silicon nitride (a-SiN$_X$:H). The plasma-enhanced chemical vapour deposition technique is described and the impact of process conditions on film properties is investigated. The passivation stability over time of Al$_2$O$_3$/a-SiN$_X$:H stacks is studied in this chapter.

- The fourth and the fifth chapters investigate passivation degradation mechanisms related to Al$_2$O$_3$/a-SiN$_X$:H stacks. First, the fourth chapter address the degradation occurring at the c-Si/Al$_2$O$_3$ interface, *i.e.* blistering. Then, the fifth chapter explores the impact of a-SiN$_X$:H capping on the electrostatic properties of the passivation stack.

Finally, this work is summarised in a conclusion section, which summaries our achievements and provides further research perspectives.

Chapter **1**

Theoretical and experimental context

Contents

.

1.1 Solar cells physics

1.1.1 Device performance

The solar cells power conversion efficiency (η) as defined by equation (1.1) cannot exceed 29.4 % for a single bandgap material like silicon [53]. Indeed, photons having energy greater than the bandgap will lose the difference by thermalisation while photons with energy lower than the bandgap will not be absorbed. For a more complete description of the solar cells physics, the reader may refer to the book by Peter & Uli Würfel [54], while we focus here on parameters relevant to understand the surface passivation.

$$\eta = \frac{I_{SC} \cdot V_{OC} \cdot FF}{P_{in}}$$

(1.1)

With:

- I_{SC} : the short-circuit current
- V_{OC} : the open-circuit voltage
- FF : the fill factor
- P_{in} : the incoming solar power

As previously mentioned, the conversion efficiency of 29.4 % has never been reached so far due to several losses among which photo-generated carrier recombination is one of the most important. Electrons and holes can recombine by different mechanisms (see next section) reducing the three numerator factors of the equation (1.1) numerator. In the case of a constant photon flux reaching the silicon surface, the electron-hole pair generation rate (G) in the silicon can be assumed constant over time. The carrier density (Δn) is then only proportional to the recombination rate (R) in the device. The V_{OC} is the most impacted by the carrier recombination as its value is proportional to the photo-generated carrier density in silicon. For a p-type c-Si cell with a dopant density N_A, the V_{OC} can be expressed by equation (1.2). The passivation aims to reduce the recombination in a solar cell and its quality is often judged after the solar cell V_{OC}.

$$V_{OC} = \frac{kT}{q} \ln \left(\frac{(N_A + \Delta n)\Delta n}{n_i^2} \right)$$

(1.2)

With:

- k : the Boltzmann constant
- T : the absolute temperature
- q : the elementary charge
- n_i : the intrinsic carrier density
- Δn : the injected carrier density

1.1.2 Recombination

Recombination can be divided in two terms, the one that is intrinsically linked to the use of semiconductors and the one that is due to external factors.

Regarding intrinsic recombination mechanisms, the first one is the radiative recombination process which is the exact opposite of the photo-generation (Figure 1.1.a). An electron-hole pair recombines, emitting a photon with an energy equal to the bandgap value. Due to the indirect bandgap nature of silicon, a phonon is required to assist the reaction, decreasing the recombination rate importance associated to this mechanism. The second mechanism is the Auger recombination which involves the interaction of three carriers. It consists in the recombination of an electron from conduction band and a hole from the valence band, but rather than a photon emission, the energy is transferred to a third free carrier. This one can be either an electron in conduction band (eeh process, Figure 1.1.b) or hole in the valence band (ehh process, Figure 1.1.c). The newly exited carrier then thermalises back to the band edge.
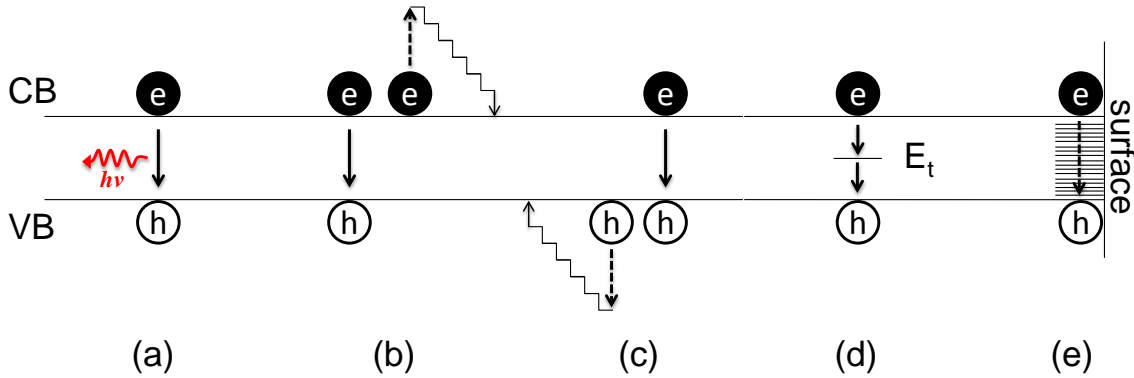
Figure 1.1: Schematic representation of (a) radiative recombination; (b) Auger recombination involving eeh (c) ehh; (d) SRH recombination and (e) surface recombination

Regarding extrinsic recombination, the one occurring through defects, named Shockley-Read-Hall (SRH) recombination [55], is directly linked to the crystalline quality of the silicon. The SRH process occurs via discrete energy levels (E_t) present in the bandgap that provide intermediate states available for electrons and holes recombination in a two, or more steps (Figure 1.1.d). These intermediate levels, designated as traps, are introduced by point defects (vacancy, interstitial atoms, substitutional atoms), 2D defects (dislocations), 3D defects (complexes, precipitates) and by the interaction between these defects. By controlling the crystal purity and quality, SRH recombination in the bulk of silicon can be strongly limited while there is another similar recombination mechanism that will remain even for a perfect silicon crystal. Silicon wafer surfaces are a brutal interruption of the crystalline lattice periodicity and are thus two dimensions defects. Indeed, silicon surface atoms do not have their 4 neighbours, so they present one or more electronic orbitals that are not participating in bonding and are named dangling bonds. Surface dangling bonds generate a high quantity of trap levels continuously distributed over the bandgap, providing a very efficient non-radiative recombination pathway (Figure 1.1.e).

The surface recombination rate (U_{surf}) can be expressed by equation (1.3). Depending on their energy levels in the bandgap, traps catch more or less efficiently one type of carriers. A capture cross-section for holes (σ_p) and electrons (σ_n) is defined for each type of traps. Traps with energies close to the centre of the bandgap are the most effective recombination centres, designated as deep defects in opposition to the shallow defects with energy levels near band edges.

$$U_{surf} = \int_{E_V}^{E_C} \frac{v_{th}(n_S p_S - n_i^2)}{\frac{n_S + n_1(E_t)}{\sigma_p(E_t)} + \frac{p_S + p_1(E_t)}{\sigma_n(E_t)}} \cdot D_{it}(E_t) \cdot dE_t \qquad (1.3)$$

$$n_1 = n_i \exp\frac{E_t - E_i}{k_B T} \qquad (1.4)$$

$$p_1 = n_i \exp\frac{E_t - E_i}{k_B T} \qquad (1.5)$$

With:

- v_{th} : the thermal velocity of charge carriers, assumed identical for electrons and holes

- n_s : the electron concentration at the surface

- p_s : the hole concentration at the surface

- n_i : the intrinsic carrier density

- n_1 : statistical factor as defined by equation (1.4)

- p_1 : statistical factor as defined by equation *(1.5)*

- E_t : the energy level of the trap

- D_{it} : the interfacial trap density

- T : the temperature

- k_B : the Boltzmann constant

- E_i : the intrinsic energy level of the trap

1.1.3   Passivation

As commonly used in metallurgy, surface passivation aims to prevent degradation mechanism of the material properties. Concerning silicon, passivation designates more the inhibition of recombination mechanisms in order to preserve its electronic properties, rather than preventing its corrosion. As intrinsic recombination processes are unavoidable, silicon passivation aims at reducing extrinsic recombination. While SRH recombination occurring in the volume of silicon can be greatly reduced by enhancing the quality of the metallurgical processes, the presence of surfaces and so surface recombination cannot be avoided. In fact, the large surface to volume ratio of silicon solar cells makes surface recombination a limiting factor to conversion efficiency. From equation (1.3), it can be seen that there are two approaches to reduce surface recombination.

The first approach consists in the reduction of the D_{it} and is named the chemical passivation. To remove energy states introduced in the bandgap by dangling bonds, one just has to satisfy this bonding requirement, as oxygen is doing when native oxide is growing at the silicon surface. The bandgap difference between silicon (1.12 eV @ 300 K) and its oxide (8.9 eV @ 300 K) is high enough to keep carriers within the silicon. However, the uncontrolled growth of native oxide on silicon surface generates a defective layer that has trap levels in its bandgap (Figure 1.2). The native oxide does not provide an efficient surface passivation and has to be replaced by another material.

Figure 1.2: Band alignment between c-Si and SiO₂. The yellow area corresponds to the bandgap between the valence band maximum (VBM) and the conduction band minimum (CBM). The zero of energy is chosen at the VBM of SiO₂. Calculated levels for various point defects in a-SiO₂ are reported on the graph. The exponent number is the net charge of the defect. From the left to the right of the horizontal axis defects are: Si-Si bonds; Si dangling bonds (Si_{DB}); Si-H; O dangling bonds (O_{DB}); peroxyl bridges (O-O); and the planar O₃⁺ (index means triply coordinated). Adapted from [34]

The second passivation approach consists in the reduction of either majority or minority carrier density at the surface and is named the field effect passivation. In order to repel one type of carrier from the surface, energy band bending can be set-up using a doping profile below the surface, as it is done on the Al-BSF back-surface. Another way is to use electrostatic charges deposited on the surface, *e.g.* corona charges [56], or embedded within an insulator material deposited on the surface. This second way is the most popular as it allows combining chemical and field effect passivation. Many dielectrics present an electrostatic charge density referred as "fixed charge density" (Q_f). The silicon surface can then be modified from an accumulation mode to an inversion mode, depending on the charge polarity, their areal density and the doping level of silicon. Although both modes effectively reduce the surface density of one type of carrier, the inversion mode causes a parasitic shunting in the transition volume where the minority and majority carrier density become equal, promoting recombination (Figure 1.3) [57]. It is why materials with negative Q_f are preferred on p-type while materials presenting positive Q_f are generally used on n-type.

Figure 1.3: Electron and hole density below the Si surface for (a) p-type and (b) n-type Si under influence of a negative fixed surface charge of Q_f =2·10^{12} cm^{-2}; (c) band bending under influence of Q_f. Data simulated by PC1D for 2 Ω.cm wafers under illumination. Taken from [37].

Historically, silicon oxide of a very good quality has been grown on the surface of wafers by dry oxidation. This thermal oxide has proven its effectiveness, reducing D_{it} to values as low as 10^{10} $eV^{-1}.cm^{-2}$ at mid-gap [58]. However, the high temperature required to grow it (~1000 °C) is not cost effective and can even degrade the bulk quality of silicon. Nowadays, several deposition techniques, such as ALD (presented in chapter II) or PECVD (presented in chapter III), allow depositing passivation materials at lower temperature (<450 °C). Amorphous hydrogenated silicon nitride (a-SiN_X:H) is the most widely used to passivate n-type surfaces as it presents positive Q_f while the negative Q_f of Aluminium oxide (Al_2O_3) predestines it to p-type surfaces, like the back-surface of PERC cells. Albeit the passivation properties of a-SiN_X:H are well understood, several questions about Al_2O_3 passivation properties need and will be addressed in this thesis.

1.1.4   The effective lifetime of minority carriers

Practically, the recombination rate is rarely considered by itself to evaluate the passivation. The effective lifetime (τ_{eff}) of minority carriers as defined by equation (1.6) is generally easier to handle. It represents the average time that a photo-generated carrier can stay as a free carrier in silicon before it recombines. A higher lifetime is the equivalent of a lower recombination rate. Exactly like the recombination rate (U), the effective lifetime can be split in intrinsic (τ_{int}) and extrinsic lifetimes (τ_{ext}), linked to each recombination mechanism (equation (1.7)).

$$\frac{\Delta n}{U} = \tau_{eff} \qquad (1.6)$$

$$\frac{1}{\tau_{eff}} = \frac{1}{\tau_{int}} + \frac{1}{\tau_{ext}} = \left[\frac{1}{\tau_{Radiative}} + \frac{1}{\tau_{Auger}} \right] + \left[\frac{1}{\tau_{SRH}} + \frac{1}{\tau_{surface}} \right] \qquad (1.7)$$

For high-quality silicon monocrystals grown by the Czochralski (Cz) or the float-zone (FZ) process, the SRH component can be neglected. Thus, the effective lifetime can be split in two components: a bulk lifetime (τ_{bulk}) related to intrinsic recombination, and two surface recombination velocities (SRV) related to recombination occurring at the front (S_{front}) and at the back (S_{back}) surfaces of the silicon wafer which has a thickness of W (Equation 1.8) [59]. Experimentally, to estimate SRV, samples fabricated for lifetime measurements, hereafter referred as lifetime samples, should have equivalent surfaces. Thus, both surfaces of the silicon wafer are passivated with the same material. S_{front} and S_{back} are assumed to be equal and the effective lifetime can be expressed as a function of the effective SRV (S_{eff}), τ_{bulk} value being tabulated.

$$\frac{1}{\tau_{eff}} = \frac{1}{\tau_{bulk}} + \left[\frac{W}{2 \cdot S_{eff}} + \frac{W^2}{D \cdot \pi^2}\right]^{-1} \qquad (1.8)$$

where D is the diffusion constant of the excess carriers.

Using the works of Altermatt *et al.* for the radiative recombination and the one of Richter *et al.* for the Auger recombination, the intrinsic silicon recombination rate and equivalent bulk lifetime can be modelled [60-62]. As plotted on figure Figure 1.4, the intrinsic lifetime is mainly ruled by the Auger mechanism as the carrier density increases above 10^{15}cm^{-3}. Quantitatively, SRV < 10 cm.s^{-1} is the typical value required to produce solar cells with η>20 % [63]. This SRV value will be our target.
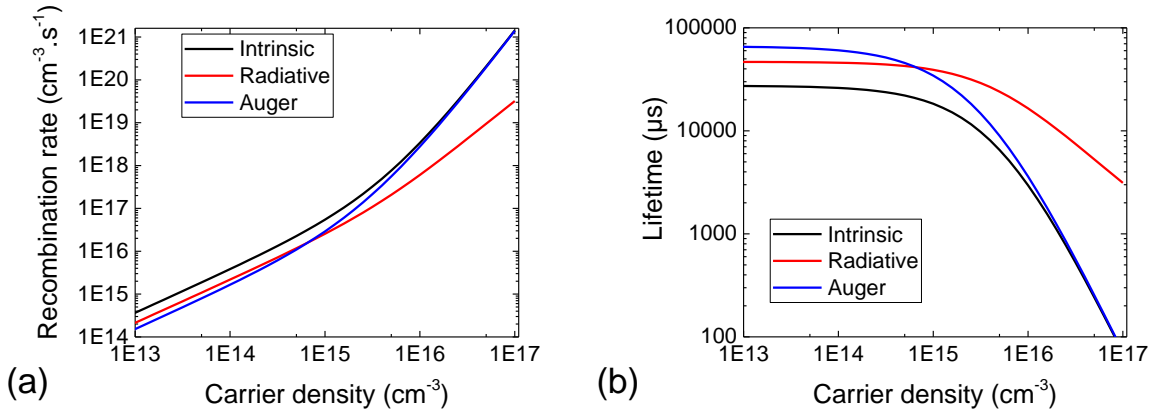
Figure 1.4: (a) Recombination rate and (b) equivalent bulk lifetime for a c-Si wafer with a dopant density N$_A$ of 4.68·10^{15} cm^{-3} at 300 K.

1.2   Characterisation techniques

1.2.1   Electrical properties

1.2.1.1   Photoconductance decay

The photoconductance decay (PCD) is the most widely used technique in the PV industry to measure the effective lifetime of minority carriers in silicon [64]. The technique is completely non-destructive. The sample is placed on top of an inductive coil that records the conductance decreasing rate in silicon due to carrier density variation. The signal is then interpreted in terms of effective lifetime as a function of the minority carrier density by the characterisation tools (Figure 1.5). The change in the carrier density is produced on purpose by external illumination, either with a flash lamp like on the "WCT-120 Sinton lifetime tester" from Sinton Instruments or a laser (λ=808 nm) like on the "LIS-R2" from BT Imaging. Both of these characterisation tools have been used in this work, each one having its own advantages, extremely quick measurement for the former and the possibility to obtain photoluminescence maps for the latter. Both tools provide similar results for minority carrier density exceeding $5 \cdot 10^{14}$ cm^{-3} (Figure 1.5). In this manuscript, the effective lifetime is always reported for minority carrier density of 10^{15} cm^{-3} if not stated otherwise.
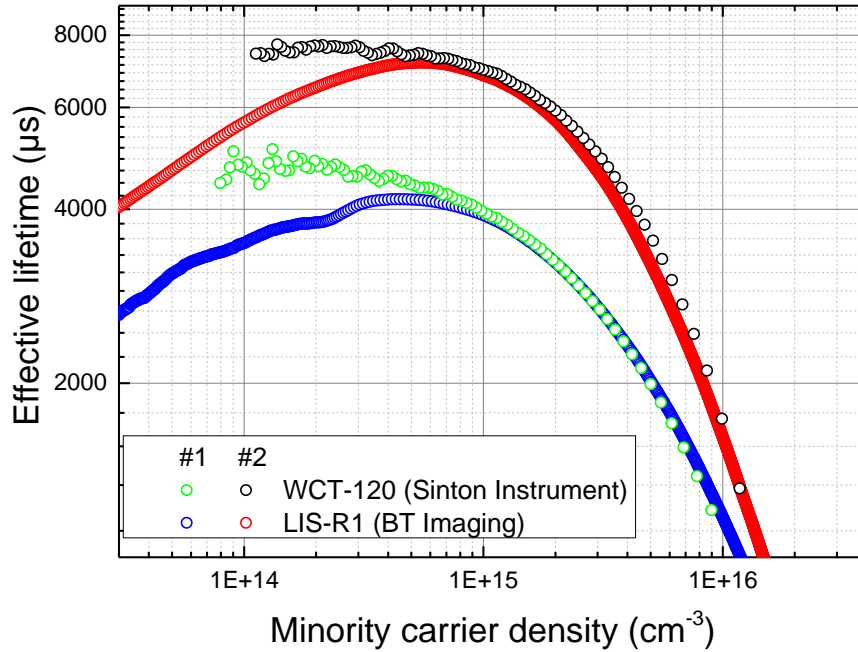
Figure 1.5: Effective lifetime of two samples (p-type) passivated by Al$_2$O$_3$/a-SiN$_X$:H stacks. Sample #1 has a 60 ALD cycle thick Al$_2$O$_3$ layer and is a quarter of 100 mm wafer while sample #2 has a 100 ALD cycles thick Al$_2$O$_3$ layer and is a full 100 mm wafer.

1.2.1.2   PCD calibrated photoluminescence mapping

The photoluminescence (PL) consists of the emission of photons following absorption of photons. As discussed in section 1.2.1, photo-generated carriers can recombine by non-radiative ways (Auger, SRH) or by the radiative one, emitting a photon that can be detected by a CCD camera of 1024x1024 pixels like in the "LIS-R2" from BT Imaging. For a given carrier density, the higher the radiative recombination rate the better the passivation. Thus, the contrast in photoluminescence maps is directly proportional to the lifetime variations. The raw picture allows evaluating the spatial uniformity of the surface passivation, but the calibration of the PL intensity by PCD is more useful to directly obtain a lifetime mapping and assess defects impact on lifetime. For example, on Figure 1.6, the oblong spot in the middle of the sample that presents a lifetime three times lower than the rest of the surface corresponds to passivation damages caused by X-ray reflectometry measurement.
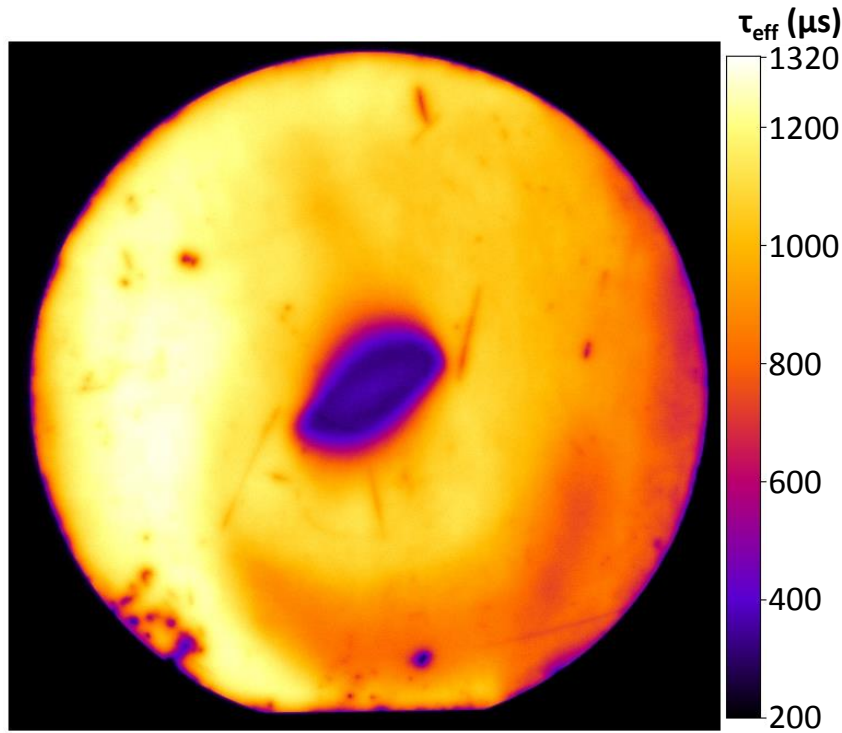
Figure 1.6: PCD-calibrated photoluminescence mapping of an intrinsic wafer of 100 mm diameter, passivated by 1000 ALD cycles deposited at 300 °C. The picture is taken for a minority carrier density of $2 \cdot 10^{15} cm^{-3}$.

1.2.1.3   Corona Oxide Characterisation Of Semiconductor

The corona oxide characterisation of semiconductors (COCOS) is a widely used technique to assess the D_{it} and the Q_f of a passivation layer deposited on silicon. The method can be summarised as follows: electric charges are deposited on top of the passivation layer with a corona gun thus changing the electric field in the dielectric and in the semiconductor. The modified surface potential is then quantified by a Kelvin probe. This procedure is repeated several times in order to switch from the accumulation to the inversion mode at the c-Si surface. Then recorded potential values allow to estimate D_{it} and Q_f values [65, 66].

Some authors even proposed to use corona charges as permanent field effect enhancer of surface passivation [56]. Theoretically the technique is non-destructive as the corona charges should be removable with isopropanol alcohol. Practically, we never manage to recover the initial passivation properties after charges removal. We then considered this technique as destructive and used it with parsimony.

In this work we used the "PV-2000A" from Semilab to perform COCOS. It has to be mentioned that the tool provides reliable measurement for single films deposited on c-Si (cross-check with Capacitance-Voltage measurement at IMEC). However, as soon as Al_2O_3/a-SiN$_X$:H stacks are measured, the data provided by the tool do not make sense compared to single layer passivation. The results for the stack present much higher D_{it} and similar Q_f than the single layer while the effective lifetime measured by PCD is generally much higher for the stack than for the single layer passivation. Therefore we limited the use of COCOS to single layer measurements.

1.2.2   Optical properties

1.2.2.1   Spectroscopic ellipsometry

Spectroscopic ellipsometry (SE) is a fast and non-destructive characterisation technique that can provide information on the thickness, the refractive index, the extinction coefficient and the bandgap of the thin films. The principle of the measurement is based on the detection of the light polarisation changes upon reflection on the surface of the thin film and the c-Si substrate (Figure 1.7). Then data are fit to a model to determine optical properties of the deposited film. For a more detailed description of the physics behind SE, the reader can refer to the ellipsometry handbook [67].

Spectroscopic ellipsometry measurements have been done using a "UVISEL 2" from Horiba Jobin Yvon and data were analysed using DeltaPsi2 software. The spectra were acquired from 1.5 to 5.5 eV. In order to model silicon alloys (a-Si:H; a-SiO$_X$:H; a-SiN$_X$:H) we used Tauc-Lorentz dispersion law [68] while we used Sellmeier dispersion law for transparent material such as Al_2O_3 [69] (Table 1.1). In this work the bandgap (E_{04}) is defined as the photon energy at which the optical absorption is equal to 10^4 cm^{-1}. In order to determine dispersion law for newly synthesised material, variable angle spectroscopic ellipsometry (VASE) was done at 65°, 70° and 75° (θ_i on Figure 1.7). Once these coefficients are determined, a single acquisition at 70° was done for a routine check of already known materials.

Table 1.1: Model parameters used for most common material in this work

Properties	Al_2O_3	a-SiN$_X$:H	a-SiO$_X$:H
Model	Sellmeier	Tauc-Lorentz	Tauc-Lorentz
Parameters	A=1.89 B=0.80 λ0=141.54	E_g=2.99 ε_∞ f=1.11 A=70.73 E_0=8.92 C=7.42	Eg=3.54 ε_∞ =1.31 A=24.91 E_0=10.55 C=2.52
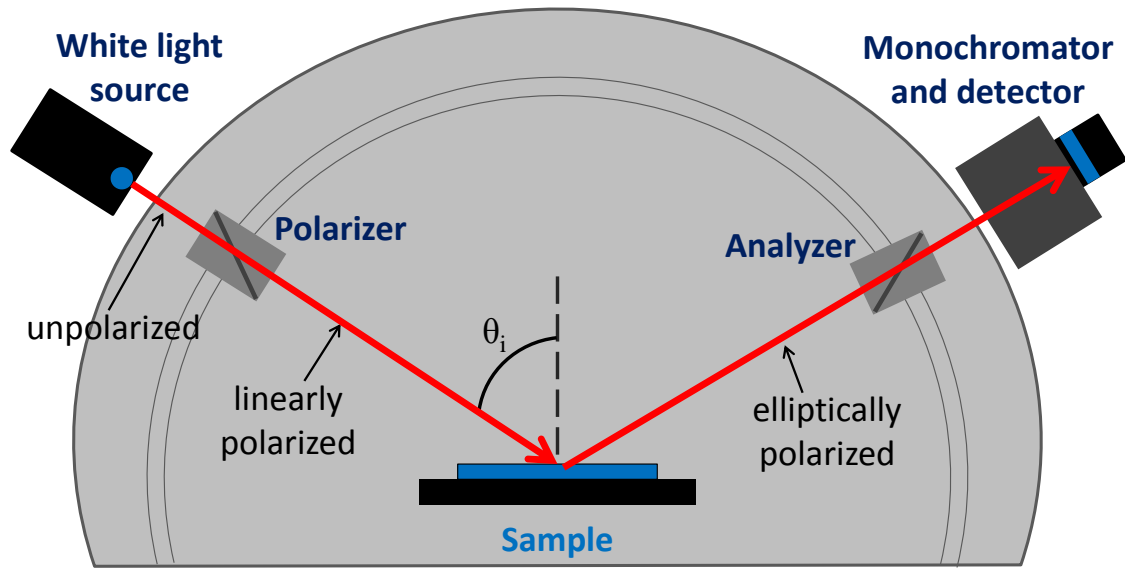
Figure 1.7: Geometry for SE measurements.

1.2.2.2   Spectrophotometry

Reflectance measurements were carried out using a "Lambda 900 UV-Vis" spectrophotometer from Perkin Elmer equipped with a 150 mm integrating sphere. Data were acquired from 250 nm to 1200 nm but the effective reflectance (R_{eff}) was determined by the equation (1.9) only between 300 nm to 1000 nm. Indeed, for the wavelength below 300 nm the solar irradiance is negligible, and for the wavelength above 1000 nm the reflectance increase is due to the back surface of the sample.

$$R_{\text{eff}} = \frac{\int_{300\,\text{nm}}^{1000\,\text{nm}} R(\lambda)S_{\text{AM1.5}}(\lambda)d\lambda}{\int_{300\,\text{nm}}^{1000\,\text{nm}} S_{\text{AM1.5}}(\lambda)d\lambda} \qquad (1.9)$$

With:

- R_λ : the spectral reflectance
- $S_{\text{AM1.5}}$: the AM1.5 solar spectral irradiance

1.2.3   Material properties

1.2.3.1   X-ray Reflectometry

X-ray Reflectometry (XRR) was used to determine the film thickness and density. It is a non-destructive analytical technique for the material bulk but it strongly degrades the electronic properties of the layer/substrate interface (Figure 1.6). XRR has been performed with a "D8 Discover" goniometer from Bruker with the specular scattering geometry depicted on Figure 1.8. Data were fit with Leptos software. XRR allows determining the thickness (from 0.1 nm to 200 nm) and the density of a layer. The interference of the waves reflected from the interfaces causes oscillations of period directly proportional to the layer thickness. XRR probes the laterally averaged electron density: the higher the electron density of a material the higher the critical angle (θ_c). While thickness can be directly determined from interfringes period, the density determination required modelling. Indeed, θc is proportional to the density of a defined material stoichiometry that can vary a lot for amorphous materials (Figure 1.9). Moreover, when the stoichiometry of the amorphous film differs from the crystalline one, the real stoichiometry of the film needs to be entered into the model to improve the accuracy of the fit. The amplitude of the fringes increases with increasing density contrast between the film and the substrate, making silicon rich layer difficult to analyse when deposited on c-Si. For a more detailed description of the technique, the reader can refer to [70].
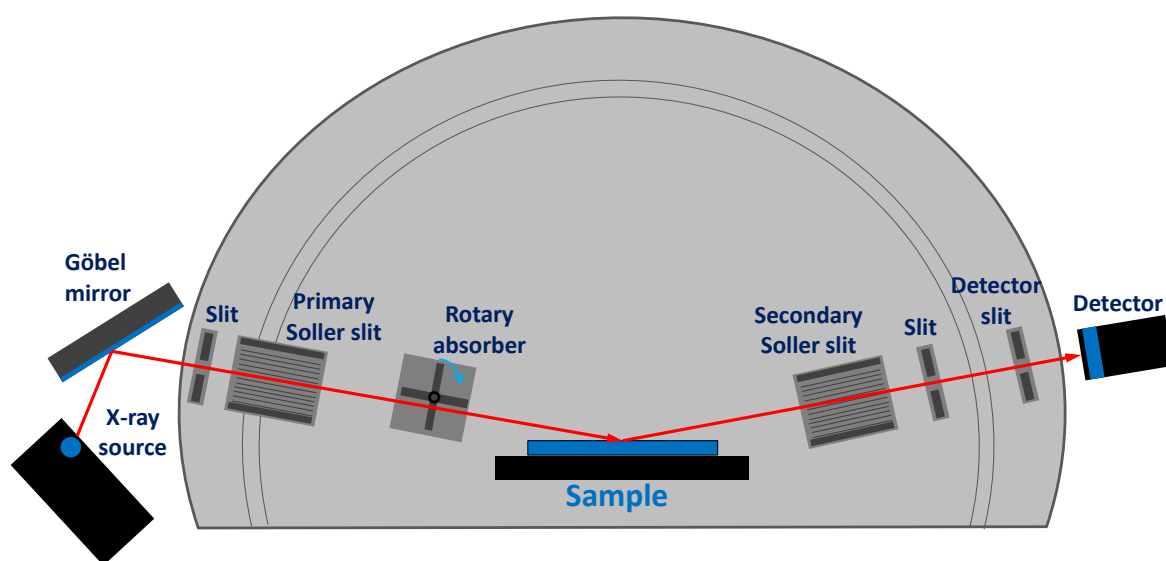
Figure 1.8: Geometry for XRR measurements. The detector slit was 0.6 mm wide, other slits were 0.1 mm wide, primary Soller was axial (2.5°) while secondary Soller was equatorial (0.3°). The X-ray source operated at a voltage of 40 kV and current 40 mA, producing a monochromatic radiation of λ = 1.54 Å (Cu K$_{a1}$).
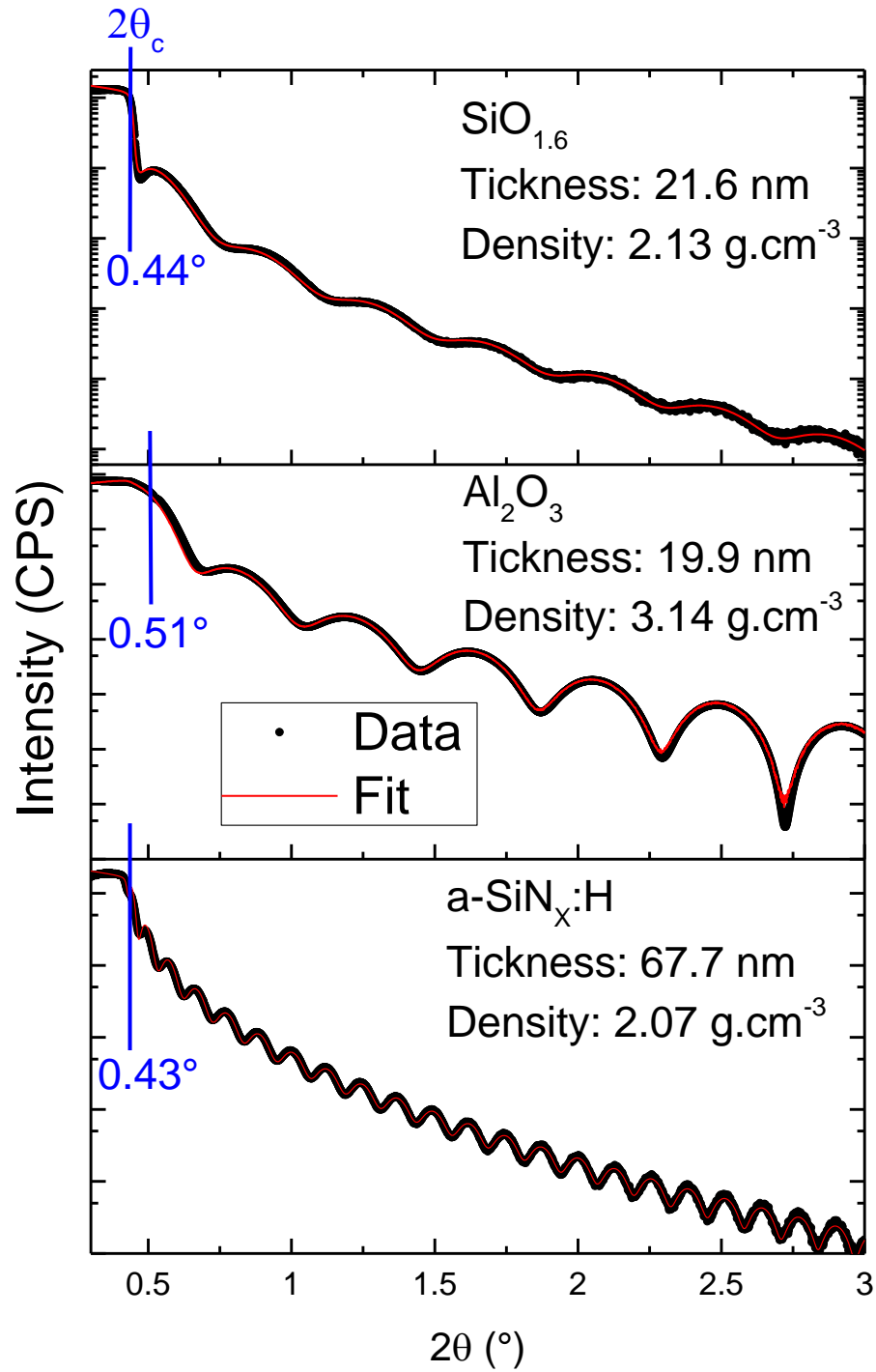
Figure 1.9: XRR experimental data (black dots) and fits (red lines) for three amorphous materials deposited on c-Si. The Al₂O₃ layer was deposited by 200 ALD cycles at 250 °C (chapter 2), the a-SiNₓ:H layer was deposited by PECVD (chapter 3) and the SiO₁.₆ was also deposited by PECVD (chapter 5). For reference, c-Si density is 2.33 g.cm⁻³.

1.2.3.2   Ion beam analysis technique

Rutherford backscattering spectrometry (RBS) and elastic recoil detection analysis (ERDA) have been used to assess the films stoichiometry and to quantify the hydrogen content respectively. The particle accelerator ARAMIS [71] hosted by the "Centre de Sciences Nucléaires et de Sciences de la Matière" (CSNSM) in Orsay (France) was used for both techniques (Figure 1.10). Materials were probed by He$^+$ ions accelerated at an energy of 1.6 MeV and data were fit with SimNRA software. Secondary Ion Mass Spectroscopy (SIMS) was mainly used to quantify carbon content in the thin films. SIMS analysis where out-sourced from the laboratory to a private company. The reader can refer to [72-74] for a detailed description of these techniques.
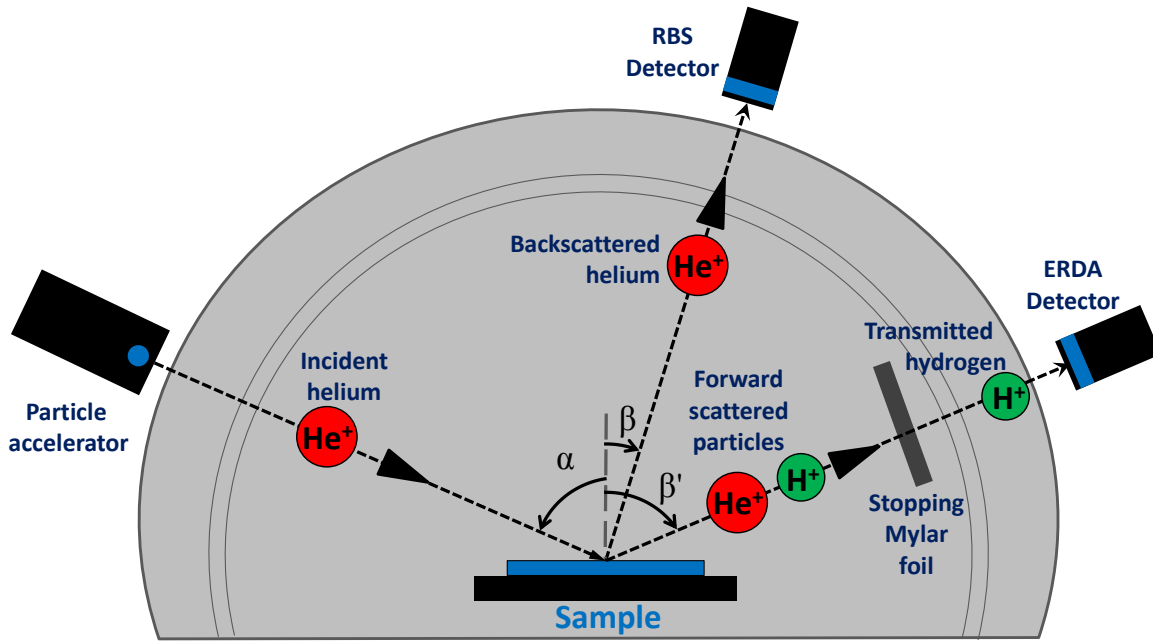
Figure 1.10: Geometry for RBS (a=0°; β=30°) and ERDA (a=75°; β'=75°) measurements. Incident He$^+$ energy was 1.6 MeV, the Mylar foil thickness was 8 µm.

1.2.3.3   Thermal Desorption Spectroscopy

Thermal desorption spectroscopy (TDS) has been performed in a homemade exo-diffusion tool pumped down to $1 \cdot 10^{-5}$ Pa and equipped with a "PRISMA 80" mass spectrometer from Pfeiffer Vacuum to measure the partial pressure of H_2 and H_2O. The heating rate of the furnace from Thermo-Fisher Scientific was 10 °C·min^{-1}.

1.2.3.4   Vibrational spectroscopy

Chemical bonding has been qualitatively evaluated by Fourier transform infrared spectroscopy (FTIR) performed using "Vertex 70" from Bruker. The reader can refer to [75] for a detailed description of these techniques.

Al$_2$O$_3$ deposition and basic properties

Contents

.

2.1 State of the art of atomic layer deposition of aluminium oxide

2.1.1 Atomic Layer Deposition

2.1.1.1 Concept

Atomic Layer Deposition (ALD) is a technique based on the self-limited reaction of precursors sequentially pulsed into a deposition reactor. This self-limited growth mechanism allows a very accurate thickness control with a good uniformity and conformality [76]. Aluminium oxide grown from trimethylaluminum (TMA) and H_2O is the most studied case as it is synthesised through a nearly perfect ALD mechanism [77, 78]. For the sake of simplicity, we consider a crystalline silicon (c-Si) substrate with a hydroxylated surface (— OH groups). As shown on Figure 2.1, the initial surface is exposed to a first TMA vapour pulse. Ligand exchange between TMA and — OH releases methane (CH_4) following equation 2.1). When all sites are saturated, chemical reaction stops by itself. A purge step is done with neutral gas (Ar or N_2) in order to remove by-products and remaining TMA. Water vapour is then pulsed into the chamber to react with methyl groups of TMA following equation (2.2), until saturation. Another purge is done to remove by-products and remaining water. The surface presents hydroxyl groups and is ready for the next ALD cycle. By repeating the ALD cycle three times, a layer of roughly 3 Å is grown on the substrate surface, with a growth per cycle (GPC) of 1 Å. The separation between each step can be temporal or spatial, the latter giving faster deposition rate than the former for a similar GPC [79-81].

$$nOH^* + Al(CH_3)_3 \rightarrow O_nAl(CH_3)^*_{3-n} + nCH_4 \tag{2.1}$$

$$Al(CH_3)^* + H_2O \rightarrow AlOH^* + CH_4 \tag{2.2}$$

$$Al(CH_3)^* + \frac{4}{3}O_3 \rightarrow AlOH^* + CO_2 + H_2O \tag{2.3}$$

$$Al(CH_3)^* + 4O \rightarrow AlOH^* + CO_2 + H_2O \tag{2.4}$$
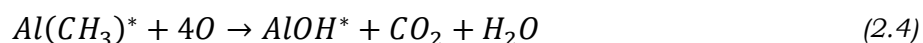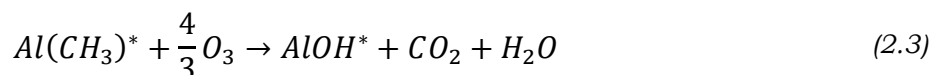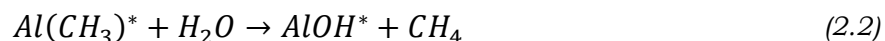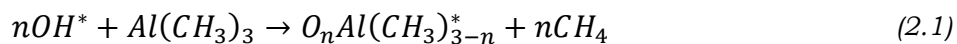
a surface group is denoted by (*) and n = 1 or 2

The self-limited growth of ~1 Å/cycle is theoretically verified over a certain range of deposition temperatures called ALD window. In reality, there is a strong variation of the GPC depending on the process conditions. The complete site saturation is never reached, as demonstrated by Ylivaara et al. [9] that repeated five times each half-cycle to increase the GPC. Several factors prevent perfect ALD growth as presented in Figure 2.1. Some important ones are: i) steric hindrance of precursors [35, 77, 82, 83], ii) lack of precursor reactivity [84] and iii) self-dehydroxylation of the surface, *i.e.* elimination of — OH groups. The last two factors both depend on the surface temperature [78, 85]. Material properties resulting from different deposition temperatures are expected to vary and will be discussed below.

The ALD process relies on thermal activation of precursors and is typically referred as thermal ALD. Water can be replaced by other oxidants such as ozone (O$_3$) [86, 87]; a mix of H$_2$O and O$_3$ [88, 89]; ammonium hydroxide (NH$_4$OH) [90] or oxygen radicals produced by an oxygen plasma [91]. The latter mostly relies on the oxygen dissociation in the plasma and is referred as plasma-enhanced or plasma-assisted ALD (PE-ALD or PA-ALD). The oxidation pathways provided by these alternative precursors are more combustion-like reactions as described in Equations (2.3) and (2.4).
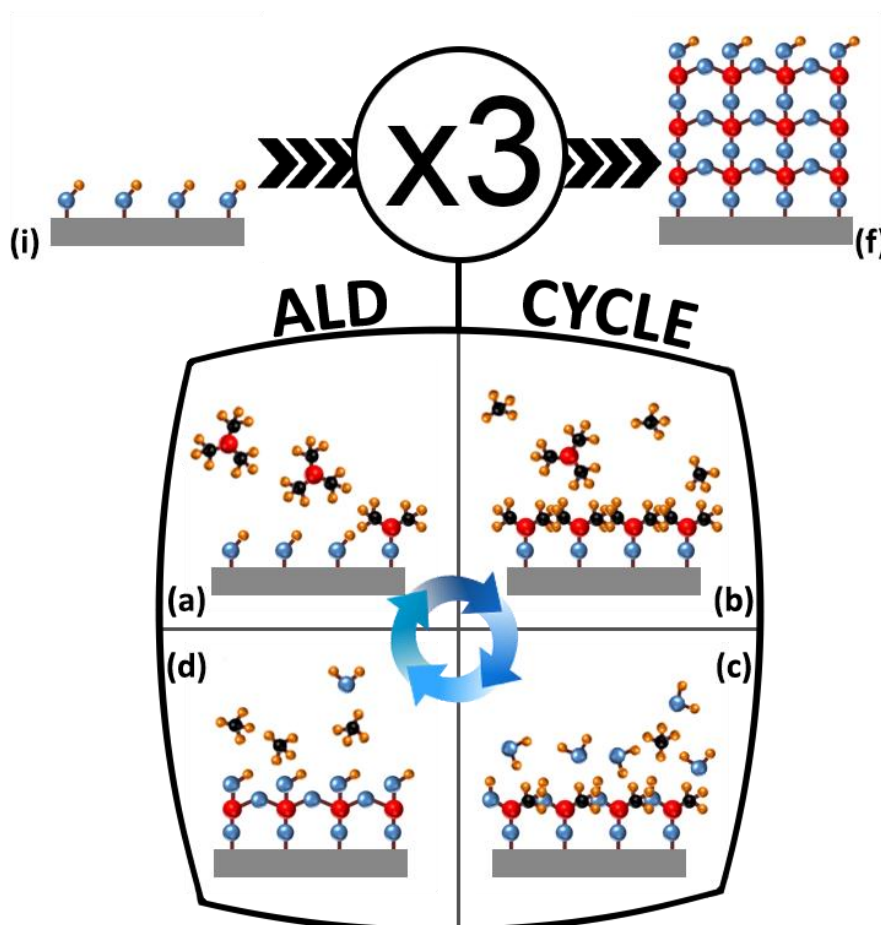
Figure 2.1: Principle of ALD process based on TMA and H$_2$O. Blue, yellow, red and black spheres are atoms of oxygen, hydrogen, aluminium and carbon respectively. An ALD cycle consists of (a) TMA pulse (b) Purge of by-products and remaining TMA (c) H$_2$O pulse (d) purge of by-products and remaining H$_2$O. From initial surface (i), by repeating the ALD cycle 3 times (from a to d) the final surface (f) is covered by an ALD film of approximately 3 Å.

2.1.1.2 Importance of the initial surface

Native oxide, which is naturally present on the c-Si surface under standard conditions, serves a good nucleation surface for growth of Al$_2$O$_3$ by ALD. Indeed, TMA efficiently reacts with both silanol groups and siloxane bridges that are present at the oxide surface [92-95]. However, this oxide contains electronic defects (P$_B$ type recombination centres), which are undesirable for c-Si surface passivation [96].

In microelectronics and most of the PV industry, native oxide is either removed and/or replaced by a thin and well-defined thermal or chemical oxide (5~40 Å) [97-100]. Chemical (or thermal) silicon oxide protects the c-Si surface from further uncontrolled oxidation, thus simplifying the storage of the wafers during the manufacturing process [101]. Such an oxide, however, is not a prerequisite to the growth of Al_2O_3 by ALD. After removal of the native oxide by HF, the c-Si surface consists of Si-H groups which react neither with TMA nor water [83, 102-104]. Just above 300 °C, water starts to oxidise the silicon surface, offering nucleation sites to TMA, which starts decomposing in the same temperature range [104, 105]. The interaction between H-terminated Si surface and the ALD cycle is not well understood. Experimentally, a Volmer—Weber growth mode (island growth) has been identified during the first tens of thermal ALD cycles, switching to a Frank—van der Merwe growth mode (layer by layer), when islands start to collapse [83, 106]. Despite an initial H coverage of the Si surface, an interfacial SiO_x layer is formed between the c-Si substrate and the Al_2O_3 layer. Its origin is believed to be related to substrate oxidation during the first ALD cycles. It is noted that reactive plasma oxidation gives an interfacial oxide 3 times thicker (1.5 ± 0.5 nm) than the water oxidation (0.5 ± 0.3 nm) [107, 108].

2.1.1.3   Process definition

For industrial applications, the thermal ALD process involving water oxidation is the simplest. Thanks to spatial ALD, it allows a deposition throughput of more than 3600 wafers per hour [81]. It is one of the reasons to focus on the passivation properties provided by this oxidant despite the fact that PE-ALD has been recognised to offer a higher passivation level [109]. One drawback of thermal ALD technique is the large back deposition, *i.e.* deposition of the material on the edge of the back surface, even if the substrate is placed on a very flat substrate holder. Gas diffusion between the wafer and the holder can hardly be avoided in temporal ALD systems while in spatial ALD tools, neutral gas flux repel precursor from the back surface.

In this doctoral work, the temporal ALD system "R-200 advanced" from Picosun with the thermal ALD recipe described in Table2.1 was used. As illustrated on Figure 2.2.a, the deposition of the front surface in a first run and then the back surface in a second run generates a thicker layer at the edge of the wafer. For a wafer having a diameter of 100 mm, this thicker crown, ~15 mm wide, represents 50 % of the surface. This strong surface inhomogeneity is not the only problem. To estimate SRV, lifetime samples should have equivalent surfaces. The first deposited layer will undergo twice the thermal budget of the deposition, while the second surface might see its native oxide regrowth during the deposition of the first side. To solve these problems of back deposition and symmetrical passivation, a specific substrate holder was used (Figure 2.2.b). It allows diffusion of precursors on both surfaces, providing homogeneously and symmetrically passivated samples in a single deposition run.

Table 2.1: ALD cycle used in this thesis. Deposition chamber pressure is around 10 Pa and continuously flowed by 600 sccm of nitrogen.

TMA	→	Purge	→	H_2O	→	Purge	Total duration
0.1 s		4 s		0.1 s		6 s	10.2 s/cycle
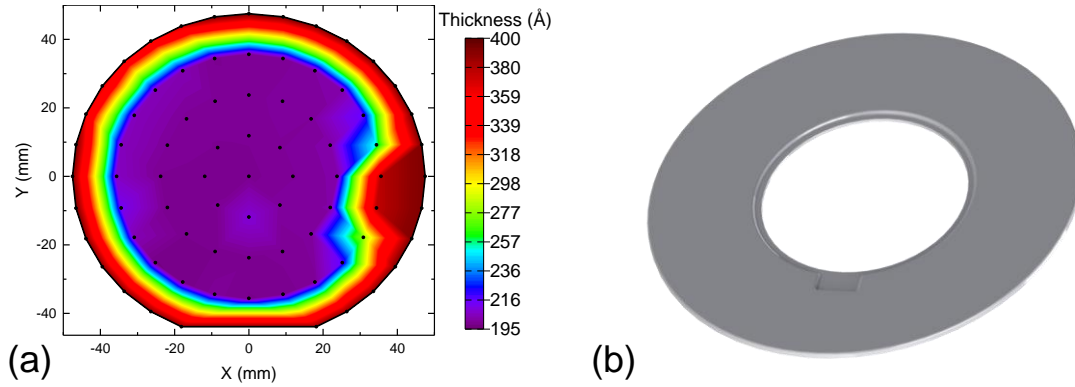
Figure 2.2: (a) Thickness mapping (80 points) obtained by SE after the deposition of 200 ALD cycles on each side. (b) Opened substrate holder allowing a double side deposition.

2.1.2   Material properties

In order to evaluate material properties resulting from our ALD cycle, we applied 1000 ALD cycles on double side polished intrinsic (5 kΩ.cm) FZ wafers at different substrate temperatures, ranging from 150 °C to 350 °C. Native oxide was not removed before the deposition, to avoid previously mentioned nucleation troubles. This native oxide was estimated by XRR to be around 8 Å thick and to have a density of 2.2 g.cm^{-3} before the Al$_2$O$_3$ deposition which is consistent with reported values in literature [110-112]. For each deposition temperature, the GPC was estimated both by XRR and by SE taking into account the presence of the native oxide. Very good agreement between these two characterisation techniques can be noticed on Figure 2.3.a. The GPC of our material is 50 % higher than the one reported by Ylivaara *et al.* [9] (at 150 °C) for the standard ALD cycle. However, GPC reported in this work is consistent with values they obtained by repeating half cycles 5 times [9] and to values reported by Groner *et al.*[8], supporting the hypothesis of an efficient surface saturation for each half cycle under our process conditions.
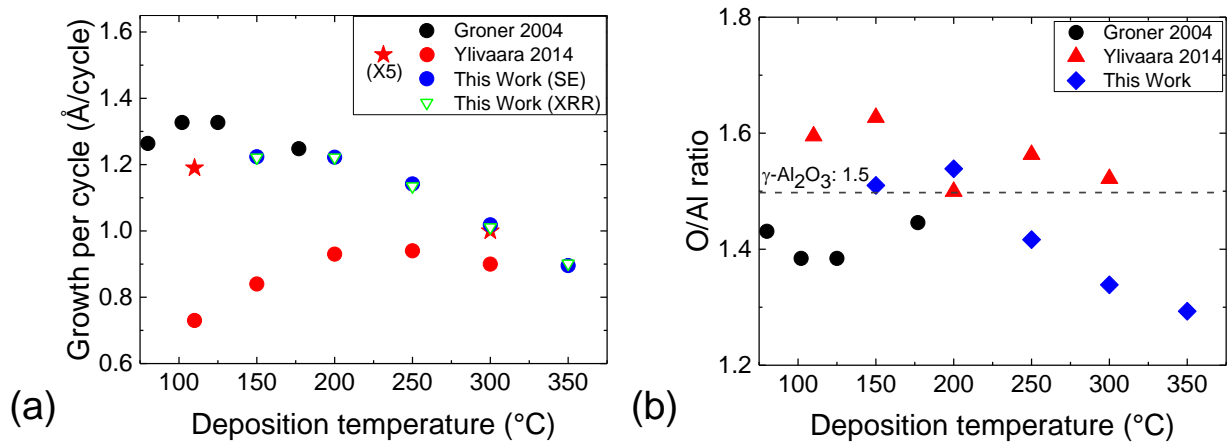
Figure 2.3: (a) Growth per cycle as a function of the deposition temperature. The stars from Ylivaara et al. are the repetition of each half cycle 5 times before switching to the other half cycle. (b) Oxygen/Aluminium ratio (determined by RBS) as a function of the deposition temperature.

The higher chemical reactivity at higher substrate temperature [84] is supported by the spread of GPC value distribution becoming narrower at 300 °C for our recipe and the one of Ylivaara *et al*. The TMA decomposition, reported to start above 300 °C [105], and surface dehydroxylation both contribute to GPC reduction between 250 °C and 350 °C. Stoichiometric γ-Al_2O_3 has an O/Al ratio of 1.5, however, in ALD grown films it varies in the range from 1 to 8 (higher oxygen content at the c-Si/Al_2O_3 interface). We observe a decreasing tendency of this ratio when the temperature increases (Figure 2.3.b). This trend is similar to the one occurring during the dehydroxylation of pseudo-boehmite to γ-Al_2O_3 [113]. Despite this high chemical reactivity at high deposition temperature, ALD Al_2O_3 films exhibit neither the same density (Figure 2.4.a) nor the same refractive index (Figure 2.4.b) than γ-Al_2O_3.
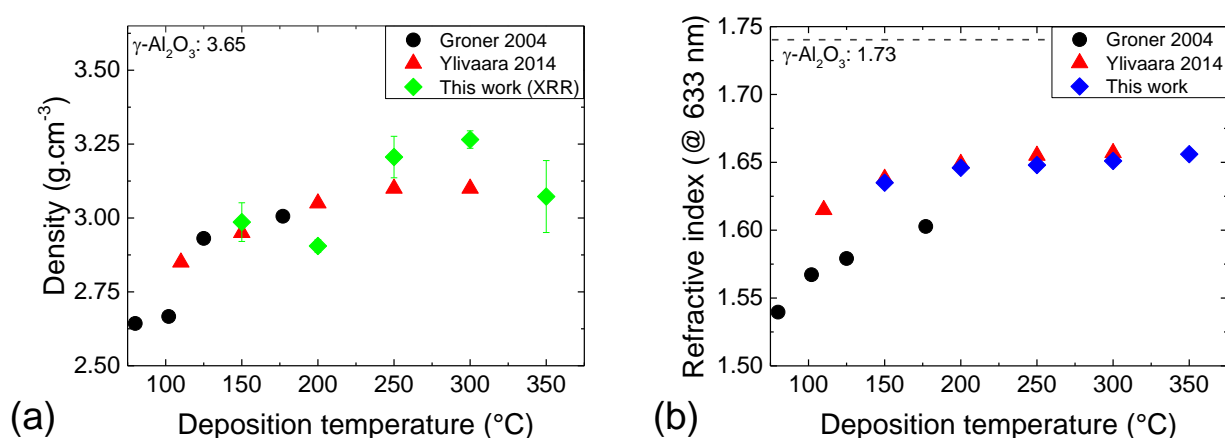
Figure 2.4: (a) Film density as a function of the deposition temperature. Reported values for this work are the average density as a density gradient is necessary to fit the data. Error bars are the standard deviation due to this gradient. (b) Refractive index determined by SE at 633 nm using Sellmeier dispersion law.

In fact, Al_2O_3 layers deposited by ALD are fully amorphous, regardless of the deposition temperature window [114]. Such amorphous films crystallise in γ-Al_2O_3 when annealed at temperatures above ~ 800 °C [115-117]. This crystallisation temperature strongly depends on the film thickness: the thinner the film, the higher the crystallisation temperature. It can be explained by the higher probability of nucleation in thicker films [118]. The resulting γ-phase is an unexpected result as its thermal stability is lower than the α-phase [119]. Aluminium coordination in the ALD films might be the reason of this crystallisation structure. Both tetrahedral (T_d) and octahedral (O_h) coordination are reported for aluminium atoms in the γ and amorphous phases while only octahedral environment is present in the α-phase [119]. Despite this closer structural configuration between the γ and the amorphous phases, the T_d/O_h ratio is higher for the amorphous one [107, 120, 121]. This predominant T_d bonding is responsible for the bandgap widening with phase transitions: E_g (amorphous) < E_g (γ) < E_g (α) [18, 122]. Comparative properties of these three phases are summarised in Table 2.2.

Table 2.2: comparative Al$_2$O$_3$ properties.

Name/Type	α-Al$_2$O$_3$	γ-Al$_2$O$_3$	ALD Al$_2$O$_3$	Refs
Crystalline structure	Rhombohedral	Cubic defective spinel	Amorphous	[1, 2]
Density (g.cm^{-3})	3.97	3.65	2.5 - 3.2	[7-10]
Refractive Index (@ 2 eV)	1.76	1.73	1.50 - 1.65	[7, 8, 12]
Bandgap (eV)	8.8	7.1 - 8.7	6.1 – 7.0	[14-20]
Conduction band offset to c-Si (eV)	2.8	2.5	2.0	[2, 22-24]
Dielectric constant	9.0	7.5	3.0 - 7.7	[19, 22, 29, 30]

During crystallisation, a mass loss of ~5 %, a densification of ~20 % and an increase of the dielectric constant and the bandgap are reported [2, 118, 123]. Most of the mass loss is attributed to contaminants outgassing. Hydrogen and carbon are the two obvious contaminants in Al$_2$O$_3$ deposited from TMA and H$_2$O due to incomplete chemical reactions or chemisorption of by-products (Figure 2.5). Carbon content is rather low (<0.5 %$_{at}$) compared to hydrogen content, up to 6%$_{at}$ for our material deposited at 150 °C. The quantity of hydrogen depends on the deposition temperature and is mainly present as hydroxyl groups [124, 125]. Dehydroxylation is pointed out to be the main mass loss mechanism during crystallisation. This is supported by two facts: i) the bandgap widening impacts mainly the valence band side, i.e. oxygen anion reorganisation, ii) the chemical environment of aluminium probed by XPS does not significantly change contrary to the one of oxygen [2, 126].
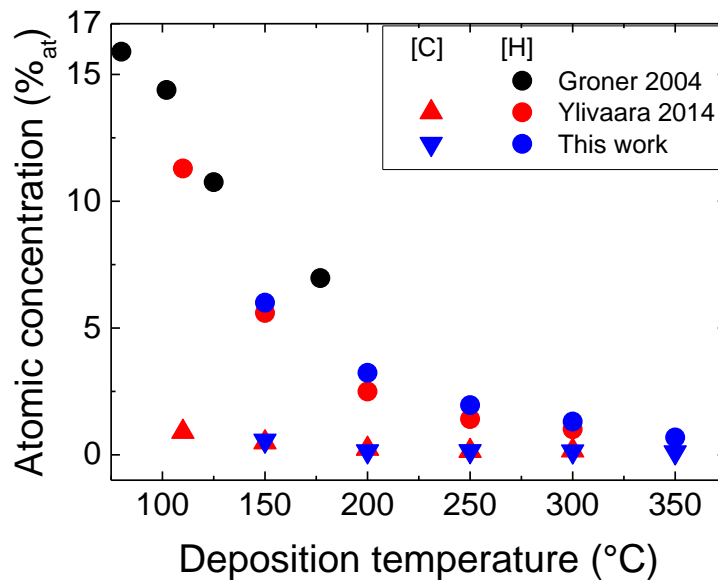
Figure 2.5: Hydrogen and carbon concentration in Al$_2$O$_3$ layers as a function of the deposition temperature. For this work, hydrogen content has been measured by ERDA while carbon has been quantified by SIMS measurements calibrated thanks to NRA.

The densification of the films is not the main reason to pay attention to this mechanism. In fact, dehydroxylation is pointed out as the main contributor to the surface passivation of c-Si by ALD Al_2O_3. As mentioned earlier, dehydroxylation starts at lower temperature than crystallisation. This can be easily observed on ERDA spectra of as-deposited samples (Figure 2.6.a). For a layer with homogeneous hydrogen (hydroxyl) distribution across its thickness, the spectra should have a Gaussian shape, like the one obtained for the lowest deposition temperature of 150 °C. The top of the energy distribution curve becomes flat or even inclined, indicating increase of hydrogen concentration variation as the deposition temperature increases. Indeed, 1000 ALD cycles take 2 hours and 50 minutes to be fully completed. The dehydroxylation probability being a function of time and temperature [127], the very long deposition duration of the films allows us to observe this gas release being strongest for the atomic layers deposited in the first place. The use of intrinsic silicon with a bulk lifetime >150 ms ensures high detection sensitivity in terms of surface passivation variation. The effective lifetime increases by three orders of magnitude as the deposition temperature increases from 150 °C to 300 °C (Figure 2.6.b). The lifetime increases exponentially from 150 °C to 250 °C, followed by an abrupt increase up to 10 ms for the deposition temperatures ≥300 °C. It suggests a higher passivation of the silicon substrate at deposition temperatures higher than 250 °C.
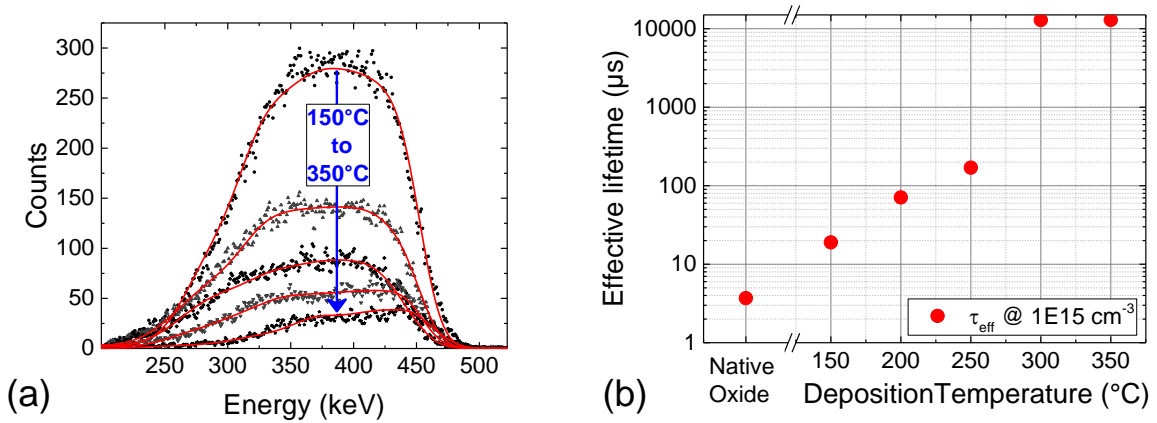
Figure 2.6: (a) ERDA spectra of the 5 samples deposited at different temperatures. Discrete points are acquired data and red curves are data fits. (b) Effective lifetime of the as deposited samples with 1000 cycle Al₂O₃.

Besides these increasing trends in material properties and passivation results, there are some constraints related to the use of ALD Al_2O_3 for c-Si solar cells surface passivation that need to be taken into account. The use of 1000 ALD cycles at 300 °C for 3 hours of deposition is not compatible for industrial applications. To keep the cost per watt of photovoltaic energy as low as possible, manufacturing throughput has to be as high as possible, up to thousands of wafers per hour. Due to low deposition rate of Al_2O_3 by ALD, passivation should be ensured with the minimum number of cycles (fewer than 100). Keeping this in mind, passivation properties offered by 20 to 200 ALD cycles will be explored in this research.

2.1.3 Passivation properties of Al₂O₃

2.1.3.1 Substrate specifications

In order to study surface passivation performance of Al$_2$O$_3$ deposited by ALD, the silicon substrates with the characteristics summarised in Table 2.3 are used within the scope of this work (unless otherwise stated). Electrical properties of these substrates are similar to those used for PERC solar cells [48]. Since the suppliers provide specifications as an interval of values, certain values were set (listed in Table 2.3) in order to perform calculations and to provide inputs to some characterisation tools, *e.g.* Sinton WTC-120. The FZ crystal growth ensures many advantages over the CZ, such as low crystalline defects and impurity content. For example, p-type Si grown by FZ method has lower oxygen content ([O]$\sim 10^{16}$ cm^{-3}) as compared to the CZ method ([O]$\sim 10^{18}$ cm^{-3}). Thus, using FZ reduces considerably the light induced degradation attributed to the formation of B-O metastable complexes [128-130]. Due to these characteristics, we estimate that SRH recombination in the bulk is negligible and thus the bulk lifetime is only limited by radiative and Auger recombination. Using Altermatt *et al.* and Richter *et al.* parametrisation [62, 131], bulk lifetime is set to 18300 µs for an injection level of 10^{15} cm^{-3}. With such a high bulk lifetime, surface passivation variations will be easily observable. Sometimes, n-type wafers with similar properties will be used. Indeed, with a bulk lifetime of 34200 µs and a surface passivation by Al$_2$O$_3$ operating by inversion layer, these samples are even more prone to detect lifetime variations.

Table 2.3: Topsil silicon substrate characteristics

Properties	Supplier specifications	Considered values
Diameter (mm)	99.8 ~ 100.2	100
Thickness (µm)	260 ~ 300	280
Growth method	PV-FZ	FZ
Orientation	<100> ± 1°	<100>
Finish	Double side polished	Double side polished
Type / Dopant	p-type / Boron	p-type / Boron
Resistivity (Ω.cm)	1 ~ 5	3
Doping level (cm^{-3})	-	$4.68 \cdot 10^{15}$
Bulk lifetime (µs)	> 1000	18300

In order to evaluate reachable lifetime values with these substrates, finite element simulations have been performed with ATLAS software from Silvaco. We benefit from the presence of a symmetry plane to simulate only one half of the sample structure as depicted in Figure 2.7.a. Continuity, transport (drift-diffusion) and Poisson's equations are solved self-consistently in the silicon, while only Poisson's equation was considered for the dielectrics. Concerning the top interface boundary condition on Al$_2$O$_3$, we set the surface work function to 4.98 eV with respect to vacuum level, corresponding to the Si bulk Fermi level in equilibrium. Concerning the back boundary condition in the middle of the Si substrate, we consider a flat band condition with zero surface recombination. In the Si bulk, intrinsic recombination is modelled using Richter's parameterisation [62]. The capture cross sections of surface defects (defined only at midgap energy) are similar to those of a c-Si/SiO$_2$ interface as an interfacial SiO$_X$ layer is always present

after Al_2O_3 deposition, even on a Si-H surface [132]. Lifetime curves as a function of the minority carrier density have been simulated for diverse D_{it} and Q_f values at the c-Si/Al_2O_3 interface (Figure 2.7.b). A low D_{it} is the prerequisite to benefit from field effect passivation provided by a high Q_f [133, 134]. For the 400 simulated conditions, the calculated lifetime values at the injection level of 10^{15} cm^{-3} have been extracted and plotted on Figure 2.7.c. Dash lines delimit an area with typically reported D_{it} and Q_f values for ALD grown Al_2O_3 synthesised with water oxidation [125, 135, 136]. In this area, minimum lifetime is 140 µs and maximum lifetime can reach 5300 µs. The solid line crossing the area represents a lifetime of 1300 µs (SRV = 10 cm.s^{-1}), i.e. the minimum passivation specification to reach. In other words, half of the commonly reported Q_f and D_{it} values provide passivation below the objective and so Al_2O_3 deposition conditions have to be optimised.
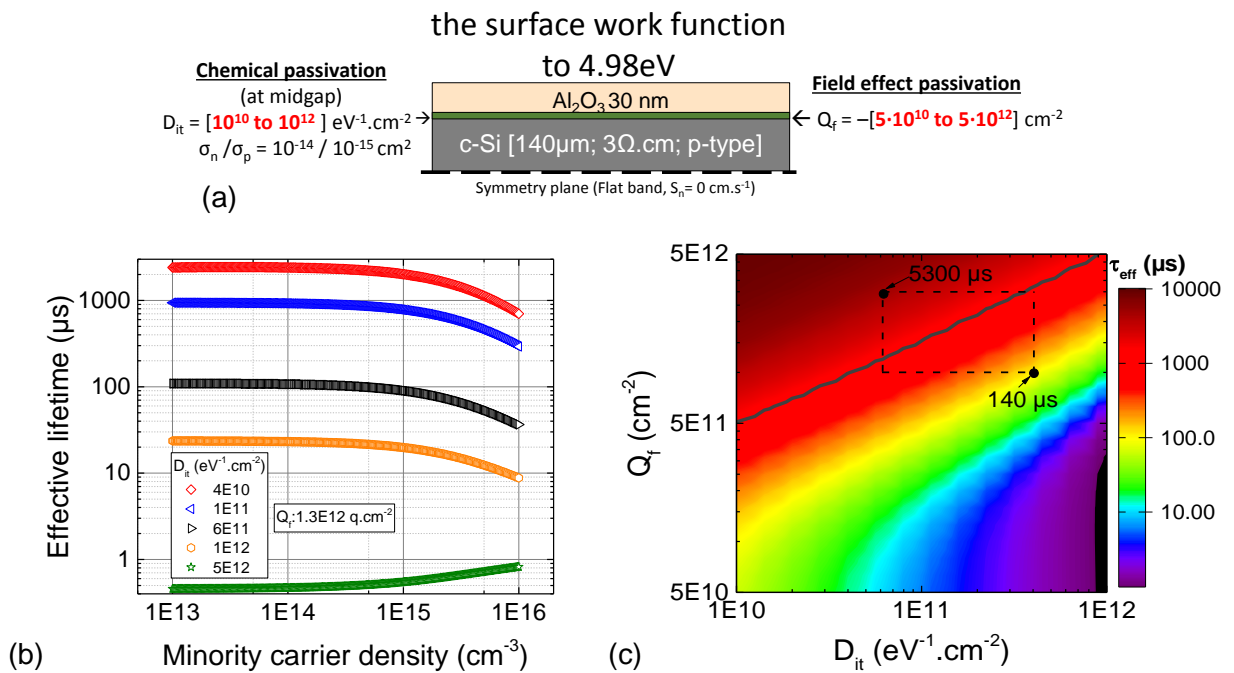
Figure 2.7: (a) Simulation model used to evaluate the minority carrier lifetime. (b) Effective lifetime as a function of the injection level for one value of Q_f and several D_{it}. (c) Effective lifetime as a function of Q_f and D_{it} for an injection level of 10^{15} cm^{-3}. The solid line corresponds to the lifetime of 1300 µs (SRV=10 cm.s^{-1}) and dashed lines delimit values reported in the literature for ALD Al_2O_3 from TMA and H_2O.

In order to explore the effects of the deposition temperature on passivation properties while reducing as much as possible Al_2O_3 thickness, 20 wafers were passivated with 20, 40, 60, 100 or 200 ALD cycles at substrate temperatures of 150, 200, 250 and 300 °C. Prior to the deposition, native oxide was removed by 30 s dip in HF (5 %), ensuring reproducible Si-H surface from one sample to another one over the 3 years of research. Contrary to the extremely thick layer previously studied, thin layers provide poor passivation levels in as-deposited state (Figure 2.8), well below the reachable 5300 µs predicted by the model (Figure 2.7.c). A slight effect of the thickness and the deposition temperature can be noticed due to the higher dehydroxylation probability of thicker films.
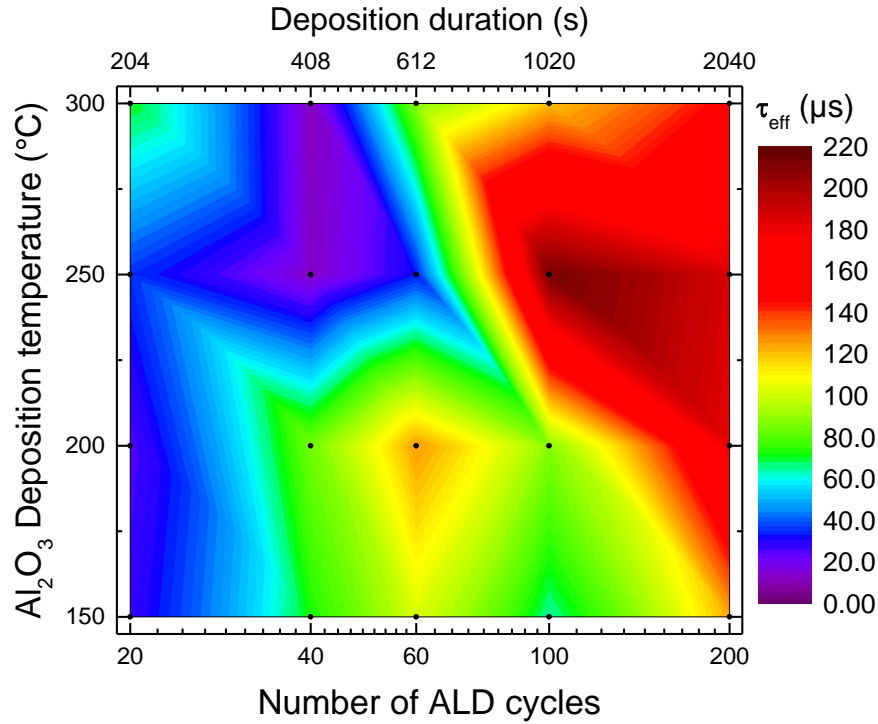
Figure 2.8: Effective lifetime provided by different Al₂O₃ thicknesses deposited at different substrate temperatures.

Passivation activation by annealing is mandatory to obtain higher lifetime values. Several phenomena take place during this post-deposition annealing (PDA), increasing the influence of both chemical and electrostatic passivation. The typical process flow used to produce lifetime samples is depicted on Figure 2.9. After annealing, the Al$_2$O$_3$ film remains amorphous even after a firing step of few seconds at temperature >800 °C. Thus, the improvement of the passivation does not happen due to crystallisation of Al$_2$O$_3$ [137] and has to be studied in more details.
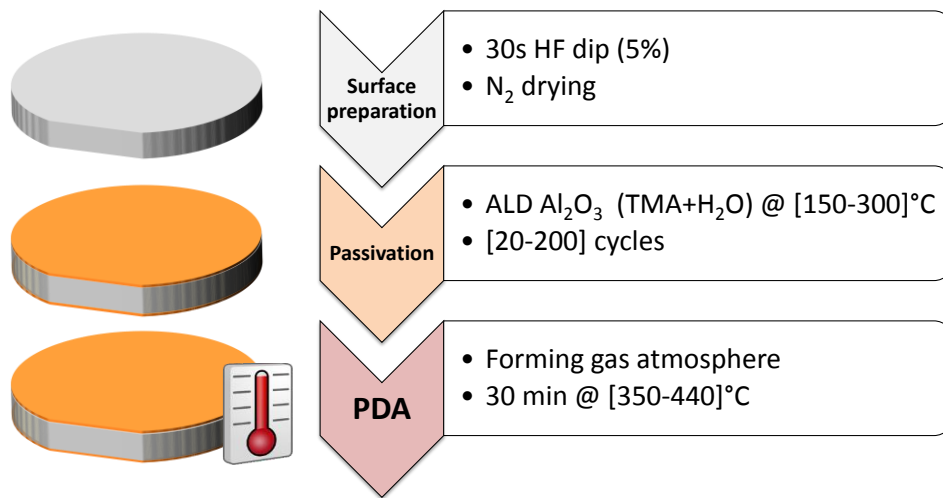
Figure 2.9: Process flow used to produce lifetime samples. Numbers between brackets are parameter ranges of interest.

2.1.3.2   Chemical passivation

Samples coated by ALD Al_2O_3 present a lack of chemical passivation in as-deposited state. Indeed, despite the presence of the passivation layer, D_{it} is not low enough to observe significant lifetime increase. The defects at the c-Si/Al_2O_3 interface are reported to be the same as for a SiO_2/c-Si interface, *i.e.* P_b type defects (dangling bonds, •Si≡Si_3, but with different physical orientations and nonequivalent Si backbonds) [138-141]. This is not surprising as the presence of an interfacial SiO_X layer is reported between the c-Si substrate and the Al_2O_3 layer even when starting the deposition on a Si-H surface. The post-deposition annealing step rubs out these chemical defects in different ways.

In the case of thermally grown SiO_2 on (100) c-Si, P_b type centres occupy ~0.7 % of the interface after the oxidation, which is still too high regarding expected passivation properties [142]. A post deposition annealing in forming gas atmosphere (N_2+H_2) is performed to fill these remaining dangling bonds. The P_b type centres start to behave like "H_2 mills" above 200 °C, optimal temperature being 400-430 °C [143]. For Al_2O_3 layers, forming gas atmosphere does not provide better hydrogenation than pure N_2 atmosphere [144]. Indeed, the hydrogen source in Al_2O_3 is the film itself; where hydrogen is bonded as hydroxyl groups. It is important to say a few words about the chemical reactions occurring here.

The hydroxyl groups can be linked to Al atoms in the bulk of the film but also to Si atoms from the initial surface as TMA does not completely saturate the Si surface with Si-OH, or from interfacial SiO_X grown during the Volmer-Weber growth mode. Dehydroxylation of vicinal silanols following equation (2.5) starts at temperatures as low as 200 °C and is maximum around 300 °C, while it is required to exceed 400 °C to release isolated silanols [145, 146]. Similar water release by aluminium oxide dehydroxylation can be described by equation (2.7), starting at temperatures above 200 °C for vicinal groups, while isolated groups start to move above 350 °C [113, 147, 148]. Water released from the aluminol groups (Al—OH) by dehydroxylation can diffuse to the c-Si surface and dissociate on dangling bonds or weak Si-Si bonds (2.6) [104, 149]. Then silicon surface can be oxidised after further dehydroxylation of newly formed silanols [150]. On the one hand, this silicon oxidation by water may explain the interfacial SiO_X thickening observed after PDA [106, 124, 136, 151]. This SiO_X thickening is reported to be more important for thicker Al_2O_3 films [100], *i.e.* with higher hydroxyl quantity. Interestingly, passivation level follows the same trend, increasing drastically with the film thickness up to a "saturation" level where the dependency on the film thickness is not verified any more, *i.e.* a certain hydroxyl quantity is necessary [152]. For thermal ALD with water oxidation, this minimal film thickness is reported to be around 10 nm [152], which might be a problem regarding the objective of film thickness reduction. On the other hand, the non-negligible H_2 release also recorded during TDS of Al_2O_3 cannot be explained by this water release [153, 154]. Generally, H_2 release is ascribed to a metallic Al/Al_2O_3 interface (equations (2.)(2.))[155]. Formation of metallic Al clusters cannot be completely excluded for layers deposited on Si-H surface with water oxidation [156, 157]. However, Al-Al bonds seem to be absent when using O_3 oxidation or Si-OH as starting growth surface [86, 157, 158], but H_2 release remains. There is here a missing source of H_2.

$$\text{Si–OH } + \text{ HO–Si } \rightarrow \text{ Si–O-Si } + \text{ H}_2\text{O}_{(g)} \qquad\qquad (2.5)$$

$$\text{Si–Si } + \text{ H}_2\text{O}_{(g)} \rightarrow \text{ Si–OH } + \text{ Si–H} \qquad\qquad (2.6)$$

$$\text{Al–OH } + \text{ HO–Al } \rightarrow \text{ Al–O–Al } + \text{ H}_2\text{O}_{(g)} \qquad\qquad (2.7)$$

$$2\text{Al } + 4\text{H}_2\text{O } \rightarrow \text{ 2AlOOH } + \text{ 3H}_{2(g)} \qquad\qquad (2.8)$$

$$2\text{Al } + 6\text{AlOOH } \rightarrow \text{ 4Al}_2\text{O}_3 + \text{ 3H}_{2(g)} \qquad\qquad (2.9)$$

$$\text{Al–OH } + \text{ HO–Si } \rightarrow \text{ Al–O–Si } + \text{ H}_2\text{O}_{(g)} \qquad\qquad (2.10)$$
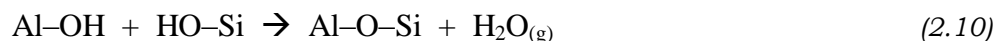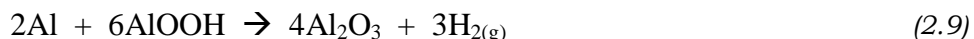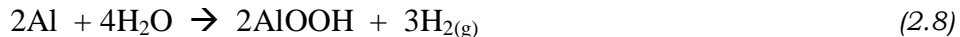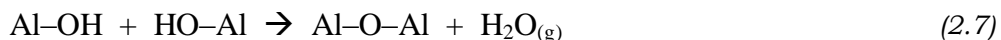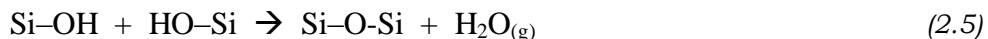
In fact, the different Al$_2$O$_3$ phases have been used for decades for their exceptional catalytic properties, particularly the γ-Al$_2$O$_3$ [119-121, 148, 159, 160]. Dehydroxylation of γ-Al$_2$O$_3$ generates strong Lewis acid sites, *i.e.* fivefold, fourfold and threefold coordinated aluminium atoms, by acidic strength [147, 161]. While aluminium atoms show Lewis activity, oxygen atoms act as Brønsted acid allowing high H mobility through protons hopping for temperatures between 200 °C and 400 °C [162-164]. Among all its catalytic properties, the γ-phase can carry out water splitting, resulting in atomic adsorbtion of O and rapid H$_2$ generation [165]. Another very interesting property of this material is its ability to perform the heterolytic splitting of H$_2$ [166].

As previously discussed, the γ-phase shares a lot of common structural features with ALD amorphous films, especially the T$_d$ aluminium coordination, which is pointed out as the core of the catalytic properties. A similar chemical behaviour is then expected from the similar chemical environment as demonstrated for different crystalline phases of alumina [121, 167]. Finally, at the interface between the substrate and the film, bonds between aluminium oxide and silicon oxide can be created following equation (2.10). This aluminosilicate interface seems to also present strong catalytic activity that is slightly different to the one of pure alumina [168-170]. It is important to underline that tetrahedrally coordinated aluminium atoms are not homogeneously distributed over the film thickness. After PDA, the T$_d$/O$_h$ ratio at the SiO$_X$/Al$_2$O$_3$ interface increases from 0.5 to 0.7 [107]. The interfacial silicon oxide thickening and reorganisation during PDA is believed to influence this preferential T$_d$ bonding. Contrary to aluminium, silicon atoms can hardly adopt octahedral configuration outside geological strata [171]. Thus silica imposes its bonding environment to alumina that can accommodate with it, generating a buffer region with predominant T$_d$ coordinated Al atoms.

To summarise, a post-deposition annealing contributes to dehydroxylation of both the Al$_2$O$_3$ film and the SiO$_X$ interface. Due to catalytic properties of T$_d$ coordinated aluminium atoms, a lot of chemical species are generated, notably at the Al$_2$O$_3$/SiO$_X$ interface. These species can diffuse both out of the film and to the c-Si surface to passivate chemical defects. This special catalytic behaviour might also explain why passivation at the c-Si/SiO$_2$ interface is improved after a PDA when Al$_2$O$_3$ capping layer is deposited on a thick (~100 nm) SiO$_2$ layer: there is a direct hydrogen injection from the Al$_2$O$_3$ into the SiO$_2$ [154, 172]. The main requirement for hydrogen release by the Al$_2$O$_3$ films is the use of PDA temperature higher than during the deposition. For example, the low deposition temperature of 100 °C provides a reasonable reduction of D$_{it}$ after PDA at 250 °C [151, 173, 174].

2.1.3.3   Electrostatic passivation

While the D_{it} reduction can be well explained, the origin of the high fixed charge density reported for Al_2O_3 synthesised by thermal ALD or PA-ALD is still a matter of debate. Before PDA, Q_f is generally low for thermal ALD ($< |10^{12}|$ cm^{-2}) or has even a positive polarity, while a high negative fixed charge density is already present in PA-ALD films. For thermal ALD, the PDA increases the fixed charge density to the high negative values that made its popularity, while in PA-ALD D_{it} reduction is the main contributor to the lifetime increase [175, 176].

Q_f has been reported to be located within the first nanometres above the c-Si surface and to be independent of the Al_2O_3 thickness above this nanometre [152, 177, 178]. Tetrahedral coordination <AlO$_4$> where the net charge of the Al atom would be -1 is considered as a possible origin of this fixed charge density, given its predominant concentration at the interface [107, 179-182]. The major interfacial T_d bonding increase due to PDA would perfectly fit with the formation of Q_f, but the same T_d configuration increase is also reported for PA-ALD while Q_f is already present [37, 107]. Another candidate to explain these charges is interstitial oxygen atoms (O_i). Indeed, excessive oxygen concentration is detected by XPS at the c-Si/Al_2O_3 interface in comparison to the c-Si/thermal SiO_2 interface [106]. The silanol dehydroxylation following equation (2.11) has been proposed to explain generation of oxygen excess [106], as well as molecular hydrogen. On the other hand, the presence of interstitial oxygen at this interface is most likely to originate from Al_2O_3 catalytic activity rather than from the reaction described by equation (2.11). However, as reminded by Iwata et al. [112], due to the presence of silanols (aluminol) in silicon oxide (Al_2O_3), the O/Si intensity ratio detected by XPS is expected to be greater than the one of pure SiO_2. Indeed, two oxygen atoms are required to satisfy two silicon atoms through hydroxyl configuration (2 x $\equiv$Si—OH) whereas only one oxygen atom can satisfy two silicon atoms in SiO_2 ($\equiv$Si–O–Si$\equiv$) [112].

$$Si–OH \ + \ HO–Si \ \rightarrow \ Si–O–Si \ + \ H_{2(g)} \ + \ O_i \qquad\qquad (2.11)$$
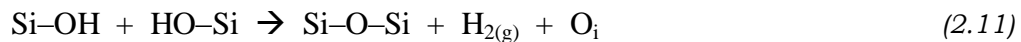
While the origin of fixed charges is still not fully understood and its discussion will continue towards the end of this chapter, an important observation has to be mentioned here. The density of fixed charges that is supposed to be created during the PDA through chemical configuration of atoms (T_d coordination of Al and/or interstitial O) can be modified after PDA by simple illumination. The Q_f and lifetime may be increased by more than 50 % [31, 35] when certain illumination conditions are used. This is a significant effect that needs to be clarified before comparing the impact of different process parameters on the passivation.

2.2   Light Induced Field Effect Enhancement

2.2.1   A well-known fact

The well-known pioneering work of Hezel and Jaeger published in 1989 [31] is the starting point for the use of Al$_2$O$_3$ as a passivation layer containing negative fixed charges contrary to commonly used SiO$_2$ and a-SiN$_X$:H which contain positive charges. In their work, the sensitivity of APCVD Al$_2$O$_3$ films to UV illumination was also reported at that time [31], with a Q$_f$ increase of 56 %, but this particularity did not attract much attention. Twenty years later, Dingemans *et al.* also reported this "beneficial ageing" effect of UV illumination, which leads to an increase of the lifetime of p-type sample by 40 % [35]. Then some other studies were carried out, each one reporting lifetime increase around 50 %, independently of the substrate type or the Al$_2$O$_3$ deposition method (Table 2.5).

Table 2.4: Illumination effect reported in the literature

| Al$_2$O$_3$ type | Light source | Passivation properties | | Ref |
		Initial	Enhancement	
96 nm (APCVD @ 460 °C)	Xe lamp (10 mW.cm^{-2})	-3.2·10^{12} cm^{-2}	+56 % (p-type)	[31]
30 nm (PA-ALD @ 200 °C)	Hg lamp (100 W$_{electrical}$)	1190 µs	+40 % (p-type)	[35]
30 nm (PA-ALD @ 200 °C)	AM1.5	6217 µs	+42 % (n-type)	[39]
30 nm (Th-ALD @ 200 °C)	AM1.5	1007 µs	+45 % (p-type)	[40]
		1520 µs	+60 % (n-type)	
11 nm (PA-ALD @ 200 °C)	725 nm laser (100 mW)	-5.4·10^{12} cm^{-2}	+59 % (n-type)	[23]

To explain this increase of Q$_f$, a direct electron injection from the c-Si valence band to the Al$_2$O$_3$ conduction band (with tunnelling through the SiO$_X$) was proposed (Figure 2.10, mechanism ①). Considering the offset of ~2 eV between the conduction bands of ALD Al$_2$O$_3$ and c-Si (Table 2.2), UV photons with energies greater than 3.12 eV are required to ensure this transition. However, while characterising Q$_f$ by second harmonic generation, Gielis *et al.* showed the possibility to inject electrons by photons of much lower energy [23]. Thus, a second mechanism based on multiple photon interaction was proposed (Figure 2.10, mechanism ②). In their experiment, the electron injection can be avoided depending on the laser photon flux, contrary to the UV illumination for which both low UV flux (AM 1.5) and high UV flux (Hg lamp) provide similar lifetime increase of 40 % (Table 2.4). This Light-Induced Field Effect Enhancement phenomenon (referred as LIFE$_2$ thereafter) would be of prime interest if it would be permanent. The long-term stability study conducted by Liao *et al.* showed that the injected charges are released from the Al$_2$O$_3$ layer when not exposed to the light, bringing the lifetime back to its initial value [40]. However, since the injection is done within tens of minutes to hours, and that the complete charge release takes weeks, LIFE$_2$ remains a phenomenon of interest on a daily basis for solar cells exposed to a photon flux.
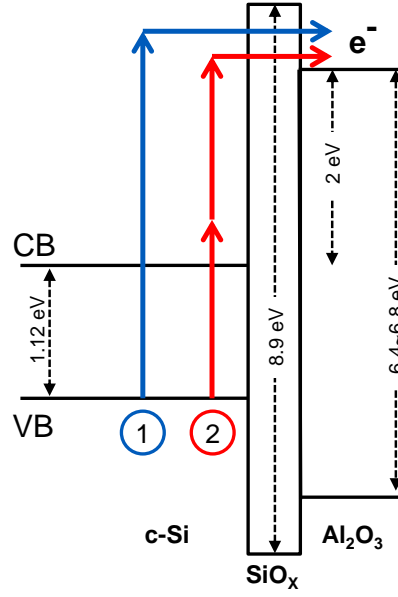
Figure 2.10: Photo-injection models from the c-Si valence band to the Al₂O₃ conduction band as proposed by [23]. The injection can occur through a: ①: 1 photon absorption if this one has an energy > 3.12 eV. ②: multiple photons absorption if their energy is < 3.12 eV.

Despite the apparent dependence on the photon energy, all the experiments reported in Table 2. share a common point: a high carrier generation rate at the c-Si surface. For the different light sources, the generation rate along the wafer thickness can be estimated by equation (2.12).

$$G(x) = \int_{250}^{1110} \alpha(\lambda) \cdot \phi_0(\lambda) \cdot \left(1 - R(\lambda)\right) \cdot e^{-\alpha(\lambda) \cdot x} \cdot d\lambda \qquad (2.12)$$

With:

- λ : a specific wavelength
- ϕ_0 : the photon flux reaching the sample surface
- R : the surface reflectance
- α : the absorption coefficient as defined by equation (2.13)

$$\alpha(\lambda) = \frac{4\pi k(\lambda)}{\lambda} \qquad (2.13)$$

With:

- λ : a specific wavelength
- k : the extinction coefficient

The generation rates depth profiles in silicon due to the different illumination conditions summarised in Table 2.4 were calculated by equation (2.12). To do so, typical xenon and mercury lamp spectra were used [183], with a power density adjusted according to the reported experimental parameters. The laser spectrum was approximated by a Dirac function at its nominal wavelength while the standard AM1.5 spectrum [184] was used. The silicon optical properties from Green *et al.* [185] were used and the photon fluxes were considered between 250 nm and 1110 nm. The reflectance values are tabulated for a flat Si/air interface and not for a Si/Al$_2$O$_3$ interface. This leads to an underestimation of the generation rate, mainly in the first nanometres below the surface due to high UV reflection (up to 70 %). However, it is clearly visible on Figure 2.11 that the generation rate at the surface is higher than 10^{20} cm^{-3}.s^{-1} for all these experiments.
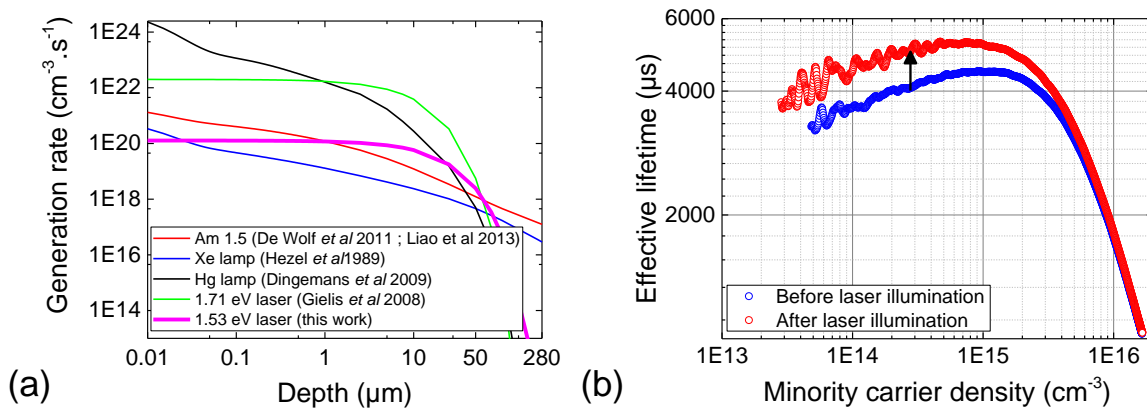
Figure 2.11: (a) Generation rate as a function of depth for different illumination parameters reported in literature. (b) Effective lifetime before and after an illumination of an n-type c-Si samples passivated by 10 nm of Al$_2$O$_3$ deposited at 200 °C and activated at 380 °C for 5 min. 400 s illumination at a photon flux of 4.94·10^{17} cm^{-2}.s^{-1} (@1.53 eV).

The excess carrier density (Δn) is linked to the generation rate and the lifetime (τ$_{eff}$) by equation (2.14). It can be quite arbitrary to evaluate the lifetime from one experiment to another. However, choosing a very conservative value of 100 μs would result in a minimal local carrier density near the Si/Al$_2$O$_3$ interface of 10^{16} cm^{-3} for all these experiments. For such carrier density, the Auger recombination mechanism is already predominant regarding other mechanisms and might be responsible for the electron injection in the Al$_2$O$_3$ through an eeh interaction (see chapter 1, recombination part). It would also explain why LIFE$_2$ has been avoided in Gielis *et al.* [23] work by reducing the laser power, *i.e.* the photon flux. This hypothesis is also supported by the reported kinetic results: to reach the maximum enhanced lifetime; 20 min were enough to Dingemans *et al.* [35] with a generation rate below the surface around 10^{24} cm^{-3}.s^{-1} while it took hours to Liao *et al.* [40] to reach the maximum lifetime with a generation rate around 10^{20} cm^{-3}.s^{-1}.

$$\Delta n = G \cdot \tau_{eff} \qquad\qquad (2.14)$$

A quick experiment is conducted in order to check if LIFE$_2$ observed with UV containing sources is due to photon energy higher than the energy difference between the silicon valence band and the Al$_2$O$_3$ conduction band or to the carrier density near the Si/Al$_2$O$_3$ interface. A FZ n-type wafer passivated at 200 °C with 100 ALD cycles and activated by a PDA of 5 min at 380 °C was used for this experiment. The initial lifetime of the sample after PDA was measured with the LIS-R2 at 4440 µs. Then, without moving the sample or opening the door of the characterisation tool, we used the large area illumination laser dedicated to photoluminescence mapping in the LIS-R2 as the photon source. The wavelength of excitation is 808 nm (1.53 eV) and its intensity can be set up to $4.94 \cdot 10^{17}$ photons.cm^{-2}.s^{-1}. The sample was illuminated for 400 s with the maximum photon flux. After illumination, a lifetime of 5204 µs is measured, which means a lifetime increase of 17 %. The generation rate depth profile is plotted on Figure 2.11. With the lowest generation rate at the sample surface (in the top 50 nm) among all the plotted illumination conditions and with photon energy of 1.53 eV, LIFE$_2$ is still observed. Thus the UV contribution to this phenomenon through mechanism ① (Figure 2.10) is not confirmed. It means that for a cloudy season, when the photon flux is reduced to about 1 % of AM1.5, LIFE$_2$ might not happen any more. A reduction in Q$_f$ and so in the passivation level might reduce the cell efficiency and be detrimental to the solar panel reliability. The next part is dedicated to the photon intensity and wavelength impacts on the LIFE$_2$ effect.

2.2.2   Detailed study of LIFE$_2$

2.2.2.1   Monofacial vs bifacial effect

In order to lay the foundations of this study, we determined if it is the local carrier density (carrier generation rate) that matters or if the carrier density is homogenised in the wafer thickness. Indeed, the high quality and the low doping level of the silicon bulk allow very high diffusion length of carriers. The diffusion length of minority carriers, electrons in the p-type bulk, is defined by (2.15) and is twice larger than the wafer thickness (~550 µm) for an effective lifetime as low as 100 µs. It means the carrier density can be homogenised in the wafer thickness, equalising the carrier concentration at both c-Si/Al$_2$O$_3$ interfaces. In this case, it would result in a LIFE$_2$ on both surfaces, while illuminating only one.

$$L = \sqrt{D \cdot \tau_{eff}} \qquad (2.15)$$

With:

- D : *the electron diffusivity*

- τ_{eff} : *the effective minority carrier lifetime*

To address this question, we used the AM1.5 light source of an Oriel solar simulator class AAA from Newport. As depicted on Figure 2.11, the generation rate between the front and the back surfaces decrease by three orders of magnitude. If the average carrier density rules the charge injection in Al$_2$O$_3$, the illumination of the front surface should also result in the injection of carriers from the c-Si into the Al$_2$O$_3$ present at the back surface.
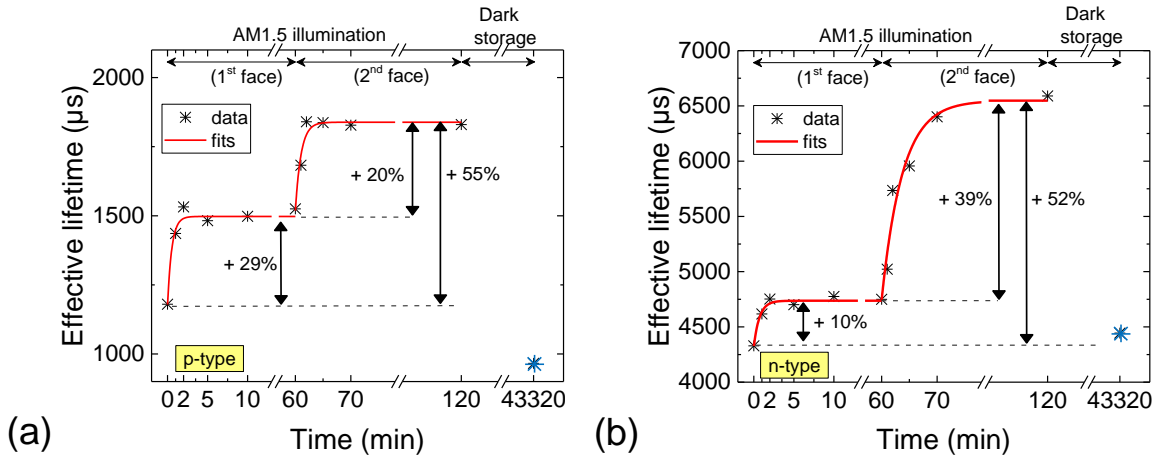
Figure 2.12: Lifetime's follow-up of set n°1 along AM1.5 illumination one face a time (a) p-type c-Si substrate. (b) n-type c-Si substrate. Lines correspond to the fit of data according to equation (2.16). Wafers were passivated at 200 °C with 100 ALD cycles and activated by a PDA of 5 min at 380 °C. The blue dots after dark storage show the fact that photo-injected charges are released from the Al$_2$O$_3$ during the storage.

Two sets of samples with both p-type and n-type wafers in each one were prepared. The passivation recipe was 100 ALD cycles of Al$_2$O$_3$ deposited at 200 °C and activated via an annealing at 380 °C for 5 min. A particular attention has been taken to avoid all illumination sources when the sample is removed from the furnace after the PDA. For the first set, samples were regularly measured by the Sinton WCT-120 over one hour of illumination on the same surface. Then the samples were flipped and the protocol was repeated for the second surface. For the second set of samples, the same illumination duration is done for both surfaces before each measurement.

The results of the first set (Figure 2.12) clearly show that the electron injection in an Al$_2$O$_3$ layer is related to the local carrier generation rate beneath it (or the UV illumination). For the p-type substrate the illumination of the second surface provides similar enhancements than for the first one (+ 29 % and + 20 %). On the contrary, the n-type substrate shows a higher lifetime increase when the sample is flipped (+ 10 % and then + 39 %), matching very well the increase of + 17 % previously observed with the IR laser. It might be due to a weak inversion layer initially present at the surfaces. When the passivation quality of the front surface increases, the effective lifetime is still limited by the back-surface. Then when the n-type wafer is flipped, the second surface is not any more limiting the lifetime resulting in a strong improvement of the passivation. The overall lifetime has been increased by 55 % and 52 % for the p-type and n-type samples respectively. These values agree very well with these reported in Table 2.4. For the second set (Figure 2.13), the lifetime increases quickly to its final value (within ~5 minutes), but the overall lifetime enhancement is slightly lower than for the first set, even if absolute values are higher.
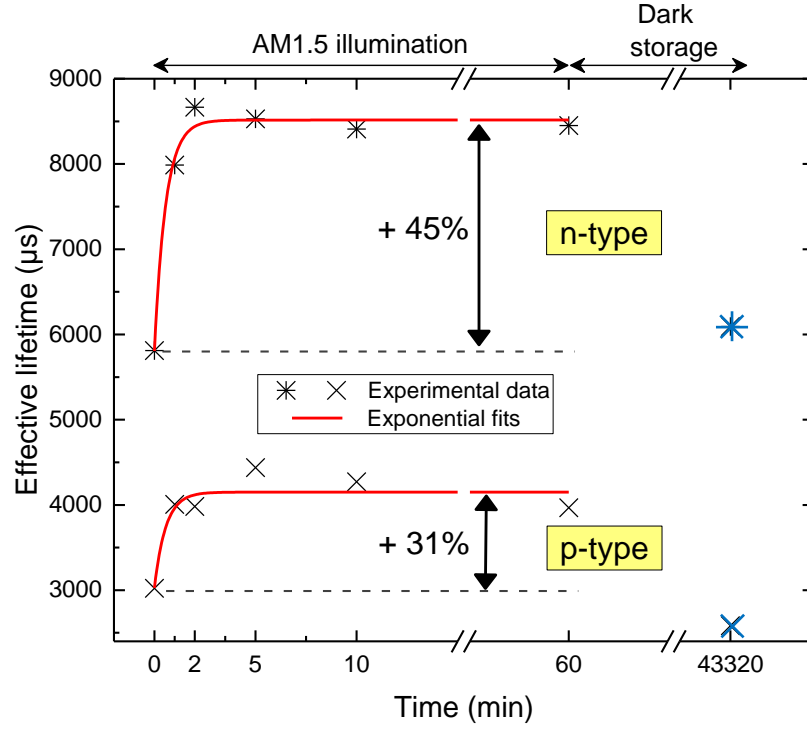
Figure 2.13: Lifetime's follow-up of set n°2 along AM1.5 illumination on each face before measurement. Lines correspond to the fit of data according to equation (2.16). Wafers were passivated at 200 °C with 100 ALD cycles and activated by a PDA of 5 min at 380 °C. The blue dots after dark storage show the fact that photo-injected charges are released from the Al_2O_3 during the storage.

The $LIFE_2$ process corresponds to the accumulation of electrical charges at a dielectric surface, so data were fitted with an exponential function (equation (16)) commonly used for capacitors to compare the kinetics. For the first set of samples, the kinetic of each face has been fitted separately. Results of the fit are summarised in Table 2.5 and plotted with experimental data on Figure 2.12 and Figure 2.13.

$$\tau = \tau_0 + A \cdot \exp\left(-\frac{t - t_0}{T_k}\right) \qquad (2.16)$$

Globally the goodness of fit (R^2) is rather low, but generally slightly better in the case of n-type substrates. Maybe the electrical activity at the interface with an inversion layer is closer to capacitor behaviour than for p-type. Both samples of the second set have similar characteristic time of the kinetic (T_k) in the 30 s range, which underlines an exceptionally fast process. For samples of the first set, T_k is at least twice longer for the second surface than for the first one, maybe charge release already starts at the first surface when this one is not illuminated any more.

Table 2.5: Exponential fit results of the lifetime increase for set n°1 and n°2

Substrate	Set n°	R²	T$_k$ (min)
p-type	1 (1st face)	0.89	0.53
	1 (2nd face)	0.89	1.02
	2	0.74	0.56
n-type	1 (1st face)	0.92	0.77
	1 (2nd face)	0.91	3.74
	2	0.97	0.56

To assess the stability of the LIFE$_2$ treatment, after the illumination, all the samples were stored in a dark cabinet for one month. Similarly to what has been reported by Liao *et al.* [40], the charges are released by Al$_2$O$_3$ and the lifetime returns to its initial value (Figure 2.12 and Figure 2.13). A noticeable result has to be pointed out, for n-type substrates the lifetime after storage remains slightly above its initial value while for the p-type values, this one is significantly below the initial value.

From this first experiment there are some key facts to remember. The LIFE$_2$ treatment is a very fast process at AM1.5, relying on the local carrier density at the surface which results from the high generation rate. Charge injection at the non-illuminated c-Si/Al$_2$O$_3$ interface surface does not happen or is negligible. In order to properly estimate SRV evolution, the illumination has to be performed on both surfaces at the same time. The LIFE$_2$ treatment is not permanent. However, the used passivation recipe generates large blisters, *i.e.* delamination of the passivation layer and so electronic defects. The blistering phenomenon will be more intensively studied in chapter 4. Blisters impact on the LIFE$_2$ stability cannot be excluded as a delaminated area is equivalent to an unpassivated area offering recombination centres.

2.2.2.2 Low intensity bifacial illuminator (LIBI)

In order to pursue investigation on the LIFE$_2$, a set-up allowing bifacial illumination has been built (Figure 2.14.a). Inside a big black box (600 mm x 630 mm x 780 mm), two rows of lights have been installed, the first at the bottom, the second at the ceiling of the box. Each row consists of twelve fluorescent tubes split into two groups allowing to turn on only half of the row (one on two tubes). This electrical wiring allows choosing between an illumination at the full or 50 % of the row power. Despite the close-packed arrangement of the fluorescent tubes, it remains twelve linear light sources. A 5 mm thick ground glass is placed at 90 mm of each row to make the light intensity uniform across the surfaces. In the middle of the black box, rails are fixed in order to place the sample surfaces at 230 mm from the ground glasses. To ensure the complete illumination of surfaces, wafers are not directly put on the rails but inside square plastic boxes (120 mm x 120 mm) which are placed on the rails. Due to reflectivity at the plastic/air interface, these boxes transmit 90 % of the light in the wavelength range of 400-1100 nm (Figure 2.14.b). Below 400 nm, the plastic starts to absorb the light, slowly decreasing the transmission from 90 % to 60 % when reaching 300 nm. These optical characteristics are good enough to allow photons with energies up to 4 eV to reach the sample surface. In order to avoid potential parasitic effect of the ambient humidity, transparent boxes can be sealed in transparent bags with N$_2$ atmosphere. These bags also present very good optical properties that are compatible with the LIFE$_2$ study (Figure 2.14.b).
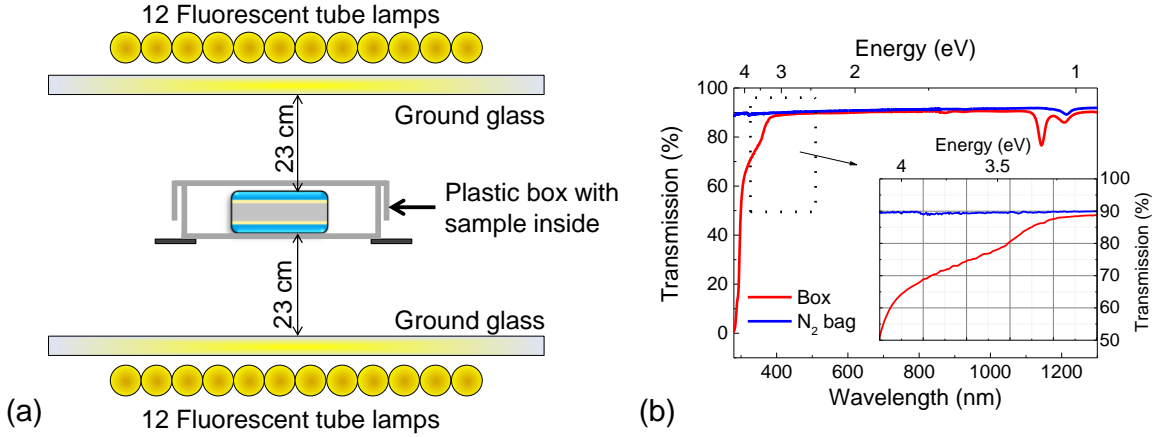
Figure 2.14: (a) Schematic view of the low intensity bifacial illuminator. (b) Transmission spectrum of plastic box and nitrogen bag.

The homogeneously illuminated surface is about 370 mm by 500 mm, offering enough space to treat multiple samples in the same time. An iHR320 spectrophotometer from Horiba Jobin-Yvon was calibrated using De Izarra and Gitton protocol [186]. The integrated power density from 300 nm to 1200 nm was measured at each sample surface and is about 1.2 mW.cm^{-2} when all the fluorescent tubes are turned on. It represents about 1% of the sunlight intensity but the photon flux reaching the sample surface in our system is obviously different from the one of the AM1.5 as it does not originate from a black body emission (Figure 2.15.a). However its emission is continuous between 300 nm to 1100 nm, even if not monotonically increasing like a black body one. The corresponding depth profile generation rate is similar to the one of AM1.5 but lower by 2 orders of magnitude (Figure 2.15.b). If we consider again a lifetime of 100 µs near the surface, it will result in a carrier density of 10^{15}cm^{-3}, which corresponds to the transition region between SRH and Auger recombination. The bifacial illumination mode allows a symmetrical generation rate, ensuring symmetrical evolution of surface passivation and so accurate determination of the SRV evolution.
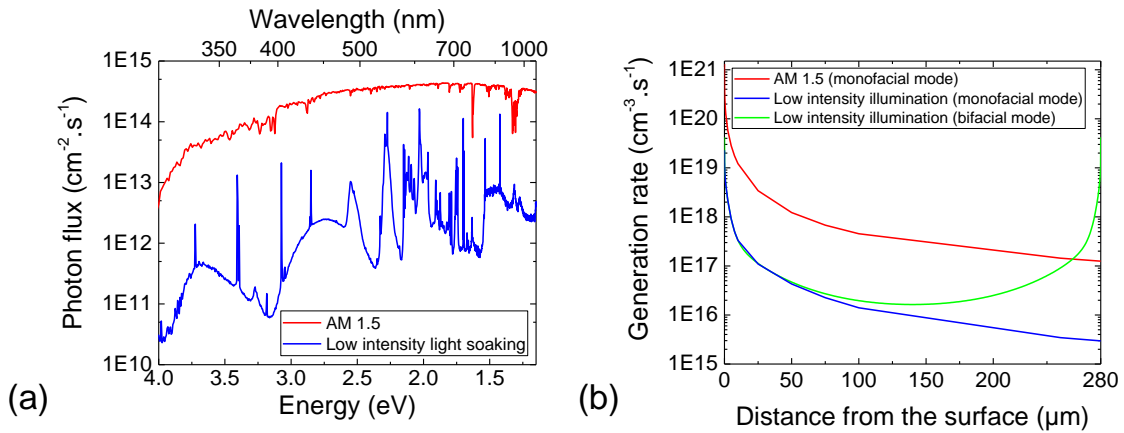
Figure 2.15: (a) Photon flux reaching the samples surfaces. (b) Generation rates in the silicon volume.

The kinetics of the LIFE$_2$ treatment in the LIBI is studied using freshly passivated samples with the same Al$_2$O$_3$ thickness, deposition temperature and PDA temperature as the one previously illuminated by AM1.5. The Sinton WTC-120 was moved next to the LIBI to minimise potential charge release by the Al$_2$O$_3$ due to measurement duration, *i.e.* a no illumination period. That way, the samples were out of the LIBI only 10 s for a lifetime measurement. For each type of sample, one was illuminated at 100% of the power density (1.2 mW.cm^{-2}), the second was illuminated at 50 % of the power density (0.6 mW.cm^{-2}) and the third was stored in a dark cabinet at the shelter of any light. After a lifetime follow-up of roughly 6 hours, illuminated samples are stored in the dark cabinet with the non-illuminated one for five days.
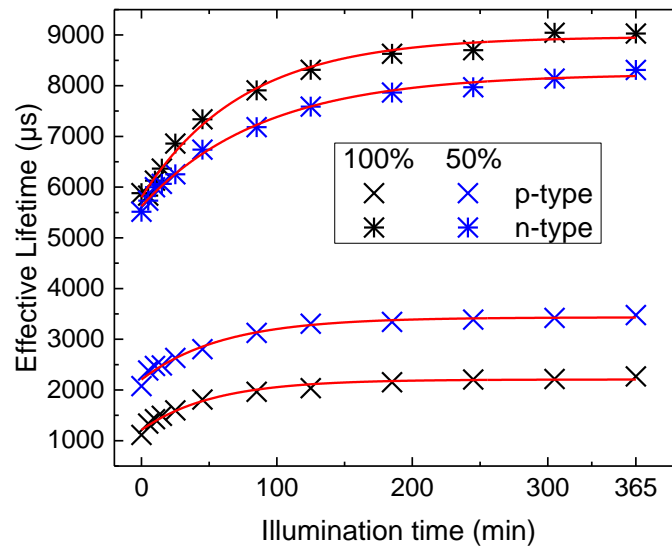
Figure 2.16: Lifetime evolution in the LIBI for p-type and n-type samples passivated by 100 ALD cycles of Al$_2$O$_3$ deposited @ 200 °C and activated for 5 min @ 380 °C.

The lifetime evolution as a function of the illumination time in the LIBI is shown on Figure 2.16. Data are fitted with an exponential decay (increasing form) function (equation (2.16)), fit parameters are summarised in Table 2.6. The goodness of fit is far better for the lifetime follow-up in the LIBI than for the AM1.5, maybe due to the bifacial illumination. The same trends are observable for these results as for AM1.5 but trends are clearer with the LIBI. The impact of the substrate type is obvious with a longer T_k for n-type substrates at both illumination powers. When the power density is reduced to 50 % of its nominal value, T_k is longer for both types of wafer. The most remarkable results are the values of T_k. For a generation rate two orders of magnitude lower in the LIBI compared to AM1.5, T_k is two orders of magnitude longer. Regarding lifetime enhancements, the increase is about 54 % and 51 % for n-type samples illuminated at full and half-power density respectively. For the p-type substrate, the full power illumination results in an improvement of 104 % while the lifetime is only improved by 67 % for the half power. However, it is important to pay attention to the initial lifetimes of these samples. The p-type samples illuminated under half of the power density already presented a lifetime clearly higher than the p-type (1113 µs < 2078 µs). In contrast, the n-type samples presented similar initial lifetime (5880 µs ~ 5514 µs), and so allow to conclude that the power density only impacts the kinetics of LIFE$_2$, not its amplitude.

Table 2.6: Exponential decay fit results of the lifetime evolution in the LIBI.

Substrate	Power density (%)	R^2	T_k (min)
p-type	100	0.98	53
	50	0.98	60
n-type	100	0.99	75
	50	0.99	89

After five days of storage in the dark cabinet, the lifetime of all the samples was measured again. For the samples that did not undergo the LIFE$_2$ treatment, the lifetime variation is lower than 5 %. For the other samples that received LIFE$_2$, the lifetime degradation is about 20 %, but the charge release is not completed yet as the storage was not long enough. It allows us to confirm that we are looking at the same effect in the LIBI than under AM1.5 despite the extremely different light sources. With a final lifetime around 9000 µs (n-type) for a power density about 1 % of the sunlight intensity, this LIFE$_2$ phenomenon is definitely interesting.

The key fact here is that the light intensity (generation rate) seems to slightly impact the kinetic of the phenomenon, not its amplitude. The importance of UV illumination in this process is not yet confirmed and is discussed below.

2.2.2.3   Impact of the wavelength

There are many ways to study the impact of the wavelength on LIFE$_2$. However, in the previous experiments, lifetimes from one sample to another varied despite the use of the same passivation recipe. It might be due to uncontrolled blistering or different surface contamination. To limit these possible perturbations, the wavelength impact has been studied on the same sample surface. The passivation layer was deposited on a p-type wafer at 250 °C rather than 200 °C and the number of ALD cycles was double (200 cycles). The reason is twofold, on the one hand, the higher deposition temperature leaves less hydrogen in the film, considered as one of the blistering sources (refer to chapter 4), on the other hand, a thicker film is preferable as the COCOS technique was used to quantified Q$_f$. As explained in the first chapter, this technique deposits positive ions on the Al$_2$O$_3$ surface. The LIFE$_2$ model suggesting electrons injection in the Al$_2$O$_3$ conduction band, we wanted to reduce as much as possible the capture probability of electrons by a positive ion present at the surface but keeping a realistic film thickness. The PDA was done for a longer time at a lower temperature (20 min at 350 °C) to reduce the dangling bond density as much as possible following Stesmans model [143].

In order to avoid experimental complexity that would result in inaccurate results, the LIFE$_2$ was carried out only on the front surface of the sample, the back surface being protected against illumination by an opaque sample holder. The LIFE$_2$ treatment will be characterised through the quantification of Q$_f$ at the front surface. The creation of areas selectively illuminated by different wavelengths was achieved thanks to a shadow mask with optical filters mounted on it (Figure 2.17.a). These filters are bandpass filters (360 nm, 430 nm, 543.5 nm and 970 nm) with a full width at half maximum of 10 nm. The LIFE$_2$ phenomenon seems to be related to carrier interaction, we will therefore consider the photon energy rather than the wavelengths, *i.e.* filters respectively select photons with energies of 3.44±0.05 eV, 2.88±0.04 eV, 2.28±0.04 eV and 1.28±0.02 eV. At their nominal energy, filters do not all present the same transmission, ranging from 25 % to 70 %, creating different generation rate depth profiles (Figure 2.17.b). Normally, at such low generation rate and considering a hypothetical lifetime of 100 µs below the surface, the carrier density would be about 10^{14} cm^{-3}. In this domain of carrier density, the SRH

recombination is dominant, so the electron injection in the Al$_2$O$_3$ is unlikely to happen if it involves Auger like particles interaction. Moreover, filters centred at 3.44 eV and 2.28 eV have similar generation rates in the first 10 nanometres below the surface. If photon energy matters (Figure 2.10), LIFE$_2$ should happen only below the former filter while nothing noticeable should happen below the latter. However, in order to not miss a possible LIFE$_2$ effect occurring with a slow kinetic due to low generation rate, the samples and the mask were sealed in a N$_2$ bag and the illumination was held for 160 hours.
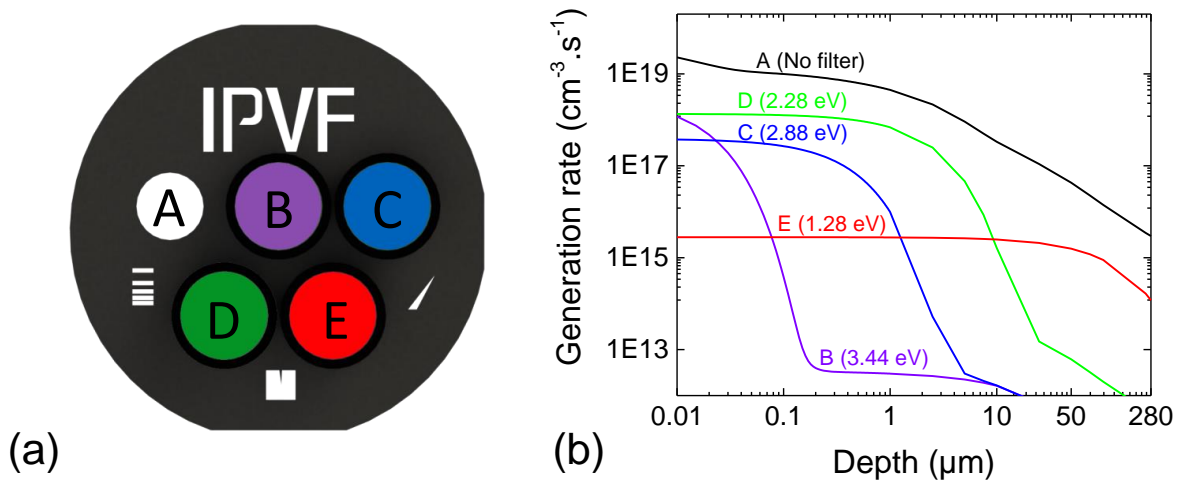
Figure 2.17: (a) Stainless-steel shadow mask with optical filters mounted on it. The mask covers the sample during the full duration of the illumination. Letters from A to E are the different locations of filters: A is no filter, B: 3.44 eV; C: 2.88 eV; D: 2.28 eV E: 1.28 eV. (b) Generation rate depth profiles for mask location A to E.

After illumination, a lifetime PCD calibrated photoluminescence mapping was acquired to observe if LIFE$_2$ was visible (Figure 2.18.a). It might be feared that the PL laser (E(λ)=1.53 eV) can participate to LIFE$_2$. First, considering the low photon flux ($5 \cdot 10^{15}$ photons.cm^{-2}.s^{-1}) and the short acquisition time (~10 s), it is unlikely to happen. Secondly, if it does happen, it would be homogeneously done over the surface, still allowing area differentiation. The areas without filters present a lifetime enhancement of +47 % compared to non-illuminated areas. The only area below a filter presenting obvious LIFE$_2$ is the one below the 3.44 eV filter (+17 %). However, as the back surface was not exposed and will remain limiting, a small LIFE$_2$ effect cannot be excluded below other filters even if not detected by PL, quantification of Q$_f$ is required. The COCOS was performed on the areas A to E and the results suggest an undeniable impact of the wavelength (Figure 2.18.b). The LIFE$_2$ does not impact chemical passivation, D$_{it}$ remaining similar for all the areas ($1.4 \pm 0.2 \cdot 10^{11}$ eV^{-1}.cm^{-2}) but really modifies the field effect passivation. The area which received the full spectrum has a Q$_f$ of $-1.2 \cdot 10^{12}$ cm^{-2}, the one illuminated by UV has a Q$_f$ of $-6.9 \cdot 10^{11}$ cm^{-2} while all the other areas presented Q$_f$ of $-3.3 \pm 0.4 \cdot 10^{11}$ cm^{-2}. To confirm that no LIFE$_2$ effect occurred at areas C, D and E, a final measurement was performed on a non-exposed area, this measurement confirming that LIFE$_2$ did not happen on these areas. These results clearly confirm that both LIFE$_2$ mechanisms described on Figure 2.10 take place, but their effectiveness seems different.

From the previous experiment on $LIFE_2$ kinetics in the LIBI, the charge injection was stopped after 300 min as the lifetime did not increase any more. In this experiment this charge saturation has certainly been reached due to the illumination duration of 9600 min, corresponding to a Q_f of $-1.2 \cdot 10^{12}$ cm^{-2}. For the surface below the 3.44 eV filter, the Q_f is only $-6.9 \cdot 10^{11}$ cm^{-2}, so a charge injection only completed by 57 %. Considering their respective carrier generation rates in the first ten nanometres below the surface, a total generation of $4.1 \cdot 10^{23}$ carriers allowed reaching 100% of the Q_f while only 57 % of the maximum Q_f is reached with $6.8 \cdot 10^{23}$ carriers generated only by UV. The photon flux, and so the carrier generation, seems to be more important than the photon energy to inject electrons into Al_2O_3. An interesting fact can be noticed, despite the concentration difference of about one order of magnitude, it seems that there is no lateral diffusion of the electrical charges as it would be expected from Fick's laws.
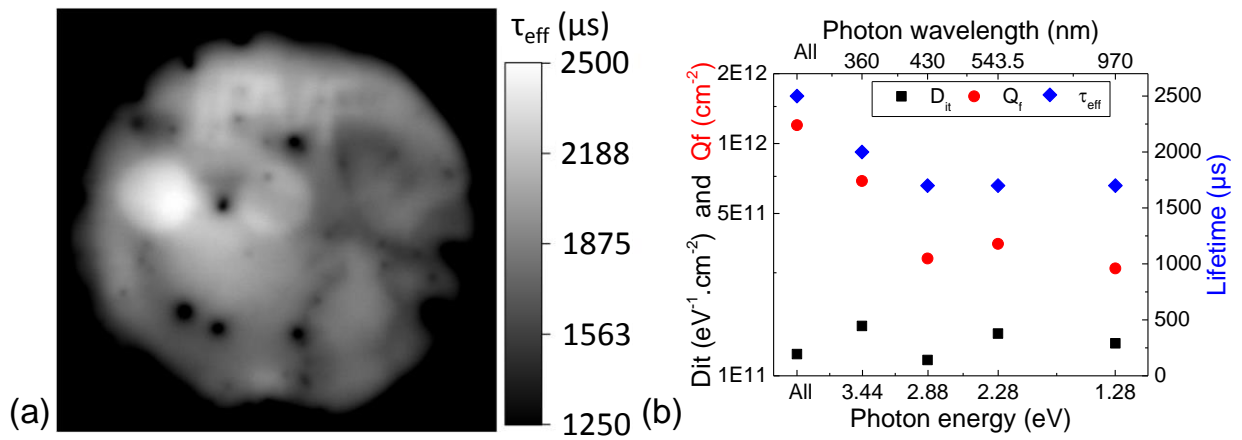
Figure 2.18: (a) PCD calibrated photoluminescence picture of the lifetime sample after 160h of illumination. (b) Passivation results for the five different locations receiving different photon energy.

The key fact here is that after a PDA, there is a very low "fixed" charge density at the c-Si/Al_2O_3 interface, in the range of $1 \cdot 10^{11}$ cm^{-2}. Such low charge densities are reported as "zero charges" in the literature [187] and are generally obtained by stacking Al_2O_3 with another material, this point being discussed later. The real value of Q_f could be even lower; the measurement itself can generate some charges as an illumination is required in the COCOS technique to split the quasi-Fermi levels. However, at least 70% of these charges are in fact injected from the silicon into the Al_2O_3, increasing Q_f to values in the range of $1 \cdot 10^{12}$ cm^{-2}, corresponding to commonly reported values. This can take place through a mechanism of direct injection (UV photon) or through a multiple particles interaction, proportional to the generation rate at the c-Si/Al_2O_3 interface. These charges are generally reported to be created during the PDA while it was not the case here. In fact, the PDA is a crucial step in which many chemical and physical phenomena occur. The next section tries to sort out possible reasons for this discrepancy.

2.2.2.4   The crucial role of post deposition annealing

During post-deposition annealing, several chemical reactions take place, reducing the D$_{it}$ at the silicon surface and in some cases injecting charges in Al$_2$O$_3$. A model of this charge injection has been recently proposed by Kühnhold *et al.* [176] where electrons are injected through dangling bonds to interstitial oxygen atoms at the Al$_2$O$_3$/SiO$_X$ interface. The reduction of dangling bonds during the annealing would impede the charge release after the PDA. For other authors, the increase of the T$_d$ conformation at the interface is the origin of the Q$_f$ apparition during the PDA [107]. In these models there are two facts that are not considered, the way that the sample is heated and the rise of the intrinsic carrier density with temperature. Concerning the first point, the heat transfer to the sample in the furnace can be achieved by conduction or by radiation. The latter one is very popular (Table 2.7) as no contact with the substrate is required, limiting possible contamination. It is important to clarify the consequences of such heat transfer because radiation means photons and so carrier generation in the silicon.

Table 2.7: Heat transfer mode for some popular RTP furnaces.

Company	Model	Heat transfer	
		Radiation	Conduction
Jipelec	Qualiflow JetFirst	X	
AnnealSys	AS-One	X	
Allwin21	AccuThermo	X	
Applied Materials	Vantage	X	
ATV Technologie	SRO		X
Levitech	Levitor		X

The radiative heat transfer is generally achieved through surface illumination by IR lamps. The tungsten filament of the lamp behaves as a grey body, *i.e.* its spectral irradiance is calculated exactly like the one of a black body, but corrected by its own emissivity factor, which is a function of the wavelength and of the filament temperature (~0.3 to 0.5 for tungsten) [186]. Thus, the light spectrum emitted by the filament depends only on its temperature, this one being simply controlled by the electrical current flowing through it. In order to calculate the spectral irradiance and so to estimate the generation rate depth profile, we considered the characteristics of the lamp model present in our furnace. Each lamp has an effective filament length of 240 mm that can reach the temperature of 2400 K at its maximal power of 750 W. The filaments are coiled with a very small whorl step around a large centre, so it has been approximated by a rectangular flat surface. The light reflector placed at the back of the lamp tube is not taken into account, underestimating the overall photon flux. For the sake of simplicity, we considered a piece of silicon having a surface of 50x50 mm, receiving only the photon flux from a piece of filament (50x1 mm) centred in front of it at a distance of 10 mm. The resulting generation rate depth profiles for filament temperatures ranging from 700 K to 2400 K are plotted on Figure 2.19.a. The temperature increase does not result in a simple generation rate upshift. Indeed, as expressed by the Wien's displacement law, the photon emission is blue-shifted by the temperature increase and so the generation rate depth profile becomes less constant across the thickness. However, a filament temperature of 1300 K would generate enough carrier density at both surfaces to inject electrons in Al$_2$O$_3$ films present at these two surfaces. It should be kept in mind that these considerations take into account only the underestimated generation due to a filament portion of 50 mm length, while there might be 10 times more filaments in a furnace.

Concerning the second point, the temperature rise promotes carriers to the conduction band of silicon, increasing the free carrier density in the whole silicon volume (Figure 2.19.b). For the common Al_2O_3 PDA temperature of 400 °C, it corresponds to a carrier density of $1.9 \cdot 10^{16} cm^{-3}$. To obtain an equivalent carrier density with a photon flux, this one would have to allow a generation rate of $1.9 \cdot 10^{20}$ $cm^{-3}.s^{-1}$ if we still take into account the low lifetime value of 100 µs. Such high generation rate near the surface would result into electron injection in Al_2O_3 as we already observed with the LIS-R2 laser (Figure 2.11.b, Figure 2.19.a). Together, the sample irradiation and intrinsic carrier density rise might impact the measured Q_f after a PDA. It is difficult to separate these effects in a furnace operating by radiative heat transfer as a higher annealing temperature involves both a higher photon flux but also a higher intrinsic carrier density.
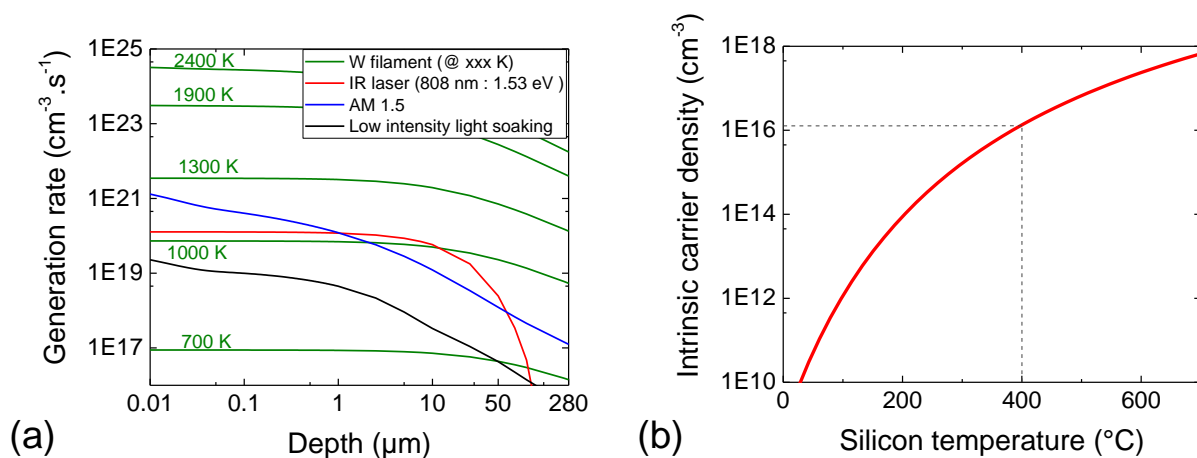
Figure 2.19: (a) Generation rate depth profiles for different W filament temperatures and other light sources as references. (b) Effect of temperature on the intrinsic silicon free carrier concentration.

In this work, the furnace was a SRO-704 from ATV Technologie in which the heat transfer is achieved by conduction through a SiC coated graphite hotplate. The hotplate itself is radiatively heated by eight IR lamps arranged side by side, each lamp having an equivalent flat filament surface of 240x1 mm. It is possible to switch from a conductive to a radiative heat transfer by replacing the opaque graphite hotplate with a transparent one (Figure 2.20). We used two different transparent plates, the first was made of fused silica ($E_g \sim 5$ eV) and the second was made of Corning glass (EAGLE XG®, $E_g \sim 3.5$ eV). Of course these materials can heat-up and transfer heat to the substrate by conduction, but their thermal conductivity are two orders of magnitude lower than the one of SiC or graphite. In both configurations, a thermocouple is measuring the temperature on the silicon, ensuring reproducible thermal cycle. In order to quantify by COCOS the Q_f after the PDA, we used lifetime samples passivated with the same recipe (200 ALD cycles deposited at 250 °C) as for the wavelength effect study.

Conductive heating

Radiative heating

Controlled atmosphere

Sample

Opaque hot plate

Transparent plate

IR Lamps
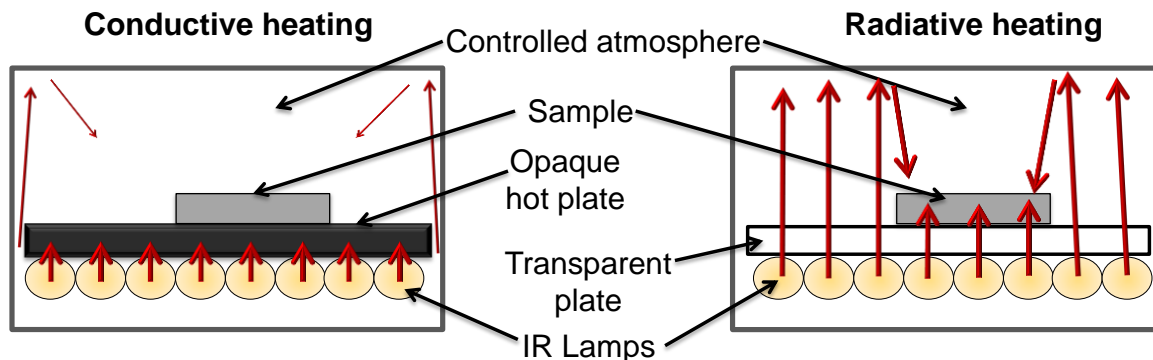
Figure 2.20: (left) Conventional configuration of the furnace with a SiC coated graphite hot plate. (right) New configuration of the furnace with a transparent plate.

The first and the second sample were annealed at the temperature of 400 °C for which the intrinsic carrier density rise has been discussed above. After 20 min of PDA, both samples presented similar passivation results despite the use of either silica or Corning glass as plates. Indeed, UV radiation is really low in the IR lamp spectrum, so such transparency consideration has minor impact on the photon flux. The effective lifetime was 2938 ± 38 µs corresponding to a D_{it} of $1.2 \cdot 10^{11} \pm 0.6$ eV^{-1}.cm^{-2} and to a Q_f of $-7.6 \pm 0.4 \cdot 10^{11}$ cm^{-2} for the two samples and at their two surfaces. This symmetric charge trapping can arise from the intrinsic carrier density but also from the fact that both surfaces receive illumination, the furnace presenting highly reflective walls. The third sample was annealed on fused silica using the thermal process of the previous section (350 °C for 20 min). Its lifetime was 2667 µs with a similar D_{it} as the first two samples but with a slightly lower Q_f of $-6.7 \cdot 10^{11}$ cm^{-2}. The three samples present a minimal increase of 100 % in their Q_f compared to samples that were not illuminated during the annealing. Despite illumination during the annealing, Q_f remains lower than what can be reached by illumination after the PDA and to what is commonly reported in the literature. It might come from the furnace configuration, which is not optimised for direct radiative heating of the sample. It might also be due to the temperature decrease from the PDA temperature to the room temperature, which is constant for all the PDA and was set to 7 min. Such long cooling time in the obscurity might keep the sample at a temperature high enough to allow some charge release from the Al$_2$O$_3$ to the c-Si. It will allow us to study how the Al$_2$O$_3$ passivation evolves as a function of the field effect variation, but also to detect what are important parameters to maximise this field effect. LIFE$_2$ can serve to probe the c-Si/Al$_2$O$_3$ interface quality.

The key fact to keep in mind here is that a direct illumination of the sample during the PDA of Al$_2$O$_3$ increases the Q_f value. The impact of the temperature itself cannot be ruled out as it is directly linked to the photon flux of the lamp, but also to the intrinsic carrier density.

2.2.2.5 Electron trapping in Al_2O_3

Several energy states are introduced in the bandgap of Al_2O_3 by intrinsic point defects and carbon contamination. These defect levels can trap holes or electrons, resulting in trapped charges. On Figure 2.21.a (adapted from the calculations of Choi *et al.* [3, 4]) the defect transition level (q/q'), are defined as the Fermi-level position below which the defect is most stable in charge state q and above which the same defect is stable in charge state q'. Calculations are made for a crystalline structure, so the absolute energy values will differ for an amorphous structure but the relative energy position of a defect levels in the bandgap remains similar [188, 189]. Considering the Fermi level in the middle of the silicon bandgap, several defects can be responsible for electrons trapping. The point defects that are the most stable when negatively charged are aluminium vacancies (V_{Al}) and oxygen dangling bonds (O_{DB}). However, these defect levels located well below the silicon valence band maximum would be automatically charged by electrons that tunnel through the thin interfacial SiO_2. These levels can be referred as "fixed charges" in the sense that electrons stay trapped there.
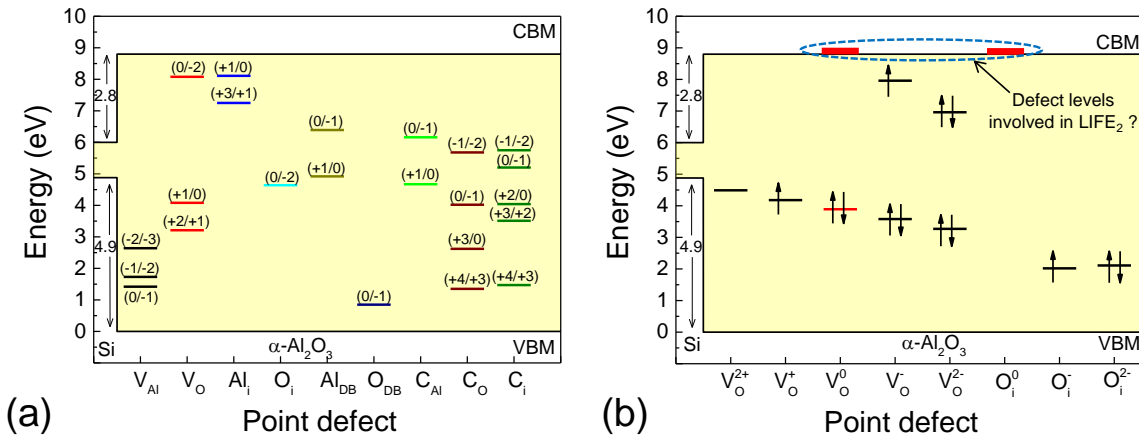
Figure 2.21: (a) Calculated energy levels and occupancy for the intrinsic point defects in α-Al₂O₃, and carbon contamination point defects. Adapted from [3, 4] (b) Switching charge-state levels of oxygen related defects in α-Al₂O₃, adapted from [3, 11].

Energy levels located in the same energy range as the silicon bandgap are more prone to charge trapping and release. The carbon point defects would fit this criterion, but the carbon content is extremely low in the films. $LIFE_2$ phenomenon has also been reported for other metallic oxide materials such as HfO_2 [190] and TiO_2 [191]. Thus, oxygen related point defects are pointed out as responsible for electrons trapping [192, 193]. Indeed, oxygen vacancies (V_O) and interstitial oxygen (O_i) atoms present energy levels close to the silicon valence band maximum and are thus good candidates for stable electrons trapping. The oxygen vacancy can usually exist in all five charged states from -2 to +2 but seems to be the most stable when electrically neutral [194]. However, the V_O energy level responsible for the negative charge is located just below the Al_2O_3 conduction band minimum. It can explain the necessity of electrons injection from the c-Si valence band to the Al_2O_3 conduction band to obtain the charge trapping. Experimentally, negatively charged traps have been found in the region between 1.6 eV and 2.2 eV below the Al_2O_3 conduction band minimum [195] where the V_O^{2-} energy level has been calculated to be located (Figure 2.21.a).

However it does not rule out the contribution of O$_i$ in the electron capture process that occurs under illumination. Indeed, the O$_i$ and V$_O$ energy levels responsible for negative charge states are located at the bottom of the Al$_2$O$_3$ conduction band (Figure 2.21.b). These energy levels switch to a lower energy position in the bandgap when filled with at least one electron. Thus, trapped electrons on interstitial oxygen sites should be more stable than the one trapped by oxygen vacancies. The presence of O$_i$ sites at the c-Si/Al$_2$O$_3$ interface can be expected as some by-products of split molecules by tetrahedrally coordinated aluminium can remain there. It would explain the excess of oxygen detected at the c-Si/Al$_2$O$_3$ interface.

Some researchers report the possibility to obtain uncharged Al$_2$O$_3$. The most common way is to grow Al$_2$O$_3$ on another dielectric layer like SiO$_2$. This way, Q$_f$ steadily decreases with the SiO$_2$ underlayer thickening [134, 196, 197]. Likewise, by replacing SiO$_2$ by a thinner HfO$_2$ layer, the Q$_f$ is also null [178, 187]. This equivalent effect obtained with a thinner layer might be due to the higher dielectric constant of HfO$_2$ (25>3.9). It underlines the charge injection mechanism from c-Si into Al$_2$O$_3$ by tunnelling through the underlayer, either SiO$_X$ that appears during the growth and subsequent PDA, either another dielectric on which Al$_2$O$_3$ has been willingly deposited. Other research groups used external electrical bias to trap/release charges at the c-Si/Al$_2$O$_3$ interface [108, 198, 199]. The charge trapping in the Al$_2$O$_3$ layer has been reported to be proportional to the applied electrode bias but an excessive bias also leads to a D$_{it}$ increase [198, 200].

2.3 Conclusion

The properties of Al$_2$O$_3$ deposited by ALD with water oxidation are highly dependent on the deposition temperature. There is a certain consensus about the low D$_{it}$ obtained after PDA of the Al$_2$O$_3$. This passivation must be the result of several chemical reactions occurring at the Al$_2$O$_3$/c-Si interface, but the reactions themselves might be difficult to disentangle. Indeed, due to catalytic properties of aluminium atoms in tetrahedral coordination particularly present at this interface, D$_{it}$ reduction might be the result of different competing reactions. However, the fact is that after a PDA, a SiO$_X$ interlayer is present at the Al$_2$O$_3$/c-Si interface, and if SiO$_X$ was already present before the PDA, its thickness increases. Dangling bonds present before the PDA are filled with either oxygen or hydrogen atoms.

Regarding the field effect passivation, in the light of the results that we reported, some hypotheses are unlikely to be confirmed. Despite the increasing number of tetrahedrally coordinated Al atoms at the interface during a PDA, this chemical configuration cannot be responsible for more than 30% of the observed Q$_f$. What is generally named "fixed charges" are indeed trapped charges in their majority as demonstrated by the LIFE$_2$ study that we carried out.

Taking into account this trapping characteristic of Al$_2$O$_3$, we have to be sure that the traps are filled while trying to sort out how Al$_2$O$_3$ parameters impact the passivation. The apparent transient characteristic of the field effect needs to be understood, as the stabilisation of these trapped charges would result in a non-negligible passivation enhancement.

Chapter 3

Light induced field effect enhancement of Al$_2$O$_3$/a-SiN$_X$:H stacks

Contents

.

3.1   The a-SiN$_X$:H film

3.1.1   The necessity of a capping layer

3.1.1.1   Optical requirements

To ensure the lowest reflection of the sunlight most intense wavelength (~630 nm) at the air/silicon interface, the optimal ARC properties, *i.e.* refractive index and thickness, can be calculated using equations (3.1) and (3.2) respectively [185, 201, 202]. For a layer with a refractive index that differs from 1.97, the film thickness just has to be adjusted by using the film refractive index instead of n$_{opt}$ in equation (3.2) in order to keep good antireflection properties.

$$n_{opt} = \sqrt{n_{Si} \cdot n_{air}} = \sqrt{3.879 \times 1} = 1.97 \tag{3.1}$$

$$T_{opt} = \frac{(2m + 1)\lambda}{4n_{opt}} = 79.95 \text{ nm} \quad (\text{for } m = 0 \text{ and } \lambda = 630 \text{ nm}) \tag{3.2}$$

With:

- n_{opt} : the optimal refractive index of an ARC between silicon and air
- n_{Si} : the silicon refractive index
- n_{air} : the air refractive index
- T_{opt} : the optimal ARC thickness
- m   : an integer
- λ : the wavelength for which the reflectance is minimal

Depending on the architecture, the Al$_2$O$_3$ layer will cover the front and/or the back surface of the solar cell and have to act as ARC. Therefore, there are two reasons to not use standalone Al$_2$O$_3$ passivation layers. First, despite the very high transparency of ALD Al$_2$O$_3$, which is the first obvious requirement for layers exposed to the sunlight, its refractive index around 1.64 does not make it the most suitable material for ARC. Second, to act as ARC, an Al$_2$O$_3$ layer thickness of 96 nm is required, which is not compatible with industrial requirements. Thus, an additional ARC has to be deposited on top of the Al$_2$O$_3$. In order to minimise the parasitic optical effect of Al$_2$O$_3$ layer between c-Si and the ARC, the thinner the Al$_2$O$_3$ the better the optical properties.

3.1.1.2   Stability requirements

Another reason not to use standalone Al$_2$O$_3$ layers is related to their stability. Al$_2$O$_3$ films are relatively efficient barriers to humidity depending on their thickness. As shown by Carcia *et al.*, an increase from 5 nm to 10 nm of Al$_2$O$_3$ film thickness reduces the water permeability by one order of magnitude (85 % RH, 38 °C) [203]. Despite this moisture barrier property, standalone Al$_2$O$_3$ passivation does not withstand damp-heat test [204]. Indeed, Al$_2$O$_3$ surface has a hygroscopic behaviour used in many humidity sensors [205]. Passivation annihilation by humidity seems to be related to field effect cancellation [206]. A capping layer is thus required to stabilise passivation properties provided by Al$_2$O$_3$. The a-SiN$_X$:H capping is a very efficient moisture barrier that protects Al$_2$O$_3$ passivation layer, even under 100 % RH [206] and as it is also a good ARC, this is the predilection material for Al$_2$O$_3$ capping.

3.1.1.3   Passivation requirements

The use of thin ALD Al_2O_3 capped by another material is nowadays common, but the aim is not only humidity resistance. Thinner Al_2O_3 layers allow higher ALD throughput [207], but as discussed in chapter 2, chemical passivation decreases with Al_2O_3 thickness reduction below 10 nm. So, the a-SiN_X:H capping layer can provide the missing chemical passivation by hydrogen release during a post-capping annealing. Hydrogen diffusion to the c-Si surface is facilitated when the Al_2O_3 layer is thinner [208-211]. However, to keep an efficient field effect passivation, a minimal Al_2O_3 thickness of 2 nm seems to be required [209].

3.1.1.4   Metallisation constraints

Passivation stacks made of Al_2O_3/a-SiN_X:H have to be locally opened in order to collect charge carriers from silicon with electrodes. The screen printing of aluminium paste to form the electrode is the state of the art industrial metallisation process. It requires a final firing step at a temperature generally higher than 700 °C. This is not compatible with the low temperature process that is aimed within the IPVF project. Nickel copper electroplating has been chosen to replace standard Al screen printing. In the metallisation process developed at IPVF, the nickel silicide formation requires an annealing step at 380 °C for 20 min [212]. To ensure the compatibility of developed passivation stacks with the metallisation process, all the passivated samples received this thermal step before lifetime measurement. This "metallisation like" annealing at 380 °C for 20 min is referred hereafter as post-capping annealing (PCA).

3.1.2   Plasma-Enhanced Chemical Vapour Deposition

In the industry, the a-SiN_X:H is currently deposited by plasma-enhanced chemical vapour deposition (PECVD). This deposition technique uses gaseous precursors to deposit the film at substrate temperatures lower than conventional CVD. The plasma assistance is used to provide missing thermal energy for precursor dissociation.
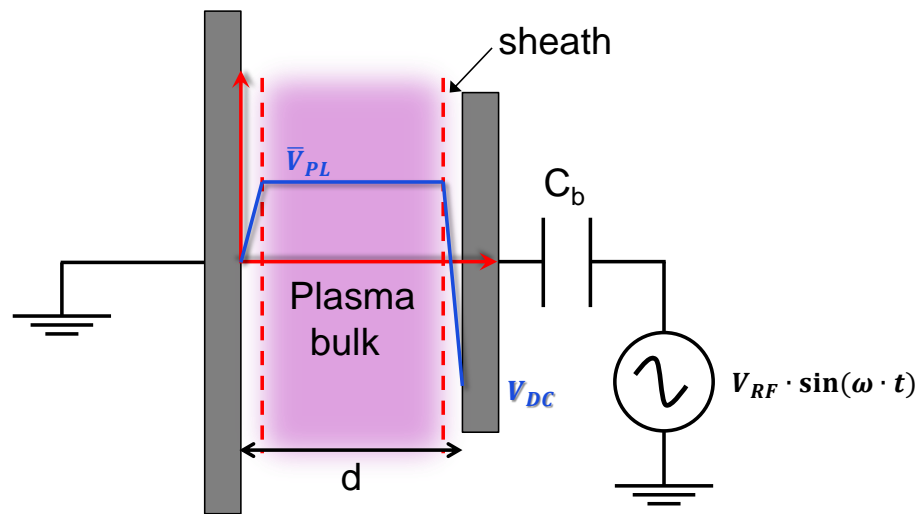
Figure 3.1: Schematic of a geometrically asymmetric RF CCP reactor.

The use of plasma has some drawbacks like the radiation of the plasma that can contain deep UV radiation with energy high enough to generate electrical defects within the silicon. The second drawback is the ion bombardment of the substrate surfaces. Indeed the plasma has its own positive potential while the powered electrode adopts a negative self-bias (V_{DC}) (Figure 3.1). The V_{DC} arises from the asymmetric RF discharge due to the electrode area ratio < 1, where the powered electrode has the smallest area. The electric potential drop taking place in the sheaths between the plasma bulk and the electrodes lead to ion bombardment that is proportional to this potential difference. To minimise this ion bombardment, the silicon substrate is placed on the grounded electrode.

Regarding energy dissipation pathways (Figure 3.2), most of it ends-up as surface heating. If this one can be useful to organise the deposited film/c-Si interface [213, 214], it can be detrimental to the Al_2O_3 passivation layer already present at the c-Si surface. For a more detailed lecture in plasma physics, the reader can refer to the book by Chabert and Braithwaite [215].
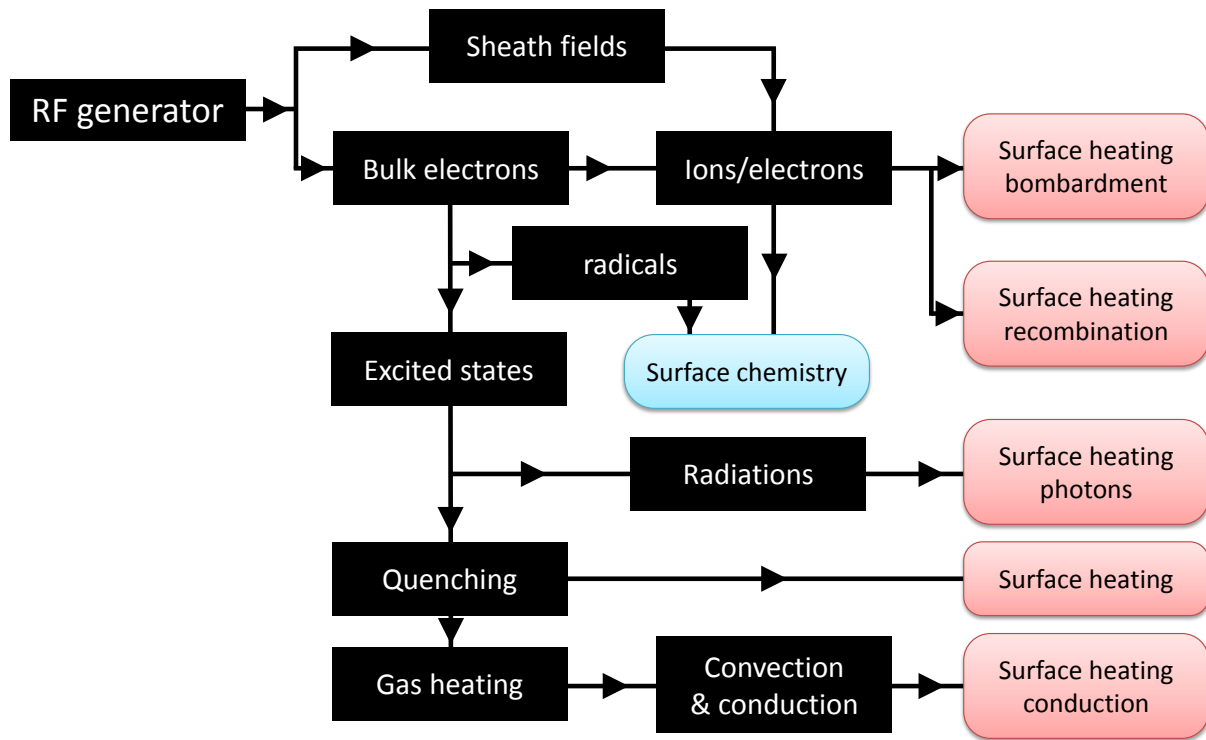
Figure 3.2: Energy flow in discharge plasmas [21].

There are many parameters that enter into a PECVD process, but some of them will have more impact on material properties than others. The applied power to the electrode is the first one, the distance between electrodes (d) is the second one, the deposition pressure is the third one and the gaseous atmosphere composition is the last one. Each of these parameters will have its own impact on the deposited film properties (density, refractive index…). In this thesis, we used a capacitively coupled plasma reactor from an MVS cluster tool (Figure 3.3) where plasma is generated between two electrodes by a radio frequency excitation at 13.56 MHz. We used silane (SiH_4) and ammonia (NH_3) as gas precursors for a deposition pressure that can vary from 13 to 400 Pa. The substrate was set to the maximum temperature of 300 °C which is lower than the commonly used 400 °C for state of the art a-SiN_X:H [216].
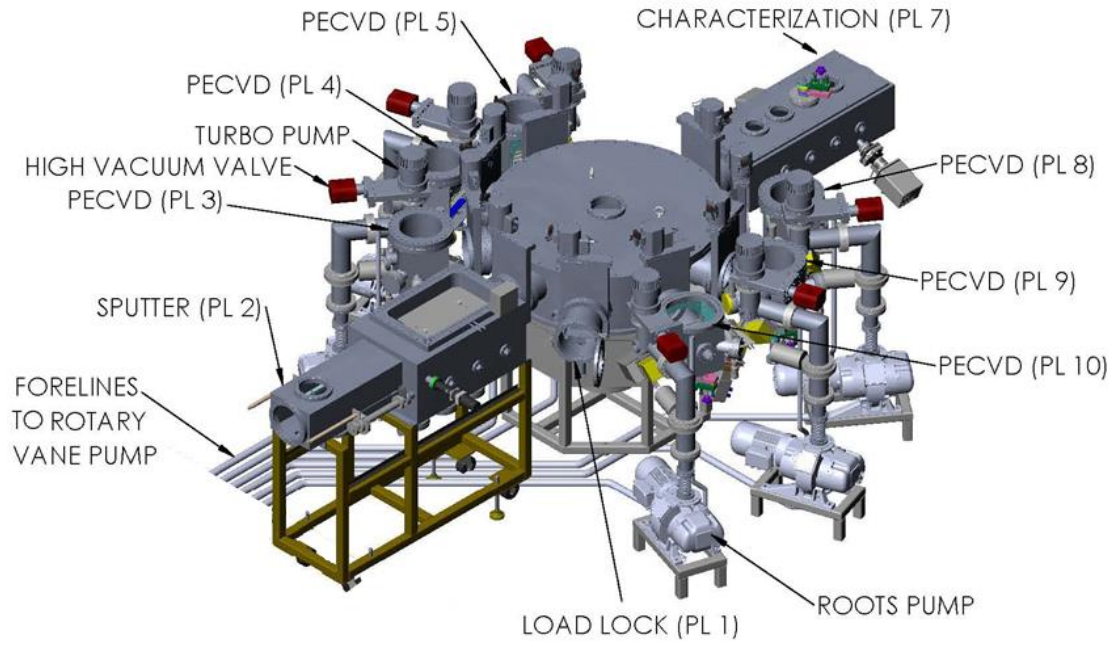
Figure 3.3: the MVS cluster tool.

It can be useful to monitor what is happening inside the plasma during the deposition to guide the process optimisation. Optical emission spectroscopy is a diagnostic technique suitable to give a rough idea of the composition inside the plasma. The light emitted by the plasma is collected by an optical fibre through a quartz window (cut-off wavelength at 200 nm) and analysed with a "Maya2000Pro" spectrometer from Ocean Optics. Monitoring of certain wavelength intensities provides a qualitative idea of the plasma activities. For our purpose, we monitored mainly the intensity of the plasma emission. Indeed, in order to study the LIFE$_2$ phenomenon after capping, the charge trapping in Al_2O_3 due to plasma light has to be minimised.

The second plasma parameter that needs to be monitored is the plasma potential. The maximum ion energy that can reach the substrate surface is directly proportional to the plasma potential. A too high ion energy can damage the thinnest Al_2O_3 layers and so V_{PL} also has to be minimised. V_{PL} can be determined by equation (3.3). The V_{DC} measurement is provided by the matching box of the generator and the V_{RF} was measured with an "OctIV" probe from Impedans.

$$V_{PL} = \frac{1}{2}(V_{RF} + V_{DC}) \qquad (3.3)$$

3.1.3   a-SiN$_X$:H properties

There are some minimal requirements for an acceptable a-SiN$_X$:H capping layer of Al_2O_3 for low temperature passivation stacks. The first consideration regards its ARC function. The a-SiN$_X$:H film has to be as much transparent as possible and its refractive index has to be around the optimal one, *i.e.* 1.97. However, variations around this value would just require some thickness adjustment to provide correct ARC properties, *i.e.* variation of the deposition time. Regarding its capping properties, it has to protect Al_2O_3 against moisture degradation and it has to provide enough hydrogen to the c-Si/Al_2O_3 interface to compensate the missing quantity in the thin Al_2O_3 films. This hydrogen can be provided during the deposition or during the 20 min of post-capping annealing at 380 °C that will be done to mimic the electroplating thermal step.

A standard PECVD process condition was provided by the cluster tool manufacturer (Table 3.1), but OES of its plasma shows a large and intense UV peak around 3.7 eV (Figure 3.5) that has to be minimised. Moreover, the high power density of this process condition might also favours ion bombardment.

Table 3.1: PECVD recipes for an inter-electrode distance of 20 mm.

Process condition	Pressure (Pa)	Power Density (mW.cm^{-2})	Gas ratio (NH$_3$/SiH$_4$)
Manufacturer	67	180	20
DOE full factorial	[53→100]	[36→216]	[1→3]
Sample #1 (from the DOE)	53	36	1
Optimised	100	36	9

A full-factorial design of experiments (DOE) has been carried out in order to confirm the influence of the different PECVD parameters on the plasma potential and radiation. For the plasma optical emission, we focused on the two most intense emission lines, *i.e.* the one centred at 335 nm (3.7 eV) and the one centred at 413 nm (3 eV) respectively related to NH* and SiH* deexcitation [217, 218]. A full factorial DOE consists in all the combinations of extreme parameters (the minimum and the maximum values) resulting in 2^n combinations, 8 deposition conditions for us. Starting from the a-SiN$_X$:H process condition provided by the tool manufacturer, we took the DOE parameters around this point (Table 3.1). However, the gas ratio of the manufacturer process condition (20) is so high that the UV peak generated by ammonia dominates the whole emission. We decrease the gas ratio from 3 to 1. For example, the deposition parameter of the first DOE sample (sample #1, Table 3.1) combines all the minimum values, a deposition pressure of 53 Pa, an applied power density of 36 mW.cm^{-2} and gas ratio of 1 that results in OES peaks of similar intensities (Figure 3.5.a).

The data analysis was performed with the statistical software "JMP" from SAS. The software built a mathematical model for each response, the plasma potential, the intensity of the 335 nm emission line and the intensity of the 413 nm emission line. The goodness of fit (R²) of each model was respectively 0.93, 0.96 and 0.93. Figure 3.4 shows the influence of different process parameters on the light emission and plasma potential.

The photon emission is directly linked to gas excitation, so the applied power density to the electrode is the ruling parameter for the plasma radiation intensity. A low power density is then preferable to limit light emission, but it also limits ion bombardment as the V_{PL} is also mainly ruled by the power density. In comparison, the gas ratio and the deposition pressure seem to have a minor impact on the results. By setting a desirability function to each response, here "minimise the response", the software provides optimal deposition parameters that fit the desirability. This process conditions consists of the lowest power density (10 mW.cm^{-2}) at the highest pressure (100 Pa) with the gas ratio of 1. The higher pressure is indeed a good option in our case as for an equal V_{PL}, the higher the pressure, the lower the ion bombardment due to the increase of collision frequency in the sheaths.
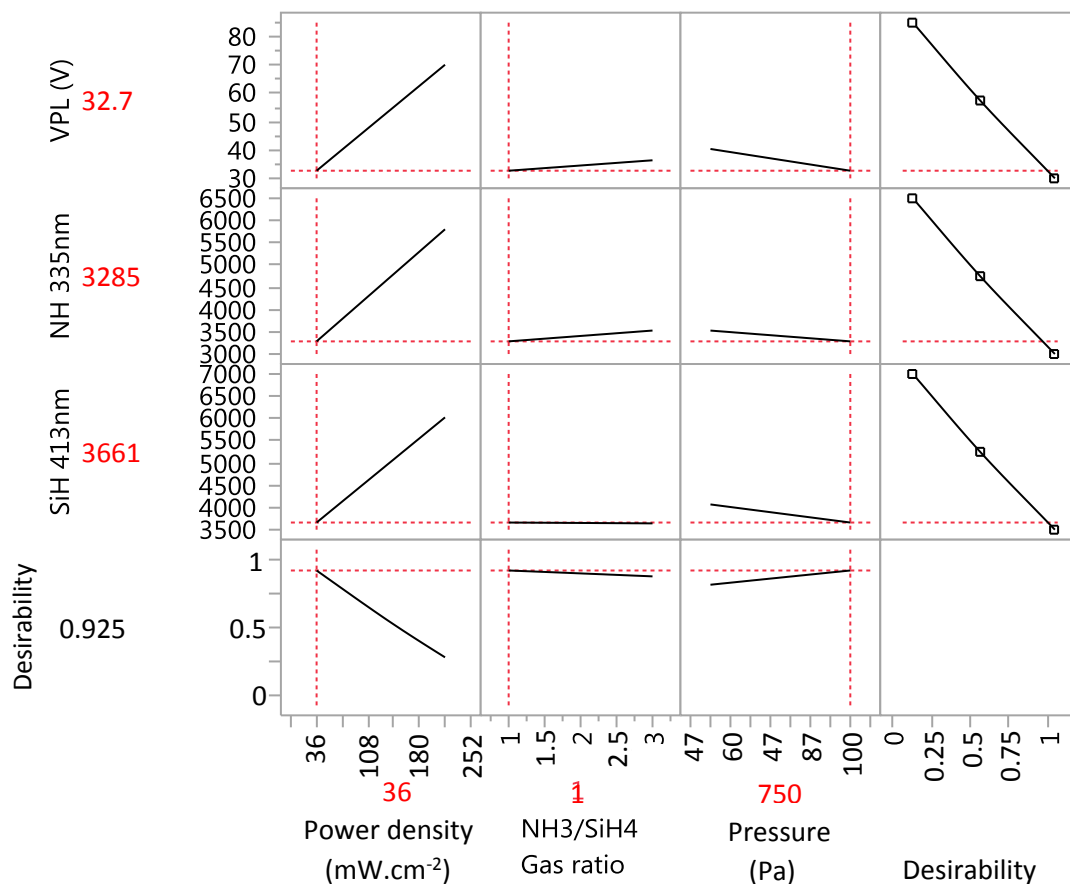
Figure 3.4: Full-factorial DOE results concerning intensities of SiH and NH* emission lines and V$_{PL}$ as a function of process conditions. Red numbers are the results of the maximised desirability.*

We used the process conditions that result in the lowest plasma radiation intensity and the lowest plasma potential to deposit an a-SiN$_X$:H film on c-Si. The plasma produced by these process conditions is not very shiny, as required, but the resulting a-SiN$_X$:H properties do not fit refractive index and transparency requirements. Indeed, with a refractive index of 3 and an optical bandgap of 2.2 eV (Figure 3.5.b), this material belongs to the so-called Si-rich silicon nitride family, with properties close to those of amorphous silicon.

The deposition parameter that has the lowest impact on the V$_{PL}$ and on the plasma radiation intensity is the gas ratio, so we increased it from 1 to 9. The bandgap monotonously increases as the NH$_3$/SiH$_4$ gas ratio increase (Figure 3.5.b). The gas ratio of 7 would be the best to fit the optimal refractive index of 1.97; but we preferred to choose the gas ratio of 9 that results in a wider a-SiN$_X$:H bandgap. These optimised process conditions (Table 3.1) generate a very pale plasma that is difficult to distinguish from the noise of the OES (Figure 3.5.a) with a V$_{PL}$ that increases from 32.7 to 34.2 for a gas ratio of 1 to 9.
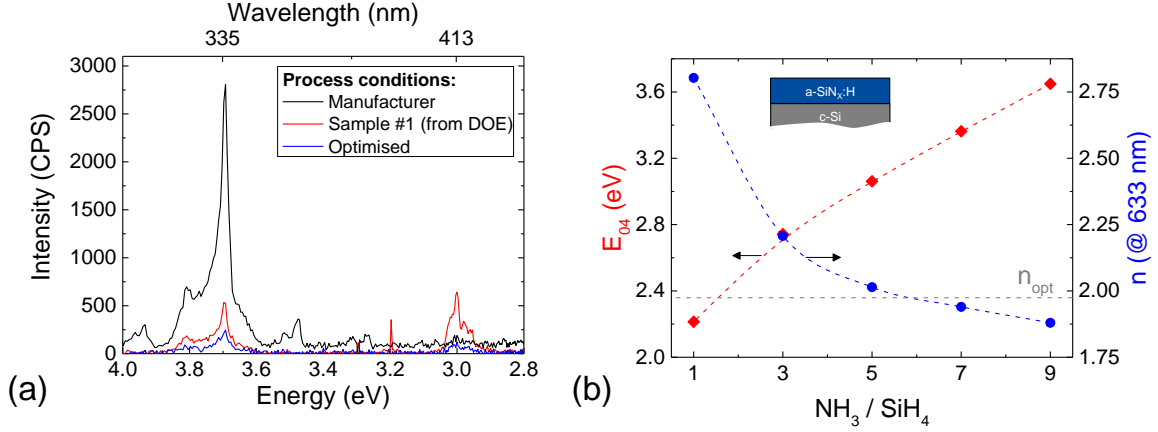
Figure 3.5: (a) OES of the different plasma conditions. (b) Optical properties of a-SiN$_X$:H deposited at 53 Pa with a power density of 36 mW.cm^{-2} and a gas ratio varying from 1 to 9.

The optimised a-SiN$_X$:H film has an optical bandgap of 3.65 eV and a refractive index of 1.88. The refractive index is lower than the ideal one between silicon and air, but it minimises the optical impact of the Al$_2$O$_3$ layer (n=1.64) that will be present below it. Indeed, for a normal incidence, the reflection at an interface is proportional to the square of the refractive index difference, the higher the difference, the higher the reflection (equation (3.4)).

$$R = \left| \frac{n_1 - n_2}{n_1 + n_2} \right|^2 \qquad (3.4)$$

Considering the refractive index of 1.88, the optimal capping layer thickness for ARC purpose would be 84 nm, but once more it does not take into account the presence of an underneath Al$_2$O$_3$ layer. Two possibilities can be considered. The first would consist in a complementary thickness approach, *i.e.* the capping thickness would be equal to 84 nm minus the Al$_2$O$_3$ thickness. The capping layer thickness would then range between 64 nm and 82 nm, for Al$_2$O$_3$ thicknesses ranging from 20 nm to 2 nm respectively. Even if it would be an elegant way to proceed, it would introduce more variables in the passivation study while we want to focus on Al$_2$O$_3$ properties. The second possibility, which has been selected, is to use the same a-SiN$_X$:H thickness for all Al$_2$O$_3$ thicknesses. We decided to use the average value of the complementary thicknesses, *i.e.* 75 nm.

Surface reflectance measurements have been carried out in order to assess the ARC properties of the capping layer. Double side polished c-Si wafers presenting either bare surface, either 60 ALD cycles of Al$_2$O$_3$ capped by 75 nm of a-SiN$_X$:H on its surface have been measured (Figure 3.6). For the wavelength of 630 nm, the reflectance decreases from 36 % for the bare c-Si surface to less than 1 % for the surface with the Al$_2$O$_3$/a-SiN$_X$:H stack. The effective reflectance decreases from 38 % to 13 % when the stack is present on the silicon surface. To further reduce the effective reflectance, surface texturing is required. The Al$_2$O$_3$/a-SiN$_X$:H stack has been deposited on random pyramids textured c-Si surface, reducing the effective reflectance down to 4 %. It has to be mentioned that we used the same deposition time of the a-SiN$_X$:H for both the flat and the textured surfaces. It results in a lower film thickness on the textured surface, explaining the blueshift of the minimal reflectance position to the wavelength of 500 nm.
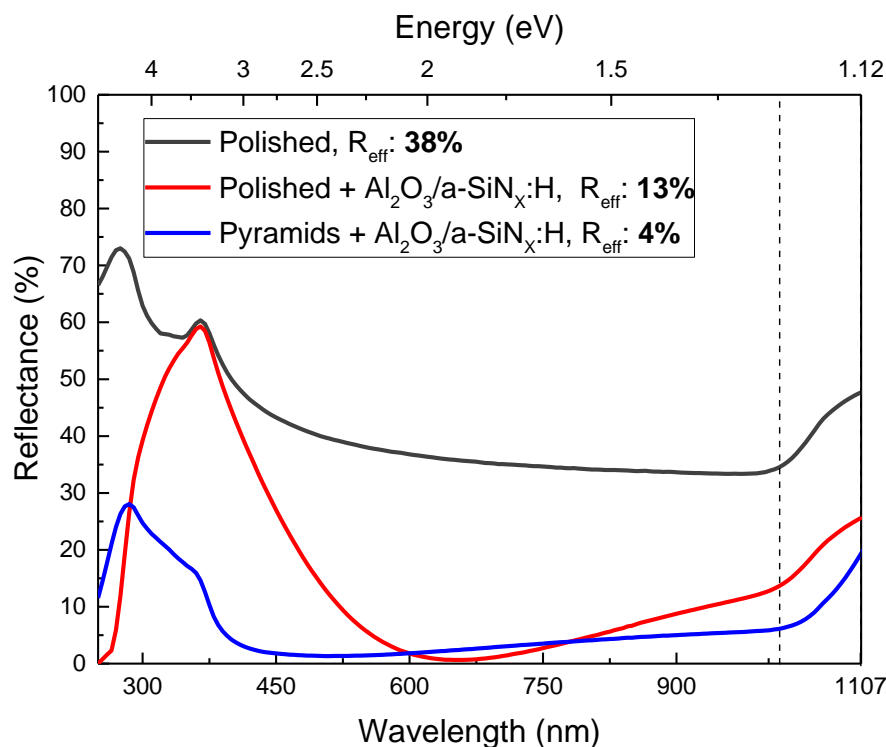
Figure 3.6: Reflectance measurements of double side polished wafers with bare surfaces or Al_2O_3/a-SiN_X:H stacks and random pyramid textured surfaces with Al_2O_3/a-SiN_X:H stack. The reflectance increase between the dash line and the wavelength of 1107 nm is due to the back surface reflectivity.

The optimised PECVD process conditions (high pressure, low power density and low ion bombardment) promote a radical growth mechanism, resulting in a polymeric-like a-SiN_X:H film. The polymeric-like characteristic of the a-SiN_X:H film is supported by XRR measurements (Figure 1.9). The film shows the same critical angle (0.215°) in as-deposited state (not shown) and annealed state (bottom graph on Figure 1.9) suggesting the same density (2.07 g.cm^{-3} after annealing). However, it has never been possible so far to fit the data obtained for the as-deposited film. The data acquisition was repeated on different samples with longer acquisition time on the same Bruker goniometer but without further success in data treatment. Another attempt has been made with a more advanced XRR goniometer at the Rigaku centre in Germany, not conclusive either. Thus we concluded that before annealing the film bulk is not homogenous enough to be modelled.

ERDA results show the high hydrogen content of the film, around 25%$_{at}$ (Figure 3.7.a). The FTIR spectrum (Figure 3.7.b) shows a larger Si-H absorption intensity compared to N-H content. The polymeric like film that contains a high fraction of organics is not thermally stable. Indeed, TDS results show that the hydrogen release begins at 300 °C and is maximal at 450 °C. Considering these TDS results, the post-capping annealing carried out at 380 °C should release enough hydrogen able to diffuse to the Al_2O_3/c-Si interface. ERDA measurement performed on the a-SiN_X:H film after PCA confirms that the post-capping annealing releases 45 % of the hydrogen content. It decreases from 25%$_{at}$ in as-deposited state to 15%$_{at}$ after PCA (Figure 3.7.a). It has to be noted that, despite the huge hydrogen release during PCA at 380 °C, no changes have been noticed in the film thickness and optical properties.
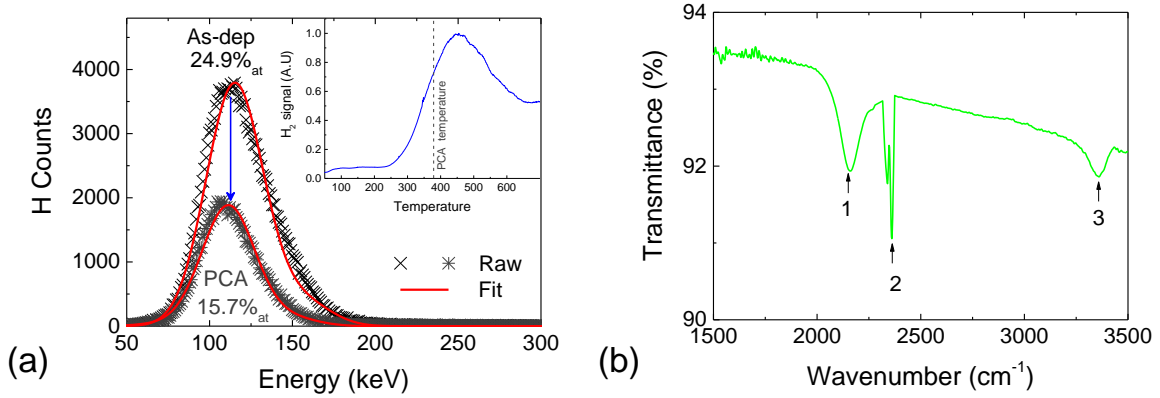
Figure 3.7: (a) ERDA and TDS (inset) spectra; (b) FTIR spectrum. Peak 1 is Si-H stretching (2160 cm⁻¹); peak 2 is CO₂ stretching (2340 cm⁻¹ and 2360 cm⁻¹); peak 3 is N-H stretching (3365 cm⁻¹) [26].

In order to evaluate its standalone passivation properties, the a-SiN$_X$:H film was deposited on n-type substrates. Before deposition, one sample was cleaned by HF dip while the other one kept its native oxide. After PECVD, there was already a slight lifetime difference between the two samples, which became greater after the PCA (Figure 3.8). The sample that received the HF cleaning had its lifetime doubled by the PCA while the sample that kept the native oxide has henceforth a five times higher lifetime. For the sample that received the HF clean, there might be a poor film/substrate interaction that hydrogen release during the PCA hardly improves. For the second sample, a poor chemical passivation is already partially fulfilled by the native oxide, the a-SiN$_X$:H then just act as a capping. The PCA can restructure the oxide but also provide hydrogen to fill electronic defects at the c-Si/native oxide interface.
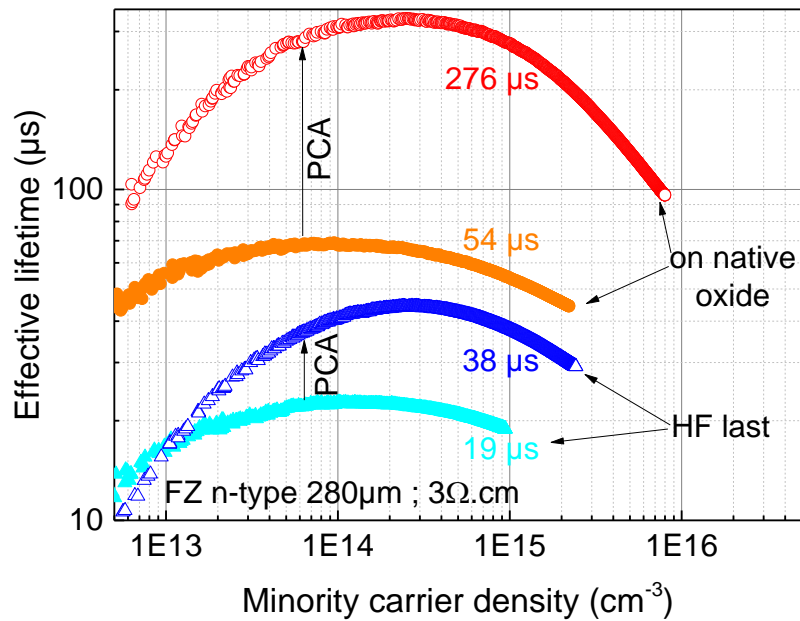
Figure 3.8: Effective lifetime of n-type c-Si passivated by an a-SiN$_X$:H deposited with the optimal process condition, either on HF cleaned wafer or directly on native oxide. Lifetimes are reported for a carrier density of ·10¹⁵ cm⁻³.

Despite both good optical and chemical properties of the a-SiN_X:H film, the deposition by PECVD might fill the Al_2O_3 electron traps due to plasma radiation and compromise our passivation study. In order to check that, we used a p-type substrate passivated by 60 ALD cycles at 250 °C and activated by 30 min of PDA at 380 °C. Contrary to the wavelength impact study presented in the previous chapter, we reduced the Al_2O_3 thickness to minimise the blistering. The latter is reported increasing when an a-SiN_X:H capping is deposited on Al_2O_3 (see chapter 4). In order to compare surfaces with and without capping, the front surface is capped only on its upper half, the lower one being protected during PECVD (Figure 3.9.b). The back surface remains passivated only by Al_2O_3. The post capping annealing is performed and then the back-surface is protected from illumination with an opaque substrate holder. The shadow mask used in the previous chapter is applied on the front surface but optical filters were removed (Figure 3.9.a). The whole system is sealed in a nitrogen bag and placed in the LIBI for 264 hours.

A PCD calibrated photoluminescence mapping is taken after mask removal (Figure 3.9.c). There is a very nice surface patterning due to the LIFE$_2$. On the lower half of the sample (pure Al_2O_3), LIFE$_2$ resulted in a lifetime enhancement of 35% while in the upper (Al_2O_3/a-SiN_X:H stack) the lifetime increased by 62%. First it can be concluded that the PECVD step does not fill the Al_2O_3 traps. Second, the capping seems to nearly double the LIFE$_2$ impact, maybe due to a better hydrogen diffusion from the a-SiN_X:H to the Al_2O_3/c-Si interface. The developed a-SiN_X:H capping seems to be perfectly suitable to study the impact of Al_2O_3 parameters on the resulting passivation properties.
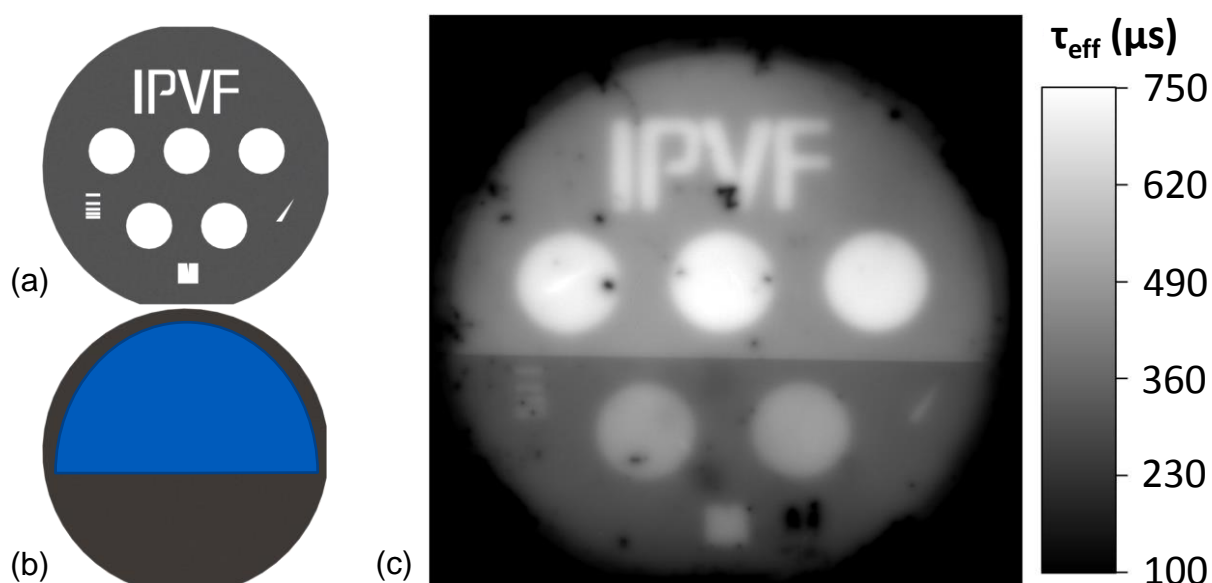
Figure 3.9: (a) Shadow mask without optical filters. (b) Lifetime sample passivated by 60 ALD cycles of Al$_2$O$_3$ @ 250 °C PDA @ 380 °C for 30 min on both surfaces. The a-SiN$_X$:H capping has been deposited only on the half of the top surface (blue area), not on the back surface, then a PCA of 20 min @ 380 °C was carried out. (c) PCD calibrated photoluminescence mapping of the lifetime sample after 264 h in the LIBI.

3.2   Impact of capped Al₂O₃ parameters on LIFE₂

3.2.1   Process flow

Ideally, the thinner the Al_2O_3, the higher the industrial throughput and the lower the Al_2O_3 optical impact below the ARC. So in the ALD thickness range obtained for a number of cycles comprised between 20 and 200 cycles. The chosen step was not constant, we choose to test layers thicknesses obtained from 20, 40, 60, 100 and 200 ALD cycles. The process flow used to produce lifetime samples is depicted on Figure 3.10. After the HF cleaning to remove native oxide, the ALD was carried out at 150, 200, 250 or 300 °C on the full 100 mm p-type c-Si wafers. Before the post deposition annealing, the wafers are cut in 4 pieces to produce 4 lifetime samples. The PDA that activates Al_2O_3 was performed at 350, 380, 410 or 440 °C for 30 min. The capping deposition temperature at 300 °C was the same for all the samples, followed by the post-capping annealing at 380 °C for 20 min that mimics the metallisation thermal step. During the manufacturing process, a particular attention has been paid to avoid sample illumination between each step. Likewise, the annealing was performed with the furnace in hotplate mode to limit the charge trapping during the sample manufacturing.
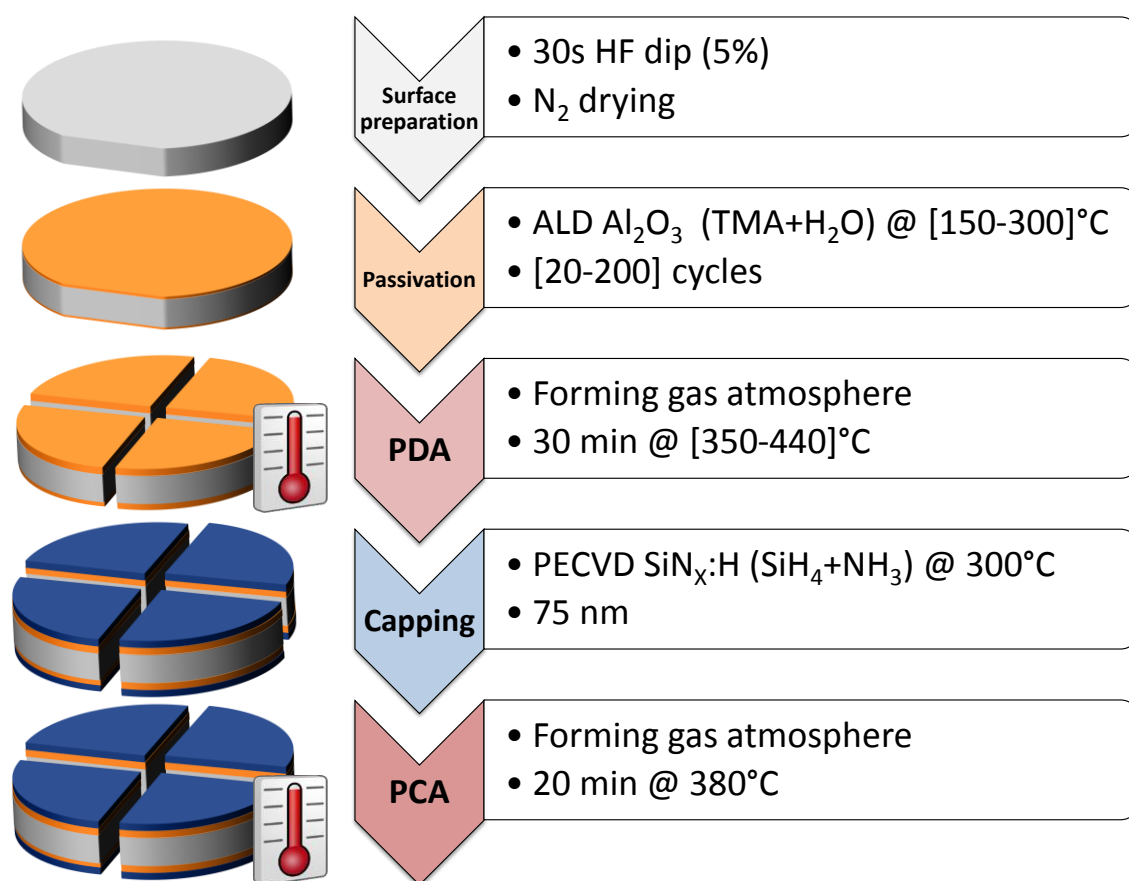
Figure 3.10: Process flow used to produce lifetime samples. Numbers between brackets are parameter ranges that have been tested. Before PDA, the wafers were cut in 4 pieces to produce 4 different lifetime samples.

3.2.2 Expected passivation trends

Some expected trends have to be reminded regarding hydrogen content and evolution in the passivation stacks as it is often pointed out as the passivating agent. Based on the material analysis of the previous chapter (chapter 2), some general trends (summarised on Figure 3.11.a) should be verified. The first one concerns the hydrogen content in the bulk of Al$_2$O$_3$, being higher for lower deposition temperatures. As this hydrogen is volume distributed, the thicker the layer the higher the hydrogen content. The second trend is about the hydrogen diffusion from the capping to the Al$_2$O$_3$/c-Si interface. Its diffusion across the Al$_2$O$_3$ to the c-Si surface is easier for thinner Al$_2$O$_3$ layers and should be facilitated by a lower Al$_2$O$_3$ density, *i.e.* deposited at lower temperature. Regarding the PDA impact (Figure 3.11.b), the higher its temperature, the higher the chemical species mobility. It might be beneficial for thick Al$_2$O$_3$ layers that do not contain a lot of hydrogen, but the diffusion is not only directed towards the c-Si surface so it can result in a layer that outgassed its hydrogen. Moreover, a higher PDA temperature might also result in a denser film, decreasing the hydrogen diffusivity from the capping toward the c-Si surface during the post-capping annealing.
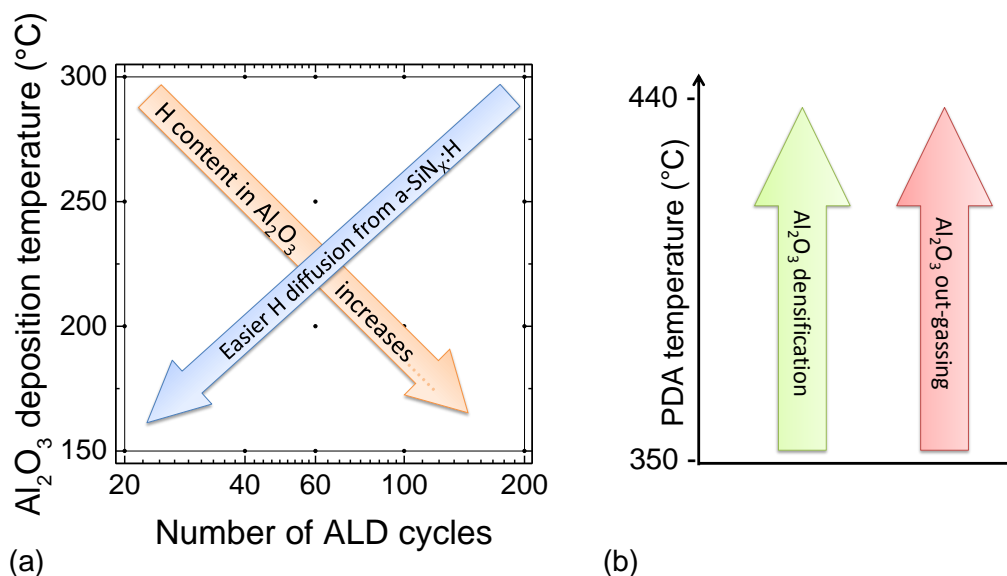
Figure 3.11: Schematic representation of hypotheses on: (a) Hydrogen content and evolution in the Al$_2$O$_3$/a-SiN$_X$:H passivation stack as a function of Al$_2$O$_3$ parameters. (b) Impact of PDA temperature on Al$_2$O$_3$

3.2.1 Passivation study

Keeping these material trends in mind, the passivation analysis can start. After the final annealing (PCA), the effective lifetime was measured by PCD (Figure 3.12.a; point α). Then the samples were placed in the LIBI and the lifetime evolution was monitored over one week to ensure proper trapping of electrons in the Al$_2$O$_3$, the lifetime was considered as saturated after this week in the LIBI (Figure 3.12.a; point β). Samples were removed from the LIBI and placed in a dark cabinet. To evaluate the charge de-trapping, the lifetime was monitored over one month and will be referred as "stabilised lifetime" after this month (Figure 3.12.a; point χ).

For a defined PDA temperature, 350 °C for example, the initial lifetime, the saturated lifetime and the stabilised lifetime can be plotted as a function of the Al_2O_3 thickness and deposition temperature (Figure 3.12.b, Figure 3.12.c and Figure 3.12.d respectively). From a passivation performance point of view, areas with SRV lower than 10 cm.s^{-1} can be traced and passivation conditions providing a lifetime around 4500 µs can be easily identified. By looking at the maps, it's visually striking that the LIFE$_2$ treatment had an impact on the passivation performances but it is difficult to evaluate quantitatively this impact and its stability during the dark storage. These lifetime mappings are more helpful than absolute lifetime values, so we decide to plot the lifetime enhancement due to the LIFE$_2$ treatment and the degradation of the saturated lifetime along the dark storage. The first value is calculated from the initial and the saturated lifetime, while the second is calculated from the saturated and the stabilised lifetimes. It will allow a simpler extraction of passivation properties trends as a function of Al_2O_3 deposition parameters.
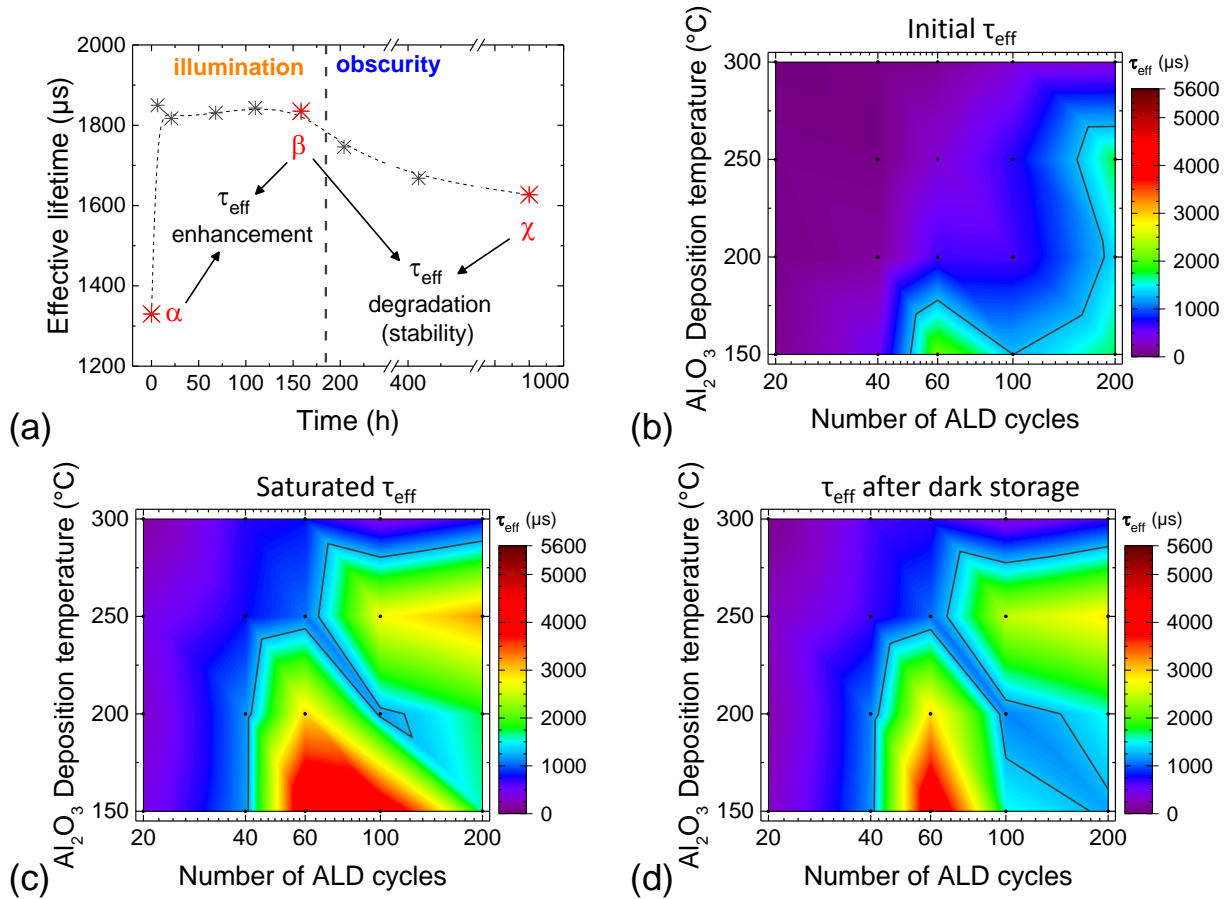
Figure 3.12: (a) Lifetime follow-up of a sample passivated with 200 ALD cycles deposited at 250 °C and activated at 380 °C, line is a guide to the eye. (b) Initial lifetime of Al_2O_3/a-SiN_X:H passivation stacks as a function of Al_2O_3 thickness (abscissa) and deposition temperature (ordinate) for the PDA of 350 °C. (c) Saturated lifetime, after LIFE$_2$ in the LIBI. (d) Lifetime after storage in the dark cabinet. Black lines delimits areas with SRV < 10 cm.s^{-1} i.e. lifetime higher than 1300 µs.

On Figure 3.13, each map in a row concerns the same PDA temperature and each map in a column the same parameter, i.e. the lifetime enhancement due to $LIFE_2$ (left column), the saturated lifetime (central column) and the lifetime degradation during the dark storage (right column). For each sample, these three values allow retrieving the initial and the stabilised lifetimes if needed, but what we want to understand is how Al_2O_3 parameters (thickness, deposition temperature and PDA temperature) impact the passivation performances and stability. The $LIFE_2$ treatment is just a way to observe the surface passivation variation due to field effect modification.

We start by discussing the first row of Figure 3.13 that concerns the PDA at 350 °C. Regarding the lifetime enhancement, it seems to be quite constant between 20 and 100 ALD cycles for the deposition temperature of 150 °C while for the three other deposition temperatures, the lifetime enhancement mainly depends on the Al_2O_3 thickness and less on its deposition temperature. The 40 ALD cycles looks like a hinge around which the lifetime enhancement steadily decreases. An extremely high lifetime enhancement about 900 % is calculated for these thicknesses, corresponding to a saturated lifetime around 1000 µs, which is not so high compared to the previously obtained 4500 µs provided by 60 ALD cycles.
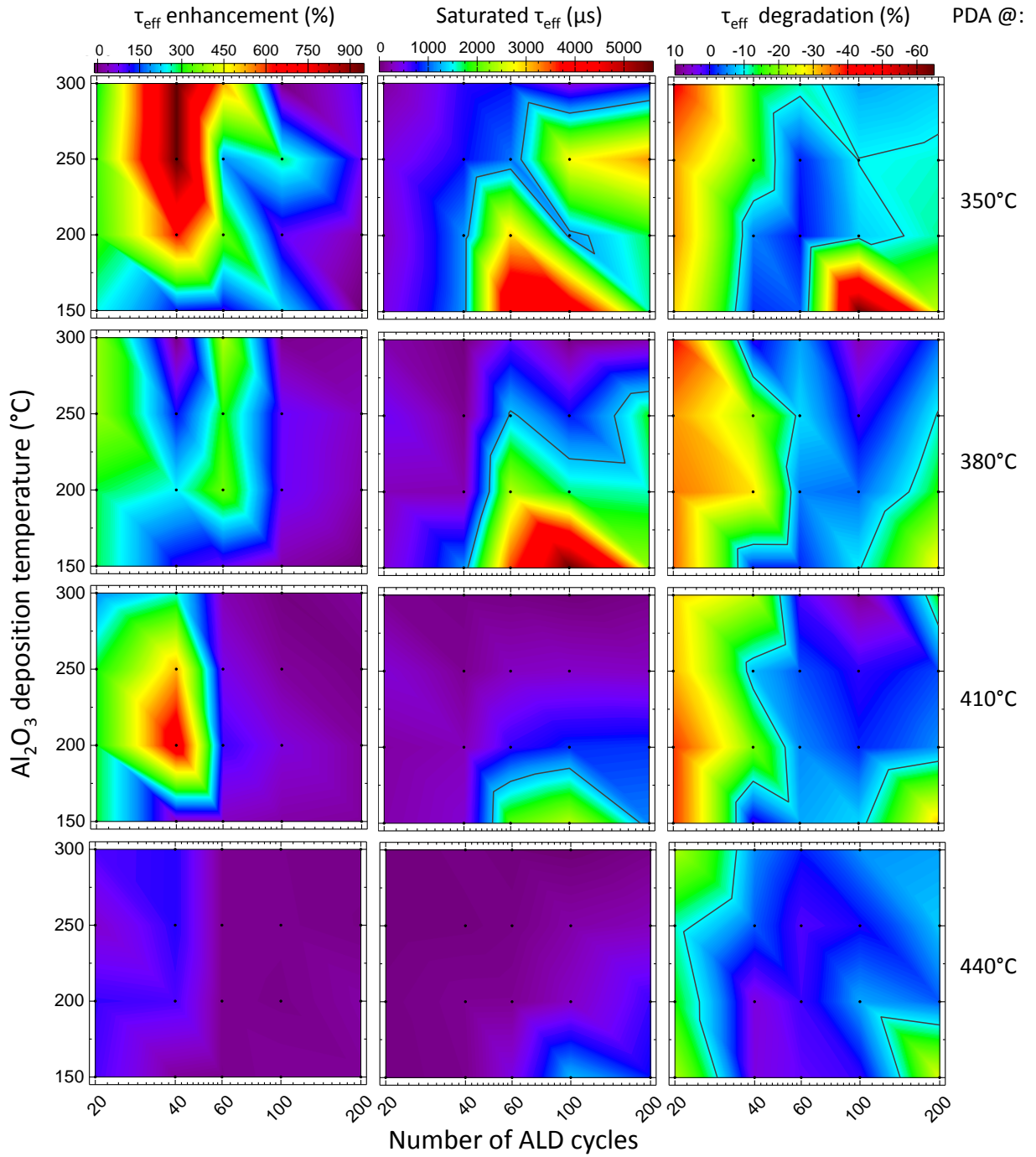
Figure 3.13: τ_{eff} enhancement due to LIFE₂ treatment (left column), saturated τ_{eff} (central column) and degradation of the saturated τ_{eff} during dark storage (right column) as a function of Al₂O₃ thickness and deposition temperature. The difference between each row is the PDA temperature before a-SiN_X:H capping as indicated on the right side of rows. The colour scale above each column stands for the four graphs of the column. Black lines on the central column graphs represent areas with τ_{eff} higher than 1300 µs, i.e. SRV < 10 cm.s⁻¹. On the right column, black lines delimit areas where the degradation during the dark storage is lower than 10 %.

Considering the saturated lifetime, it is not obtained for the highest hydrogen content in the Al_2O_3 layer (200 ALD cycles deposited at 150 °C), maybe due to the presence of blisters for these layers (see chapter 4). The saturated lifetime is the highest when there is a trade-off between hydrogen content in Al_2O_3 and facilitated diffusion of hydrogen through the Al_2O_3 layer. Surprisingly, for the thinnest Al_2O_3 layers for which the "ocean" of hydrogen contained in the capping layer can easily reach the Al_2O_3/c-Si interface and fill remaining dangling bonds, the saturated lifetime is low (<1000 μs) and seems quite independent of the deposition temperature. This is interesting because it might underline that it is not only the hydrogen content that matters in the case of passivation by Al_2O_3 layers but also the way it is released. Indeed a-SiN_X:H generally releases molecular H_2 while Al_2O_3 is a good proton conductor [162]. Another possibility is that, dehydroxylation of Al_2O_3 releases hydrogen but might also release oxygen atoms (see chapter 2, page 30) that can strengthen the interfacial SiO_2, this one being a good chemical passivation layer. It would fit with the commonly reported interfacial SiO_2 thickening during PDA [124] and the exceptional passivation increase by a PDA conducted in pure O_2 atmosphere [144].

Regarding the stability of the saturated lifetime during the storage in a dark cabinet, this one can be excellent in some cases. For example, the sample passivated by 60 ALD cycles at 200 °C had a lifetime enhancement of 348% (660 μs → 2958 μs) and a saturated lifetime degraded by less than 1% (2958 μs → 2940 μs) during the month of storage in the dark cabinet. On the degradation maps, the black lines delimit areas where the degradation is lower than 10% over the month of storage in the dark cabinet. It brings out two separated degradation areas. The first one for Al_2O_3 layers with thicknesses below 60 ALD cycles, showing similar lifetime degradation between 20 and 40 ALD cycles for the whole range of deposition temperatures. The second one seems to follow the same trend as the initial hydrogen content in Al_2O_3 layers, and might be related to the presence of blistering for samples in this area (visible to the naked eye on tilted samples, Figure 3.14).

Figure 3.14: Al_2O_3/ a-SiN_X:H passivated sample presenting blistering.

.

For all the PDA temperatures, the trends are similar. The thinnest Al_2O_3 layers are the most sensitive to $LIFE_2$ treatment, but the percentage of enhancement generally decreases as the PDA temperature increases. The saturated lifetime is the highest in the same regions but its absolute value decreases when the PDA temperature increases, maybe due to higher out-gassing and Al_2O_3 densification. There are still two distinct areas with degradation higher than 10% but their extent and absolute values decrease as the PDA temperature increases.

3.3   Conclusion

The observed passivation trends are all schematically summarised on Figure 3.15. The stability zone (green zone 2 on Figure 3.15) is enlarged when the deposition temperature increases. In this zone, the highest lifetime is generally obtained for the lowest deposition temperature, i.e. the highest hydroxyl content. In our case, the highest passivation level among all the samples was obtained for 100 ALD cycles deposited at 150 °C and activated at 380 °C. It provides a lifetime of 5546 µs (saturated) decreasing to 5013µs when stabilised (-10 %), nearly the highest expected value from the modelling results of chapter 1. The use of LIFE$_2$ is a good way to simply probe the passivation quality and stability. However, the stability zone is between two zones of lifetime instability (red zones 1 and 3). It is reasonable to think that lifetime degradation mechanisms that happen in these zones also impact in some way the apparent stable lifetime of zone 2.
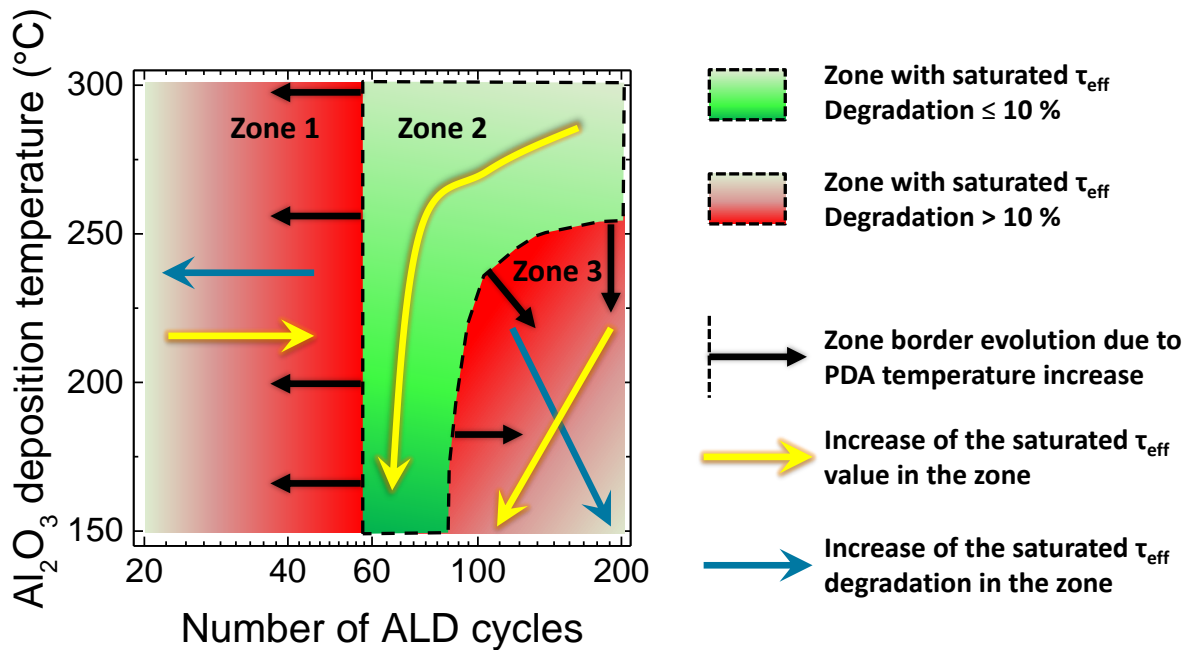
Figure 3.15: Schematic summary of passivation trends observed for Al$_2$O$_3$/a-SiN$_X$:H passivated samples.

The low passivation level in zone 1 is unexpected, maybe linked to a missing chemical passivation despite the presence of hydrogen from the capping. It could underline that the dehydroxylation from the Al$_2$O$_3$ is more important for chemical passivation than the dehydrogenation from the capping. The low passivation level could also be linked to field effect passivation instability as the saturated lifetime degradation amplitude increase when the film becomes thinner, *i.e.* when the tunnelling probability of electrons through the Al$_2$O$_3$ film increases. These hypotheses will be explored in chapter 5.

The high but unstable lifetime that can be reached in zone 3 seems to be linked to the hydroxyl content in the Al$_2$O$_3$ layer but also to the possibility for dehydroxylation by-products to be out-gassed from the film. Blisters are visible on samples in this area and are good candidates to explain the lifetime degradation in this zone. This blistering phenomenon will be explored in the next chapter.

4

Blistering: witness of the Al_2O_3/c-Si interface degradation

Contents

.

4.1   Blistering

4.1.1   Overview

Visually, blisters look like hillocks dispersed all over the surface (Figure 4.1.a, Figure 4.1.b). In the c-Si/Al_2O_3/a-SiN_X:H stack there are two interfaces that can be suspected of delamination, the one between crystalline silicon and aluminium oxide or the one between aluminium oxide and silicon nitride. We found that blistering always occurs at the c-Si/Al_2O_3 interface, as the presence of a capping layer is not a prerequisite to observe this phenomenon (Figure 4.1.g) [219]. Blisters can either pop-up leaving the c-Si surface exposed to the ambient atmosphere, or remain closed (Figure 4.1.c, d, e and e). Observed from the top with optical microscope, the latter look like a Fresnel lens (Figure 4.1.f).
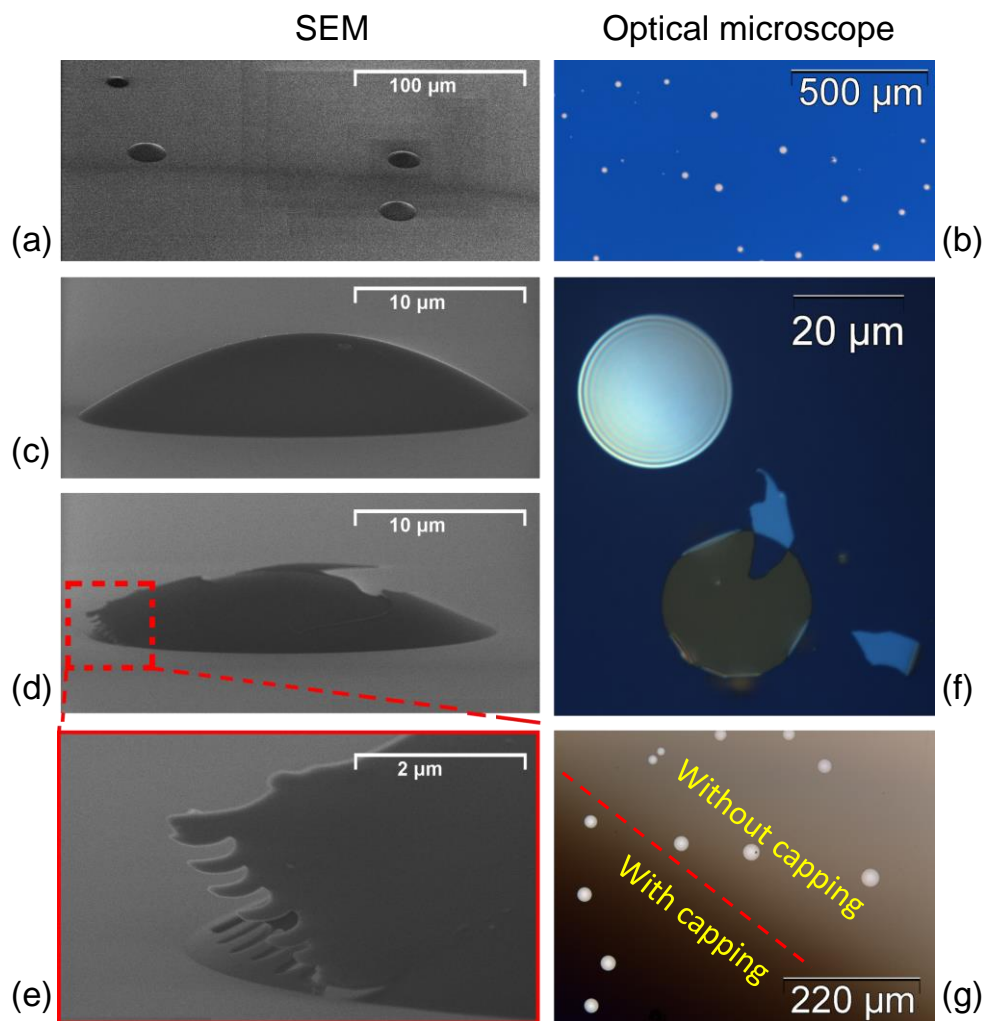
Figure 4.1: Blistering images from Al_2O_3/a-SiN_X:H stacks (left column SEM tilted top-view; right column optical microscope). (a) and (b) macroscopic views of the surface. (c) intact blister, (d) exploded blister, (e) zoom on the exploded blister showing a stamp-like pattern (f) intact blister on top and fully exploded one, (g) blister of Al_2O_3/a-SiN_X:H stacks near the edge of the sample, were a-SiN_X:H capping is not deposited.

These blisters with a Fresnel lens aspect are in fact not the only defects present on the surface. While pushing up the luminosity of the optical microscope, the iridescent aspect of blisters leaves room to saturated white discs and reveals other small spots around them (Figure 4.2.a). These are very small, around 1µm of diameter for a height well below 1µm (Figure 4.2.b) and will be thereafter referred to as blisters of type I, while the bigger ones showing Fresnel lens aspect will be referred to as blisters of type II.
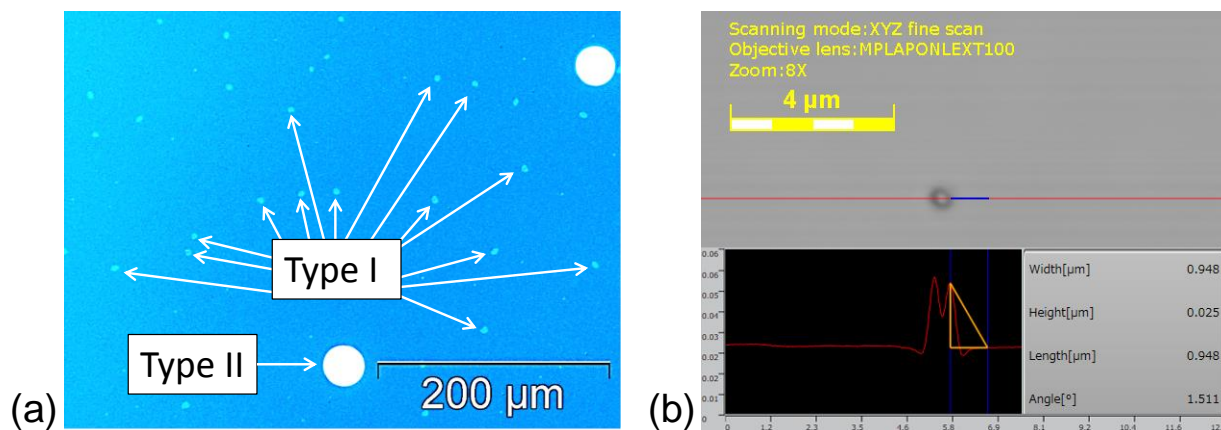
Figure 4.2: (a) Blistering of type I and type II on the same surface observed by optical microscope (100 ALD cycles deposited @ 200 °C and capped with 75 nm of a-SiN_X:H); (b) Confocal picture of type I blister.

Blistering origins are still under debate, but several concordant facts are reported in the literature. Blistering is a well-known phenomenon occurring at the a-Si:H/c-Si interface [220, 221], resulting from the accumulation of molecular H_2 at this interface. Despite the lower hydrogen concentration in Al_2O_3 compared to a-Si:H, blistering is a phenomenon that is difficult to avoid for this passivation material. The accumulation of gaseous species such as H_2 and H_2O at the Al_2O_3/c-Si interface is unanimously pointed out as the main source of the delamination. The discussion thereafter will follow this hypothesis. However, the reader has to keep in mind that most of the arguments that will be discussed in terms of gas release can also be transposed in terms of mechanical stress [153], but this parameter has not been evaluated during this thesis.

During the TDS analysis of the material, H_2 and H_2O are released above 300 °C [153]. For some authors, H_2 release might also be due to CH_X cracking at high temperature (firing > 700 °C) [222] but regarding the extremely low carbon content (Figure 2.5), it is unlikely to be the main H_2 source. The gaseous origin of blistering is supported by several observations: the deposition temperature (ruling hydroxyl group content) and the post-deposition thermal budget (ruling dehydroxylation and diffusion) have a strong impact on blisters size and quantity [222-226]. The film thickness also impacts blistering: the thicker the film the higher the blistering density (number of blisters per square centimetre) [219]. Apart from the higher hydroxyl group content in a thicker film, the latter represents a more efficient barrier to gas diffusion [153, 224, 225, 227].

Blistering at the c-Si/Al_2O_3 interface has been reported for films deposited by thermal ALD [225], PA-ALD [222] and also by PECVD [181, 219]. It underlines a general trend of the Al_2O_3/c-Si interface to blister, mainly linked to its chemical nature rather than to its deposition technique. The catalytic behaviour of the T_d coordinated Al atoms mainly present at this interface might explain the gas production there, gaseous species which cannot easily diffuse through the film.

At first, we tried to corroborate the reported trends and to clarify blistering origins. Then, as blistering deteriorates the optical and electrical properties of Al_2O_3/a-SiN_X:H stacks [153, 223, 228], we tried to avoid it. The first obvious impact of blisters is the de-passivation of the surface below the hillocks, as visible on Figure 4.3. However, it has never been possible so far to establish a clear link between blister quantity on the surface and the effective lifetime of minority carriers [225, 228].
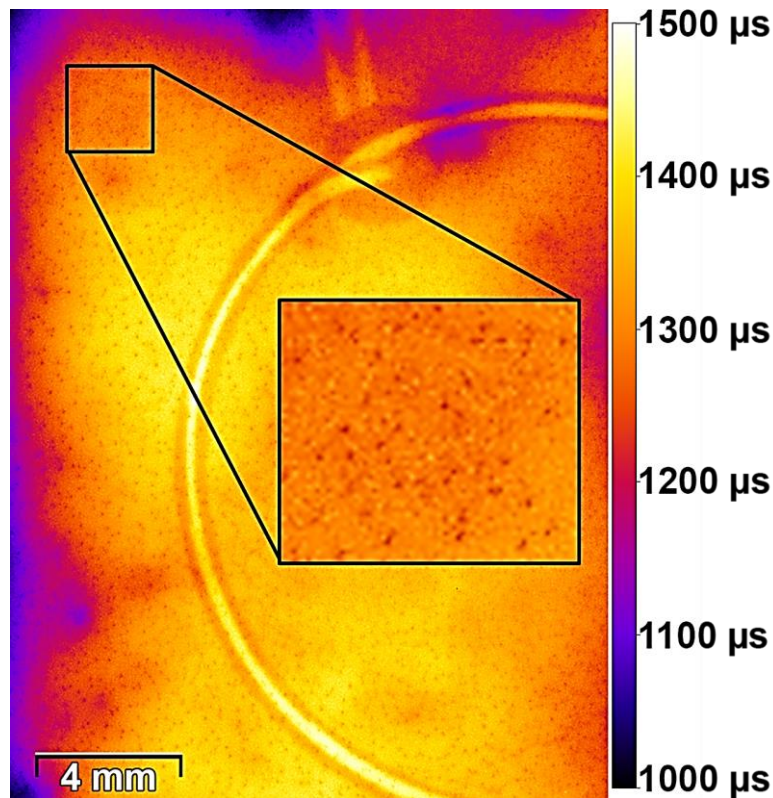
Figure 4.3: High magnification PCD calibrated photoluminescence picture of a blistered sample (300 ALD cycles of Al_2O_3 capped by 75 nm of a-SiN_X:H). Dark spots are blisters; the large ring is the Sinton stage detector. The inset view in the middle is a zoom of the top left corner area.

4.1.2   Gas release

We performed TDS measurements on the samples deposited with 1000 ALD cycles at 150 °C, 200 °C and 250 °C (Figure 4.4.a). When the temperature reaches 350 °C in the TDS equipment, the H_2 effusion starts, but without a pronounced difference between the three samples. At 450 °C the film deposited at 150 °C instantly releases a huge H_2 quantity, while the film deposited at 200 °C shows a sharp H_2 release only at 550 °C and with a lower magnitude. A second peak is visible for these two samples above 600 °C, while the sample deposited at 250 °C does not show these effusion peaks. In fact, these temperatures are not representative of the dehydroxylation kinetics that occurs similarly for the three samples as demonstrated by the water release. The latter starts around 300 °C and steadily increases to reach its maximum between 500~600 °C. The water quantity is slightly higher for the Al_2O_3 deposited at lower temperature, which is consistent with higher content of hydroxyl groups in the film. The maximum H_2 effusion temperatures correspond in fact to the blisters explosion. Indeed, the three samples show blistering after TDS.

The sample deposited at 150 °C has 95 % of its blisters open (Figure 4.4.b), while only 15 % is exploded for the sample deposited at 200 °C (Figure 4.4.c) after TDS. Regarding the blistering density, it is almost the same for both samples (~5·10⁴ blister.cm⁻²), but blisters are a bit larger for the deposition temperature of 200 °C (1.5 to 2 times wider). The sample deposited at 250 °C also presents blisters that have similar size than the ones of the sample deposited at 150 °C, but none of these ones are open. These results support the singular behaviour of the Al_2O_3/c-Si interface. Considering the smaller size of H_2 molecules compared to H_2O, detected molecules during TDS cannot originate from the same location in the Al_2O_3 film. Indeed, the dehydroxylation of Al_2O_3 produces water that is able to out diffuse from the film as the temperature increases but H_2 escapes from the film principally when blisters explode. It underlines an H_2O production proportional to the whole thickness of Al_2O_3 while H_2 production occurs mainly at the c-Si/Al_2O_3 interface, where T_d coordination of Al atoms is predominant. These results are consistent with the observations reported by Vermang *et.al.* [153] who observed a temperature delayed detection of H_2 when the Al_2O_3 film thickness increase from 5 nm to 30 nm.
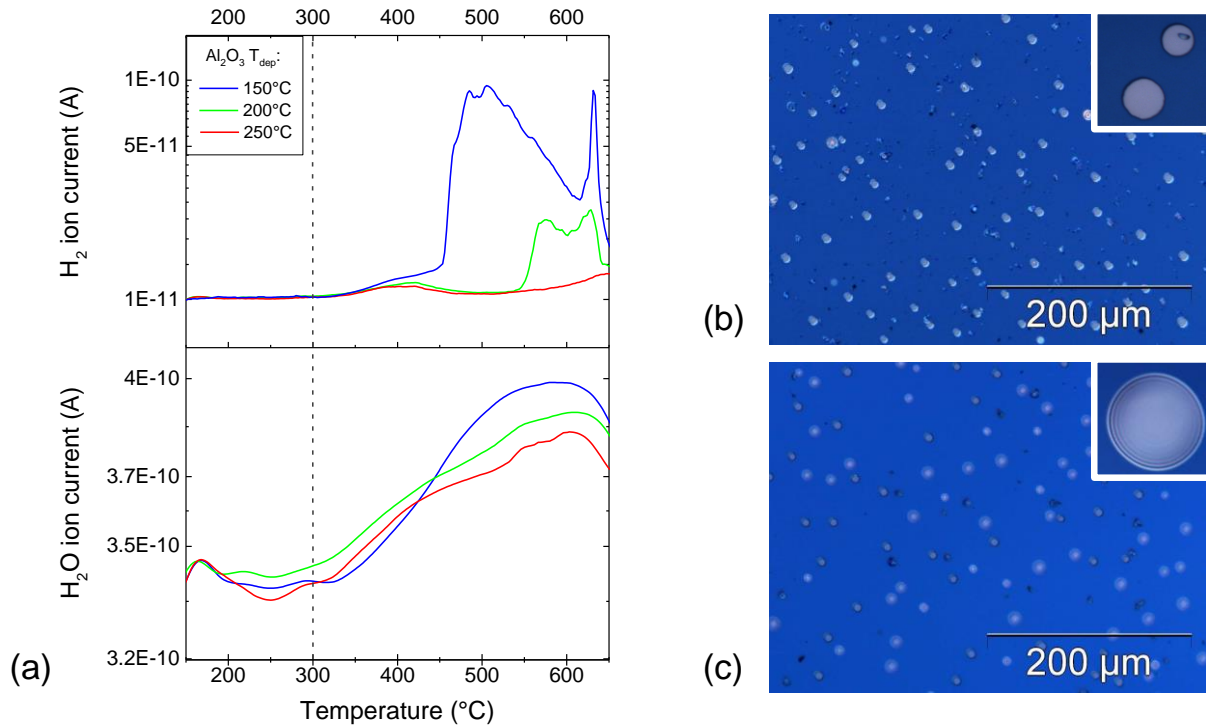
Figure 4.4: (a) TDS of Al_2O_3 deposited at different temperatures (1000 ALD cycles). (b) and (c) optical microscope picture of blisters that appear during TDS for Al_2O_3 deposited at 150 °C and 200 °C respectively. A X10 zoom of blisters is visible in the top right corner of each picture. Blisters presented in the zoom of (b) are totally exploded, the silicon surface is exposed to the atmosphere.

4.1.3   Blistering statistics

The 80 samples passivated with Al_2O_3/a-SiN_X:H stacks (Figure 3.11) were analysed by optical microscopy. The blistering density was evaluated by averaging values from five different places over the sample surface. The blister diameter is the average of 30 values (when there are at least 30 blisters on the surface) for type II blisters while the size distribution was not evaluated for the type I blisters due to optical limits of the microscope. The standard deviation of distribution will be represented as the error bar on the results graphs. The proportion of delaminated interface has been calculated assuming a disk surface of the average diameter multiplied by the average blistering density. Before entering into a quantitative description, qualitative overview of blistering will be discussed.

Type II blisters are visible on all samples having an Al_2O_3 film obtained by 100 ALD cycles or 200 ALD cycles, except for those deposited at 300 °C. Interestingly, type I blisters are present only for samples with 60 ALD cycles deposited at 150 °C and 200 °C, while type II blisters are absent. Type I blisters coexist with type II blisters for the Al_2O_3 thickness of 100 ALD cycles whereas samples with 200 ALD cycles present only type II blisters. As summarised on Figure 4.5.a, the smallest blisters (Type I) show up for the highest hydrogen content in the Al_2O_3 films with 60 ALD cycles (150 °C and 200 °C). When the Al_2O_3 thickness is increased to 100 ALD cycles (higher hydrogen content, thicker barrier to gas effusion), bigger blisters (Type II) start to show up among the small blisters. When doubling the Al_2O_3 thickness to 200 ALD cycles, the smallest blisters (type I) are not visible any more and only type II blisters remain.

(a)   (b)
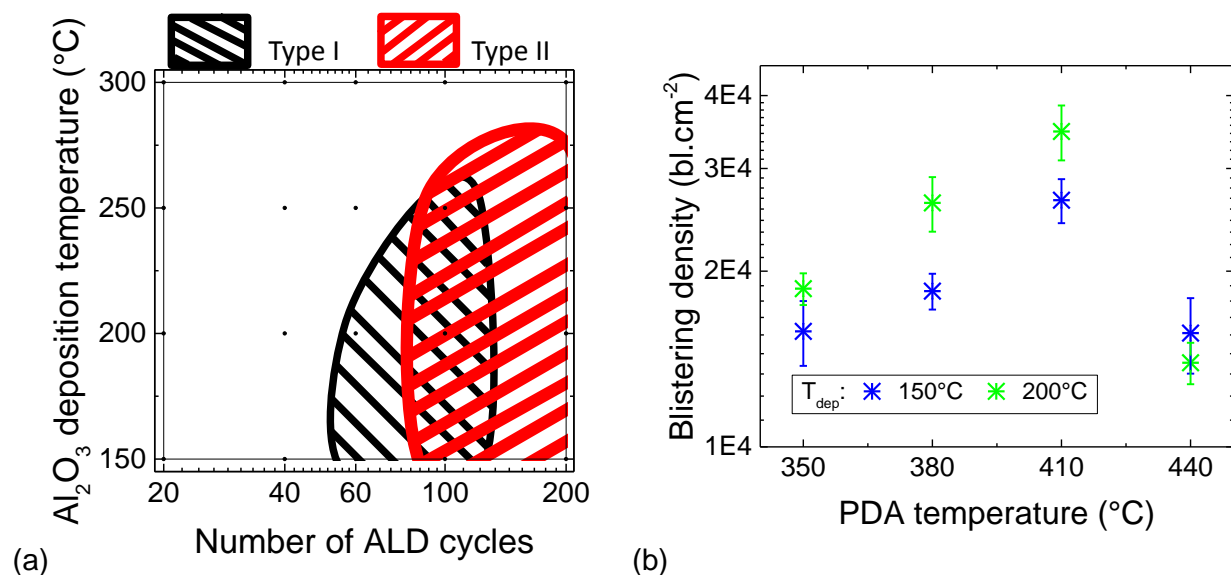
Figure 4.5: (a) Blistering map of the Al_2O_3/a-SiN_X:H passivation stack depending on Al_2O_3 thickness and deposition temperature. The a-SiN_X:H capping is 75 nm thick. (b) Type I blistering density for the stack having 60 ALD cycles of Al_2O_3 capped by 75 nm of a-SiN_X:H.

The type I blistering density on samples with 60 ALD cycles shows a clear dependence on the PDA temperature (Figure 4.5.b). Between 350 °C and 410 °C the blistering density monotonously increases but drastically decreases for samples annealed at 440 °C. Considering a constant diameter of 1 µm for all type I blisters, it results in a delaminated area portion below 0.06 % for all these samples.

For the samples having an Al$_2$O$_3$ thickness obtained by 100 ALD cycles, the type I blistering density looks completely random (not shown) while the deposition temperature clearly rules the type II blistering density (Figure 4.6). The lower the deposition temperature, the higher the type II blistering density. While clear trends are not noticeable regarding the PDA temperature effect on Al$_2$O$_3$ deposited at 200 °C and 250 °C, it has a small impact on the blistering density of Al$_2$O$_3$ deposited at 150 °C. The blister size is more or less constant for each deposition temperature, the lowest giving slightly bigger blisters. It results in a delaminated area portion that depends mainly on the deposition temperature. The lower the deposition temperature, the higher the delaminated area portion, regardless of the PDA temperature. This delaminated area portion is between 0.2 % and 0.45 % for the samples with 100 ALD cycles deposited at 150 °C, so 4 to 6 times higher than for samples with 60 ALD cycles deposited at the same temperature.

For the samples with 200 ALD cycles, the difference between the T$_{dep}$ of 150 °C and 200 °C disappears, these samples showing very similar blistering sizes and densities. The blistering density increases with increasing PDA temperature, but the latter does not have a clear impact on the blister size. Compared to samples with 100 ALD cycles, the blistering density and so the delaminated area portion is greater for samples with 200 ALD cycles, up to 2.3 %.

When we tried to model (statistical analysis) with JMP software the type I blistering density dependence on the deposition temperature and PDA temperature, the goodness of fit is only of 0.6 for samples with 60 ALD cycles. The R² of such model decreases to 0.03 if we address the type I blistering density of samples with 100 ALD cycles, while R² is about 0.7 for type II blistering on these samples. For samples with 200 ALD cycles, the modelling of blistering density and size as a function of deposition temperature and PDA temperature gives better results, R² = 0.78 and R² = 0.80 respectively. All these blistering trends are consistent with the hydrogen content that increases when the Al$_2$O$_3$ thickness increases or the deposition temperature decreases. In the same way, higher PDA temperatures result in higher dehydroxylation and so higher gas production.

When the film thickness decreases, small blisters (type I) disappear to the benefit of bigger blisters (type II), with a surface density two orders of magnitude lower. This observation is consistent with nucleation, coalescence and growth process of the blisters. The coexistence of both blister types for the intermediate thickness does support this hypothesis.
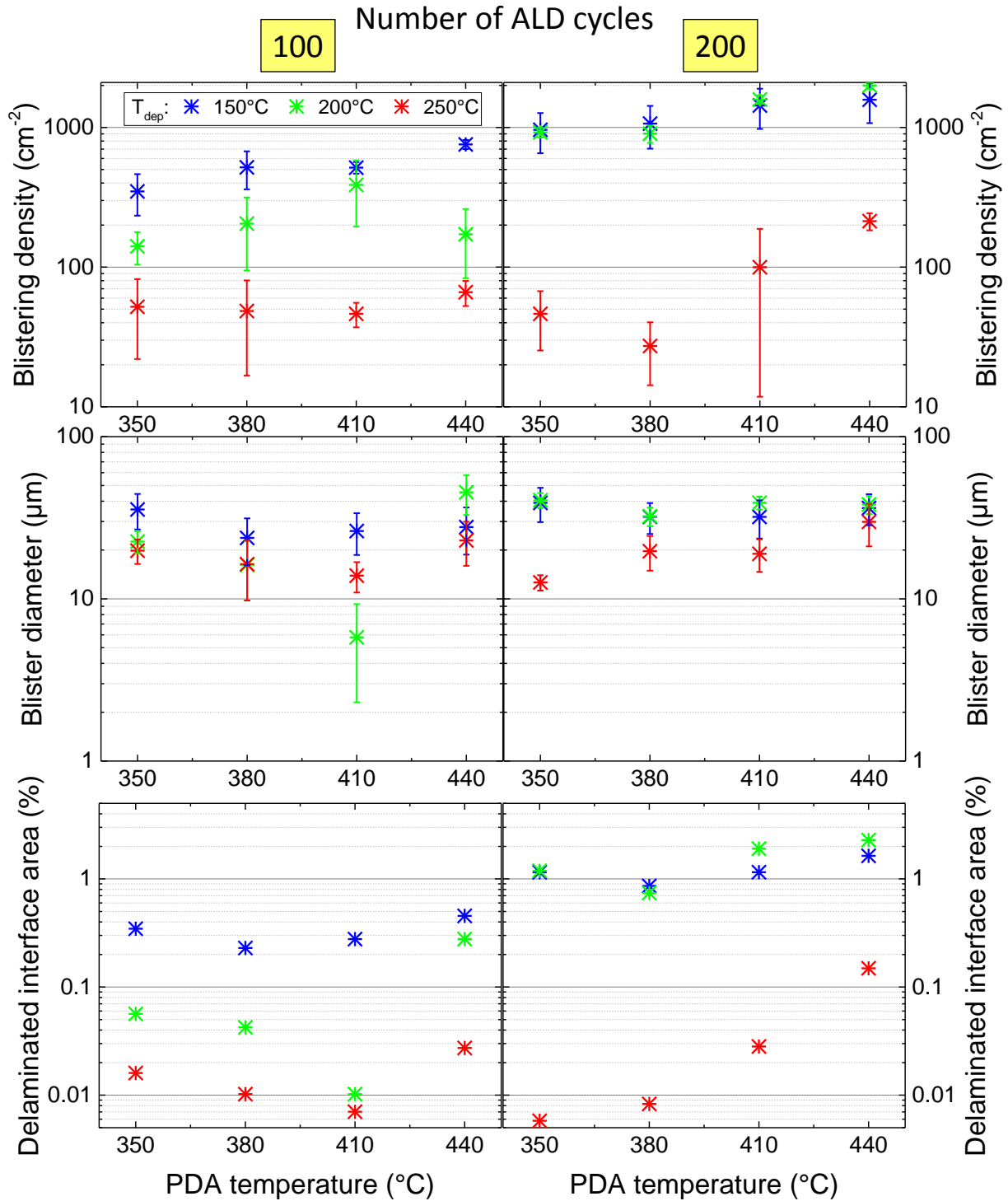
Figure 4.6: Type II blistering statistics for 100 and 200 ALD cycles capped by 75 nm of a-SiN$_X$:H. Determined by optical microscopy.

However, while trying to link blistering (size and density) to the lifetimes measured in chapter 3 (Figure 3.11), no correlation can be established so far. The goodness of fit never exceeds 0.4, which means that at least 60 % of the lifetime response cannot be explained by the blistering observations. Considering that blisters are in fact the macroscopic manifestation of gas accumulation at the c-Si/Al$_2$O$_3$ interface, it is possible that we are not able to detect interface degradation that does not lead to blistering. During the systematic blisters counting by optical microscope, some atypical type II blisters have been encountered (Figure 4.7.a). Despite an apparent morphological difference, these blisters share a common feature: a non-homogenous delamination. Analysed with confocal microscope (Figure 4.7.b), the apparently non-delaminated area in the middle of the blister is measured at the same height as the surface surrounding the blister, i.e. the centre of the blister is still stuck to the c-Si surface. This underlines a contribution of the adhesion parameter to the blistering, as proposed in the literature [229], but this parameter could not be evaluated.
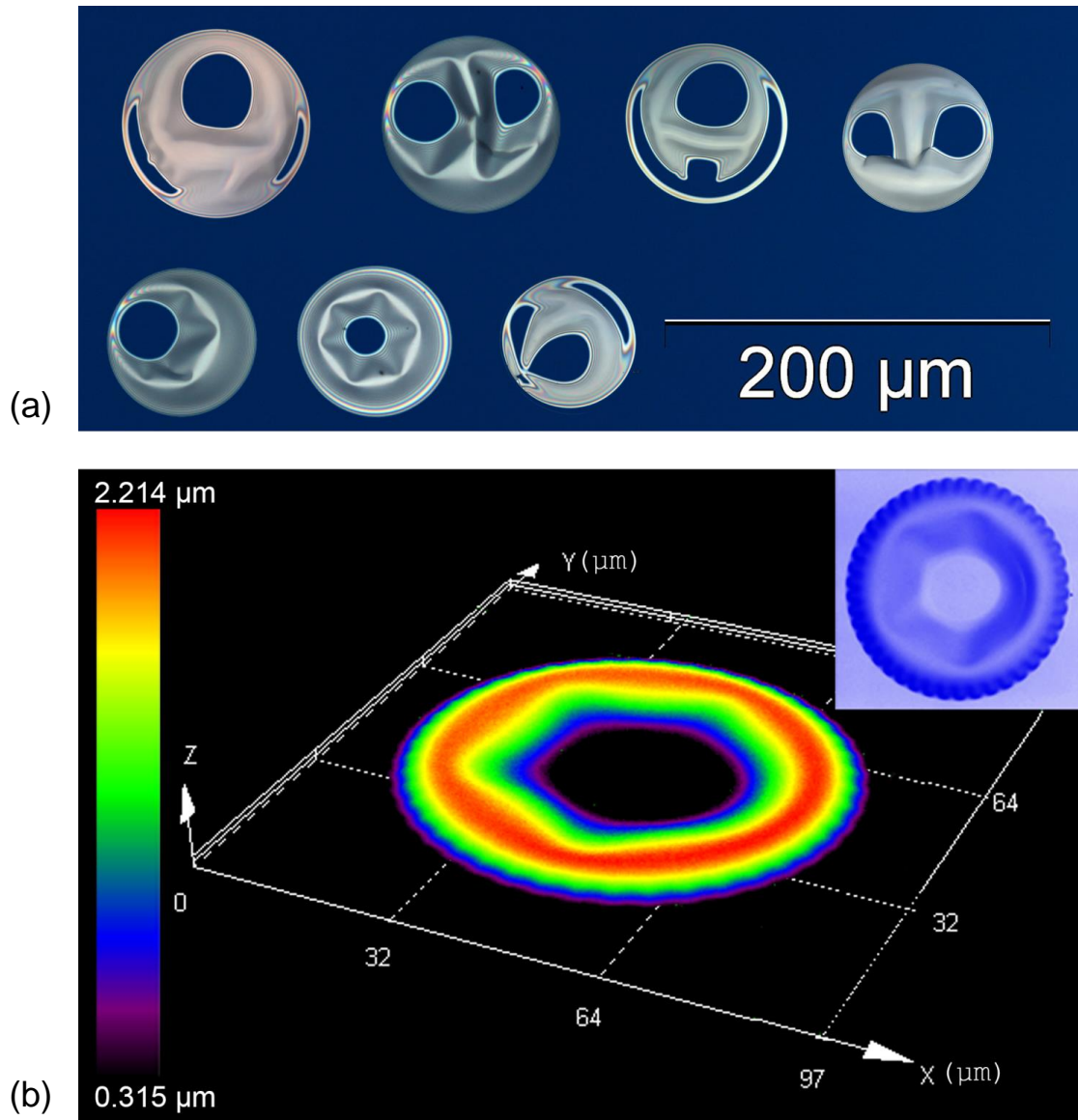
Figure 4.7: (a) Selection of non-homogeneously delaminated blisters observed with optical microscope. (b) Confocal mapping of a non-homogeneously delaminated blister.

4.1.4   Al₂O₃/c-Si interface analysis by coloured picosecond acoustics microscopy

The coloured picosecond acoustics (APiC) microscopy is a suitable technique to detect the adhesion degradation at the c-Si/Al₂O₃ interface. Its typical set-up is described on Figure 4.8.a. and relies on a pump and probe scheme. It consists in the generation of an acoustic wave on-top of the passivation stack with an ultrashort IR pulse (pump, λ=800 nm), the sample being metallised with a thin Al layer (12 nm) for this purpose (Figure 4.8.b). Part of the blue probe (λ=400 nm) is transmitted through this thin Al layer and is reflected at the c-Si surface. It is the reflectivity variation of the c-Si surface that is recorded. Indeed, the c-Si surface reflectivity is modified when the acoustic wave generated by the pump crosses it (Figure 4.8.b, 1st point). A part of the acoustic wave is reflected back to the free surface. This wave being fully reflected at the Al/Air interface, several round trips of the acoustic wave in the passivation stack can be detected at the c-Si surface until total energy dissipation (Figure 4.8.c).
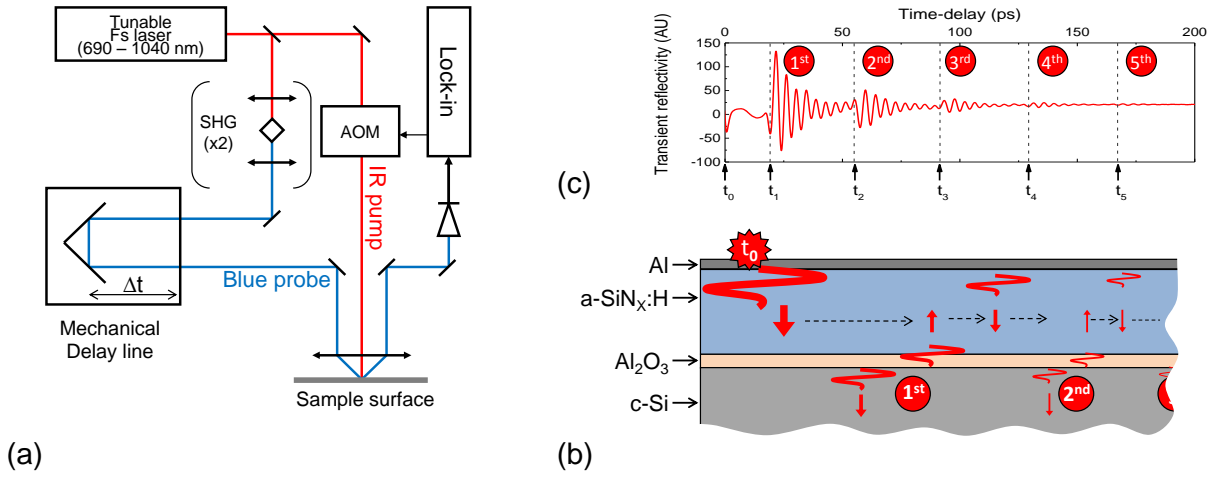
Figure 4.8: (a) Schematic diagram of APiC setup: The pump beam is chopped at high frequency (100 kHz) thanks to an acousto-optic modulator (AOM). The reflected probe beam is detected by an optical detector and the signal is amplified through a lock-in scheme in order to extract the relative change in reflectivity ($\Delta R/R$ = transient reflectivity) at the c-Si surface. (b) Schematic representation of the acoustic wave propagation in the passivation stack, for the sake of clarity, phenomena that are temporally separated are drawn shifted to the right (dotted black arrows are temporal translation, not spatial). An acoustic wave is generated at the sample surface with the pump laser (t₀). The wave propagates through the dielectric stack (red arrow) toward the Al₂O₃/c-Si interface. There, a part of the acoustic wave is transmitted to the c-Si substrate and the other part is reflected back (1ˢᵗ point). The propagation of the acoustic wave through the Al₂O₃/c-Si interface modifies the c-Si surface reflectivity; this variation is monitored with the probe beam and detected at t₁. The part of the acoustic wave which propagates toward the free surface is fully reflected at the Air/Al interface and propagates again toward the c-Si/Al₂O₃ interface producing a 2ⁿᵈ echo detected at t₂. This reflection scheme is repeated until the acoustic wave energy is fully dissipated. (c) Recorded signal from the acoustic wave generation (t₀) to the total wave dissipation (t₀ + 200 ps). The time delay of 36 ps between each echo detection (t₁→t₂→t₃ etc.) corresponds to the round trip of the acoustic wave between the Air/Al interface and the Al₂O₃/c-Si interface.

For a given interface, the acoustic reflection coefficient (R_a) is proportional to the acoustic impedance difference of the two materials as given by equation (4.1). Any variation in the interface adhesion properties results in an increased R_a and so in a longer time before the acoustic wave vanishes in the passivation stack (Figure 4.9.a). Practically, the interface quality can be summarised by its R_a coefficient. Rather than looking for acoustic impedance of materials, R_a value is determined by fitting the mean echo number (n) with a power law R_a^n. The lower the R_a, the better the adhesion quality. For example, the interface quality of sample 1 on Figure 4.9.b is better than the one of sample 2. We will stick to this acoustic reflection coefficient definition for our purpose. The readers can refer to [230, 231] for more detail on the APiC and related material physics.

$$R_a = \frac{(Z_2 - Z_1)}{(Z_2 + Z_1)}$$

(4.1)

With:

- Z_X : The acoustic impedance of material X
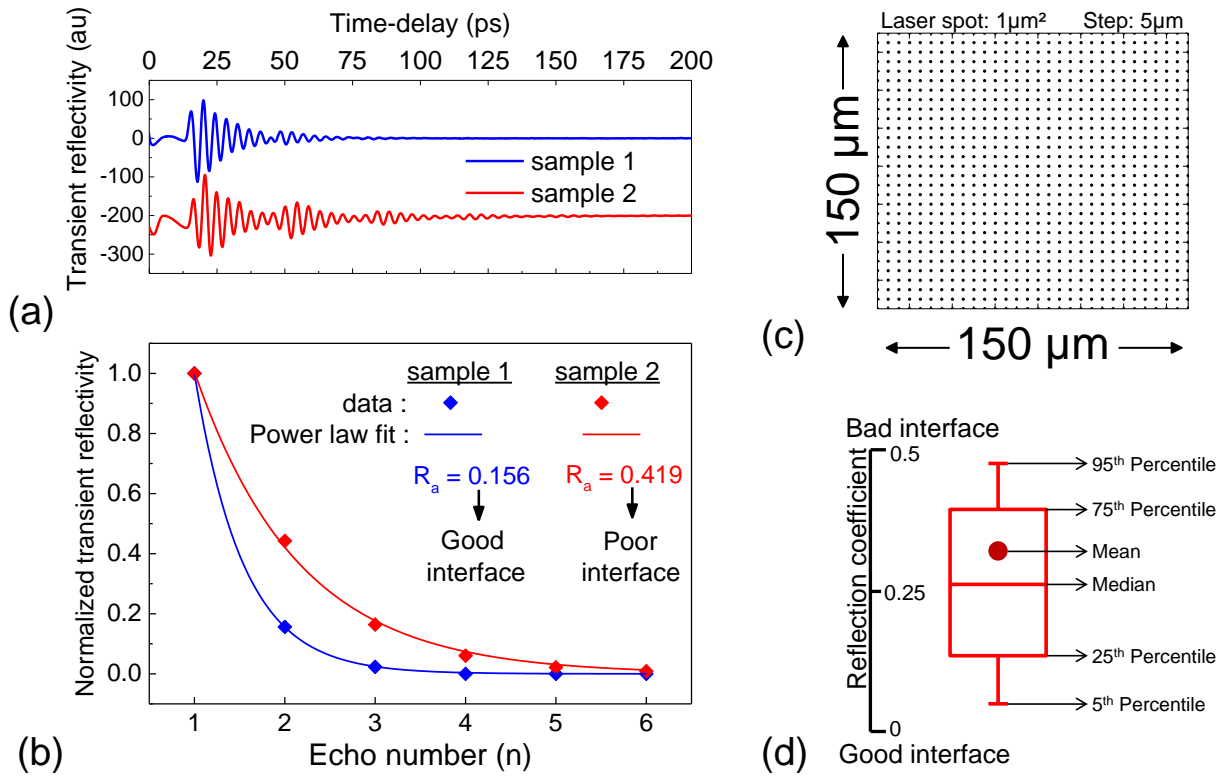
Figure 4.9: (a) Transient reflectivity signal recorded for two samples. (b) Determination of the reflectivity coefficient (R_a) from the signal recorded for the two samples of graph (a). The normalised intensity of the echo is fitted with a power low R^n. The results are presented in two ways in this thesis: (c) a 900 points mapping of the reflectivity coefficient determined over a surface of 150 x 150 µm. The step between measurement points (black dot) is 5 µm for a laser spot area smaller than 1 µm². (d) Statistical box charts are used to summarise the 900 measured values of a R_a mapping.

As blistering underlines an adhesion inhomogeneity over the surface, just one R_a value cannot be considered as representative for the whole interface quality. An acoustic reflection coefficient mapping is performed over a surface of 150 μm x 150 μm with a distance step of 5 μm between each probed place (Figure 4.10.c). This thin mesh provides a qualitative description of the interface homogeneity and the statistical treatment of these 900 R_a values can be considered as representative of the interface quality (Figure 4.9.d). The standard deviation of 30 measurements on the same spot gives a standard deviation about 5 %, supporting a good reproducibility of the measurement. To evaluate the potential links between blistering and adhesion, samples passivated with 60 and 100 ALD cycles deposited at 150, 200 and 250 °C and that received a PDA at either 350 °C (Figure 4.10) or 410 °C (Figure 4.11) were analysed by APiC.
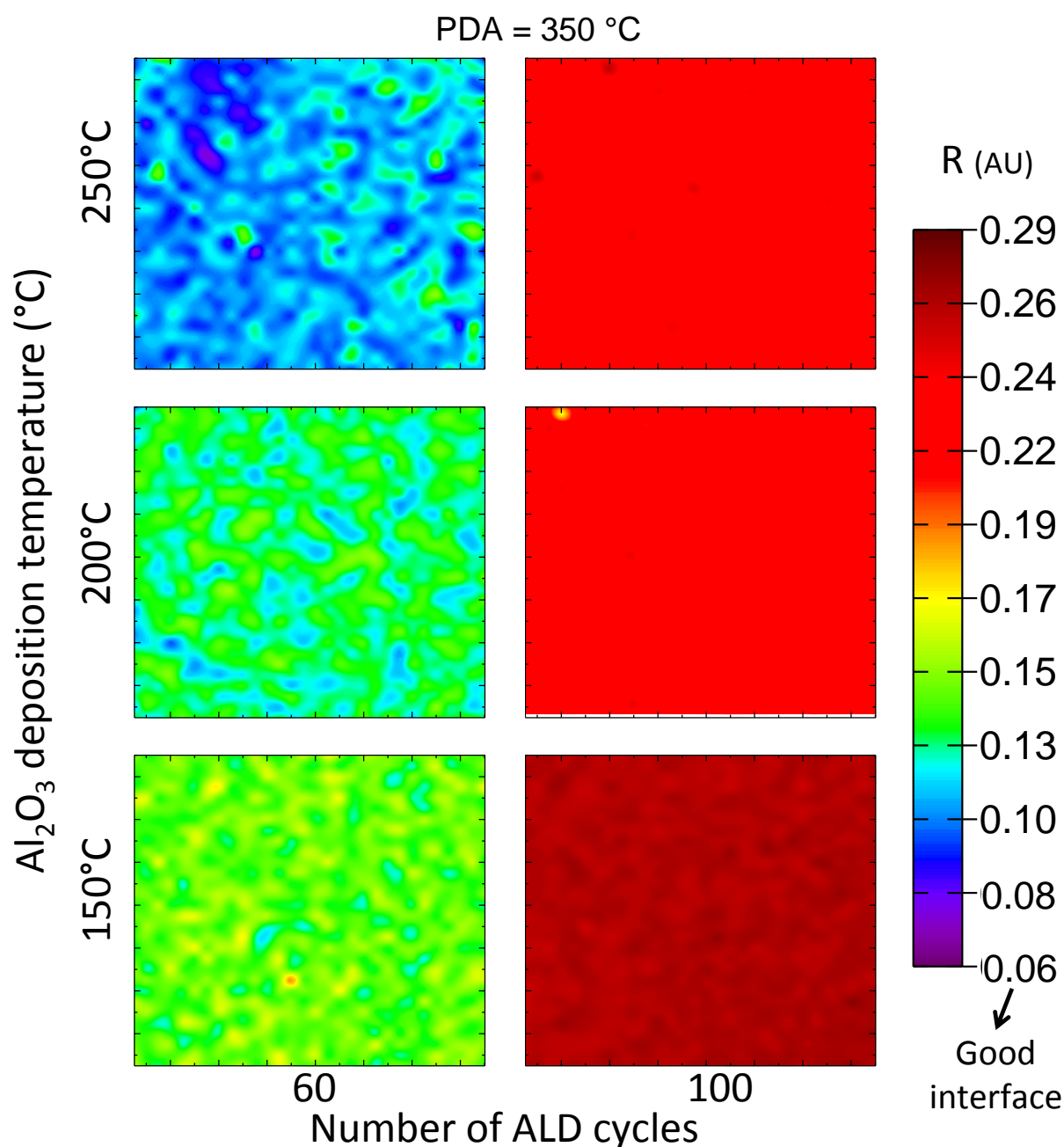
Figure 4.10: APiC mapping of the Al₂O₃/c-Si interface for 60 ALD cycles (left column) and 100 ALD cycles (right column) deposited at 150 °C, 200 °C and 250 °C annealed at 350 °C for 30 minutes.
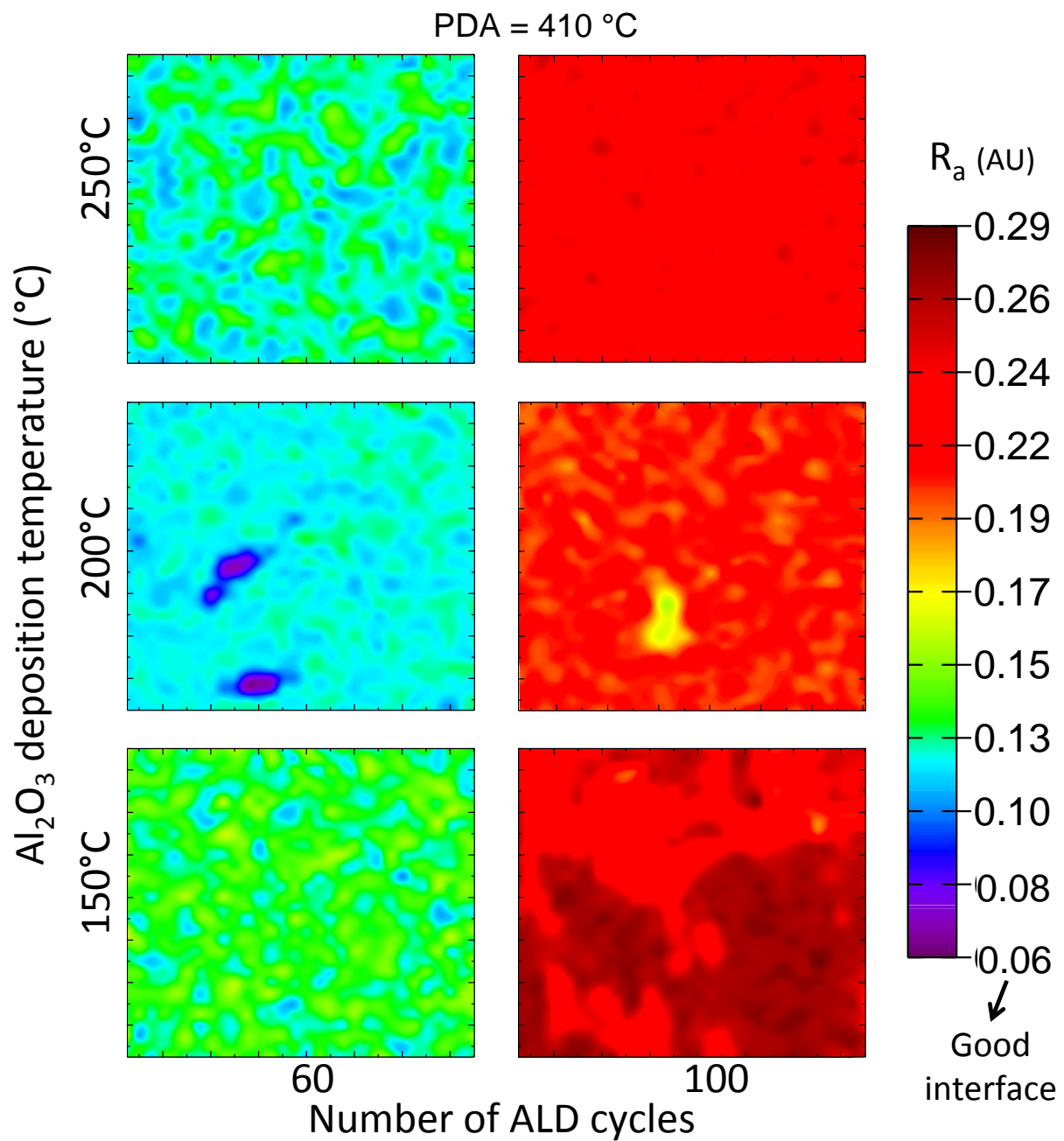
Figure 4.11: APiC mapping of the Al$_2$O$_3$/c-Si interface for 60 ALD cycles (left column) and 100 ALD cycles (right column) deposited at 150 °C, 200 °C and 250 °C annealed at 410 °C for 30 minutes.

The APiC mapping of samples provides useful information. The lowest acoustic coefficient that has been measured is 0.06; any value above this one reveals adhesion degradation. Each mapping consists of interwoven areas with high and low R_a, showing that adhesion inhomogeneity are present at the microscopic scale even if blistering was not visible with the optical microscope, *e.g.* 60 ALD cycles deposited at 250 °C. Even if APiC mapping is useful to qualitatively characterise the variation of the acoustic coefficient, a statistical representation is easier to discuss (Figure 4.12).

The most impacting parameter regarding the adhesion is the ALD film thickness. An increase of the Al_2O_3 thickness from 60 to 100 ALD cycles nearly doubles the acoustic coefficient, regardless of the deposition temperature or the PDA temperature, which is consistent with higher hydrogen content in the thickest films. In the same way, the second impacting parameter is the deposition temperature of the Al_2O_3 films, the lower the deposition temperature, the higher the acoustic reflection coefficient. For samples deposited at 150 °C and 200 °C, a post-deposition annealing at higher temperature slightly improved the interface quality while it deteriorates the one of samples deposited at 250 °C.
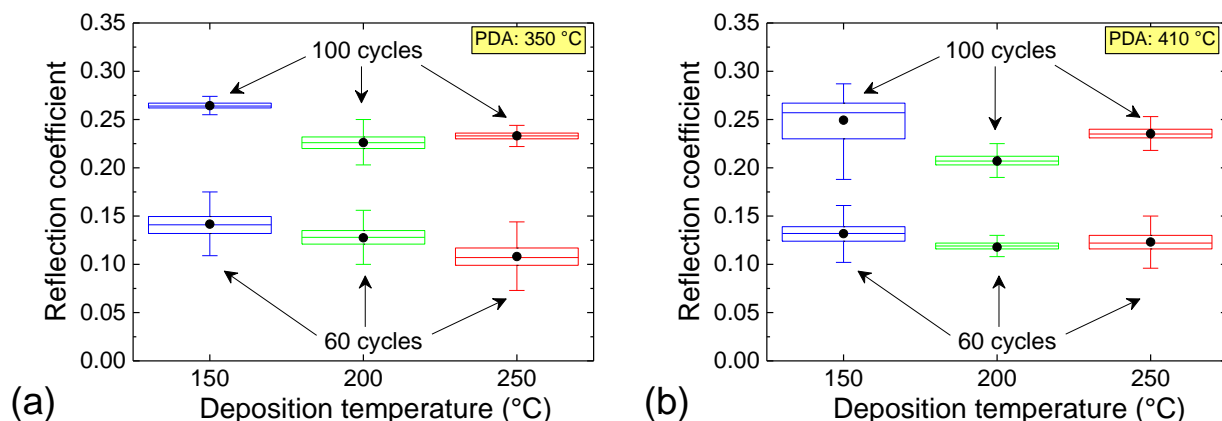
Figure 4.12: Reflection coefficient distribution of the Al_2O_3/c-Si interface for 6 nm and 10 nm of Al_2O_3 deposited at 150 °C, 200 °C and 250 °C. The PDA of 30 minutes was carried out at (a) 350 °C (b) 410 °C.

These trends are consistent with the hydrogen content that becomes higher when the deposition temperature decreases and when the film thickness increases. It suggests that the increase of hydrogen content weakens the adhesion between the Al_2O_3 film and the c-Si substrate, leading to blistering. In order to support these observations, the correlation between the mean value of R_a and the blistering size (and density) has been evaluated thanks to JMP software for the type II blisters. The correlation coefficient is a number that quantifies the dependence of a factor to another one. It takes absolute values between 0 (not correlated at all) and 1 (complete correlation). The correlation coefficient between the mean value of R_a and the blister size is 0.92 and of 0.78 between the mean value of R_a and the blistering density. These high correlation coefficients support well the strong link between adhesion and blistering. No correlation was found between blistering of type I and the R_a mean value (0.24), but as previously discussed, type I blisters are difficult to count and seem to disappear to the benefit of type II blisters, jamming the statistical trends.

The control of the hydrogen incorporation and release in the film is a real challenge that needs to be addressed in order to limit the degradation of the adhesion at the Al_2O_3/c-Si interface.

4.2   Hydrogen management during ALD

4.2.1   Concept of the Thermal Drift Atomic Layer Deposition

4.2.1.1   Current strategies to avoid blistering

In the literature, several approaches have been proposed to limit the blistering phenomena:

- ➢ Out-gassing of Al$_2$O$_3$ at high temperature (600~700 °C) prior to PECVD capping [232, 233].
- ➢ Use of a thin SiO$_2$ oxide at the c-Si surface, allowing faster film nucleation and so a nearly direct layer by layer growth mode of the Al$_2$O$_3$ film. This leaves lower hydrogen content at the c-Si surface and then prevents the blistering [101].
- ➢ Use of Al$_2$O$_3$ with lower hydrogen content thanks to oxidant combination [224].
- ➢ Use of thinner Al$_2$O$_3$ to limit the barrier to diffusion effect, optimal thickness being different depending on the deposition temperature and the oxidant [207, 209].

The first two solutions introduce extra steps in the process that are undesirable (extra cost) and not compatible with the low temperature objective that we are looking for. The third solution requires ozone generators, while the last one is just a trade-off optimisation. Indeed, performing ALD at 250 °C or 300 °C does not lead to blistering but lifetime seems to strongly suffer from this lack of hydrogen.

Conceptually, one can imagine depositing an extremely thin layer at low temperature and anneal it at higher temperature to release the excess of hydrogen. As the film is very thin, the diffusion barrier effect is very small. Then, the rest of the layer can be deposited at higher temperature to limit hydrogen incorporation.

As it has been reminded in chapter 2, Al$_2$O$_3$ dehydroxylation starts as soon as the substrate temperature is brought above the deposition temperature [151]. So practically, a constant increase of the substrate temperature during the deposition process can be a solution to release the excess of hydrogen. It incorporates the required hydrogen quantity at the c-Si/Al$_2$O$_3$ interface and releases the excess during the deposition of upper layers, while the barrier to hydrogen out-gassing is still thin. This concept will be referred thereafter as the thermal-drift atomic layer deposition (TD-ALD).

4.2.1.2   TD-ALD process simulation

TD-ALD can be easily implemented on a spatial ALD tool such as the Levitrack were the successive deposition zones can be set at different deposition temperatures. However, the temperature control of a temporal ALD reactor operating at low pressure (10 Pa) and that has not been designed for quick temperature variation is not obvious. In order to test the possibility to use such thermal process, finite element simulations were carried out thanks to COMSOL Multiphysics software. The Picosun R200 design has been reproduced as it is shown on Figure 4.13.a.

The instationary simulation of the substrate heating was carried out taking into account the radiative and the conductive heat transfers. The convective heat transfer was not considered as it requires solving the Navier-Stokes equations. The reactor is filled with N$_2$ at a pressure of 10 Pa in the deposition chamber and 100 Pa outside the chamber. A natural convection boundary

condition was fixed on the external walls of the reactor (h = 1 W.m^{-2}.K^{-1}). To account for radiative heat transfer, an emissivity (ε) of 0.8 was considered for the steel surfaces and 0.6 for the silicon surfaces. A thermal contact resistance was considered between the substrate and the substrate holder, and between the substrate holder and the "substrate-holder" holder.
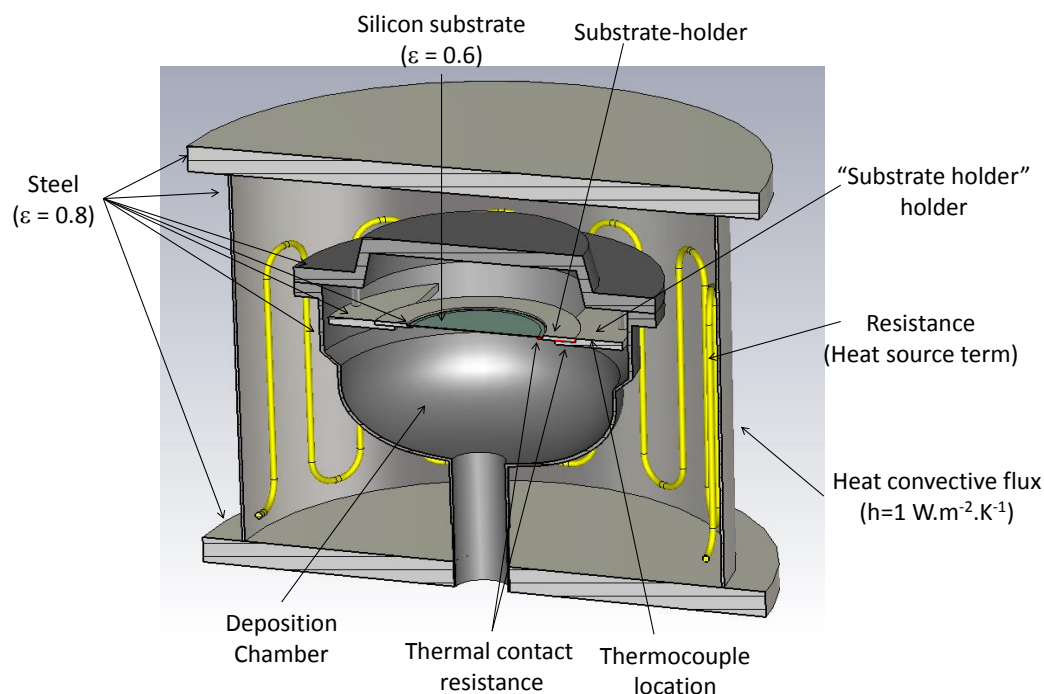
Figure 4.13: Cross-sectional view of the modelled "Picosun R200" architecture.

The simulation of the substrate-holder (and silicon substrate) introduction at room temperature into the deposition chamber that is stabilised at 300 °C was carried out in two steps. First, the reactor is heated to the desired temperature (for example 300 °C). During this first step, the substrate and the substrate-holder thermal conductivity were considered equal to zero. A parametric study allowed determining the required heat source resistor value to reach the desired temperature set point. Second, the silicon substrate and the substrate-holder thermal conductivities were restored. During this step, the heat source value applied to the resistor is kept constant.

The temperature is monitored on the silicon surface and on the "substrate holder" holder (Figure 4.14, thermocouple location). As soon as the substrate holder is introduced into the chamber a fast heat transfer occurs from the "substrate holder" holder and the silicon. The sample surface quickly heats-up. In 30 s, the silicon surface already reached 250 °C, but three additional minutes are required to reach 295 °C. This thermal profile would allow to deposit ~5 ALD cycles in a strong thermal drift and then to complete it at roughly constant deposition temperature with as many cycles as required to obtain the final film thickness.

This simulated temperature profile is one among many. Another temperature profile is easily obtained by changing both the chamber temperature and the substrate holder temperature. The substrate holder itself can be considered as an adjustment variable to obtain the desired temperature profile (different heat capacity). The simulated model did not take into account the 600 sccm of nitrogen that are constantly flowing through the reactor and the real temperature profile might be different.
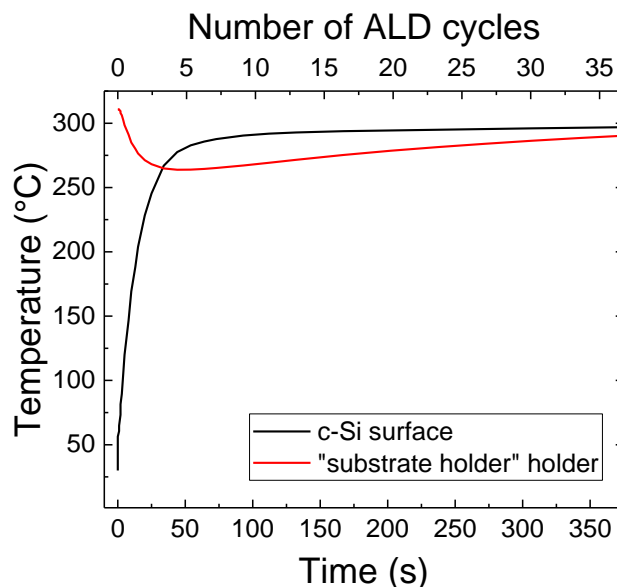
Figure 4.14: Modelled temperature evolution of the c-Si substrate versus time. The substrate-holder and the silicon substrate are introduced at room temperature in a Picosun ALD system heated at 300 °C.

4.2.2   Standalone TD-ALD Al_2O_3

Experimentally, the ALD chamber can be kept at a defined temperature while the substrate holder is introduced at a lower temperature into the chamber thanks to a load-lock. To check the silicon substrate temperature, we used non-reversible temperature labels stuck on the substrate surface. It consists of small pads that switch from white colour to black colour when a preset temperature is reached, each pad having its own transition temperature. As suggested by the label name, this colour change is not reversible. The real heating rate of the silicon surface is a bit lower than the one obtained by simulation (Figure 4.15.a). The first temperature profile (profile #1) was obtained as follows: the deposition chamber is set at 250 °C, the substrate holder is placed into the deposition chamber for 1 hour to bring it from room temperature to the reactor temperature. Then, the substrate holder is unloaded, brought to atmospheric pressure and the silicon substrate is quickly placed on it before loading back into the deposition chamber. This procedure ensures to have the silicon substrate loaded at a temperature of 130 °C (Figure 4.15.a). After 5 minutes, the silicon surface reaches 190 °C, temperature at which we decided to start the deposition. The temperature drifts from 190 °C to 230 °C for a deposited thickness of 200 ALD cycles, thinner films undergoing smaller thermal drifts (shorter deposition times).

Using the temperature profile #1, Al_2O_3 films with 20, 60, 100 and 200 ALD cycles were deposited on silicon after HF dip. Compared to the standard ALD process carried out at constant deposition temperature, the TD-ALD allows high passivation levels in as-deposited state, *e.g.* SRV=9.5 cm.s^{-1} for 200 ALD cycles (Figure 4.15.b). The dehydroxylation during the deposition results in passivation activation during the ALD processes itself, providing an effective lifetime increasing linearly with the film thickness. This is mainly linked to the longer deposition time that is equivalent to a longer annealing for the first deposited Al_2O_3 layers, rather than higher hydrogen content in thicker films. Indeed, the temperature variation between 100th and 200th ALD cycle is negligible, and so is the dehydroxylation of these last 100 atomic layers.

This small thermal drift shows very interesting as-deposited passivation results, paving the way to infinite TD-ALD temperature profiles. For example, a silicon substrate was passivated with 100 ALD cycles using the TD-ALD temperature profile #2 that presents a stronger temperature drift than the profile #1 (Figure 4.15.a). The temperature profile #2 is obtained by loading the substrate holder and the silicon wafer at room temperature into the deposition chamber which is set at 300 °C. After 1 minute, the silicon surface reaches 150 °C and the deposition begins. The temperature drifts from 150 °C to 240 °C during the 100 ALD cycles. The sample passivated with the TD-ALD profile #2 shows a lifetime nearly three times higher than that of the sample passivated with the same number of ALD cycles but using the temperature profile #1. Once more, a nice passivation level has been reached (SRV=7.1 cm.s^{-1}) while the thermal budget was kept below 250 °C and this time with only 100 ALD cycles.
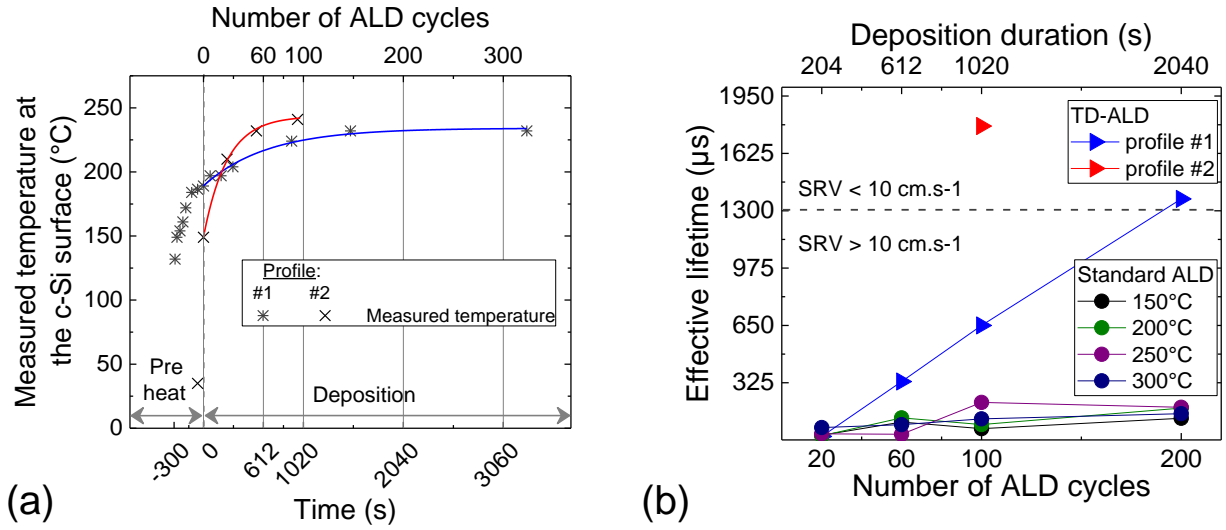
Figure 4.15: (a) Experimental temperature profiles measured on the substrate with non-reversible temperature labels, lines are guides to the eyes showing temperature evolution during the deposition process.(b) As-deposited lifetime for standard ALD and TD-ALD with profile #1 and profile #2. Lines are a guide to the eyes.

COCOS was performed on the sample passivated with 200 ALD cycles deposited with TD-ALD profile #1 (initial τ_{eff} = 1367 µs). The high passivation level is due to an extremely good chemical passivation (D_{it} = 6.4·10^{10} eV^{-1}.cm^{-2}) as the field effect passivation is extremely low (Q_f = -2.5·10^{11} cm^{-2}). To improve the passivation, the LIFE$_2$ treatment was applied in the LIBI for 20 hours, but the resulting lifetime was 5 times lower than the initial one (τ_{eff} = 256 µs). We tried to measure D_{it} and Q_f changes with COCOS but the passivation state did not allow to determine any value. In order to restore the passivation level, the sample was annealed at 380 °C for 30 minutes and then exposed to light in the LIBI for 20 hours (τ_{eff} = 1729 µs). COCOS measurement confirm the charge trapping in Al$_2$O$_3$ after PDA and light exposure in the LIBI (Q_f = -2.0·10^{12} cm^{-2}; D_{it} = 3.1·10^{11} eV^{-1}.cm^{-2}). The same behaviour has been observed for the sample passivated with 100 ALD cycles (TD-ALD profile #2) with an as-deposited lifetime of 1780 µs that decreases to 328 µs after 20 hours in the LIBI and that increases to 2810 µs after PDA and light exposure in the LIBI.

This is a completely unexpected behaviour regarding passivation of c-Si by Al_2O_3. The post-deposition annealing seems to be a requirement to benefit from $LIFE_2$. It suggests a different c-Si/Al_2O_3 interface between the as-deposited and the after PDA states despite the fact that a low D_{it} is measured in both cases. As the field effect passivation was already absent in as-deposited state, the lifetime decrease of TD-ALD samples certainly results from the chemical passivation reduction due to illumination. It reminds the well-known Staebler-Wronski effect [234] that takes place for the a-Si:H/c-Si interface (Si-H and weak Si-Si bond breaking). However, the UV power density is very low in the LIBI (< 20 μW.cm^{-2} for wavelength range from 300 nm to 400 nm). In order to assess the effectiveness of LIBI to produce the Staebler-Wronski effect, a test was conducted on amorphous silicon (a-Si:H) passivation layers deposited by PECVD with the parameters summarised in Table 4.1.

Table 4.1: passivation parameters of n-type, FZ <111>, DSP wafers, both sides passivated after 30 s of HF. The thickness is measured by SE

Sample	Pressure (Pa)	Gas ratio (H_2/SiH_4)	Applied power Density (mW/cm^2)	Inter-electrode distance (mm)	Thickness (nm)
#1	16	4	15.87	15	21.2
#2	16	4	9.52	15	19.8

The two n-type wafers passivated by ~20 nm of intrinsic a-Si:H are treated in the LIBI for 64 H at the full power density on both faces. The lifetime of the first sample dropped from 3892 µs to 2773 µs while for the second sample, the lifetime decreased from 3350 µs to 2411 µs (Figure 4.16). It represents a lifetime degradation of 28.75 % and 28.02 % for the first and the second samples respectively, confirming that the UV power in the LIBI is high enough to produce the Staebler-Wronski effect.
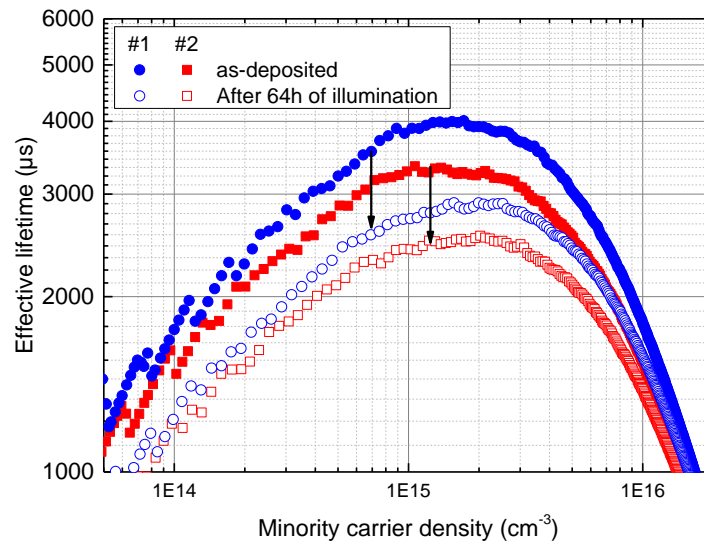
Figure 4.16: Minority carrier lifetime of n-type samples, FZ <111>, DSP wafers, both sides passivated by ~20 nm of a-Si:H after 30 s of HF. Double side illumination duration in the LIBI was conducted for 64 h.

One can ask why the UV dose degrades the lifetime of a-Si:H passivated samples only by 28% while it degrades the lifetime of Al_2O_3 passivated samples by 81 %. This is certainly due to the extremely high transparency of Al_2O_3 to UV radiation ($E_g > 6$ eV) that will be absorbed at the c-Si surface, while most of the UV do not reach the c-Si surface in the case of a-Si:H passivation layer (Eg <2 eV). This is consistent with plasma-induced damage at the c-Si/ a-Si:H interface due to UV radiation from the plasma that we observed and reported elsewhere [235].

So, the Al_2O_3/c-Si interface of samples deposited with standard and TD-ALD might be similar, but part of the remaining dangling bonds that are present in the case of standard ALD are filled with hydrogen during the deposition in the case of TD-ALD. Then, these Si-H bonds break under UV exposure due to their weaker energy bonds compared to Si-O bonds, 3.0 eV vs 8.2 eV respectively [236]. This scheme makes sense as the TD-ALD purpose is to release part of the hydrogen content that is present in the Al_2O_3 film. The hydrogen can easily out-diffuse from the film but part of it can passivate c-Si dangling bonds. Interestingly, the lifetime of as-deposited TD-ALD samples decreases after illumination to a similar level than the one deposited by standard ALD, i.e. hundreds of microseconds, supporting this hypothesis of supplementary Si-H passivation in TD-ALD growth mode compared to standard ALD.

A pragmatic question immediately arises regarding the improved stability of the Al_2O_3/c-Si interface after PDA: what does the PDA change to allow $LIFE_2$ phenomenon rather than lifetime degradation? The PDA leads to the dehydroxylation of the Al_2O_3 like the TD-ALD is partially doing. However, the maximum temperature undergone by the sample during TD-ALD is rather low (230 °C for profile #1; 250 °C for profile #2), compared to PDA temperature (>350 °C). The Al_2O_3 has been reported behaving as a proton conductor [162-164] in this TD-ALD temperature range, so hydrogen diffusion might be easier than oxygen or water diffusion during the TD-ALD process. The interfacial SiO_2 thickening / reorganisation that occurs during PDA [100, 124] might not take place during the TD-ALD process resulting in a lower stability to light exposure of the as-deposited films compared to films that received a PDA.

This would underline the crucial role of the interfacial SiO_2 layer regarding the chemical passivation stability of an Al_2O_3 film. Thus, talking about the importance of hydrogen content in Al_2O_3 to obtain a good chemical passivation after a PDA, it is not the hydrogen itself that is important but mainly the oxygen to which it is bonded. Indeed, dehydroxylation releases 2 hydrogen atoms but also 1 oxygen atom (refer to Chapter 2, dehydroxylation). These atoms can be released under various combinations that are different between the bulk of Al_2O_3 and the Al_2O_3/c-Si interface that presents catalytic activity. Indeed, in the bulk of Al_2O_3, oxygen is released with hydrogen as water molecules, while at the c-Si/Al_2O_3 interface there is just H_2 that is released, oxygen remaining somewhere at the c-Si/Al_2O_3 interface and can be the source of SiO_2 thickening. This would fit our experimental results, the passivation level decreases a lot when Al_2O_3 becomes thinner (lower hydroxyl content), even if a capping layer is used to provide hydrogen to the c-Si surface (Figure 3.11).

This is also supported by several results reported in the literature: a better chemical passivation is reported for the PDA conducted in pure oxygen atmosphere rather than in hydrogen atmosphere [144]. In the same way, to maintain good passivation while reducing the Al_2O_3 thickness below 4 nm, Schuldis *et al.* [209] had to switch from water oxidation to plasma oxidation (stronger oxidation of c-Si surface) and to increase the annealing temperature from 400 °C to 800 °C (higher oxygen mobility).

Results reported by Wensheng *et al.* [208] the same year follow the same trend. On the one hand, the passivation provided by Al$_2$O$_3$/a-SiN$_X$:H stack with alumina thickness of 4 nm slightly improves when the annealing temperature increases from 300 °C to 800 °C. On the other hand, for the stacks with 1 nm thick alumina, the passivation level strongly improves as a function of the annealing temperature between 500 °C to 800 °C, surpassing the passivation level of the previous stack with 4 nm alumina at 800 °C. Regarding the extremely thin layer in the latter case, this strong improvement cannot just be the result of better hydrogen diffusion at a higher temperature but mainly oxide reorganisation.

Bordihn *et al.* [237] have shown that if an SiO$_2$ layer is chemically grown at the c-Si surface before ALD, a PDA of 30 seconds at 400 °C is enough to observe passivation improvement while 2 minutes are required to observe equivalent results when Al$_2$O$_3$ is deposited directly on c-Si after HF.

Nevertheless, even if hydrogen might not be the main passivating agent, its release by the Al$_2$O$_3$ films also participates to saturate remaining dangling bonds that are also present in the SiO$_2$ oxide (E centres), like in the case of FGA after silicon passivation with thermal oxide. Thus, for low temperature process that we are aiming, for annealing at temperatures higher than 350 °C is a prerequisite to stabilise the chemical passivation and allow LIFE$_2$. In the same way, for Al$_2$O$_3$ films deposited by thermal ALD using water oxidation, a minimum film thickness might be required to provide enough oxygen at the c-Si/Al$_2$O$_3$ interface.

4.2.3   TD-ALD for Al$_2$O$_3$/a-SiN$_X$:H passivation stacks

As previously discussed, the reactor is not designed for TD-ALD but we managed to obtain two temperature profiles. It was easier and faster to use profile #1 rather than profile #2 as it took an extremely long time to bring the substrate holder back to room temperature after a deposition. Thus, profile #1 has been selected hereafter. Following the aim of Al$_2$O$_3$ thickness reduction, we focused on the 60 ALD cycles for which good passivation levels were obtained despite the presence of blistering. Samples passivated by 60 TD-ALD cycles were fabricated using the same PDA, capping and PCA than the one passivated by 60 standard ALD cycles. After PCA, the LIFE$_2$ treatment was done in the LIBI and the saturated lifetime is plotted on Figure 4.17.a.
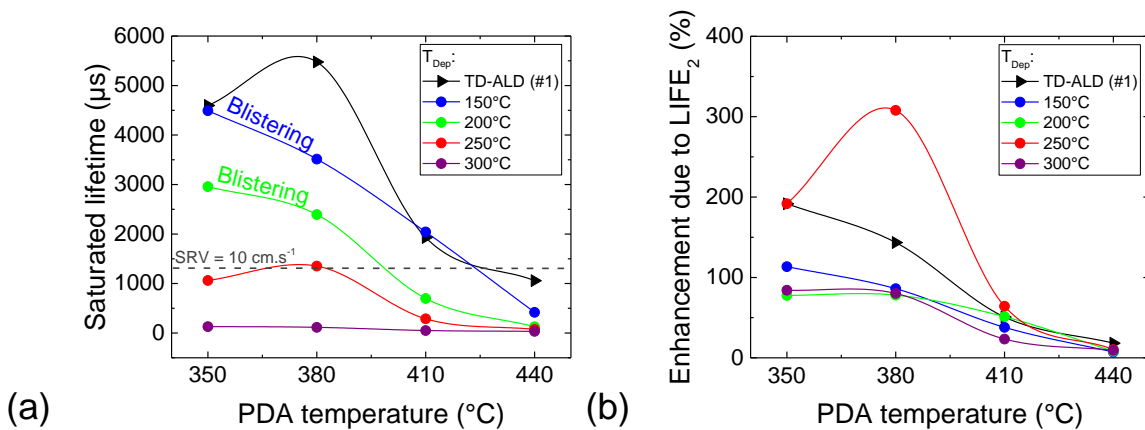
Figure 4.17: Lifetime results of Al$_2$O$_3$/a-SiN$_X$:H passivation stacks for standard ALD and TD-ALD (profile #1) with different PDA (a) saturated lifetime (b) lifetime enhancement due to LIFE$_2$. Lines are guides to the eye.

The small thermal drift of +30 °C between 190 °C and 220 °C for 60 TD-ALD cycles provides a passivation level at least as good as the standard ALD performed at 150 °C for the whole range of PDA temperatures. However, the lifetime enhancement due to charge trapping is higher in the case of the TD-ALD compared to films deposited with standard ALD at 150 °C or 200 °C (Figure 4.17.b). The PDA temperature of 380 °C stands out among the others, providing a lifetime of 5476 µs, *i.e.* an SRV of 1.8 cm.s^{-1}. Blistering was not detected with optical microscope for all the samples deposited with TD-ALD, but as previously discussed, blisters absence is not obviously synonym of good interface adhesion.

The sample passivated with TD-ALD that presents the highest lifetime was analysed by APiC microscopy (Figure 4.18.a). First, the interface is not very contrasted in terms of acoustic reflection contrary to previous mappings (Figure 4.10 and Figure 4.11). Second, for the same number of cycles, the mean acoustic coefficient and its standard deviation are very low for TD-ALD compared to standard ALD (Figure 4.18.b), underlining a pretty good adhesion of the film to the c-Si substrate.
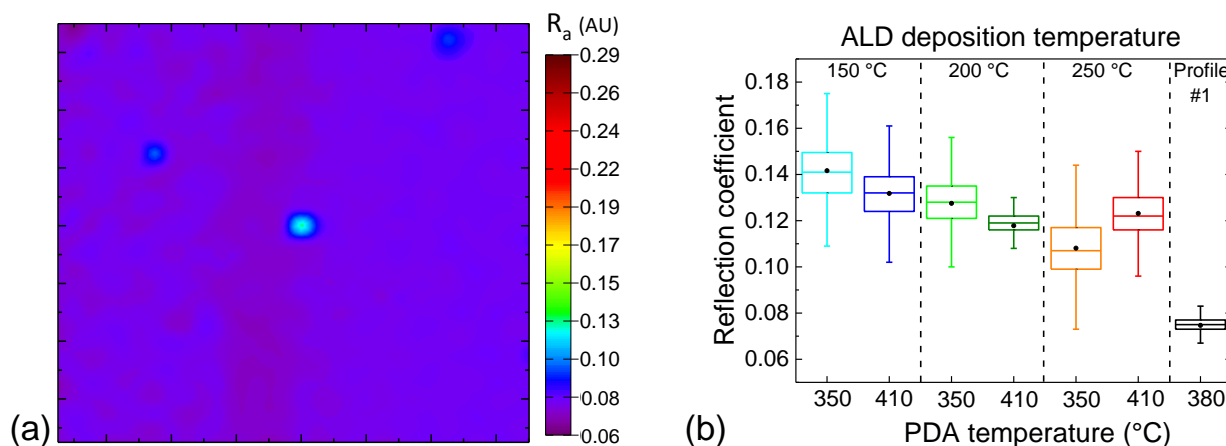
Figure 4.18: (a) APiC mapping of the Al$_2$O$_3$/c-Si interface for 60 TD-ALD cycles (profile #1) that received a PDA of 30 min at 380 °C before capping and PCA. (b) reflection coefficient distribution of the Al$_2$O$_3$/c-Si interface for 60 ALD cycles deposited at constant temperature (150 °C, 200 °C and 250 °C) and TD-ALD with temperature profile #1.

4.3   Conclusion

In this chapter we showed that the blistering is a macroscopic manifestation of Al$_2$O$_3$/c-Si adhesion degradation. The formation of blisters results from a nucleation/growth process and so optical microscopy is not the most suitable characterisation to determine adhesion degradation. Coloured picosecond acoustics microscopy is the most relevant characterisation to assess the adhesion quality at the c-Si/Al$_2$O$_3$ interface. It allowed us to show adhesion degradation when the deposition temperature of Al$_2$O$_3$ decreases and when the film thickness increases. These two trends are consistent with a hydrogen accumulation at the c-Si/Al$_2$O$_3$ interface.

We proposed to use a thermal drift during the atomic layer deposition process to release part of the Al$_2$O$_3$ hydrogen content during the deposition. It allowed high passivation levels (SRV < 10 cm.s^{-1}) of the c-Si surface by Al$_2$O$_3$ in as-deposited state while the substrate temperature never exceeded 250 °C. This TD-ALD concept is the subject of a patent application.

However this passivation seems to be mainly due to Si-H bonds that can break under UV exposure. We suggest that a post-deposition annealing at temperatures higher than 350 °C is a prerequisite to stable chemical passivation, *i.e.* Si-O bonds rather than Si-H at the c-Si/SiO$_X$ interface. The implementation of TD-ALD in the passivation process flow allowed reaching lifetime of 5476 µs, *i.e.* an SRV of 1.8 cm.s^{-1} and with a sample surface free of blistering.

Chapter 5

Interaction between Al_2O_3 and its a-SiN$_X$:H capping layer

Contents

.

5.1   LIFE$_2$ instability for thin Al$_2$O$_3$

5.1.1.1   Electrostatic charges in a-SiN$_X$:H

As depicted by results on Figure 3.13 and summarised on Figure 3.15, the passivation stack embedding Al$_2$O$_3$ thinner than 60 ALD cycles (~60 Å) are subject to strong LIFE$_2$ instability. As these layers are too thin to be a barrier to hydrogen diffusion, interface adhesion problem was not the first hypothesis that came to our mind to explain this charge trapping instability. We focused our attention towards the a-SiN$_X$:H capping layer that has been used for decades to passivate n-type surfaces thanks to its well-known positive fixed charges [216].

PECVD a-SiN$_X$:H films have their bandgap that increases as the portion of nitrogen content increases [238]. From the extended work of Robertson on silicon alloys [25, 239], defect levels in a-SiN$_X$:H can be sorted in two categories (Figure 5.1.a):

> ➢ Shallow defects that participate to band tails, like the Si-Si bonds (one level close to the valence band, the other level close to the conduction band); the nitrogen dangling bonds, namely N-centres (energy levels close to the valence band) and the over-coordinated N atoms (energy levels just below the conduction band). However, the presence of N dangling bonds have been reported only for N rich a-SiN$_X$:H and the over-coordination of N is impeded by its small size and is only possible if bonded to one or more H atoms.

> ➢ Deep defects in the bandgap due to N-N bonds that generate shallow levels (0.5 eV π*) and also deep levels (4 eV σ*) but these bonds are unlikely due to their very weak binding energy (1.7 eV). The main and deepest levels are due to silicon dangling bonds when the Si atom is back bonded to three nitrogen atoms (Si≡N$_3$). These defects are known as K centres, generating defect levels in the middle of the a-SiN$_X$:H bandgap. K centres have been reported to have negative correlation energy, *i.e.* the neutral charge state, K^0, is less stable than K$^+$ or K$^-$ [240]. Exactly like for crystalline silicon, dangling bonds in a-SiN$_X$:H are neutralised by hydrogen bridging. Indeed, Si-H and N-H bonds are found to give states outside the bandgap.

Generally the K$^+$ centres are predominant in a-SiN$_X$:H films and so the resulting net charge is positive [241]. The Q$_f$ in a-SiN$_X$:H is highly dependent on its stoichiometry and has been reported to be maximum for x values between 0.5 and 1.5 [242]. Contrary to Al$_2$O$_3$ negative charge centres (Oxygen vacancies and interstitials, Figure 2.21), the switching charge-state levels of K centres and N centres are not strongly different in terms of energy and so these defects are very versatile (Figure 5.1.b). The net charges of a-SiN$_X$:H can be easily manipulated using corona discharges or UV illumination, these changes being totally reversible [240, 243].
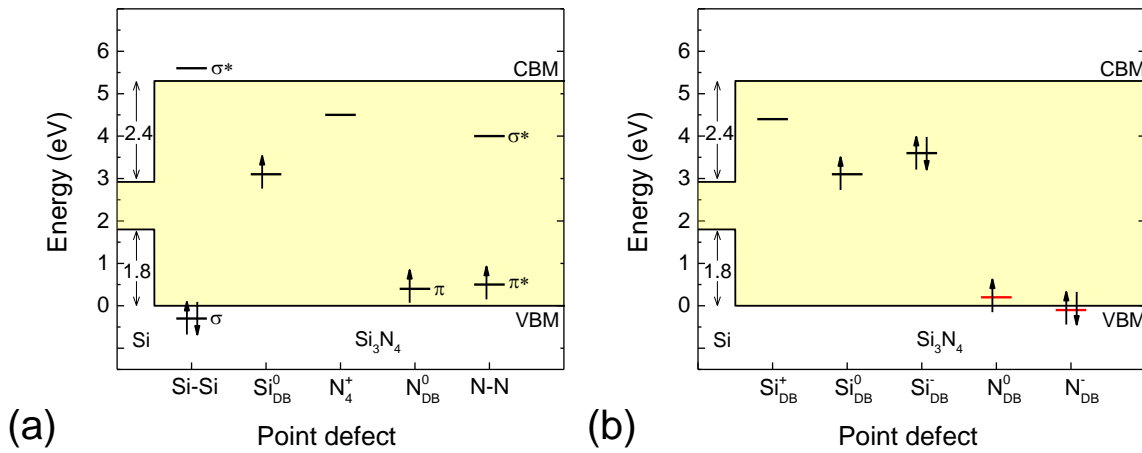
Figure 5.1: (a) Calculated energy levels and occupancy for the intrinsic point defects in Si$_3$N$_4$. [25] (b) Switching charge-state levels of dangling bonds in Si$_3$N$_4$. [25, 27, 28]

In light of what has just been summarised, the a-SiN$_X$:H capping layer can impact the field effect passivation in two ways. First the quantity of positive charges present in the a-SiN$_X$:H at the end of the process might compensate or even cancel the field effect passivation provided by Al_2O_3. Indeed, Wensheng *et al.* [208] showed that, for the same Al_2O_3 thickness and depending on the a-SiN$_X$:H stoichiometry, the measured C-V curves suggest an effective Q_f at the c-Si surface that varies from $-1.5·10^{12}$ to $+5.1·10^{10}$ cm^{-2}. For our samples, the same a-SiN$_X$:H capping is used for all Al_2O_3 thickness, so if the negative Q_f in Al_2O_3 is really located in the first nanometre above the c-Si surface, the field effect cancellation should not depend on the Al_2O_3 thickness that we tested (from 2 nm to 20 nm).

The second possible effect of charged centres in the a-SiN$_X$:H is a direct electronic interaction between Al_2O_3 centres and a-SiN$_X$:H centres. We often focus on the electronic defects presents at the Al_2O_3/c-Si interface, but it has to be reminded that a thin film has two interfaces that can present different defects. The interface between Al_2O_3 and a-SiN$_X$:H may host several defects that are different from the Al_2O_3 side to the a-SiN$_X$:H side (Figure 5.2.a; Si$_{Al}$ and Si$_O$ have been found to also generate levels in the gamma-Al_2O_3 bandgap, these levels are not plotted in the Alpha Al_2O_3 bandgap due to uncertain energy position [244]). By reducing the Al_2O_3 thickness, interfaces of the thin films get closer to each other and the insulation role of the bulk Al_2O_3 becomes negligible (Figure 5.2.b). The strong versatility of K centres plus the probable presence of an "electronic ladder" (Figure 5.2.b) at the Al_2O_3/a-SiN$_X$:H interface (combination of all the defects plotted on Figure 5.2.a) might help some charge release from Al_2O_3 traps. The negatively charged oxygen vacancies that are pointed out as the main Al_2O_3 charge traps have electronic levels high enough in the bandgap to forward some electrons to other defects. Once a doubly negatively charged oxygen vacancy releases two electrons and becomes neutral, the newly empty energy state is going back to the Al_2O_3 conduction band. It limits further capture of electrons by the vacancy (see switching charge-state levels of oxygen vacancies in Al_2O_3 on Figure 2.21). It is less probable that the oxygen vacancy further releases electrons to become positively charged. The electronic level that has to capture electrons to bring back the vacancy to neutral electric state remains below the c-Si fermi level.
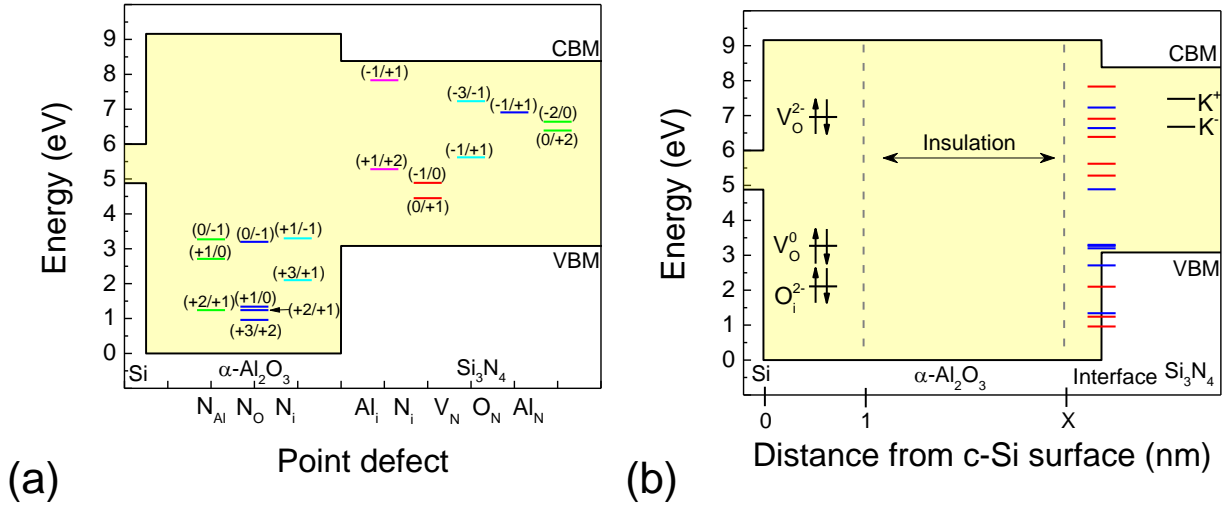
Figure 5.2: (a) Position of thermodynamic transition levels in Al₂O₃ and in a-SiNₓ:H for intrinsic and extrinsic point defect levels arising from atomic inclusions of the Al₂O₃ film in the a-SiNₓ:H film and vice versa [5, 6]. (b) Schematic of electronic defects location in an Al₂O₃/a-SiNₓ:H passivation stack. Point defects suspected to capture electrons in Al₂O₃ are supposed to be located in the first nanometre above the surface. The X value represents the Al₂O₃ film thickness, from 2 nm to 20 nm. The Al₂O₃/a-SiNₓ:H interface transition levels are all those of Figure 5.2.a, referred to as an "electronic ladder" in the text. Red bars show the transition levels related to positive or null charge state, and blue bars show the transition levels related to null or negative charge state.

The a-SiN$_X$:H film that we used in this manuscript was deposited on c-Si after HF dip in order to quantify its positive Q$_f$ value by COCOS. The layer presented a positive fixed charge density of $1.9 \cdot 10^{12}$ cm^{-2} in as-deposited state that decreased to $1.0 \cdot 10^{12}$ cm^{-2} after PCA, underlining network reorganisation during PCA. This Q$_f$ value is typically in the same range as Al$_2$O$_3$ negative fixed charge density. So, the presence of a "positive field effect" on top of the Al$_2$O$_3$ is suspected to partially compensate or even annihilate the passivation due the "negative field effect" provided by Al$_2$O$_3$ at the c-Si surface. This interaction will be defined hereafter as electrostatic shading. If the charge transfer between all the defects present at the Al$_2$O$_3$/a-SiN$_X$:H interface is pretty hard to analyse, the electrostatic shading resulting from positive Q$_f$ in a-SiN$_X$:H is easier to model.

5.1.2   Simulation of the electrostatic shading

In order to evaluate if some electrostatic shading takes place due to the positive Q_f in the a-SiN_X:H capping layer, we performed finite element modelling thanks to ATLAS software from Silvaco. The model depicted on Figure 5.3 is similar to the one that we used in chapter II to evaluate reachable lifetime with standalone Al_2O_3 films (Figure 2.7.a) but this time we added the capping layer on top of Al_2O_3. The interfacial trap density at the Al_2O_3/c-Si is set to 10^{11} eV.cm^{-1} which is reasonable considering values that were measured in previous chapters. The Al_2O_3 and a-SiN_X:H permittivities were set to 7.6 and 6.1 respectively. Two cases were simulated, one with a Q_f of 0 cm^{-2} and the second with a Q_f of $+10^{12}$ cm^{-2} at the Al_2O_3/a-SiN_X:H interface (Figure 5.4). As we now know, Q_f in Al_2O_3 results from charge trapping, so the Q_f of Al_2O_3 was also varied (from -5·10^{10} to -5·10^{12} cm^{-2}) to evaluate the necessity of this charge trapping in the passivation stack. Continuity, transport (drift-diffusion) and Poisson's equations are solved self-consistently in the silicon, while only the Poisson equation was considered for the dielectrics.

Surface work function = 4.98 eV

Chemical passivation (at midgap)

a-SiN_X:H [75 nm]

$\leftarrow Q_f = $ **+1x10^{12}** cm^{-2}

Field effect passivation

$D_{it} = 1x10^{11}$ eV^{-1}.cm^{-2}

$\sigma_n / \sigma_p = 10^{-14} / 10^{-15}$ cm^2

Al_2O_3 [20 nm]

$\leftarrow Q_f = $ **−[5x10^{10} to** 5x10^{12}] cm^{-2}

c-Si [140 µm; 3 Ω.cm; p-type]

Symmetry plane (Flat band, S_n= 0 cm.s^{-1})
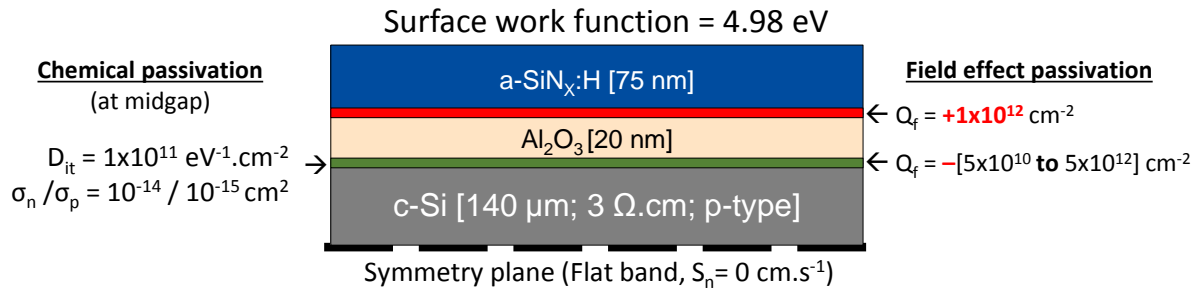
Figure 5.3: Schematic model used for Silvaco 1D simulations.

For the first simulation condition ($Q_f = 0$ cm^{-2} at the Al_2O_3/a-SiN_X:H interface; Figure 5.4.a), the curves of the effective lifetime as a function of the minority carrier density are very similar to the ones obtained without the a-SiN_X:H capping in chapter 2 (Figure 2.7). The lifetime increases monotonously with the negative Q_f increase at the Al_2O_3/c-Si interface, corresponding to the accumulation mode at the Al_2O_3/c-Si interface. Everything changes for the second simulated case, when the field effect resulting from the positive Q_f at the Al_2O_3/a-SiN_X:H interface is set to $+10^{12}$ cm^{-2} (Figure 5.4.b). There are two distinct regions determined by the Q_f value at the Al_2O_3/c-Si interface. For high negative Q_f values, the first region corresponds to the accumulation mode at the c-Si surface, while for the lowest negative Q_f, the c-Si surface is set in an inversion mode, recognisable by the strong lifetime increase at low carrier density. These two zones delimit a "death valley" where the lifetime is rapidly vanishing. One might try to just avoid this zone, but the problem is that it is centred nearby the typical Q_f value at the c-Si/Al_2O_3 interface when it is saturated, so despite high Q_f at the c-Si/Al_2O_3 interface, the lifetime is strongly degraded by the positive Q_f at the Al_2O_3/a-SiN_X:H interface.
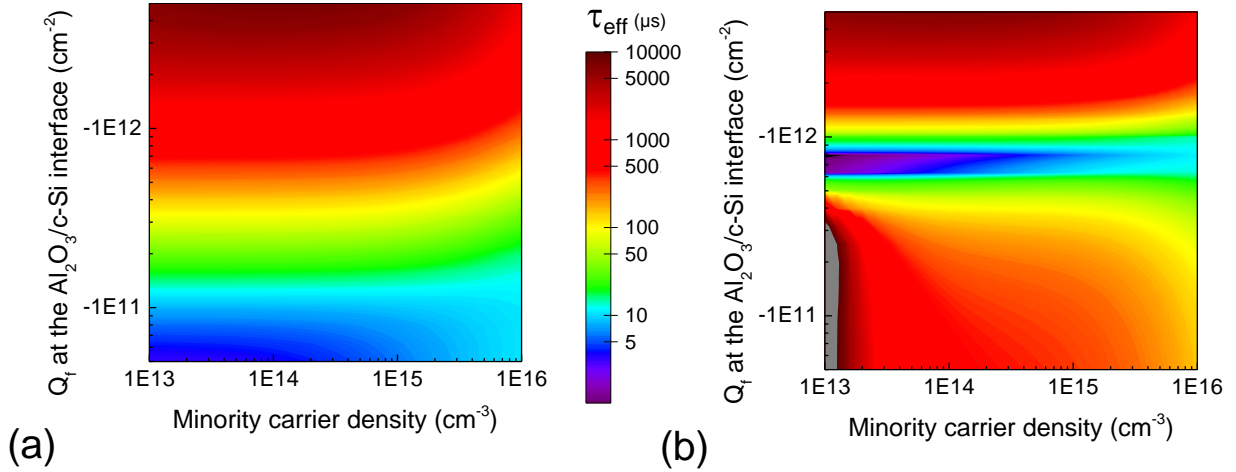
Figure 5.4: Effective lifetime as a function of the injection level for Al₂O₃/a-SiNₓ:H passivation stacks with Al₂O₃ thickness of 20 nm, a-SiNₓ:H thickness of 75 nm. and $D_{it}(Al_2O_3/c\text{-}Si)$ of 10^{11} eV⁻¹.cm⁻². (a) Al₂O₃/a-SiNₓ:H interface free of fixed charges (b) Al₂O₃/a-SiNₓ:H interface with fixed charges density of $+10^{12}$ cm⁻².

This electrostatic shading is a real problem that has to be solved. The obvious solution would be to use an a-SiNₓ:H layer free of fixed charges like it was simulated in the first case. However, the Q_f in a-SiNₓ:H is intimately linked to its stoichiometry and in practice it is very difficult to get rid of positive charges without getting closer to the composition of amorphous silicon, which leads to parasitic absorption in the capping layer (Figure 3.5.b).

To appreciate the impact of Al₂O₃ thickness on the electrostatic shading, the two simulation conditions were repeated but this time the Al₂O₃ film thickness was varied from 1 to 20 nm for each case. Effective lifetimes at the injection level of 10^{15}cm⁻³ are extracted and plotted as 2D maps (Figure 5.5). The case with Q_f of $+10^{12}$ cm⁻² that corresponds to our experimental condition is hereafter designated as the "standard case". The ideal case with an a-SiNₓ:H free of positive fixed charges ($Q_f = 0$ cm⁻²) is designated as the "Alternative #2"; the second alternative because another solution is proposed. The "Alternative #1" consists in the use of a transparent buffer layer with no charges between Al₂O₃ and a-SiNₓ:H. The role of this buffer layer would be to shield the c-Si surface from the positive Q_f of the a-SiNₓ:H. Silicon oxide is known to have a very low charge density ($+2 \cdot 10^{11}$ cm⁻²; this value was measured on samples from the next section) and has a very large bandgap suitable for this application.

These 3 cases are plotted on Figure 5.5, the effective lifetime as a function of Al₂O₃ thickness and Q_f at the Al₂O₃/c-Si interface is mapped on the bottom line while the corresponding band-bending is plotted on the upper line.
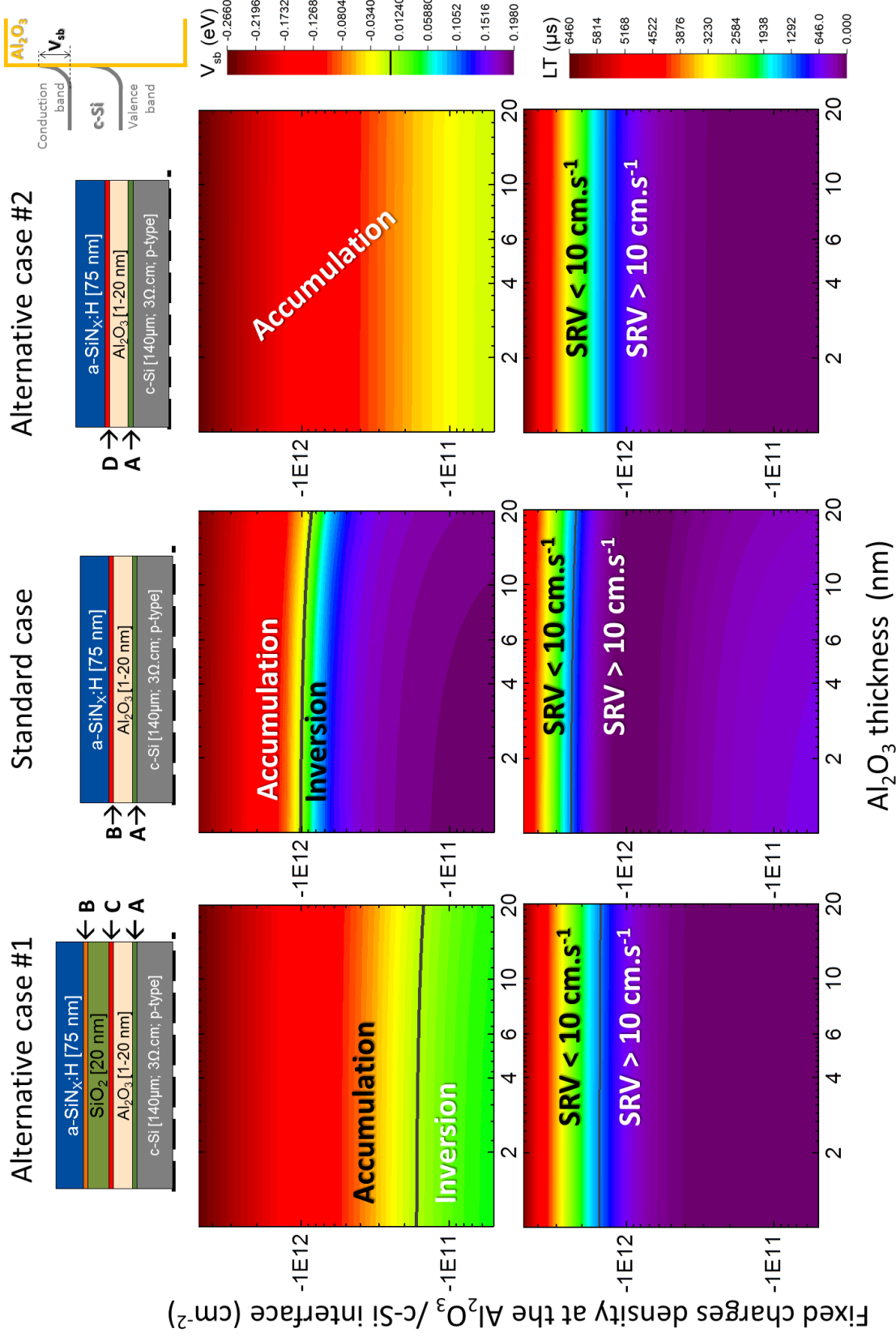
Figure 5.5: Simulation results of band bending at the c-Si surface (top graphs line) and resulting lifetime (bottom graph row), grey line is the flat band condition) and resulting lifetime (bottom graph row, black line is equivalent to SRV of 10 cm.s⁻¹) for an injection level of 10^{15} cm⁻³. Capital letters on the top schematic dielectric stacks represent charges density values used for simulation. $A=[-5 \cdot 10^{10}$ to $-5 \cdot 10^{12}]$ cm⁻²; $B= +10^{12}$ cm⁻²; $C= 2 \cdot 10^{11}$ cm⁻² and $D= 0$ cm⁻². The band structure on the top right corner shows the V_{SB} definition.

We start by discussing the standard case results first. For the Al_2O_3 thickness of 1 nm, the flat-band conditions are obtained when the absolute Q_f value at the c-Si/Al_2O_3 is equal to the one at the a-SiN_X:H/Al_2O_3 interface (-10^{12} cm^{-2}). When the Al_2O_3 becomes thicker, the required quantity of charges at the c-Si/Al_2O_3 interface to reach flat-band conditions slightly decreases to $-8.5 \cdot 10^{11}$ cm^{-2} for 20 nm of Al_2O_3. The effective lifetime resulting from the band structure is the lowest nearby the flat-band conditions, quickly increasing up to 6000 µs when the surface is in the accumulation mode while in inversion mode the lifetime is lower by one order of magnitude. The lifetime "death valley" shows a very low dependence on the Al_2O_3 thickness. The necessary Q_f value at the Al_2O_3/c-Si interface changes only from $-2.4 \cdot 10^{12}$ to $-2.2 \cdot 10^{12}$ cm^{-2} in order to reach SRV of 10 cm.s^{-1}. When the a-SiN_X:H does not present positive Q_f (alternative case #2), the surface is always in the accumulation mode regardless of the negative Q_f value at the c-Si/Al_2O_3 interface. The Al_2O_3 thickness does not impact any more the band bending. For the considered interfacial trap density (10^{11} eV^{-1}.cm^{-2} at midgap), Q_f of $-1.4 \cdot 10^{12}$ cm^{-2} is necessary to reach SRV of 10 cm.s^{-1}. It represents 41% less charge density than for the standard case, so the presence of positive Q_f in the a-SiN_X:H has a non-negligible impact on the charge trapping required in Al_2O_3 to reach the passivation objectives. For the alternative case #1 which uses a SiO_2 buffer layer between Al_2O_3 and a-SiN_X:H, the flat-band conditions are shifted towards lower Q_f at the Al_2O_3/c-Si interface, providing lifetime results very similar as the alternative case #2. The required Q_f at the c-Si/Al_2O_3 to reach SRV of 10 cm.s^{-1} is then about $1.5 \cdot 10^{12}$ cm^{-2}. It is just 7 % higher than the ideal alternative case #2 where the a-SiN_X:H capping layer should be free of positive fixed charges.

5.2   Optimisation of the electrostatic stacking

5.2.1   Alternative case #1: the SiO₂ buffer layer

5.2.1.1   Experimental environment

We explored the possibility of shielding the c-Si surface from the positive charges density in the a-SiN_X:H capping layer by the insertion of a buffer layer between Al_2O_3 and a-SiN_X:H. This project was conducted at the "Thin-Film Technologies in Energetics" (TF-TE) laboratory in Saint Petersburg. The ALD tool was a FlexAl chamber from Oxford Instruments and the PECVD chamber was a Plasma Pro 100 also from Oxford Instruments, both plugged on the same cluster tool. The first chamber was used to deposit Al_2O_3 and the second chamber was only used for the buffer layer deposition. All the a-SiN_X:H capping layers were deposited in the MVS reactor at the LPICM. In order to avoid hazardous comparison, reference samples with only Al_2O_3 (no buffer layer) were also deposited at the TF-TE and then capped at the LPICM. Indeed, the FlexAl reactor configuration did not allow the double side deposition like in the Picosun reactor. Moreover, for the same temperature set point, the real substrate temperature is not the same [245] and the ALD cycle was also different than the one used in the Picosun (Table 5.1).

Table 5.1: ALD Cycle used in the FlexAl reactor. Deposition chamber is out-gassed at 0.05 Pa after substrate loading and then the deposition pressure is raised around 11 Pa.

TMA	→	Purge	→	H₂O	→	Purge	Total duration
0.02 s		1.5 s		0.07 s		10 s	11.59 s/cycle

5.2.1.2   Synthesis of the buffer layer

The ALD cycle for the Al_2O_3 was provided by the tool manufacturer, but PECVD process conditions to synthesise SiO_2 were not available. We started from the typical process condition of a-SiO$_X$:H synthesised from silane, carbon dioxide and dihydrogen used for silicon heterojunction solar cells [246-248] (Table 5.2). Despite a wider optical bandgap compared to a-Si:H, E_{04} remains low, *i.e.* 2.2 eV as shown in Figure 5.6. Therefore we continuously increased the CO_2/SiH$_4$ gas ratio to widen the bandgap (Figure 5.6).

Table 5.2: PECVD parameters for a-SiO$_X$:H deposition. Set-point temperature was 200 °C (165 °C measured on substrate), the inter-electrode distance was 28 mm and the RF frequency 40 MHz.

Material	Pressure (Pa)	Power Density (mW.cm^{-2})	Gas ratio H$_2$/SiH$_4$	Gas ratio CO_2/SiH$_4$
a-SiO$_X$:H	53	50	10	0.7

The increase of CO_2/SiH$_4$ gas ratio allowed widening the bandgap from 2.2 eV to 5.4 eV, corresponding to a refractive index decrease from 3.35 to 1.50. This SiO$_X$ with E_{04} = 5.4 eV is the most transparent and will be referred as buffer #1, while the buffer #2 corresponds to the same process conditions but for a temperature set point of 250 °C. This increase of substrate temperature slightly reduces the optical bandgap from 5.4 eV to 4.9 eV and increases the refractive index from 1.50 to 1.52.
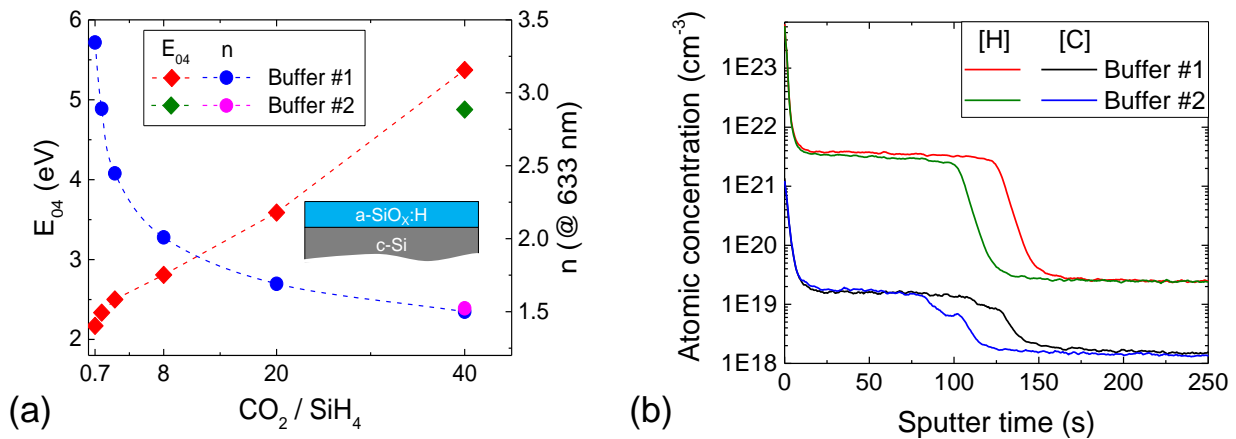
Figure 5.6: (a) Optical bandgap and refractive index of a-SiO$_X$:H (determined by SE) as a function of the CO_2 to SiH$_4$ ratio. The deposition temperature is 200 °C for buffer #1 and 250 °C for buffer #2 (b) SIMS profiles of as-deposited buffer #1 and #2.

The hydrogen and carbon content of the layers were determined by SIMS calibrated with SiO_2 implanted samples (Figure 5.6). The carbon content is 2 orders of magnitude lower than the hydrogen content for both layers. The oxygen/silicon ratio was determined by RBS to be 1.6 and 1.5 for buffer layers #1 and #2 respectively. The hydrogen content was measured by ERDA, its concentration is ~$1.2\%_{at}$ for both buffers, which is rather low. A slight density difference was measured by XRR, buffer #2 being denser than buffer #1. Some material properties are summarised in Figure 5.3.

Table 5.3: Material properties of buffer #1 and buffer #2

Properties	Characterisation technique	Buffer #1	Buffer#2
Stoichiometry	RBS	$SiO_{1.6}$	$SiO_{1.5}$
H ($\%_{at}$)	ERDA	1.2	1.2
density (g.cm^{-3})	XRR	2.13 ± 0.02	2.17 ± 0.03
Refractive index (@ 633 nm)	SE	1.50	1.52
Optical bandgap (eV)	SE	5.4	4.9

5.2.1.3   Insertion of the buffer layer in the stack

Three groups of samples were realised using p-type wafers passivated by 60 ALD cycles deposited at 250 °C in the FlexAl reactor. The first group received the buffer layer #1 (20 nm) on-top of Al_2O_3, the second group received the buffer layer #2 (20 nm) on-top of Al_2O_3, and the third group did not receive any buffer layer and was the control group. A PDA was performed at 350, 380, 410 or 440 °C in forming gas atmosphere for all samples. Finally, the a-SiN_X:H capping was deposited on all samples before performing the post-capping annealing (30 min @ 380 °C). The insertion of a 20 nm thick buffer layer between Al_2O_3 and a-SiN_X:H affects the optical properties of the stack. We used "Essential Macleod" software to determine the optimal a-SiN_X:H thickness that is required to preserve the lowest reflectivity at the incident wavelength of 633 nm for a stack composed of 6 nm of Al_2O_3 (n=1.64), 20 nm of a-SiO_X (n=1.5) and Y nm of a-SiN_X:H (n=1.88). The software gives a Y value of 55.60 nm, the PECVD deposition duration of the a-SiN_X:H capping has been shortened in consequence in order to obtain this value for the first and the second groups.

The initial lifetime was measured after the PCA and then samples received the $LIFE_2$ treatment in the LIBI. It has to be noted that neither type I nor type II blisters were reported, underlining the difference between Al_2O_3 films deposited in the Picosun and in the FlexAl. The saturated lifetime and the lifetime enhancement due to the $LIFE_2$ treatment are plotted on Figure 5.7.a. Both the lifetime values and the percentage of the lifetime enhancement due to $LIFE_2$ are consistent between the control groups deposited in the FlexAl (Figure 5.7.a) and the previous samples deposited in the Picosun (Figure 4.17). Regarding the passivation performance of groups #1 and #2, these are unexpectedly poor. The group #1 samples show better lifetime than the group #2 samples but these values are well below these of the control group. The lifetime enhancement of both groups does not exceed 10%, either due to already saturated lifetime and/or poor chemical passivation and poor charge trapping. Both hypotheses might result from the a-SiO_X deposition: indeed CO_2 plasma emits deep UV [249, 250] which can create deep defects in the first nanometres of the c-Si and also saturate the Al_2O_3 traps. Considering the high CO_2 content in the gas mixture (78%), this effect cannot be excluded.

One could expect that, after both PDA and PCA, hydrogen could heal most of these defects; however this does not seem to be the case. The relatively high Al$_2$O$_3$ deposition temperature (250 °C) might have limited the hydrogen content in the layer and the low hydrogen content in the buffer layer (Table 5.3) might not help to feed the c-Si surface with hydrogen. But one role of the a-SiN$_X$:H capping is to bring the missing hydrogen to the c-Si surface, so something went wrong with this expected hydrogen feeding.

In order to investigate what happened, n-type wafers were passivated with 20 nm of either buffer #1 either buffer #2 directly after HF dip. These samples did not present lifetimes higher than 1 µs after 20 min of FGA at 380 °C, which is particularly low. Other samples were passivated with a-SiO$_X$ and then capped by a-SiN$_X$:H before the FGA. This time the effective lifetime increases up to 9 µs for the stack embedding buffer layer #1 and to 6 µs for the stack containing the buffer layer #2. This passivation quality is worse than the one provided by the stacking of a-SiN$_X$:H on native oxide (278 µs, Figure 3.8).
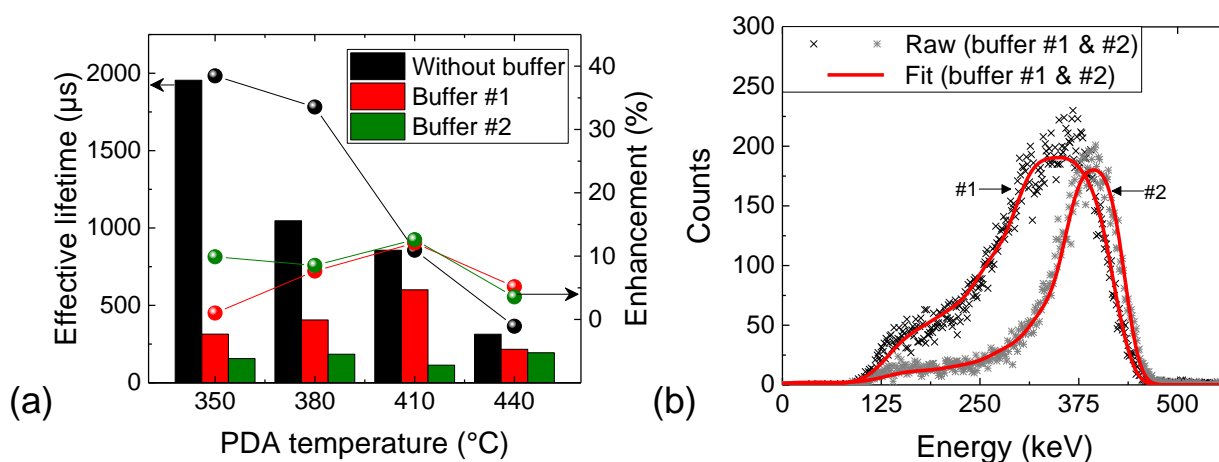
Figure 5.7: (a) Effective lifetime (columns) and lifetime improvement due to LIFE$_2$ in the LIBI (dots) for samples passivated with 60 ALD cycles of Al$_2$O$_3$, deposited at 250 °C, capped by 75 nm of a-SiN$_X$:H (black symbols, control group) or by a stack comprising 20 nm of a-SiO$_X$ (buffer #1 in red = group #1, buffer #2 in green = group #2) and 55 nm of a-SiN$_X$:H. (b) ERDA spectra of buffer #1 and #2 (deposited directly on c-Si) after FGA for 20 nm of buffer layers #1 and #2.

ERDA spectra show interesting hydrogen profiles for samples passivated only by a-SiO$_X$ and that received FGA (Figure 5.7.b). The hydrogen is mainly located at the samples surface and its diffusion through the buffer layers is drastically reduced for the buffer layer #2 compared to the #1. The analysis of the data suggests a hydrogen content that increases from 1.2%$_{at}$ to 3.6%$_{at}$ and 2.1%$_{at}$ due to FGA for buffer layers #1 and #2 respectively. Both buffer layers to H$_2$ diffusion, this effect being more pronounced for buffer #2. The stoichiometry (O/Si <2) of both layers indicates that there might be a lot of silicon dangling bonds in the a-SiO$_X$ films that can fix hydrogen that is supposed to diffuse toward the c-Si surface. This is supported by the fact that for the buffer layer #1, the higher PDA temperature of 410 °C (higher hydrogen mobility) is the most appropriate to improve the passivation.

Finite element simulations of the alternative case #1 (Figure 5.5) were repeated with a D_{it} value of 10^{12} eV^{-1}.cm^{-2} rather than 10^{11} eV^{-1}.cm^{-2} (Figure 5.8). This D_{it} value shifted up the flat band condition towards higher Q_f values at the Al$_2$O$_3$/c-Si interface and the resulting lifetimes become extremely low. For Q_f in the range of interest, between -10^{12} cm^{-2} to $-3 \cdot 10^{12}$ cm^{-2}, the expected lifetimes do not exceed 600 μs, which is consistent with the measured values (Figure 5.7.a).
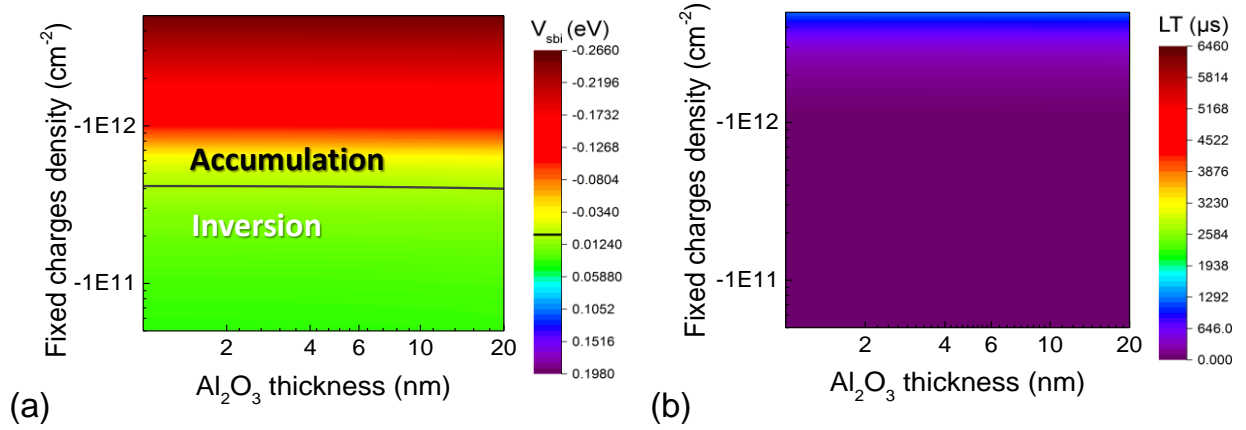
Figure 5.8: (a) Band bending at the c-Si surface and (b) effective lifetime resulting from the band bending for the alternative case #1 (Figure 5.5) but with D_{it} set at 10^{12} eV^{-1}.cm^{-2}.

So, despite their high transparency, synthesised buffer layers are not suitable for passivation, as their deposition can deteriorate the c-Si/Al$_2$O$_3$ interface (UV from the plasma) and because they also act as a sink for hydrogen that should diffuse from the a-SiN$_X$:H capping toward the c-Si surface. The alternative case #2, based on replacing the standard a-SiN$_X$:H that we used by another one with lower positive fixed charges density was thus explored.

5.2.2   Alternative case #2: a-SiN$_X$:H capping replacement

5.2.2.1   Approach and specification of the desired a-SiN$_X$:H

Several material properties should be maintained between the standard a-SiN$_X$:H and the new one that we are looking for: optimal refractive index of 1.97, high transparency, high hydrogen release during PCA, but we are looking now for a lower Q_f. For the synthesis of the standard a-SiN$_X$:H, the inter-electrode distance remained fixed at 20 mm. We varied this distance in the present study, raising the PECVD parameter to four: gas ratio, applied power density, pressure and inter-electrode distance. Considering at least 4 values for each of the 4 parameters, it represents $4^4 = 256$ possible combinations, which is not feasible. We used a design of experiment approach to mesh the parameters space with a minimal number of samples. The full-factorial design is not suited in this case as it lacks of sensitivity regarding response modulations in the middle of the parameter space. We use the Box-Behnken response surface design of experiments [251, 252] to mesh the process condition space. Only 25 different process conditions are necessary to model the a-SiN$_X$:H properties as a function of these process conditions. Similarly to the full factorial DOE, deposition parameters are set to their minimal value (-), their maximal value (+) or their middle value (0), but contrary to the full factorial DOE, the surface response DOE places much more points in the middle of the parameters space (Table 5.4).

Table 5.4: Box-Behnken surface response DOE parameters

Sample	Configuration	Inter-electrode distance (mm)	Pressure (Pa)	Power density (mW.cm^{-2})	Gas ratio
1	0−+0	25	40	216	2.25
2	−−00	20	40	126	2.25
3	0000	25	70	126	2.25
4	0−−0	25	40	36	2.25
5	0++0	25	100	216	2.25
6	+00−	30	70	126	1.50
7	0+−0	25	100	36	2.25
8	0+0−	25	100	126	1.50
9	00++	25	70	216	3.00
10	0−0+	25	40	126	3.00
11	0−0−	25	40	126	1.50
12	−+00	20	100	126	2.25
13	+0−0	30	70	36	2.25
14	−00+	20	70	126	3.00
15	+−00	30	40	126	2.25
16	0+0+	25	100	126	3.00
17	+00+	30	70	126	3.00
18	+0+0	30	70	216	2.25
19	00−+	25	70	36	3.00
20	−0+0	20	70	216	2.25
21	−0−0	20	70	36	2.25
22	00−−	25	70	36	1.50
23	00+−	25	70	216	1.50
24	−00−	20	70	126	1.50
25	++00	30	100	126	2.25

5.2.2.2 Synthesis of the new a-SiN$_X$:H capping

As the K-centres are distributed in the volume of a-SiN$_X$:H [243], it is of prime importance to compare films of the same thickness. The same deposition time (150 s) was used for the 25 process conditions. Film thicknesses were measured by SE in order to determine the growth rate and so to adapt the required deposition time of each process condition to obtain a film thickness of 75 nm. Thanks to these data it was possible to model the growth rate with JMP software (Figure 5.9). The deposition pressure is by far the parameter that impacts the more the growth rate. The higher the pressure, the faster the deposition rate. The inter-electrode distance has also a significant impact; changing this distance from 20 mm to 30 mm leads to an increase of the deposition rate by 30 % when the pressure is 100 Pa.
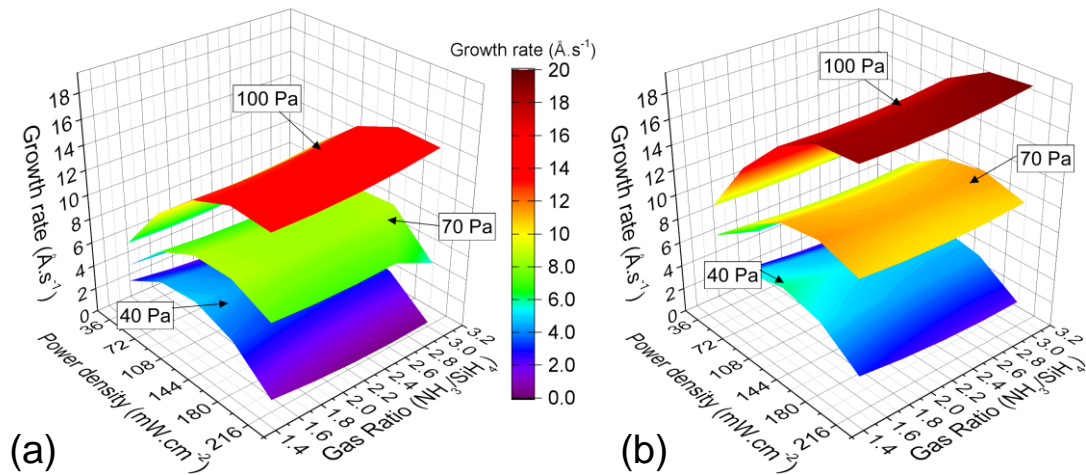
Figure 5.9: Modelled growth rate for an inter-electrode distance of (a) 20 mm. and (b) 30 mm.

Thanks to the determined growth rate, 25 n-type wafers were passivated by 75 nm of a-SiN$_X$:H after HF dip. Wafers were then cut in half in order to perform the measurement on both the as-deposited and the annealed state of the films. During PECVD, V$_{RF}$ and V$_{DC}$ were monitored in order to determine the V$_{PL}$. The refractive index (at 633 nm) and the extinction coefficient (at 300 nm) were determined by SE. XRR was performed on all films, the critical angle of the measure was used as a proxy of the density, the latter being excessively long to determine considering the variety of film compositions. The film density is not the most relevant parameter for passivation, but it is an important parameter to avoid ghost plating during metallisation [253]. COCOS measurements were performed on all samples but failed for 9 of them despite several attempts. The tool manufacturer confirmed that when the dielectric properties of the film are too poor, the deposited corona charges leak into the film, making the measurement impossible. So, the model that describes Q$_f$ as a function of PECVD process conditions relies only on 16 values rather than 25. The as-deposited samples underwent TDS to qualify the hydrogen content. The H$_2$ signal recorded by the QMS was normalised by the film volume (surface determined by optical microscope and thickness by SE). The signal is then integrated between 200 °C and 700 °C or 200 °C and 380 °C, these values being considered representative of the total hydrogen content and the hydrogen release during PCA respectively. All the measured responses were modelled with reasonable goodness of fit, the extremely high one of Q$_f$ being certainly not representative due to missing data (Table 5.5).

Table 5.5: Quality of output models and the two most impacting PECVD parameters on the different model responses in order of importance

Response	R²	Most impacting PECVD parameter,
Growth rate	0.94	Pressure, power
V$_{PL}$	0.90	Power, pressure
Refractive index	0.99	Gas ratio, power
Extinction coefficient	0.98	Gas ratio, power
Critical angle	0.89	Pressure, power
Q$_f$ (after PCA)	0.99*	Power, gas ratio
Total H$_2$ content	0.86	Inter-electrode distance, pressure
H$_2$ release by PCA	0.90	Pressure, inter-electrode distance

* Model based on 16 samples
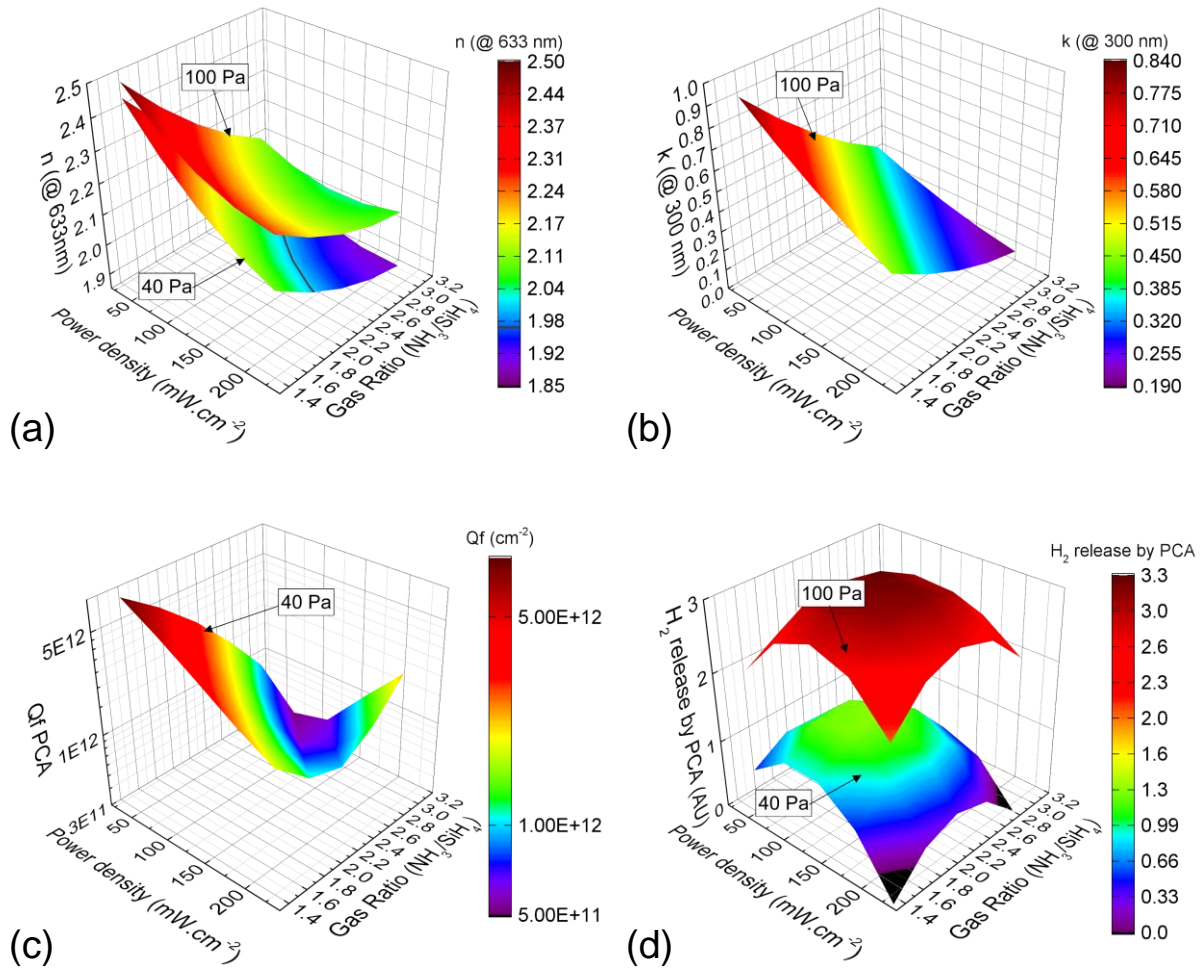
Figure 5.10: Modelled surface responses for an inter-electrode distance of 20 mm. (a) refractive index at 633 nm. (b) Extinction coefficient at 300 nm. (c) Fixed charges density after PCA. (d) Hydrogen release by PCA. For the sake of clarity, only one surface is plotted when the pressure change does not strongly impact the response.

Surface responses of the refractive index (Figure 5.10.a) and the extinction coefficient (Figure 5.10.b) are consistent with the previously obtained values (Figure 3.5.b). The gas ratio and the power density are the two main impacting parameters for these optical properties. A small gas ratio and a low power density result in silicon rich a-SiN_X:H with optical properties close to a-Si:H. The deposition pressure has a negligible impact on the extinction coefficient while it is of prime importance to consider it in order to reach the optimal refractive index of 1.97 (black line on Figure 5.10.a). The Q_f surface response (Figure 5.10.c) looks like a canyon, suggesting an ideal film stoichiometry that reduces Q_f. Indeed as previously observed (Figure 3.5.b) for a constant power density, ammonia-rich atmosphere results in N-rich films. Then, when the power density increases, ammonia dissociation also increases and less ammonia is required in the gas mix to obtain similar film composition. However, considering that 36% of the COCOS measurements failed, this Q_f model might not be very accurate. Regarding the released quantity of hydrogen during PCA (Figure 5.10.d), the pressure and the inter-electrode distance are the most impacting parameters; a pressure increase from 40 Pa to 100 Pa triples the amount of hydrogen incorporated in the a-SiN_X:H films.
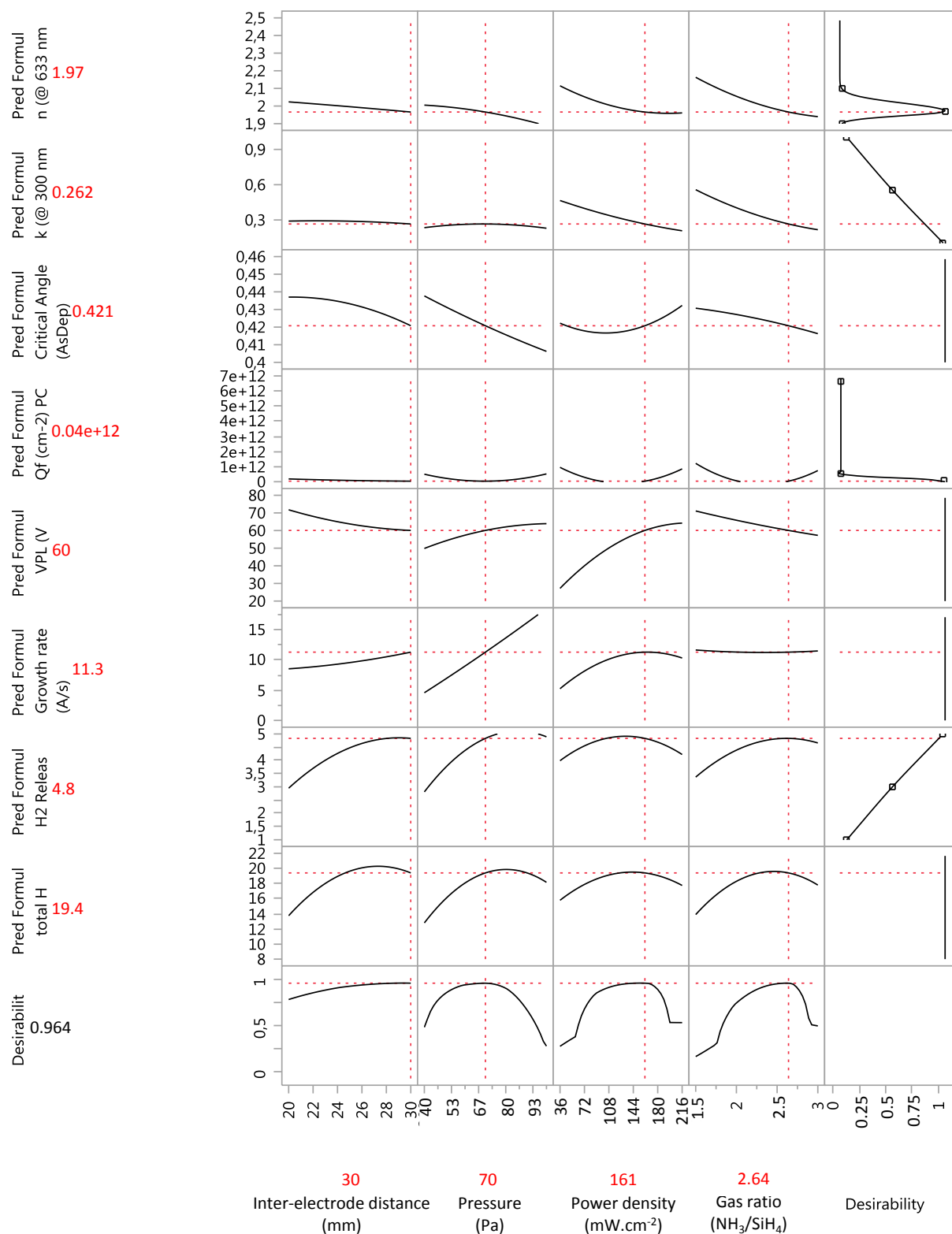
Figure 5.11: DOE results for the optimal compromise between refractive index (desirability set maximal for n=1.97), extinction coefficient (desirability set at minimising k), fixed charge density (desirability set at minimising Q_f) and hydrogen release (desirability set at maximising H_2 release). No desirability restrictions have been set on the critical angle, the plasma potential (V_{PL}), the growth rate and the total hydrogen content in order to get these values without impacting the optimisation.

All the modelled responses were gathered together to determine the optimal recipe that will provide a-SiN$_X$:H with the lowest Q_f, the highest hydrogen release by PCA, the highest transparency (lowest k) and the refractive index equal to 1.97 (Figure 5.11). Other responses like the V_{PL}, the critical angles the growth rate and the total hydrogen content were included without any constraint on the values, just for information. The software proposed the process parameters summarised in Table 5.6 which are really different from the previous ones.

Table 5.6: Comparison between the former a-SiN$_X$:H process parameters and the new a-SiN$_X$:H process parameters obtained from the DOE data treatment.

Recipe	Pressure (Pa)	Power density (mW.cm^{-2})	Gas ratio (NH$_3$/SiH$_4$)	Inter-electrode distance (mm)
Former a-SiN$_X$:H	100	36	9	20
New a-SiN$_X$:H	70	161	2.64	30

The new a-SiN$_X$:H film was deposited and analysed in the same way as the samples from the DOE. The measured data are summarised in Table 5.7 and compared with both the expected values from the model and the values of the former a-SiN$_X$:H film.

Table 5.7: comparison between former and new capping properties

Properties	Former capping	New capping Predicted	New capping measured	Model error (%)
Growth rate (A.s^{-1})	5	11.3	13.8	+22%
n (@ 633 nm)	1.876	1.97	2.06	+4.5%
k (@ 300 nm)	0.069	0.262	0.448	+71%
critical angle (2θ; °)	0.438	0.421	0.408	-3.1%
V_{PL} (V)	25	60	56	-6%
H$_2$ release (AU)	3.1	4.8	5.5	+15%
Q_f (cm^{-2})	$+1.01 \cdot 10^{12}$	$+0.04 \cdot 10^{12}$	$+0.47 \cdot 10^{12}$	+1075%

The model underestimates the growth rate by 22 %, which is twice faster than for the former film. The models are pretty accurate regarding the refractive index, the plasma potential and the critical angle values. In contrast, the extinction coefficient was underestimated and is 6.5 times higher than the one of the former a-SiN$_X$:H, resulting in a strong transparency loss as determined by equation (5.1) and plotted on Figure 5.12.

The current density loss associated to absorption in the a-SiN$_X$:H has been calculated for the AM1.5 spectrum. Assuming that one absorbed photon in the a-SiN$_X$:H results in one electron loss for the photogenerated current density in the c-Si, it results in a current density loss that increases from 0.061 mA.cm^{-2} for the former a-SiN$_X$:H to 0.815 mA.cm^{-2} for the new a-SiN$_X$:H.

$$A = \left(1 - e^{-\frac{4\pi k}{\lambda} t}\right)$$

(5.1)

With:

- k : the extinction coefficient
- λ : the wavelength
- t : the film thickness
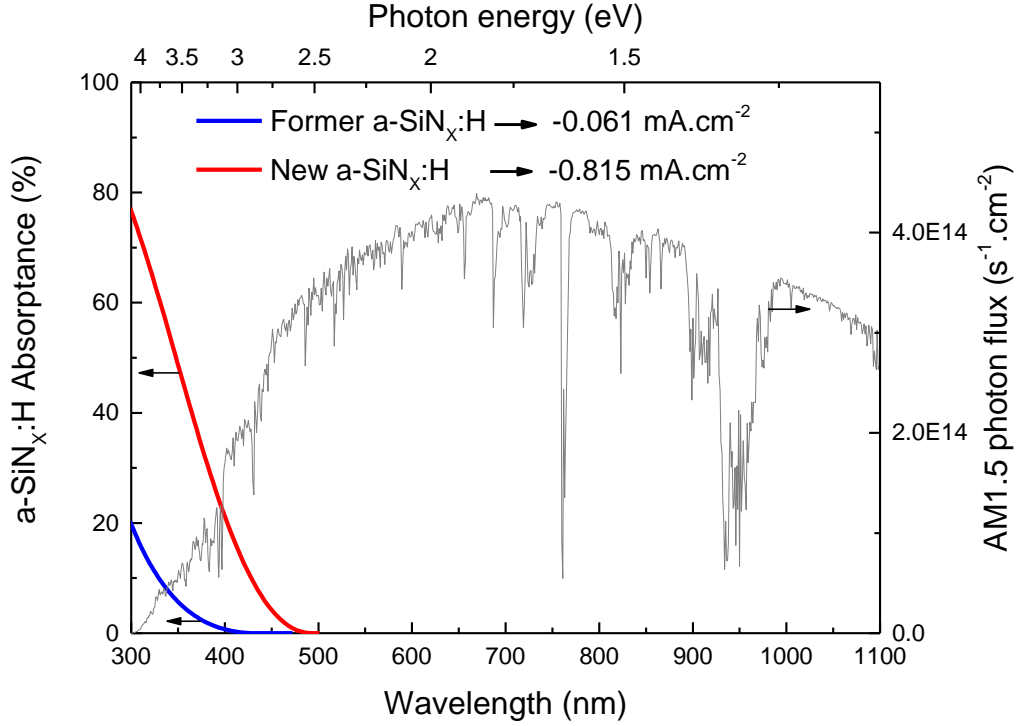
Figure 5.12: absorption of the former and the new a-SiN$_X$:H layers calculated from their respective absorption coefficient (determined by SE). The calculated current density loss associated to absorption assumes one pass of the photons in the films and no reflection at the interfaces.

Despite the loss of 0.815 mA.cm^{-2} in the photogenerated current and a non-null Q_f, the new a-SiN$_X$:H contains 50% less positive fixed charge density and releases more hydrogen than the former capping, so it is of interest to test it on Al$_2$O$_3$.

5.2.2.3   Performances of the new a-SiN$_X$:H capping

Four p-types wafers were passivated by TD-ALD with 20 ALD cycles for two wafers and 60 ALD cycles for the two others, using the thermal drift profile #1 (Figure 4.15). Samples with 60 ALD cycles received a PDA of 30 min at 380 °C while the samples with 20 ALD cycles did not receive a PDA. For each Al$_2$O$_3$ thickness, one sample was capped by the former a-SiN$_X$:H and another one by the new a-SiN$_X$:H (Table 5.6). All the samples received the PCA (20 min at 380 °C) and then the lifetime was measured. The samples were subject to LIFE$_2$ treatment in the LIBI for one week. The saturated lifetime was measured by QSS-PC (LIS-R1) before storing the samples in a dark cabinet for one month in order to determine how much the lifetime diminished after this storage.

For samples with 20 ALD cycles of Al$_2$O$_3$, the former capping remains the most efficient, allowing a lifetime increase of 300% due to LIFE$_2$ and then a lifetime degradation of 30% due to dark storage (Figure5.13.a). After PCA the initial lifetime provided by the new capping on 20 ALD cycles demonstrates similar passivation level than the former one (~100 µs). The passivation stack with the new capping is less sensitive to the LIFE$_2$ treatment, increasing lifetime just by 40% (140 µs). Then, after storage in the dark, the lifetime is going back to its initial value. The higher power density used to deposit the new a-SiN$_X$:H layer that results in higher plasma potential and so higher ion bombardment can deteriorate the already low passivation properties provides by the 20 ALD cycles.
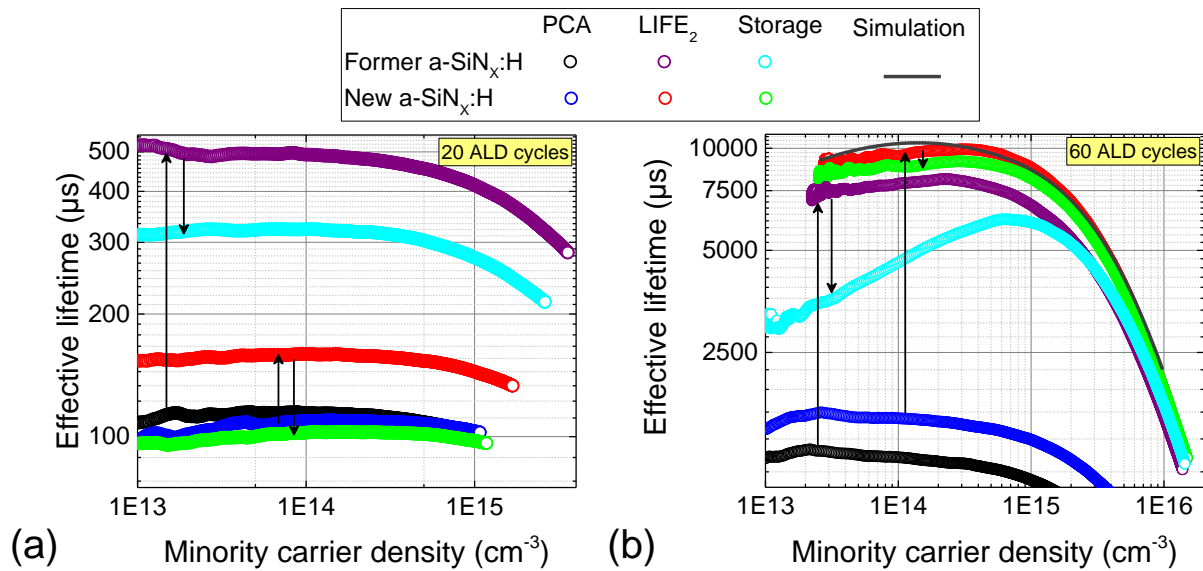
Figure 5.13: Effective lifetime of Al$_2$O$_3$/a-SiN$_X$:H passivated samples with (a) 20 ALD cycles and (b) 60 ALD cycles deposited with the thermal drift profile #1. The simulated curve was obtained using the model depicted on Figure 1.7 with an interfacial trap density of $10^{10}eV^{-1}cm^{-2}$ and a Q$_f$ of $-3\cdot10^{12}$ cm^{-2} at the c-Si/Al$_2$O$_3$ interface.

When the Al$_2$O$_3$ thickness is increased to 60 ALD cycles the effective lifetime increases by one order of magnitude compared to 20 ALD cycles (Figure 5.13.b). Before the LIFE$_2$ treatment, the new a-SiN$_X$:H already provides better passivation than the former one. For both cappings the effective lifetime increases by ~500% after LIFE$_2$, maintaining the lifetime difference between the two samples. An exceptionally high lifetime of 8774 µs is measured at 10^{15} cm^{-3} for the sample capped with the new a-SiN$_X$:H, which corresponds to a SRV of 0.83 cm.s^{-1}. The PCD calibrated photoluminescence picture shows a homogenous surface passivation and reveals areas with SRV as low as 0.55 cm.s^{-1} (Figure 5.14). If the charge density in the new capping is neglected, finite element simulation results of chapter 2 (Figure 2.7) suggest passivation properties around 10^{10} eV^{-1}.cm^{-2} for the D$_{it}$ and $-3\cdot10^{12}$ cm^{-2} for the Q$_f$ at the Al$_2$O$_3$/c-Si interface. These values are consistent with the D$_{it}$ and Q$_f$ values measured for TD-ALD passivated samples (chapter 4).

However, the superior passivation quality due to the new a-SiN$_X$:H capping cannot be attributed only to the lower positive Qf. Indeed, the positive charge density reduction in the capping is accompanied by a strong increase of the hydrogen release during PCA, that can definitely make the difference between a good and a very good passivation quality. Moreover, the new capping is less transparent to UV, so high energy photons which could break Si-H bonds at the c-Si surface will be absorbed by the new a-SiN$_X$:H layer rather than the c-Si surface. This deep UV filter function can be interesting for a stabilised passivation over time. The trade-off between the V$_{OC}$ gain due to higher passivation and the J$_{SC}$ loss (-0.815 mA.cm^{-2}) has to be evaluated at the device level.
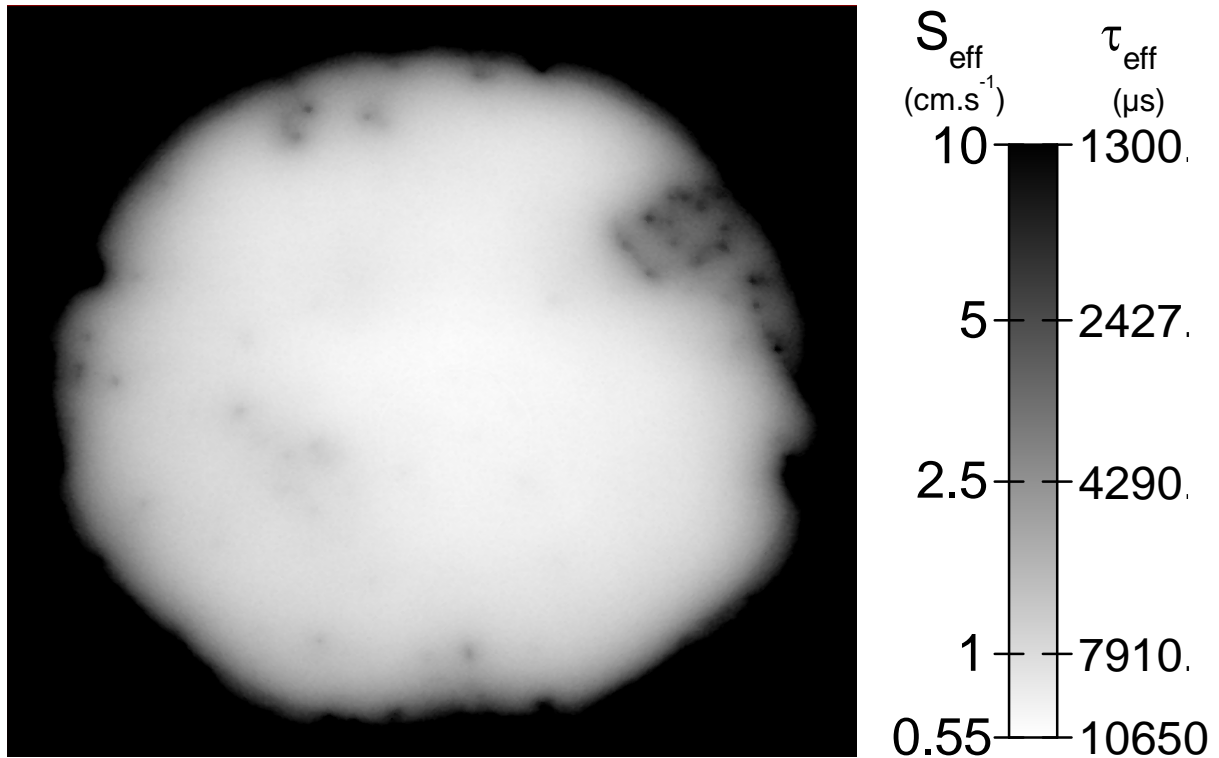
Figure 5.14: QSS-PC calibrated photoluminescence picture ($\Delta n=10^{15}cm^{-3}$) of a p-type c-Si wafer with the optimised passivation stack, i.e. 60 ALD cycles using thermal drift profile #1; annealed 30 min @ 380 °C; capped with the new a-SiN$_X$:H before PCA.

After 1 month in the dark, the sample capped with the new a-SiN$_X$:H layer shows a lifetime degradation of 7.8% while the sample capped with the former a-SiN$_X$:H shows a lifetime decrease of 10.9%. On Figure 5.13.b it is clearly visible that the lifetime degradation is nearly constant over the carrier density for the sample capped with the new a-SiN$_X$:H while the τ_{eff} degradation quickly increases as the carrier density decrease for the sample with the former capping layer. A field effect decrease is suspected but cannot be fit by the finite element model that we used in chapter 2 and chapter 4. Thus, this intriguing behaviour cannot be explained at the moment.

5.3   Conclusion

In this chapter we discussed the impact of the electronic properties of the a-SiN$_X$:H capping on the passivation provided by an Al$_2$O$_3$/a-SiN$_X$:H stack. Finite elements simulation suggests that the presence of positive Q$_f$ in the a-SiN$_X$:H capping decreases the passivation level provided by the Al$_2$O$_3$/a-SiN$_X$:H stack. Two solutions were found to overcome this problem: the use of a transparent buffer layer between the Al$_2$O$_3$ and the a-SiN$_X$:H or the replacement of the a-SiN$_X$:H layer by another one free of positive Q$_f$. Experimentally, the former solution (that seems the easiest) was not conclusive due to inappropriate material properties of the buffer layer, while the latter solution provided an exceptionally high passivation level (SRV = 0.83 cm.s^{-1}).

The main key fact here is that the development of a perfect capping layer for Al$_2$O$_3$ is extremely demanding regarding all its specifications. However, a lower transparency of a capping layer containing lower Q$_f$ can be a good trade-off between V$_{OC}$ and J$_{SC}$ and has to be numerically modelled at the device level.

Conclusion and perspectives

The surface passivation properties provided by Al_2O_3 grown from trimethylaluminium and H_2O using atomic layer deposition have been investigated in view of their application to solar cells processed at temperature lower than 400 °C. From the results presented in this thesis, we propose c-Si surface passivation by Al_2O_3 mechanisms described hereafter.

Chemical passivation: D_{it} reduction

In chapter 2 we reviewed how Al_2O_3 film properties are highly dependent on the deposition temperature. The hydrogen content of the films is the property that is the most impacted by the deposition temperature. However, despite a hydrogen content up to $6\,\%_{at}$, the passivation level provided by a thin (< 20 nm) Al_2O_3 film after deposition on c-Si is very poor ($S_{eff} \sim 140$ cm.s^{-1}). A post-deposition annealing (PDA) is required to activate the passivation properties. During this annealing, the dehydroxylation of Al_2O_3 is the main reaction that leads to c-Si passivation improvement. An isolated dehydroxylation reaction involving two aluminol groups releases two hydrogen atoms and one oxygen atom that are most of the time combined in an H_2O molecule.

Nevertheless, thermal desorption spectroscopy (TDS) experiments (chapter 4) suggest a different chemical behaviour for the Al_2O_3 free surface and the Al_2O_3/c-Si interface. Indeed, H_2O molecules are steadily released by the film when the TDS furnace temperature increases, while H_2 molecules seem to be produced and trapped at the c-Si/Al_2O_3 interface as they are mainly detected when the film breaks (blisters explosion). These different chemical behaviours can be ascribed to the catalytic properties of tetrahedrally coordinated aluminium atoms that represent more than 75 % of the Al coordination at the c-Si/Al_2O_3 interface.

So, at the c-Si/Al_2O_3 interface, the oxygen atom released by a dehydroxylation reaction is not incorporated as a gaseous species. It can remain in the network as an interstitial atom (explaining thus the excess of oxygen detected at the c-Si/Al_2O_3 interface) or more likely oxidise the c-Si surface (explaining SiO_2 thickening at this interface due to a PDA). This SiO_2 that grows between the Al_2O_3 film and c-Si substrate during the PDA seems essential for a stable passivation. Indeed, with thermal-drift atomic layer deposition (TD-ALD) process we obtained a very good chemical passivation ($D_{it} \sim 5 \cdot 10^{10}$ ev^{-1}.cm^{-2}) in as-deposited state, but this passivation is not stable against low intensity UV illumination. Considering that during TD-ALD the deposition temperature never exceeded 250 °C, the good as-deposited passivation properties might be the result of hydrogen diffusion that passivates dangling bonds rather than the oxidation of the silicon. The small bond energy of Si-H (3.03 eV) compared to Si-O (8.24 eV) results in a c-Si surface depassivation under UV illumination, similar to the Staebler-Wronski effect. A PDA carried out at temperatures higher than 350 °C seems a prerequisite to form the interfacial SiO_2 and then obtain a stable chemical passivation.

However, the hydrogen contribution to passivation cannot be neglected and might make the difference between a good and a very good passivation level.

In order to further investigate the origin of the passivation stability difference between TD-ALD Al_2O_3 films in as-deposited state and after a PDA, electron energy loss spectroscopy and XPS have to be carried out. The UV stability evaluation of an as-deposited Al_2O_3 film grown by TD-ALD on a c-Si surface presenting a thin (~1 nm) chemical SiO_2 can also be considered.

Field effect passivation: Q_f increase

Regarding the field effect passivation, it mainly results from electrons trapped in Al_2O_3 by point defects that seem to be linked to oxygen (interstitials and/or vacancies). In chapter 2, we showed that injection of electrons from the c-Si into the Al_2O_3 occurs through two mechanisms:

- A direct injection if the absorbed photon has energy higher than the difference between the c-Si valence band and the Al_2O_3 conduction band.
- An indirect injection that results from multiple particles interaction, when the photogenerated carrier density in the first nanometres below the c-Si surface is high enough to induce Auger recombination.

These electron traps can be filled during the PDA due to temperature related intrinsic carrier concentration increase or due to direct illumination of the silicon by the IR lamps of the furnace. After the PDA, the traps can be filled by low intensity UV illumination (direct injection mechanism) or high intensity illumination (indirect injection mechanism, with or without UV wavelength).

In this work, we used the light-induced field effect enhancement (LIFE$_2$) treatment to probe the stability of these trapped charges. It seems that this trapping stability is directly related to the Al_2O_3/c-Si interface quality. Indeed, as shown in chapters 3 and 4, as soon as blistering appears on the sample, the trapped charges start to be released when the sample illumination is stopped. Thanks to coloured picosecond acoustics microscopy (APiC), we showed that the blistering seems to result from an adhesion reduction that correlates with hydrogen accumulation at the c-Si/Al_2O_3 interface. The formation of blisters occurs through a nucleation/growth process linked to both the initial hydrogen quantity and the Al_2O_3 film thickness, the latter representing a barrier to gas diffusion. Thus we proposed to use a thermal drift during the ALD process in order to release the hydrogen during the deposition, *i.e.* when the Al_2O_3 film thickness is not completed. An APiC mapping allowed us to underline how much this TD-ALD concept provides very good interface quality between the c-Si substrate and the Al_2O_3 film.

In chapter 5, we showed that the deposition of an a-SiN$_X$:H film that contains positive charges on top of Al_2O_3 can reduce and even cancel the field effect passivation provided by the Al_2O_3 layer at the c-Si surface. Finite element modelling suggests two approaches to avoid this effect: i) the insertion of a thin (~20 nm) buffer layer nearly free of charge, such as SiO_2, between Al_2O_3 and a-SiN$_X$:H ; ii) the reduction of the positive charge quantity in the a-SiN$_X$:H. The latter approach has been successfully implemented on an Al_2O_3 layer deposited by TD-ALD. This Al_2O_3/a-SiN$_X$:H passivation stack reduced the surface recombination velocity down to 0.8 cm.s^{-1} and showed exceptional charge trapping stability after one month of storage in the obscurity.

In order to further investigate the degradation of the c-Si/Al_2O_3 interface adhesion, *in situ* APiC measurements during annealing would be very interesting. The APiC technique might be suitable to detect passivation degradation on PERC back surface after firing. Indeed, the acoustic wave generation requires aluminium metallisation of the surface. For a more academic understanding, coupling *in situ* APiC with *in situ* photoluminescence measurements would allow linking directly Al_2O_3/c-Si adhesion quality and passivation level during annealing.

More generally, an extended study of the TD-ALD process would be of interest. The gas release kinetics during TD-ALD might have some limitations. The implementation of the process on an industrial tool such as the spatial ALD "Levitrack" from Levitech could be very interesting to assess the process compatibility with the industrial deposition throughput.

At the solar cell level, regarding the use of Al_2O_3 in a passivation stack for p-type surfaces, we strongly recommend replacing the a-SiN_X:H by another material containing lower positive charge density such as $SiON_X$:H or AlN, or even negative charges.

It can be interesting to use Al_2O_3 on the p$^+$ surface of an n-PERT exposed to the sunlight to ensure a daily charging of the Al_2O_3 traps and so maximal surface passivation. Then, for the n-type back surface passivation, an Al_2O_3 layer nearly free of charges can be of interest. As this back surface will not be exposed to UV radiation, the use of TD-ALD is an easy way to obtain a very good surface passivation without the high negative charge density. Moreover, as shown in chapter 5, the charges of the capping impact the effective field effect at the c-Si surface. Thus, depositing a capping that presents a high density of positive charges on top of an Al_2O_3 layer that is almost free of negative charges might result in an efficient passivation stack for an n-type surface.

Another interesting use of the $LIFE_2$ phenomenon would be the field effect enhancement of the Al_2O_3 deposited on the PERC back surface. Indeed, after full surface metallisation, the back surface receives only IR wavelengths. Then, an intense IR laser illumination from the front surface of the PERC can inject electrons in Al_2O_3 through high carrier concentration at the Al_2O_3/c-Si interface.

References

[1]   S. D. Mo, Y. N. Xu, and W. Y. Ching, "Electronic and Structural Properties of Bulk γ-Al$_2$O$_3$," *Journal of the American Ceramic Society,* vol. 80, no. 5, pp. 1193-1197, 1997, https://doi.org/10.1111/j.1151-2916.1997.tb02963.x

[2]   V. Afanas' ev, M. Houssa, A. Stesmans, C. Merckling, T. Schram, and J. Kittl, "Influence of Al$_2$O$_3$ crystallization on band offsets at interfaces with Si and TiNx," *Applied Physics Letters,* vol. 99, no. 7, pp. 072103, 2011, https://doi.org/10.1063/1.3623439

[3]   M. Choi, A. Janotti, and C. G. Van de Walle, "Native point defects and dangling bonds in α-Al$_2$O$_3$," *Journal of Applied Physics,* vol. 113, no. 4, pp. 044501, 2013, https://doi.org/10.1063/1.4784114

[4]   M. Choi, J. L. Lyons, A. Janotti, and C. G. Van de Walle, "Impact of carbon and nitrogen impurities in high-κ dielectrics on metal-oxide-semiconductor devices," *Applied Physics Letters,* vol. 102, no. 14, pp. 142902, 2013, https://doi.org/10.1063/1.4801497

[5]   W. Lu, Y. Dai, F. Wang, and B. Jin, "Impact of native defects and impurities in m− HfO$_2$ and β− Si$_3$N$_4$ on charge trapping memory devices: A first principle hybrid functional study," *physica status solidi (b),* vol. 254, no. 2, 2017, http://dx.doi.org/10.1002/pssb.201600360

[6]   M. Choi, J. L. Lyons, A. Janotti, and C. G. Van de Walle, "Impact of native defects in high-k dielectric oxides on GaN/oxide metal–oxide–semiconductor devices," *physica status solidi (b),* vol. 250, no. 4, pp. 787-791, 2013, https://doi.org/10.1002/pssb.201200628

[7]   B. L. French, and S. W. King, "Detection of surface electronic defect states in low and high-k dielectrics using reflection electron energy loss spectroscopy," *Journal of Materials Research,* vol. 28, no. 20, pp. 2771-2784, 2013, https://doi.org/10.1557/jmr.2013.274

[8]   M. D. Groner, F. H. Fabreguette, J. W. Elam, and S. M. George, "Low-Temperature Al$_2$O$_3$ Atomic Layer Deposition," *Chemistry of Materials,* vol. 16, no. 4, pp. 639-645, 2004/02/01, 2004, https://doi.org/10.1021/cm0304546

[9]   O. M. Ylivaara, X. Liu, L. Kilpi, J. Lyytinen, D. Schneider, M. Laitinen, J. Julin, S. Ali, S. Sintonen, M. Berdova, E. Haimi, T. Sajavaara, H. Ronkainen, H. Lipsanen, J. Koskinen, S.-P. Hannula, and R. L. Puurunen, "Aluminum oxide from trimethylaluminum and water by atomic layer deposition: the temperature dependence of residual stress, elastic modulus, hardness and adhesion," *Thin Solid Films,* vol. 552, pp. 124-135, 2014, https://doi.org/10.1016/j.tsf.2013.11.112

[10]   J. Van Hemmen, S. Heil, J. Klootwijk, F. Roozeboom, C. Hodson, M. Van de Sanden, and W. Kessels, "Plasma and thermal ALD of Al$_2$O$_3$ in a commercial 200 mm ALD reactor," *Journal of The Electrochemical Society,* vol. 154, no. 7, pp. G165-G169, 2007, https://doi.org/10.1149/1.2737629

[11]   D. Liu, and J. Robertson, "Oxygen vacancy levels and interfaces of Al$_2$O$_3$," *Microelectronic Engineering,* vol. 86, no. 7, pp. 1668-1671, 2009, https://doi.org/10.1016/j.mee.2009.03.011

[12]   G. Balakrishnan, P. Kuppusami, S. T. Sundari, R. Thirumurugesan, V. Ganesan, E. Mohandas, and D. Sastikumar, "Structural and optical properties of γ-alumina thin films prepared by pulsed laser deposition," *Thin Solid Films,* vol. 518, no. 14, pp. 3898-3902, 2010, https://doi.org/10.1016/j.tsf.2009.12.001

[13]   I. E. Agency, *World Energy Outlook 2016,* 2016.

[14]   D. Tahir, H. L. Kwon, H. C. Shin, S. K. Oh, H. J. Kang, S. Heo, J. G. Chung, J. C. Lee, and S. Tougaard, "Electronic and optical properties of Al$_2$O$_3$/SiO$_2$ thin films grown on Si substrate," *Journal of Physics D: Applied Physics,* vol. 43, no. 25, pp. 255301, 2010, https://doi.org/10.1088/0022-3727/43/25/255301

[15]   B. Ealet, M. Elyakhloufi, E. Gillet, and M. Ricci, "Electronic and crystallographic structure of γ-alumina thin films," *Thin Solid Films,* vol. 250, no. 1, pp. 92-100, 1994, https://doi.org/10.1016/0040-6090(94)90171-6

[16]   V. Afanas'ev, A. Stesmans, and W. Tsai, "Determination of interface energy band diagram between (100) Si and mixed Al–Hf oxides using internal electron photoemission," *Applied physics letters,* vol. 82, no. 2, pp. 245-247, 2003, https://doi.org/10.1063/1.1532550

[17]   E. Bersch, S. Rangan, R. A. Bartynski, E. Garfunkel, and E. Vescovo, "Band offsets of ultrathin high-κ oxide films with Si," *Physical review B,* vol. 78, no. 8, pp. 085114, 2008, https://doi.org/10.1103/PhysRevB.78.085114

[18]   E. O. Filatova, and A. S. Konashuk, "Interpretation of the changing the band gap of Al_2O_3 depending on its crystalline form: Connection with different local symmetries," *The Journal of Physical Chemistry C,* vol. 119, no. 35, pp. 20755-20761, 2015, https://doi.org/10.1021/acs.jpcc.5b06843

[19]   N. Alimardani, S. W. King, B. L. French, C. Tan, B. P. Lampert, and J. F. Conley, "Investigation of the impact of insulator material on the performance of dissimilar electrode metal-insulator-metal diodes," *Journal of Applied Physics,* vol. 116, no. 2, pp. 024508, 2014, https://doi.org/10.1063/1.4889798

[20]   R. H. French, "Electronic band structure of Al_2O_3, with comparison to AlON and AlN," *Journal of the American Ceramic Society,* vol. 73, no. 3, pp. 477-489, 1990, https://doi.org/10.1111/j.1151-2916.1990.tb06541.x

[21]   N. S. J. Braithwaite, "Introduction to gas discharges," *Plasma sources science and technology,* vol. 9, no. 4, pp. 517, 2000, https://doi.org/10.1088/0963-0252/9/4/307

[22]   J. Robertson, "Band offsets of wide-band-gap oxides and implications for future electronic devices," *Journal of Vacuum Science & Technology B,* vol. 18, no. 3, pp. 1785-1791, 2000, https://doi.org/10.1116/1.591472

[23]   J. J. H. Gielis, B. Hoex, M. C. M. van de Sanden, and W. M. M. Kessels, "Negative charge and charging dynamics in Al_2O_3 films on Si characterized by second-harmonic generation," *Journal of Applied Physics,* vol. 104, no. 7, pp. -, 2008, http://dx.doi.org/10.1063/1.2985906

[24]   M. Lei, J. Yum, S. Banerjee, G. Bersuker, and M. Downer, "Band offsets of atomic layer deposited Al_2O_3 and HfO_2 on Si measured by linear and nonlinear internal photoemission," *physica status solidi (b),* vol. 249, no. 6, pp. 1160-1165, 2012, https://doi.org/10.1002/pssb.201100744

[25]   J. Robertson, "Defects and hydrogen in amorphous silicon nitride," *Philosophical magazine B,* vol. 69, no. 2, pp. 307-326, 1994, http://dx.doi.org/10.1080/01418639408240111

[26]   W. Lanford, and M. Rand, "The hydrogen content of plasma-deposited silicon nitride," *Journal of Applied Physics,* vol. 49, no. 4, pp. 2473-2477, 1978, https://doi.org/10.1063/1.325095

[27]   H.-M. Lee, 李弘賀, C.-T. Kuo, 郭承泰, H.-W. Shiu, 許紘瑋, C.-H. Chen, 陳家浩, S. Gwo, and 果尚志, "Valence band offset and interface stoichiometry at epitaxial Si_3N_4/Si (111) heterojunctions formed by plasma nitridation," *Applied Physics Letters,* vol. 95, no. 22, pp. 222104, 2009, https://doi.org/10.1063/1.3269601

[28]   E. Vianello, F. Driussi, P. Blaise, P. Palestri, D. Esseni, L. Perniola, G. Molas, B. De Salvo, and L. Selmi, "Explanation of the charge trapping properties of silicon nitride storage layers for NVMs—Part II: Atomistic and electrical modeling," *IEEE Transactions on Electron Devices,* vol. 58, no. 8, pp. 2490-2499, 2011, https://doi.org/10.1109/TED.2011.2156407

[29]   M. D. Groner, J. W. Elam, F. H. Fabreguette, and S. M. George, "Electrical characterization of thin Al_2O_3 films grown by atomic layer deposition on silicon and various metal substrates," *Thin Solid Films,* vol. 413, no. 1–2, pp. 186-197, 6/24/, 2002, http://dx.doi.org/10.1016/S0040-6090(02)00438-8

[30]   M. Shahjahan, N. Takahashi, K. Sawada, and M. Ishida, "Fabrication and electrical characterization of ultrathin crystalline Al_2O_3 gate dielectric films on Si (100) and Si (111) by molecular beam epitaxy," *Japanese journal of applied physics,* vol. 41, no. 12B, pp. L1474, 2002, https://doi.org/10.1143/JJAP.41.L1474

[31]   R. Hezel, and K. Jaeger, "Low-Temperature Surface Passivation of Silicon for Solar Cells," *Journal of The Electrochemical Society,* vol. 136, no. 2, pp. 518-523, February 1, 1989, 1989, https://doi.org/10.1149/1.2096673

[32]   pv.energytrend.com. "Mono-Si Cell (Per Watt) spot price," 2017.

[33]   B. Attia, M. Parikh, and T. Heggarty, "Global Solar Demand Monitor: Q2 2017," *Global Downstream Solar Service*, gtmresearch, ed., 2017.

[34]   J. Robertson, "Defects in amorphous semiconductors," *Philosophical Magazine B,* vol. 51, no. 2, pp. 183-192, 1985, http://dx.doi.org/10.1080/13642818508240562

[35]   G. Dingemans, P. Engelhart, R. Seguin, F. Einsele, B. Hoex, M. C. M. van de Sanden, and W. M. M. Kessels, "Stability of Al_2O_3 and Al_2O_3/a-SiNx:H stacks for surface passivation of crystalline silicon," *Journal of Applied Physics,* vol. 106, no. 11, pp. -, 2009, http://dx.doi.org/10.1063/1.3264572

[36]   Solargis. "World solar resource maps - Global Horizontal Irradiation (GHI)," 2017; http://solargis.com/products/maps-and-gis-data/free/download/world.

[37] G. Dingemans, and W. M. M. Kessels, "Status and prospects of Al_2O_3-based surface passivation schemes for silicon solar cells," *Journal of Vacuum Science & Technology A,* vol. 30, no. 4, pp. 040802, 2012, http://dx.doi.org/10.1116/1.4728205

[38] I. W. Group, "International Technology Roadmap for Photovoltaic (ITRPV) 2017 Results," SEMI, Berlin, Germany, 2017,

[39] S. De Wolf, B. Demaurex, A. Descoeudres, and C. Ballif, "Very fast light-induced degradation of a-Si:H/c-Si(100) interfaces," *Physical Review B,* vol. 83, no. 23, pp. 233301, 06/07/, 2011, https://doi.org/10.1103/PhysRevB.83.233301

[40] B. Liao, R. Stangl, T. Mueller, F. Lin, C. S. Bhatia, and B. Hoex, "The effect of light soaking on crystalline silicon surface passivation by atomic layer deposited Al_2O_3," *Journal of Applied Physics,* vol. 113, no. 2, pp. 024509, 2013, http://dx.doi.org/10.1063/1.4775595

[41] U. N.-D. o. E. a. s. affairs, "World Population Prospects 2017," 2017,

[42] R. Perez, and M. Perez, "Update 2015 -- a fundamental look at supply side energy reserves for the planet," *Solar update: IEA SHC Newsletter,* vol. 62, 2015,

[43] L. Szabó, "The history of using solar energy." pp. 1-8, https://doi.org/10.1109/MPS.2017.7974451

[44] A.-E. Becquerel, "Mémoire sur les effets électriques produits sous l'influence des rayons solaires," *Comptes rendus hebdomadaires des séances de l'Académie des sciences,* vol. 9, pp. 561–567, séance du Lundi 4 novembre, 1839,

[45] REN21, *Renewables 2017 Global Status Report*, 2017.

[46] S. Philipps, and W. Warmuth, ©*Fraunhofer ISE: Photovoltaics Report, updated: 12 July 2017*, 2017.

[47] T. Fellmeth, S. Mack, J. Bartsch, D. Erath, U. Jager, R. Preu, F. Clement, and D. Biro, "20.1% efficient silicon solar cell with aluminum back surface field," *Electron Device Letters, IEEE,* vol. 32, no. 8, pp. 1101-1103, 2011, https://doi.org/10.1109/LED.2011.2157656

[48] H. Huang, J. Lv, Y. Bao, R. Xuan, S. Sun, S. Sneck, S. Li, C. Modanese, H. Savin, and A. Wang, "20.8% industrial PERC solar cell: ALD Al_2O_3 rear surface passivation, efficiency loss mechanisms analysis and roadmap to 24%," *Solar Energy Materials and Solar Cells,* vol. 161, pp. 14-30, 2017, https://doi.org/10.1016/j.solmat.2016.11.018

[49] N. Chen, and A. Ebong, "Towards 20% efficient industrial Al-BSF silicon solar cell with multiple busbars and fine gridlines," *Solar Energy Materials and Solar Cells,* vol. 146, pp. 107-113, 2016/03/01/, 2016, http://dx.doi.org/10.1016/j.solmat.2015.11.020

[50] I. Shoukry, J. Libal, R. Kopecek, E. Wefringhaus, and J. Werner, "Modelling of bifacial gain for stand-alone and in-field installed bifacial PV modules," *Energy Procedia,* vol. 92, pp. 600-608, 2016, https://doi.org/10.1016/j.egypro.2016.07.025

[51] F. Fertig, N. Wöhrle, J. Greulich, K. Krauß, E. Lohmüller, S. Meier, A. Wolf, and S. Rein, "Bifacial potential of single-and double-sided collecting silicon solar cells," *Progress in Photovoltaics: Research and Applications*, 2016, https://doi.org/10.1002/pip.2732

[52] A. Cuevas, and D. Yan, "Misconceptions and Misnomers in Solar Cells," *IEEE JOURNAL OF PHOTOVOLTAICS,* vol. 3, no. 2, pp. 8, 2013, https://doi.org/10.1109/JPHOTOV.2013.2238289

[53] A. Richter, M. Hermle, and S. W. Glunz, "Reassessment of the limiting efficiency for crystalline silicon solar cells," *Photovoltaics, IEEE Journal of,* vol. 3, no. 4, pp. 1184-1191, 2013, https://doi.org/10.1109/JPHOTOV.2013.2270351

[54] P. Würfel, and U. Würfel, *Physics of solar cells: from basic principles to advanced concepts*: John Wiley & Sons, 2016.

[55] W. Shockley, and W. T. Read, "Statistics of the Recombinations of Holes and Electrons," *Physical Review,* vol. 87, no. 5, pp. 835-842, 09/01/, 1952, https://doi.org/10.1103/PhysRev.87.835

[56] R. S. Bonilla, C. Reichel, M. Hermle, P. Hamer, and P. R. Wilshaw, "Long term stability of c-Si surface passivation using corona charged SiO_2," *Applied Surface Science,* vol. 412, pp. 657-667, 2017/08/01/, 2017, http://dx.doi.org/10.1016/j.apsusc.2017.03.204

[57] B. Vermang, E. Cornagliotti, V. Prajapati, J. John, J. Poortmans, and R. Mertens, "Assessment of the illumination dependency of Al_2O_3 and SiO_2 rear-passivated p-type silicon solar cells," *physica status solidi (RRL) – Rapid Research Letters,* vol. 6, no. 6, pp. 259-261, 2012, https://doi.org/10.1002/pssr.201206154

[58] E. A. Irene, "Models for the oxidation of silicon," *Critical Reviews in Solid State and Material Sciences,* vol. 14, no. 2, pp. 175-223, 1988, http://dx.doi.org/10.1080/10408438808242183

[59]   A. Sproul, "Dimensionless solution of the equation describing the effect of surface recombination on carrier decay in semiconductors," *Journal of Applied Physics,* vol. 76, no. 5, pp. 2851-2854, 1994, https://doi.org/10.1063/1.357521

[60]   P. P. Altermatt, F. Geelhaar, T. Trupke, X. Dai, A. Neisser, and E. Daub, "Injection dependence of spontaneous radiative recombination in c-Si: experiment, theoretical analysis, and simulation." pp. 47-48, https://doi.org/10.1109/NUSOD.2005.1518128

[61]   P. P. Altermatt, "Models for numerical device simulations of crystalline silicon solar cells—a review," *Journal of computational electronics,* vol. 10, no. 3, pp. 314, 2011, https://doi.org/10.1007/s10825-011-0367-6

[62]   A. Richter, S. W. Glunz, F. Werner, J. Schmidt, and A. Cuevas, "Improved quantitative description of Auger recombination in crystalline silicon," *Physical Review B,* vol. 86, no. 16, pp. 165202, 10/09/, 2012, https://doi.org/10.1103/PhysRevB.86.165202

[63]   A. G. Aberle, "Surface passivation of crystalline silicon solar cells: a review," *Progress in Photovoltaics: Research and Applications,* vol. 8, no. 5, pp. 473-487, 2000, https://doi.org/10.1002/1099-159X(200009/10)8:5<473::AID-PIP337>3.0.CO;2-D

[64]   R. A. Sinton, and A. Cuevas, "Contactless determination of current–voltage characteristics and minority-carrier lifetimes in semiconductors from quasi-steady-state photoconductance data," *Applied Physics Letters,* vol. 69, no. 17, pp. 2510-2512, 1996, https://doi.org/10.1063/1.117723

[65]   M. Wilson, J. Lagowski, L. Jastrzebski, A. Savtchouk, V. Faifer, D. G. Seiler, P. J. Smith, A. C. Diebold, R. McDonald, and W. M. Bullis, "COCOS (corona oxide characterization of semiconductor) non-contact metrology for gate dielectrics." pp. 220-225, https://doi.org/10.1063/1.1354401

[66]   M. Wilson, Z. Hameiri, N. Nandakumar, and S. Duttagupta, "Application of non-contact corona-Kelvin metrology for characterization of PV dielectrics on textured surfaces." pp. 0680-0685, https://doi.org/10.1109/PVSC.2014.6925012

[67]   H. Tompkins, and E. A. Irene, *Handbook of ellipsometry*: William Andrew, 2005.

[68]   G. E. Jellison, and F. A. Modine, "Parameterization of the optical functions of amorphous materials in the interband region," *Applied Physics Letters,* vol. 69, no. 3, pp. 371-373, 1996, http://dx.doi.org/10.1063/1.118064

[69]   W. Sellmeier, "Zur Erkarung der abnormen Farbenfolge im Spectrum einiger. Substanzen," *Annalen der Physik und Chemie,* vol. 219, pp. 272-282, 1871,

[70]   J. Daillant, and A. Gibaud, *X-ray and neutron reflectivity: principles and applications*: Springer, 2008.

[71]   E. Cottereau, J. Camplan, J. Chaumont, R. Meunier, and H. Bernas, "ARAMIS: An ambidextrous 2 MV accelerator for IBA and MeV implantation," *Nuclear Instruments and Methods in Physics Research Section B: Beam Interactions with Materials and Atoms,* vol. 45, no. 1-4, pp. 293-295, 1990, https://doi.org/10.1016/0168-583X(90)90838-L

[72]   J. Perrière, "Rutherford backscattering spectrometry," *Vacuum,* vol. 37, no. 5-6, pp. 429-432, 1987, https://doi.org/10.1016/0042-207X(87)90327-7

[73]   F. Schiettekatte, and M. Chicoine, "Elastic recoil detection analysis," *Characterization of Materials*, 2012, https://doi.org/10.1002/0471266965.com140

[74]   P. Zalm, "Secondary ion mass spectrometry," *Vacuum,* vol. 45, no. 6-7, pp. 753-772, 1994, https://doi.org/10.1016/0042-207X(94)90113-9

[75]   N. Colthup, *Introduction to infrared and Raman spectroscopy*: Elsevier, 2012.

[76]   T. Nishinaga, *Handbook of Crystal Growth*: Elsevier, 2015.

[77]   R. L. Puurunen, "Surface chemistry of atomic layer deposition: A case study for the trimethylaluminum/water process," *Journal of Applied Physics,* vol. 97, no. 12, pp. 121301, 2005, https://doi.org/10.1063/1.1940727

[78]   M. Juppo, A. Rahtu, M. Ritala, and M. Leskelä, "In Situ Mass Spectrometry Study on Surface Reactions in Atomic Layer Deposition of Al_2O_3 Thin Films from Trimethylaluminum and Water," *Langmuir,* vol. 16, no. 8, pp. 4034-4039, 2000/04/01, 2000, https://doi.org/10.1021/la991183+

[79]   I. Cesar, E. Granneman, P. Vermont, E. Tois, P. Manshanden, L. J. Geerligs, E. E. Bende, A. R. Burgers, A. A. Mewe, Y. Komatsu, and A. W. Weeber, "Excellent rear side passivation on multi-crystalline silicon solar cells with 20 nm uncapped Al_2O_3 layer: Industrialization of ALD for solar cell applications." pp. 000044-000049, https://doi.org/10.1109/PVSC.2010.5614176

[80]   V. Kuznetsov, E. Granneman, P. Vermont, and K. Vanormelingen, "High Throughput ALD of Al$_2$O$_3$ Layers for Surface Passivation of Silicon Solar Cells," *ECS Transactions,* vol. 33, no. 2, pp. 441-446, October 1, 2010, 2010, https://doi.org/10.1149/1.3485280

[81]   E. H. A. Granneman, V. I. Kuznetsov, and P. Vermont, "Spatial ALD, Deposition of Al$_2$O$_3$ Films at Throughputs Exceeding 3000 Wafers per Hour," *ECS Transactions,* vol. 61, no. 3, pp. 3-16, March 26, 2014, 2014, https://doi.org/10.1149/06103.0003ecst

[82]   Y. Wu, S. E. Potts, P. M. Hermkens, H. C. M. Knoops, F. Roozeboom, and W. M. M. Kessels, "Enhanced Doping Efficiency of Al-Doped ZnO by Atomic Layer Deposition Using Dimethylaluminum Isopropoxide as an Alternative Aluminum Precursor," *Chemistry of Materials,* vol. 25, no. 22, pp. 4619-4622, 2013, https://doi.org/10.1021/cm402974j

[83]   R. L. Puurunen, W. Vandervorst, W. F. Besling, O. Richard, H. Bender, T. Conard, C. Zhao, A. Delabie, M. Caymax, and S. De Gendt, "Island growth in the atomic layer deposition of zirconium oxide and aluminum oxide on hydrogen-terminated silicon: Growth mode modeling and transmission electron microscopy," *Journal of applied physics,* vol. 96, no. 9, pp. 4878-4889, 2004, https://doi.org/10.1063/1.1787624

[84]   V. Vandalon, and W. M. M. Kessels, "What is limiting low-temperature atomic layer deposition of Al$_2$O$_3$? A vibrational sum-frequency generation study," *Applied Physics Letters,* vol. 108, no. 1, pp. 011607, 2016, https://doi.org/10.1063/1.4939654

[85]   R. Wind, and S. George, "Quartz crystal microbalance studies of Al$_2$O$_3$ atomic layer deposition using trimethylaluminum and water at 125°C," *The Journal of Physical Chemistry A,* vol. 114, no. 3, pp. 1281-1289, 2009, https://doi.org/10.1021/jp9049268

[86]   J. Kim, K. Chakrabarti, J. Lee, K.-Y. Oh, and C. Lee, "Effects of ozone as an oxygen source on the properties of the Al$_2$O$_3$ thin films prepared by atomic layer deposition," *Materials Chemistry and Physics,* vol. 78, no. 3, pp. 733-738, 2/28/, 2003, http://dx.doi.org/10.1016/S0254-0584(02)00375-9

[87]   D. N. Goldstein, J. A. McCormick, and S. M. George, "Al$_2$O$_3$ Atomic Layer Deposition with Trimethylaluminum and Ozone Studied by in Situ Transmission FTIR Spectroscopy and Quadrupole Mass Spectrometry," *The Journal of Physical Chemistry C,* vol. 112, no. 49, pp. 19530-19539, 2008/12/11, 2008, https://doi.org/10.1021/jp804296a

[88]   P. Repo, H. Talvitie, S. Li, J. Skarp, and H. Savin, "Silicon Surface Passivation by Al$_2$O$_3$: Effect of ALD Reactants," *Energy Procedia,* vol. 8, pp. 681-687, 2011, http://doi.org/10.1016/j.egypro.2011.06.201

[89]   G. von Gastrow, S. Li, P. Repo, Y. Bao, M. Putkonen, and H. Savin, "Ozone-based Batch Atomic Layer Deposited Al$_2$O$_3$ for Effective Surface Passivation," *Energy Procedia,* vol. 38, no. 0, pp. 890-894, //, 2013, http://dx.doi.org/10.1016/j.egypro.2013.07.361

[90]   S.-K. Oh, H.-S. Shin, K.-S. Jeong, M. Li, H. Lee, K. Han, Y. Lee, G.-W. Lee, and H.-D. Lee, "A Novel Atomic Layer Deposited Al$_2$O$_3$ Film with Diluted NH$_4$OH for High-Efficient c-Si Solar Cell," *JSTS:Journal of Semiconductor Technology and Science,* vol. 14, no. 1, pp. 40-47, 2014, https://doi.org/10.5573/jsts.2014.14.1.040

[91]   S. B. S. Heil, J. L. van Hemmen, M. C. M. van de Sanden, and W. M. M. Kessels, "Reaction mechanisms during plasma-assisted atomic layer deposition of metal oxides: A case study for Al$_2$O$_3$," *Journal of Applied Physics,* vol. 103, no. 10, pp. 103302, 2008, http://dx.doi.org/10.1063/1.2924406

[92]   R. L. Puurunen, M. Lindblad, A. Root, and A. O. I. Krause, "Successive reactions of gaseous trimethylaluminium and ammonia on porous alumina," *Physical Chemistry Chemical Physics,* vol. 3, no. 6, pp. 1093-1102, 2001, https://doi.org/10.1039/B007249O

[93]   S. D. Elliott, and J. C. Greer, "Simulating the atomic layer deposition of alumina from first principles," *Journal of Materials Chemistry,* vol. 14, no. 21, pp. 3246-3250, 2004, https://doi.org/10.1039/B405776G

[94]   J.-M. Lin, A. V. Teplyakov, and J. C. F. Rodríguez-Reyes, "Competing reactions during metalorganic deposition: Ligand-exchange versus direct reaction with the substrate surface," *Journal of Vacuum Science & Technology A: Vacuum, Surfaces, and Films,* vol. 31, no. 2, pp. 021401, 2013, https://doi.org/10.1116/1.4774031

[95]   Z. Hu, J. Shi, and C. Heath Turner, "Molecular dynamics simulation of the Al$_2$O$_3$ film structure during atomic layer deposition," *Molecular Simulation,* vol. 35, no. 4, pp. 270-279, 2009, https://doi.org/10.1080/08927020802468372

[96]   P. J. Caplan, J. N. Helbert, B. E. Wagner, and E. H. Poindexter, "Paramagnetic defects in silicon/silicon dioxide systems," *Surface Science,* vol. 54, no. 1, pp. 33-42, 1976/01/01, 1976, http://dx.doi.org/10.1016/0039-6028(76)90085-6

[97]   J. Penaud, P. Jaffrennou, A. Rothschild, and B. Lombardet, "Impact of surface preparation prior to Al_2O_3 deposition for i-PERC cells." pp. 001083-001088, https://doi.org/10.1109/PVSC.2012.6317791

[98]   H. Goverde, B. Vermang, A. Morato, J. John, J. Horzel, G. Meneghesso, and J. Poortmans, "Al_2O_3 Surface Passivation Characterized on Hydrophobic and Hydrophilic c-Si by a Combination of QSSPC, CV, XPS and FTIR," *Energy Procedia,* vol. 27, pp. 355-360, 2012, https://doi.org/10.1016/j.egypro.2012.07.076

[99]   S. Bordihn, P. Engelhart, V. Mertens, G. Kesser, D. Köhn, G. Dingemans, M. M. Mandoc, J. W. Müller, and W. M. M. Kessels, "High surface passivation quality and thermal stability of ALD Al_2O_3 on wet chemical grown ultra-thin SiO_2 on silicon," *Energy Procedia,* vol. 8, pp. 654-659, 2011, https://doi.org/10.1016/j.egypro.2011.06.197

[100]   O. Renault, L. G. Gosset, D. Rouchon, and A. Ermolieff, "Angle-resolved x-ray photoelectron spectroscopy of ultrathin Al2O3 films grown by atomic layer deposition," *Journal of Vacuum Science & Technology A: Vacuum, Surfaces, and Films,* vol. 20, no. 6, pp. 1867-1876, 2002, https://doi.org/10.1116/1.1507330

[101]   Y. Bao, S. Li, G. von Gastrow, P. Repo, H. Savin, and M. Putkonen, "Effect of substrate pretreatments on the atomic layer deposited Al_2O_3 passivation quality," *Journal of Vacuum Science & Technology A: Vacuum, Surfaces, and Films,* vol. 33, no. 1, pp. 01A123, 2015, https://doi.org/10.1116/1.4901456

[102]   T. Takahagi, A. Ishitani, H. Kuroda, Y. Nagasawa, H. Ito, and S. Wakao, "Control of the chemical reactivity of a silicon single-crystal surface using the chemical modification technique," *Journal of Applied Physics,* vol. 68, no. 5, pp. 2187-2191, 1990, https://doi.org/10.1063/1.346521

[103]   K. A. Perrine, and A. V. Teplyakov, "Reactivity of selectively terminated single crystal silicon surfaces," *Chemical Society Reviews,* vol. 39, no. 8, pp. 3256-3274, 2010, https://doi.org/10.1039/B822965C

[104]   Y. B. Kim, M. Tuominen, I. Raaijmakers, R. de Blank, R. Wilhelm, and S. Haukka, "Initial stage of the ultrathin oxide growth in water vapor on Si (100) surface," *Electrochemical and Solid-State Letters,* vol. 3, no. 7, pp. 346-349, 2000, https://doi.org/10.1149/1.1391145

[105]   D. W. Squire, C. S. Dulcey, and M. C. Lin, "Mechanistic studies of the decomposition of trimethylaluminum on heated surfaces," *Journal of Vacuum Science & Technology B: Microelectronics Processing and Phenomena,* vol. 3, no. 5, pp. 1513-1519, 1985, https://doi.org/10.1116/1.582976

[106]   V. Naumann, M. Otto, R. B. Wehrspohn, and C. Hagendorf, "Chemical and structural study of electrically passivating Al_2O_3/Si interfaces prepared by atomic layer deposition," *Journal of Vacuum Science & Technology A,* vol. 30, no. 4, pp. 04D106, 2012, http://dx.doi.org/10.1116/1.4704601

[107]   B. Hoex, M. Bosman, N. Nandakumar, and W. M. M. Kessels, "Silicon surface passivation by aluminium oxide studied with electron energy loss spectroscopy," *physica status solidi (RRL) – Rapid Research Letters,* vol. 7, no. 11, pp. 937-941, 2013, https://doi.org/10.1002/pssr.201308081

[108]   D. Suh, and W. S. Liang, "Electrical properties of atomic layer deposited Al_2O_3 with anneal temperature for surface passivation," *Thin Solid Films,* vol. 539, no. 0, pp. 309-316, 7/31/, 2013, http://dx.doi.org/10.1016/j.tsf.2013.05.082

[109]   G. Dingemans, N. M. Terlinden, D. Pierreux, H. B. Profijt, M. C. M. van de Sanden, and W. M. M. Kessels, "Influence of the Oxidant on the Chemical and Field-Effect Passivation of Si by ALD Al_2O_3," *Electrochemical and Solid-State Letters,* vol. 14, no. 1, pp. H1-H4, January 1, 2011, 2011, https://doi.org/10.1149/1.3501970

[110]   M. Morita, T. Ohmi, E. Hasegawa, M. Kawakami, and M. Ohwada, "Growth of native oxide on a silicon surface," *Journal of Applied Physics,* vol. 68, no. 3, pp. 1272-1281, 1990, https://doi.org/10.1063/1.347181

[111]   N. Awaji, Y. Sugita, T. Nakanishi, S. Ohkubo, K. Takasaki, and S. Komiya, "High-precision x-ray reflectivity study of ultrathin SiO_2 on Si," *Journal of Vacuum Science & Technology A: Vacuum, Surfaces, and Films,* vol. 14, no. 3, pp. 971-976, 1996, https://doi.org/10.1116/1.580424

[112]   S. Iwata, and A. Ishizaka, "Electron spectroscopic analysis of the SiO_2/Si system and correlation with metal–oxide–semiconductor device characteristics," *Journal of Applied Physics,* vol. 79, no. 9, pp. 6653-6713, 1996, https://doi.org/10.1063/1.362676

[113]   J. J. Fitzgerald, G. Piedra, S. F. Dec, M. Seger, and G. E. Maciel, "Dehydration studies of a high-surface-area alumina (pseudo-boehmite) using solid-state ^1H and ^{27}Al NMR," *Journal of the American Chemical Society,* vol. 119, no. 33, pp. 7832-7842, 1997, https://doi.org/10.1021/ja970788u

[114]   S. J. Yun, K.-H. Lee, J. Skarp, H.-R. Kim, and K.-S. Nam, "Dependence of atomic layer-deposited Al_2O_3 films characteristics on growth temperature and Al precursors of $Al(CH_3)_3$ and $AlCl_3$," *Journal of Vacuum Science & Technology A: Vacuum, Surfaces, and Films,* vol. 15, no. 6, pp. 2993-2997, 1997, https://doi.org/10.1116/1.580895

[115]   L. Zhang, H. Jiang, C. Liu, J. Dong, and P. Chow, "Annealing of Al_2O_3 thin films prepared by atomic layer deposition," *Journal of Physics D: Applied Physics,* vol. 40, no. 12, pp. 3707, 2007, https://doi.org/10.1088/0022-3727/40/12/025

[116]   V. Afanas' Ev, A. Stesmans, B. Mrstik, and C. Zhao, "Impact of annealing-induced compaction on electronic properties of atomic-layer-deposited Al_2O_3," *Applied Physics Letters,* vol. 81, no. 9, pp. 1678-1680, 2002, https://doi.org/10.1063/1.1501163

[117]   C. M. Tanner, M. F. Toney, J. Lu, H.-O. Blom, M. Sawkar-Mathur, M. A. Tafesse, and J. P. Chang, "Engineering epitaxial γ-Al_2O_3 gate dielectric films on 4H-SiC," *Journal of Applied Physics,* vol. 102, no. 10, pp. 104112, 2007, https://doi.org/10.1063/1.2812609

[118]   S. Jakschik, U. Schroeder, T. Hecht, M. Gutsche, H. Seidl, and J. W. Bartha, "Crystallization behavior of thin ALD-Al_2O_3 films," *Thin Solid Films,* vol. 425, no. 1, pp. 216-220, 2003, https://doi.org/10.1016/S0040-6090(02)01262-2

[119]   I. Levin, and D. Brandon, "Metastable alumina polymorphs: crystal structures and transition sequences," *Journal of the American Ceramic Society,* vol. 81, no. 8, pp. 1995-2012, 1998, https://doi.org/10.1111/j.1151-2916.1998.tb02581.x

[120]   C. Pecharroman, I. Sobrados, J. Iglesias, T. Gonzalez-Carreno, and J. Sanz, "Thermal evolution of transitional aluminas followed by NMR and IR spectroscopies," *The Journal of Physical Chemistry B,* vol. 103, no. 30, pp. 6160-6170, 1999, https://doi.org/10.1021/jp983316q

[121]   S. K. Lee, S. Y. Park, Y. S. Yi, and J. Moon, "Structure and Disorder in Amorphous Alumina Thin Films: Insights from High-Resolution Solid-State NMR," *The Journal of Physical Chemistry C,* vol. 114, no. 32, pp. 13890-13894, 2010, https://doi.org/10.1021/jp105306r

[122]   G. Pourtois, K. Sankaran, I. Radu, R. Degraeve, M. B. Zahid, S. Van Elshocht, C. Adelmann, S. De Gendt, M. M. Heyns, D. J. Wouters, J. A. Kittl, M. Jurczak, G.-M. Rignanese, and J. Van Houdt, "First-Principles Investigation of High-k Dielectrics for Nonvolatile Memories," *Meeting Abstracts,* vol. MA2010-02, no. 22, pp. 1521, July 8, 2010, 2010, https://doi.org/10.1149/1.3481628

[123]   V. Cimalla, M. Baeumler, L. Kirste, M. Prescher, B. Christian, T. Passow, F. Benkhelifa, F. Bernhardt, G. Eichapfel, and M. Himmerlich, "Densification of thin aluminum oxide films by thermal treatments," *Materials Sciences and Applications,* vol. 5, no. 08, pp. 628, 2014, http://dx.doi.org/10.4236/msa.2014.58065

[124]   L. Gosset, J.-F. Damlencourt, O. Renault, D. Rouchon, P. Holliger, A. Ermolieff, I. Trimaille, J.-J. Ganem, F. Martin, and M.-N. Semeria, "Interface and material characterization of thin Al_2O_3 layers deposited by ALD using TMA/H_2O," *Journal of Non-Crystalline Solids,* vol. 303, no. 1, pp. 17-23, 2002, https://doi.org/10.1016/S0022-3093(02)00958-4

[125]   S.-K. Oh, H.-S. Shin, K.-S. Jeong, M. Li, H. Lee, K. Han, Y. Lee, G.-W. Lee, and H.-D. Lee, "Process Temperature Dependence of Al_2O_3 Film Deposited by Thermal ALD as a Passivation Layer for c-Si Solar Cells," *JSTS:Journal of Semiconductor Technology and Science,* vol. 13, no. 6, pp. 581-588, 2013, https://doi.org/10.5573/jsts.2013.13.6.581

[126]   P. Snijders, L. Jeurgens, and W. Sloof, "Structural ordering of ultra-thin, amorphous aluminium-oxide films," *Surface science,* vol. 589, no. 1, pp. 98-105, 2005, https://doi.org/10.1016/j.susc.2005.05.051

[127]   R. Matero, A. Rahtu, M. Ritala, M. Leskelä, and T. Sajavaara, "Effect of water dose on the atomic layer deposition rate of oxide thin films," *Thin Solid Films,* vol. 368, no. 1, pp. 1-7, 6/1/, 2000, http://dx.doi.org/10.1016/S0040-6090(00)00890-7

[128] J. Schmidt, and A. Cuevas, "Electronic properties of light-induced recombination centers in boron-doped Czochralski silicon," *Journal of Applied Physics,* vol. 86, no. 6, pp. 3175-3180, 1999, https://doi.org/10.1063/1.371186

[129] D. Macdonald, F. Rougieux, A. Cuevas, B. Lim, J. Schmidt, M. Di Sabatino, and L. Geerligs, "Light-induced boron-oxygen defect generation in compensated p-type Czochralski silicon," *Journal of Applied Physics,* vol. 105, no. 9, pp. 093704, 2009, https://doi.org/10.1063/1.3121208

[130] P. Heitjans, and J. Kärger, *Diffusion in condensed matter: methods, materials, models*: Springer Science & Business Media, 2006.

[131] P. Altermatt, F. Geelhaar, T. Trupke, X. Dai, A. Neisser, and E. Daub, "Injection dependence of spontaneous radiative recombination in crystalline silicon: Experimental verification and theoretical analysis," *Applied physics letters,* vol. 88, no. 26, pp. 261901, 2006, https://doi.org/10.1063/1.2218041

[132] F. Werner, A. Cosceev, and J. Schmidt, "Interface recombination parameters of atomic-layer-deposited Al_2O_3 on crystalline silicon," *Journal of Applied Physics,* vol. 111, no. 7, pp. 073710, 2012, http://dx.doi.org/10.1063/1.3700241

[133] Y. Liu, L. Zhu, L. Guo, H. Zhang, and H. Xiao, "Surface Passivation Performance of Atomic-Layer-Deposited Al_2O_3 on p-type Silicon Substrates," *Journal of Materials Science & Technology,* vol. 30, no. 8, pp. 835-838, 8//, 2014, http://dx.doi.org/10.1016/j.jmst.2013.12.005

[134] R. Kotipalli, R. Delamare, O. Poncelet, X. Tang, L. Francis, and D. Flandre, "Passivation effects of atomic-layer-deposited aluminum oxide," *EPJ Photovoltaics,* vol. 4, pp. 45107, 2013, https://doi.org/10.1051/epjpv/2013023

[135] L. E. Black, T. Allen, K. R. McIntosh, and A. Cuevas, "Effect of boron concentration on recombination at the p-Si–Al_2O_3 interface," *Journal of Applied Physics,* vol. 115, no. 9, pp. -, 2014, http://dx.doi.org/10.1063/1.4867643

[136] B. Liao, R. Stangl, F. Ma, T. Mueller, F. Lin, A. G. Aberle, C. S. Bhatia, and B. Hoex, "Excellent c -Si surface passivation by thermal atomic layer deposited aluminum oxide after industrial firing activation," *Journal of Physics D: Applied Physics,* vol. 46, no. 38, pp. 385102, 2013, https://doi.org/10.1088/0022-3727/46/38/385102

[137] L. Q. Zhu, H. Xiao, and Y. H. Liu, "Surface passivation and antireflectance performances for atomic-layer-deposited Al_2O_3 films," *Materials Research Express,* vol. 1, no. 4, pp. 046406, 2014, https://doi.org/10.1088/2053-1591/1/4/046406

[138] E. Simoen, A. Rothschild, B. Vermang, J. Poortmans, and R. Mertens, "A Deep-Level Transient Spectroscopy Comparison of the SiO_2/Si and Al_2O_3/Si Interface States," *ECS Transactions,* vol. 41, no. 4, pp. 37-44, October 4, 2011, 2011, https://doi.org/10.1149/1.3628607

[139] B. J. Jones, and R. C. Barklie, "Electron paramagnetic resonance evaluation of defects at the (100)Si/Al_2O_3 interface," *Journal of Physics D: Applied Physics,* vol. 38, no. 8, pp. 1178, 2005, https://doi.org/10.1088/0022-3727/38/8/013

[140] J. Cantin, and H. Von Bardeleben, "An electron paramagnetic resonance study of the Si (100)/Al_2O_3 interface defects," *Journal of non-crystalline solids,* vol. 303, no. 1, pp. 175-178, 2002, https://doi.org/10.1016/S0022-3093(02)00981-X

[141] A. Stesmans, and V. V. Afanas'ev, "Electron spin resonance observation of Si dangling-bond-type defects at the interface of (100) Si with ultrathin layers of SiOx , Al_2O_3 and ZrO_2," *Journal of Physics: Condensed Matter,* vol. 13, no. 28, pp. L673, 2001, https://doi.org/10.1088/0953-8984/13/28/103

[142] A. Stesmans, B. Nouwen, and V. V. Afanas'ev, "P_{b1} interface defect in thermal (100)Si/SiO_2: ^{29}Si hyperfine interaction," *Physical Review B,* vol. 58, no. 23, pp. 15801-15809, 12/15/, 1998, https://doi.org/10.1103/PhysRevB.58.15801

[143] A. Stesmans, "Interaction of P_b defects at the (111)Si/SiO_2 interface with molecular hydrogen: Simultaneous action of passivation and dissociation," *Journal of Applied Physics,* vol. 88, no. 1, pp. 489, 2000, https://doi.org/10.1063/1.373684

[144] F. Kersten, A. Schmid, S. Bordihn, J. W. Müller, and J. Heitmann, "Role of Annealing Conditions on Surface Passivation Properties of ALD Al_2O_3 Films," *Energy Procedia,* vol. 38, pp. 843-848, 2013, https://doi.org/10.1016/j.egypro.2013.07.354

[145] O. Sneh, and S. M. George, "Thermal stability of hydroxyl groups on a well-defined silica surface," *The Journal of physical chemistry,* vol. 99, no. 13, pp. 4639-4647, 1995, https://doi.org/10.1021/j100013a039

[146] L. Zhuravlev, "The surface chemistry of amorphous silica. Zhuravlev model," *Colloids and Surfaces A: Physicochemical and Engineering Aspects,* vol. 173, no. 1, pp. 1-38, 2000, https://doi.org/10.1016/S0927-7757(00)00556-2

[147] X. Liu, "DRIFTS study of surface of γ-alumina and its dehydroxylation," *The Journal of Physical Chemistry C,* vol. 112, no. 13, pp. 5066-5073, 2008, https://doi.org/10.1021/jp711901s

[148] X. Krokidis, P. Raybaud, A.-E. Gobichon, B. Rebours, P. Euzen, and H. Toulhoat, "Theoretical study of the dehydration process of boehmite to γ-alumina," *The Journal of Physical Chemistry B,* vol. 105, no. 22, pp. 5121-5130, 2001, https://doi.org/10.1021/jp0038310

[149] Y. Ogata, H. Niki, T. Sakka, and M. Iwasaki, "Oxidation of porous silicon under water vapor environment," *Journal of The Electrochemical Society,* vol. 142, no. 5, pp. 1595-1601, 1995, https://doi.org/10.1149/1.2048619

[150] V. Misra, G. Lucovsky, and G. Parsons, "Issues in High-κ Gate Stack Interfaces," *MRS bulletin,* vol. 27, no. 3, pp. 212-216, 2002, https://doi.org/10.1557/mrs2002.73

[151] G. Seguini, E. Cianci, C. Wiemer, D. Saynova, J. A. M. van Roosmalen, and M. Perego, "Si surface passivation by Al_2O_3 thin films deposited using a low thermal budget atomic layer deposition process," *Applied Physics Letters,* vol. 102, no. 13, pp. 131603, 2013, http://dx.doi.org/10.1063/1.4800541

[152] F. Werner, B. Veith, D. Zielke, L. Kühnemund, C. Tegenkamp, M. Seibt, R. Brendel, and J. Schmidt, "Electronic and chemical properties of the c-Si/Al_2O_3 interface," *Journal of Applied Physics,* vol. 109, no. 11, pp. 113701, 2011, http://dx.doi.org/10.1063/1.3587227

[153] B. Vermang, H. Goverde, V. Simons, I. De Wolf, J. Meersschaut, S. Tanaka, J. John, J. Poortmans, and R. Mertens, "A study of blister formation in ALD Al_2O_3 grown on silicon." pp. 001135-001138, https://doi.org/10.1109/PVSC.2012.6317802

[154] G. Dingemans, F. Einsele, W. Beyer, M. C. M. van de Sanden, and W. M. M. Kessels, "Influence of annealing and Al_2O_3 properties on the hydrogen-induced passivation of the Si/SiO_2 interface," *Journal of Applied Physics,* vol. 111, no. 9, pp. -, 2012, http://dx.doi.org/10.1063/1.4709729

[155] Z. Y. Deng, J. M. Ferreira, Y. Tanaka, and J. Ye, "Physicochemical Mechanism for the Continuous Reaction of γ-Al_2O_3-Modified Aluminum Powder with Water," *Journal of the American Ceramic Society,* vol. 90, no. 5, pp. 1521-1526, 2007, https://doi.org/10.1111/j.1551-2916.2007.01546.x

[156] W. S. Yang, Y. K. Kim, S.-Y. Yang, J. H. Choi, H. S. Park, S. I. Lee, and J.-B. Yoo, "Effect of SiO_2 intermediate layer on Al_2O_3/SiO 2/n^+-poly Si interface deposited using atomic layer deposition (ALD) for deep submicron device applications," *Surface and coatings technology,* vol. 131, no. 1, pp. 79-83, 2000, https://doi.org/10.1016/S0257-8972(00)00763-5

[157] S. Jakschik, U. Schroeder, T. Hecht, D. Krueger, G. Dollinger, A. Bergmaier, C. Luhmann, and J. W. Bartha, "Physical characterization of thin ALD–Al_2O_3 films," *Applied Surface Science,* vol. 211, no. 1–4, pp. 352-359, 4/30/, 2003, http://dx.doi.org/10.1016/S0169-4332(03)00264-2

[158] J. B. Kim, D. R. Kwon, K. Chakrabarti, C. Lee, K. Y. Oh, and J. H. Lee, "Improvement in Al_2O_3 dielectric behavior by using ozone as an oxidant for the atomic layer deposition technique," *Journal of Applied Physics,* vol. 92, no. 11, pp. 6739, 2002, https://doi.org/10.1063/1.1515951

[159] M. Chandra, and Q. Xu, "Room temperature hydrogen generation from aqueous ammonia-borane using noble metal nano-clusters as highly active catalysts," *Journal of Power Sources,* vol. 168, no. 1, pp. 135-142, 2007, https://doi.org/10.1016/j.jpowsour.2007.03.015

[160] B. Lippens, and J. De Boer, "Study of phase transformations during calcination of aluminum hydroxides by selected area electron diffraction," *Acta Crystallographica,* vol. 17, no. 10, pp. 1312-1321, 1964, https://doi.org/10.1107/S0365110X64003267

[161] T. H. Ballinger, and J. T. Yates Jr, "IR spectroscopic detection of Lewis acid sites on alumina using adsorbed carbon monoxide. Correlation with aluminum-hydroxyl group removal," *Langmuir,* vol. 7, no. 12, pp. 3041-3045, 1991, https://doi.org/10.1021/la00060a022

[162] M. Caldararu, G. Postole, C. Hornoiu, V. Bratan, M. Dragan, and N. Ionescu, "Electrical conductivity of γ-Al_2O_3 at atmospheric pressure under dehydrating/hydrating conditions," *Applied surface science,* vol. 181, no. 3, pp. 255-264, 2001, https://doi.org/10.1016/S0169-4332(01)00393-2

[163] K.-D. Kreuer, "Proton conductivity: materials and applications," *Chemistry of Materials,* vol. 8, no. 3, pp. 610-641, 1996, https://doi.org/10.1021/cm950192a

[164] K. Sohlberg, S. J. Pennycook, and S. T. Pantelides, "Hydrogen and the structure of the transition aluminas," *Journal of the American Chemical Society,* vol. 121, no. 33, pp. 7493-7499, 1999, https://doi.org/10.1021/ja991098o

[165] Y.-H. Lu, and H.-T. Chen, "Hydrogen generation by the reaction of H_2O with Al_2O_3-based materials: a computational analysis," *Physical Chemistry Chemical Physics,* vol. 17, no. 10, pp. 6834-6843, 2015, https://doi.org/10.1039/C4CP05789A

[166] R. Wischert, P. Laurent, C. Copéret, F. o. Delbecq, and P. Sautet, "γ-Alumina: the essential and unexpected role of water for the structure, stability, and reactivity of "defect" sites," *Journal of the American Chemical Society,* vol. 134, no. 35, pp. 14430-14449, 2012, https://doi.org/10.1021/ja3042383

[167] J. Van den Brand, P. Snijders, W. Sloof, H. Terryn, and J. De Wit, "Acid− base characterization of aluminum oxide surfaces with XPS," *The Journal of Physical Chemistry B,* vol. 108, no. 19, pp. 6017-6024, 2004, https://doi.org/10.1021/jp037877f

[168] B. Xu, C. Sievers, J. A. Lercher, J. R. Van Veen, P. Giltay, R. Prins, and J. A. Van Bokhoven, "Strong Brønsted acidity in amorphous silica− aluminas," *The Journal of Physical Chemistry C,* vol. 111, no. 32, pp. 12075-12079, 2007, https://doi.org/10.1021/jp073677i

[169] M. Caillot, A. Chaumonnot, M. Digne, and J. A. Van Bokhoven, "The variety of Brønsted acid sites in amorphous aluminosilicates and zeolites," *Journal of Catalysis,* vol. 316, pp. 47-56, 2014, https://doi.org/10.1016/j.jcat.2014.05.002

[170] M. Valla, A. J. Rossini, M. Caillot, C. l. Chizallet, P. Raybaud, M. Digne, A. Chaumonnot, A. Lesage, L. Emsley, and J. A. Van Bokhoven, "Atomic description of the interface between silica and alumina in aluminosilicates through dynamic nuclear polarization surface-enhanced nmr spectroscopy and first-principles calculations," *Journal of the American Chemical Society,* vol. 137, no. 33, pp. 10710-10719, 2015, https://doi.org/10.1021/jacs.5b06134

[171] E. M. Stolper, and T. J. Ahrens, "On the nature of pressure-induced coordination changes in silicate melts and glasses," *Geophysical Research Letters,* vol. 14, no. 12, pp. 1231-1233, 1987, https://doi.org/10.1029/GL014i012p01231

[172] G. Dingemans, W. Beyer, M. C. M. van de Sanden, and W. M. M. Kessels, "Hydrogen induced passivation of Si interfaces by Al_2O_3 films and SiO_2/Al_2O_3 stacks," *Applied Physics Letters,* vol. 97, no. 15, pp. 152106, 2010, http://dx.doi.org/10.1063/1.3497014

[173] J. Frascaroli, G. Seguini, E. Cianci, D. Saynova, J. van Roosmalen, and M. Perego, "Surface passivation for ultrathin Al_2O_3 layers grown at low temperature by thermal atomic layer deposition," *physica status solidi (a),* vol. 210, no. 4, pp. 732-736, 2013, https://doi.org/10.1002/pssa.201200568

[174] D. S. Saynova, G. J. M. Janssen, A. R. Burgers, A. A. Mewe, E. Cianci, G. Seguini, and M. Perego, "Al_2O_3 Passivation on c-si Surfaces for Low Temperature Solar Cell Applications," *Energy Procedia,* vol. 38, no. 0, pp. 872-880, //, 2013, http://dx.doi.org/10.1016/j.egypro.2013.07.359

[175] B. Hoex, J. J. H. Gielis, M. C. M. van de Sanden, and W. M. M. Kessels, "On the c-Si surface passivation mechanism by the negative-charge-dielectric Al_2O_3," *Journal of Applied Physics,* vol. 104, no. 11, pp. -, 2008, http://dx.doi.org/10.1063/1.3021091

[176] S. Kühnhold-Pospischil, P. Saint-Cast, A. Richter, and M. Hofmann, "Activation energy of negative fixed charges in thermal ALD Al_2O_3," *Applied Physics Letters,* vol. 109, no. 6, pp. 061602, 2016, https://doi.org/10.1063/1.4960097

[177] N. M. Terlinden, G. Dingemans, M. C. M. van de Sanden, and W. M. M. Kessels, "Role of field-effect on c-Si surface passivation by ultrathin (2–20 nm) atomic layer deposited Al_2O_3," *Applied Physics Letters,* vol. 96, no. 11, pp. 112101, 2010, http://dx.doi.org/10.1063/1.3334729

[178] D. K. Simon, P. M. Jordan, T. Mikolajick, and I. Dirnstorfer, "On the Control of the Fixed Charge Densities in Al_2O_3-Based Silicon Surface Passivation Schemes," *ACS Appl Mater Interfaces,* vol. 7, no. 51, pp. 28215-22, Dec 30, 2015, https://doi.org/10.1021/acsami.5b06606

[179] N. Satoh, I. Cesar, M. Lamers, I. Romijn, K. Bakker, C. Olson, D. O. Saynova, Y. Komatsu, A. Weeber, F. Verbakel, and M. Wiggers, "Energy Band Diagram near the Interface of Aluminum Oxide on p-Si Fabricated by Atomic Layer Deposition without/with Rapid Thermal Cycle Annealing Determined by Capacitance-Voltage Measurements," *e-Journal of Surface Science and Nanotechnology,* vol. 10, pp. 22-28, 2012, https://doi.org/10.1380/ejssnt.2012.22

[180] K. Kimoto, Y. Matsui, T. Nabatame, T. Yasuda, T. Mizoguchi, I. Tanaka, and A. Toriumi, "Coordination and interface analysis of atomic-layer-deposition Al_2O_3 on Si (001) using energy-loss near-edge structures," *Applied physics letters,* vol. 83, pp. 4306, 2003, https://doi.org/10.1063/1.1629397

[181] S. Kühnhold, P. Saint-Cast, B. Kafle, M. Hofmann, F. Colonna, and M. Zacharias, "High-temperature degradation in plasma-enhanced chemical vapor deposition Al_2O_3 surface passivation layers on crystalline silicon," *Journal of Applied Physics,* vol. 116, no. 5, pp. -, 2014, http://dx.doi.org/10.1063/1.4891634

[182] R. S. Johnson, G. Lucovsky, and I. Baumvol, "Physical and electrical properties of noncrystalline Al_2O_3 prepared by remote plasma enhanced chemical vapor deposition," *Journal of Vacuum Science & Technology A: Vacuum, Surfaces, and Films,* vol. 19, no. 4, pp. 1353-1360, 2001, https://doi.org/10.1116/1.1379316

[183] N. Corporation. "www.newport.com."

[184] G. ASTM, "173-03," *Standard Tables for Reference Solar Spectral Irradiances: Direct Normal and Hemispherical on 37o Tilted Surface*, 2012,

[185] M. A. Green, "Self-consistent optical parameters of intrinsic silicon at 300K including temperature coefficients," *Solar Energy Materials and Solar Cells,* vol. 92, no. 11, pp. 1305-1310, 2008/11/01/, 2008, http://dx.doi.org/10.1016/j.solmat.2008.06.009

[186] C. De Izarra, and J.-M. Gitton, "Calibration and temperature profile of a tungsten filament lamp," *European Journal of Physics,* vol. 31, no. 4, pp. 933, 2010, https://doi.org/10.1088/0143-0807/31/4/022

[187] P. M. Jordan, D. K. Simon, T. Mikolajick, and I. Dirnstorfer, "Trapped charge densities in Al_2O_3-based silicon surface passivation layers," *Journal of Applied Physics,* vol. 119, no. 21, pp. 215306, 2016, https://doi.org/10.1063/1.4953141

[188] D. Liu, and J. Robertson, "Oxygen vacancy levels and interfaces of Al 2 O 3," *Microelectronic Engineering,* vol. 86, no. 7, pp. 1668-1671, 2009,

[189] Y. Liu, P. Stradins, H. Deng, J. Luo, and S.-H. Wei, "Suppress carrier recombination by introducing defects: The case of Si solar cell," *Applied Physics Letters,* vol. 108, no. 2, pp. 022101, 2016, https://doi.org/10.1063/1.4939628

[190] X. Cheng, P. Repo, H. Halvard, A. P. Perros, E. S. Marstein, M. Di Sabatino, and H. Savin, "Surface Passivation Properties of HfO_2 Thin Film on n-Type Crystalline Si," *IEEE Journal of Photovoltaics,* vol. 7, no. 2, pp. 479-485, 2017, https://doi.org/10.1109/JPHOTOV.2016.2645399

[191] A. F. Thomson, and K. R. McIntosh, "Light-enhanced surface passivation of TiO_2-coated silicon," *Progress in Photovoltaics: Research and Applications,* vol. 20, no. 3, pp. 343-349, 2012, https://doi.org/10.1002/pip.1132

[192] S. Kühnhold-Pospischil, P. Saint-Cast, M. Hofmann, S. Weber, P. Jakes, R.-A. Eichel, and J. Granwehr, "A study on Si/Al $_2O_3$ paramagnetic point defects," *Journal of Applied Physics,* vol. 120, no. 19, pp. 195304, 2016, https://doi.org/10.1063/1.4967919

[193] D. Liu, S. Clark, and J. Robertson, "Oxygen vacancy levels and electron transport in Al_2O_3," *Applied physics letters,* vol. 96, no. 3, pp. 032905, 2010, https://doi.org/10.1063/1.3293440

[194] L. Masoero, P. Blaise, G. Molas, J. Colonna, M. Gély, J. Barnes, G. Ghibaudo, and B. De Salvo, "Defects-induced gap states in hydrogenated γ-alumina used as blocking layer for non-volatile memories," *Microelectronic Engineering,* vol. 88, no. 7, pp. 1448-1451, 2011, https://doi.org/10.1016/j.mee.2011.03.029

[195] M. B. Zahid, D. R. Aguado, R. Degraeve, W.-C. Wang, B. Govoreanu, M. Toledano-Luque, V. Afanasev, and J. Van Houdt, "Applying Complementary Trap Characterization Technique to Crystalline-Phase-for Improved Understanding of Nonvolatile Memory Operation and Reliability," *IEEE Transactions on Electron Devices,* vol. 57, no. 11, pp. 2907-2916, 2010, https://doi.org/10.1109/TED.2010.2071071

[196] G. Dingemans, N. M. Terlinden, M. A. Verheijen, M. C. M. van de Sanden, and W. M. M. Kessels, "Controlling the fixed charge and passivation properties of $Si(100)/Al_2O_3$ interfaces using ultrathin SiO_2 interlayers synthesized by atomic layer deposition," *Journal of Applied Physics,* vol. 110, no. 9, pp. -, 2011, http://dx.doi.org/10.1063/1.3658246

[197]   N. M. Terlinden, G. Dingemans, V. Vandalon, R. H. E. C. Bosch, and W. M. M. Kessels, "Influence of the SiO_2 interlayer thickness on the density and polarity of charges in $Si/SiO_2/Al_2O_3$ stacks as studied by optical second-harmonic generation," *Journal of Applied Physics,* vol. 115, no. 3, pp. 033708, 2014, https://doi.org/10.1063/1.4857075

[198]   F. Werner, and J. Schmidt, "Manipulating the negative fixed charge density at the $c-Si/Al_2O_3$ interface," *Applied Physics Letters,* vol. 104, no. 9, pp. 091604, 2014, https://doi.org/10.1063/1.4867652

[199]   J. A. Töfflinger, A. Laades, L. Korte, C. Leendertz, L. M. Montañez, U. Stürzebecher, H.-P. Sperlich, and B. Rech, "PECVD-AlOx/SiNx passivation stacks on wet chemically oxidized silicon: Constant voltage stress investigations of charge dynamics and interface defect states," *Solar Energy Materials and Solar Cells,* vol. 135, no. 0, pp. 49-56, 4//, 2015, http://dx.doi.org/10.1016/j.solmat.2014.09.024

[200]   J. A. Töfflinger, A. Laades, C. Leendertz, L. M. Montañez, L. Korte, U. Stürzebecher, H.-P. Sperlich, and B. Rech, "PECVD-AlOx/SiNx Passivation Stacks on Silicon: Effective Charge Dynamics and Interface Defect State Spectroscopy," *Energy Procedia,* vol. 55, pp. 845-854, 2014, https://doi.org/10.1016/j.egypro.2014.08.068

[201]   C. S. Solanki, and H. K. Singh, *Anti-reflection and Light Trapping in c-Si Solar Cells*: Springer, 2017.

[202]   P. E. Ciddor, "Refractive index of air: new equations for the visible and near infrared," *Applied Optics,* vol. 35, no. 9, pp. 1566-1573, 1996/03/20, 1996, https:doi.org/10.1364/AO.35.001566

[203]   P. F. Carcia, R. S. McLean, M. D. Groner, A. A. Dameron, and S. M. George, "Gas diffusion ultrabarriers on polymer substrates using Al_2O_3 atomic layer deposition and SiN plasma-enhanced chemical vapor deposition," *Journal of Applied Physics,* vol. 106, no. 2, pp. 023533, 2009, https://doi.org/10.1063/1.3159639

[204]   *Crystalline silicon terrestrial photovoltaic (PV) modules –Design qualification and type approval* I. E. Commission, 2005.

[205]   Z. Chen, and C. Lu, "Humidity sensors: a review of materials and mechanisms," *Sensor letters,* vol. 3, no. 4, pp. 274-295, 2005, https://doi.org/10.1166/sl.2005.045

[206]   W. Liang, D. Suh, J. Yu, J. Bullock, and K. J. Weber, "Degradation of the surface passivation of plasma-assisted ALD Al_2O_3 under damp-heat exposure," *physica status solidi (a),* vol. 212, no. 2, pp. 274-281, 2015, https://doi.org/10.1002/pssa.201431256

[207]   V. I. Kuznetsov, M. A. Ernst, and E. H. A. Granneman, "Al_2O_3 surface passivation of silicon solar cells by low cost ald technology." pp. 0608-0611, https://doi.org/10.1109/PVSC.2014.6924995

[208]   L. Wensheng, K. J. Weber, and A. F. Thomson, "Effective SiNx:H Capping Layers on 1-nm Al_2O_3 for p^+ Surface Passivation," *Photovoltaics, IEEE Journal of,* vol. 4, no. 6, pp. 1405-1412, 2014, https://doi.org/10.1109/JPHOTOV.2014.2344757

[209]   D. Schuldis, A. Richter, J. Benick, P. Saint-Cast, M. Hermle, and S. W. Glunz, "Properties of the $c-Si/Al_2O_3$ interface of ultrathin atomic layer deposited Al_2O_3 layers capped by SiN_X for c-Si surface passivation," *Applied Physics Letters,* vol. 105, no. 23, pp. -, 2014, http://dx.doi.org/10.1063/1.4903483

[210]   A. Richter, J. Benick, M. Hermle, and S. W. Glunz, "Excellent silicon surface passivation with 5 Å thin ALD Al_2O_3 layers: Influence of different thermal post-deposition treatments," *physica status solidi (RRL) – Rapid Research Letters,* vol. 5, no. 5-6, pp. 202-204, 2011, https://doi.org/10.1002/pssr.201105188

[211]   A. Richter, J. Benick, and M. Hermle, "Boron Emitter Passivation With Al_2O_3 and Al_2O_3/SiN_x Stacks Using ALD Al_2O_3," *IEEE Journal of Photovoltaics,* vol. 3, no. 1, pp. 236-245, 2013, https://doi.org/10.1109/JPHOTOV.2012.2226145

[212]   J. Couderc, H. e. Belghiti, D. Aureau, J. Dupuis, P.-P. Grand, É. Delbos, A. Etcheberry, and D. Lincot, "Study of one-step annealing for plated nickel-copper contacts on n-pert bifacial monocrystalline silicon solar cells." pp. 697-702, https://doi.org/10.4229/EUPVSEC20162016-2AV.2.9

[213]   A. M. Antoine, B. Drevillon, and P. R. i. Cabarrocas, "In situ investigation of the growth of rf glow-discharge deposited amorphous germanium and silicon films," *Journal of Applied Physics,* vol. 61, no. 7, pp. 2501-2508, 1987, https://doi.org/10.1063/1.337924

[214] S. Abolmasov, P.-A. Cormier, A. Torres Rios, R. Dussart, N. Semmar, A.-L. Thomann, and P. Roca i Cabarrocas, "Probing dusty-plasma/surface interactions with a heat flux microsensor," *Applied Physics Letters,* vol. 100, no. 1, pp. 011601, 2012, https://doi.org/10.1063/1.3674290

[215] P. Chabert, and N. Braithwaite, *Physics of radio-frequency plasmas*: Cambridge University Press, 2011.

[216] A. G. Aberle, "Overview on SiN surface passivation of crystalline silicon solar cells," *Solar Energy Materials and Solar Cells,* vol. 65, no. 1–4, pp. 239-248, 1//, 2001, http://dx.doi.org/10.1016/S0927-0248(00)00099-4

[217] D. E. Kotecki, and J. D. Chapple-Sokol, "Hydrogen incorporation in silicon nitride films deposited by remote electron-cyclotron-resonance chemical vapor deposition," *Journal of applied physics,* vol. 77, no. 3, pp. 1284-1293, 1995, https://doi.org/10.1063/1.358930

[218] S. Yokoyama, M. Hirose, and Y. Osaka, "Optical Emission Spectroscopy of the SiH_4-NH_3-H_2 Plasma during the Growth of Silicon Nitride," *Japanese Journal of Applied Physics,* vol. 20, no. 2, pp. L117, 1981, https://doi.org/10.1143/JJAP.20.L117

[219] P. Saint-Cast, D. Kania, R. Heller, S. Kuehnhold, M. Hofmann, J. Rentsch, and R. Preu, "High-temperature stability of c-Si surface passivation by thick PECVD Al_2O_3 with and without hydrogenated capping layers," *Applied Surface Science,* vol. 258, no. 21, pp. 8371-8376, 8/15/, 2012, http://dx.doi.org/10.1016/j.apsusc.2012.03.171

[220] H. Shanks, and L. Ley, "Formation of pin holes in hydrogenated amorphous silicon at high temperatures and the yield strength of a-Si: H," *Journal of Applied Physics,* vol. 52, no. 2, pp. 811-813, 1981, https://doi.org/10.1063/1.328767

[221] S. Dauwe, J. Schmidt, and R. Hezel, "Very low surface recombination velocities on p- and n-type silicon wafers passivated with hydrogenated amorphous silicon films." pp. 1246-1249, https://doi.org/10.1109/PVSC.2002.1190834

[222] A. Richter, S. Henneck, J. Benick, M. Hörteis, M. Hermle, and S. Glunz, "Firing stable Al_2O_3/SiNx layer stack passivation for the front side boron emitter of n-type silicon solar cells." pp. 1453-1456, https://doi.org/10.4229/25thEUPVSEC2010-2DO.2.4

[223] M. Li, H.-S. Shin, K.-S. Jeong, S.-K. Oh, H. Lee, K. Han, G.-W. Lee, and H.-D. Lee, "Blistering Induced Degradation of Thermal Stability Al_2O_3Passivation Layer in Crystal Si Solar Cells," *JSTS:Journal of Semiconductor Technology and Science,* vol. 14, no. 1, pp. 53-60, 2014, https://doi.org/10.5573/jsts.2014.14.1.053

[224] S. Li, P. Repo, G. von Gastrow, Y. Bao, and H. Savin, "Effect of ALD reactants on blistering of aluminum oxide films on crystalline silicon." pp. 1265-1267, https://doi.org/10.1109/PVSC.2013.6744371

[225] D. Schuldis, A. Richter, J. Benick, and M. Hermle, "Influence of different post deposition treatments on the passivation quality and interface properties of thermal ALD Al_2O_3 capped by PECVD SiNx." pp. 1933-1937, https://doi.org/10.4229/27thEUPVSEC2012-2CV.6.51

[226] O. Beldarrain, M. Duch, M. Zabala, J. M. Rafí, M. B. González, and F. Campabadal, "Blistering of atomic layer deposition Al_2O_3 layers grown on silicon and its effect on metal–insulator–semiconductor structures," *Journal of Vacuum Science & Technology A,* vol. 31, no. 1, pp. 01A128, 2013, https://doi.org/10.1116/1.4768170

[227] Y. Etinger-Geller, A. Katsman, and B. Pokroy, "Density of Nanometrically Thin Amorphous Films Varies by Thickness," *Chemistry of Materials,* vol. 29, pp. 4912−4919, 2017, https://doi.org/10.1021/acs.chemmater.7b01139

[228] L. Hennen, E. Granneman, and W. Kessels, "Analysis of blister formation in spatial ALD Al_2O_3 for silicon surface passivation." pp. 001049-001054, https://doi.org/10.1109/PVSC.2012.6317783

[229] M. Acero, O. Beldarrain, M. Duch, M. Zabala, M. González, and F. Campabadal, "Effect of the blistering of ALD Al_2O_3 films on the silicon surface in Al-Al_2O_3-Si structures." pp. 1-4, https://doi.org/10.1109/CDE.2015.7087443

[230] A. Devos, "Phonons in nanoscale objects," *Handbook of nanophysics - Principles and methods*, S. K.D., ed., p. 23: Taylor & Francis, 2010.

[231] A. Devos, "Colored ultrafast acoustics: From fundamentals to applications," *Ultrasonics,* vol. 56, pp. 90-97, 2015, https://doi.org/10.1016/j.ultras.2014.02.009

[232]   X. Gay, F. Souren, B. Dielissen, M. Bijker, R. Gortzen, D. Pysch, K. Weise, B. Sander, and R. Sastrawan, "Post-deposition thermal treatment of ultrafast spatial ALD Al$_2$O$_3$ for the rear side passivation of p-type PERC solar cells," https://doi.org/10.4229/28thEUPVSEC2013-2BV.2.3

[233]   B. Vermang, H. Goverde, A. Lorenz, A. Uruena, G. Vereecke, J. Meersschaut, E. Cornagliotti, A. Rothschild, J. John, J. Poortmans, and R. Mertens, "On the blistering of atomic layer deposited Al$_2$O$_3$ as Si surface passivation." pp. 003562-003567, https://doi.org/10.1109/PVSC.2011.6185916

[234]   D. Staebler, and C. Wronski, "Reversible conductivity changes in discharge-produced amorphous Si," *Applied physics letters,* vol. 31, no. 4, pp. 292-294, 1977, https://doi.org/10.1063/1.89674

[235]   F. Lebreton, S. N. Abolmasov, F. Silva, and P. Roca i Cabarrocas, "In situ photoluminescence study of plasma-induced damage at the a-Si:H/c-Si interface," *Applied Physics Letters,* vol. 108, no. 5, pp. 051603, 2016, https://doi.org/10.1063/1.4941298

[236]   Y.-R. Luo, *Comprehensive handbook of chemical bond energies*: CRC press, 2007.

[237]   S. Bordihn, V. Mertens, P. Engelhart, F. Kersten, M. M. Mandoc, J. W. Müller, and W. M. M. Kessels, "Surface Passivation by Al$_2$O$_3$ and a-SiNx: H Films Deposited on Wet-Chemically Conditioned Si Surfaces," *ECS Journal of Solid State Science and Technology,* vol. 1, no. 6, pp. P320-P325, January 1, 2012, 2012, https://doi.org/10.1149/2.008301jss

[238]   V. Sharma, A. Bailey, B. Dauksher, C. Tracy, S. Bowden, and B. O'Brien, "Characterization and comparison of silicon nitride films deposited using two novel processes," *Journal of Vacuum Science & Technology A: Vacuum, Surfaces, and Films,* vol. 30, no. 2, pp. 021201, 2012, https://doi.org/10.1116/1.3687423

[239]   J. Robertson, "Electronic structure of silicon nitride," *Philosophical Magazine B,* vol. 63, no. 1, pp. 47-77, 1991, http://dx.doi.org/10.1080/01418639108224430

[240]   W. Warren, J. Kanicki, F. Rong, E. Poindexter, and P. McWhorter, "Charge trapping centers in N-rich silicon nitride thin films," *Applied physics letters,* vol. 61, no. 2, pp. 216-218, 1992, https://doi.org/10.1063/1.108222

[241]   H. Mäckel, and R. Lüdemann, "Detailed study of the composition of hydrogenated SiNx layers for high-quality silicon surface passivation," *Journal of Applied Physics,* vol. 92, no. 5, pp. 2602-2609, 2002, http://dx.doi.org/10.1063/1.1495529

[242]   M. Lamers, L. E. Hintzsche, K. T. Butler, P. E. Vullum, C.-M. Fang, M. Marsman, G. Jordan, J. H. Harding, G. Kresse, and A. Weeber, "The interface of a-SiNx:H and Si: Linking the nano-scale structure to passivation quality," *Solar Energy Materials and Solar Cells,* vol. 120, Part A, no. 0, pp. 311-316, 1//, 2014, http://dx.doi.org/10.1016/j.solmat.2013.04.026

[243]   V. Sharma, C. Tracy, D. Schroder, S. Herasimenka, W. Dauksher, and S. Bowden, "Manipulation of K center charge states in silicon nitride films to achieve excellent surface passivation for silicon solar cells," *Applied Physics Letters,* vol. 104, no. 5, pp. 053503, 2014, https://doi.org/10.1063/1.4863829

[244]   K. Sankaran, G. Pourtois, R. Degraeve, M. Zahid, G.-M. Rignanese, and J. Van Houdt, "First-principles modeling of intrinsic and extrinsic defects in γ-Al$_2$O$_3$," *Applied Physics Letters,* vol. 97, no. 21, pp. 212906, 2010, https://doi.org/10.1063/1.3507385

[245]   T. Lüder, T. Lauermann, A. Zuschlag, G. Hahn, and B. Terheiden, "Al$_2$O$_3$/SiN$_X$-Stacks at Increased Temperatures: Avoiding Blistering During Contact Firing," *Energy Procedia,* vol. 27, no. 0, pp. 426-431, //, 2012, http://dx.doi.org/10.1016/j.egypro.2012.07.088

[246]   J. Peter Seif, A. Descoeudres, M. Filipič, F. Smole, M. Topič, Z. Charles Holman, S. De Wolf, and C. Ballif, "Amorphous silicon oxide window layers for high-efficiency silicon heterojunction solar cells," *Journal of Applied Physics,* vol. 115, no. 2, pp. 024502, 2014, https://doi.org/10.1063/1.4861404

[247]   K. Nakada, J. Irikawa, S. Miyajima, and M. Konagai, "Silicon heterojunction solar cells with high surface passivation quality realized using amorphous silicon oxide films with epitaxial phase," *Japanese Journal of Applied Physics,* vol. 54, no. 5, pp. 052303, 2015, https://doi.org/10.7567/jjap.54.052303

[248]   J. Ge, M. Tang, J. Wong, R. Stangl, Z. Zhang, T. Dippell, M. Doerr, O. Hohn, M. Huber, P. Wohlfart, A. G. Aberle, and T. Mueller, "Investigation of Wide Process Temperature Window for Amorphous Silicon Suboxide Thin-Film Passivation Deposited by Inductively Coupled PECVD," *Photovoltaics, IEEE Journal of,* vol. PP, no. 99, pp. 1-6, 2015, https://doi.org/10.1109/JPHOTOV.2015.2397593

[249] F. Brehmer, S. Welzel, M. Van De Sanden, and R. Engeln, "CO and byproduct formation during CO_2 reduction in dielectric barrier discharges," *Journal of Applied Physics,* vol. 116, no. 12, pp. 123303, 2014, https://doi.org/10.1063/1.4896132

[250] S. Dobrea, I. Mihaila, V. Tiron, and G. Popa, "Optical and mass spectrometry diagnosis of a CO_2 microwave plasma discharge," *Romanian Reports in Physics,* vol. 66, no. 4, pp. 1147-1154, 2014,

[251] G. E. Box, and D. W. Behnken, "Some new three level designs for the study of quantitative variables," *Technometrics,* vol. 2, no. 4, pp. 455-475, 1960,

[252] R. H. Myers, D. C. Montgomery, and C. M. Anderson-Cook, *Response surface methodology: process and product optimization using designed experiments*: John Wiley & Sons, 2016.

[253] M. S. Jeong, S. J. Choi, H. S. Chang, J. I. Lee, M. G. Kang, D. Kim, and H.-e. Song, "Use of antireflection layers to avoid ghost plating on Ni/Cu plated crystalline silicon solar cells," *Japanese Journal of Applied Physics,* vol. 55, no. 3, pp. 036502, 2016, https://doi.org/10.7567/JJAP.55.036502

List of publications

Publications

[1] F. Lebreton, A. Zauner, P. Bulkin, F. Silva, S. Filonovich and P. Roca i Cabarrocas, "benefits of a thermal drift during atomic layer deposition of Al_2O_3 for c-Si passivation" in *43rd IEEE Photovoltaic Specialists Conference,* 2017, accepted

[2] F. Lebreton, A. Devos, P. Bulkin, F. Silva, S. Filonovich and P. Roca i Cabarrocas, "Blistering of Al_2O_3/a-SiN_X:H stacks: analysis of the submerged part of the iceberg by colored picosecond acoustic microscopy," in *43rd IEEE Photovoltaic Specialists Conference,* 2017, accepted

[3] F. Lebreton, R. Lachaume, P. Bulkin, F. Silva, S. Filonovich, E. V. Johnson and P. Roca i Cabarrocas, "Deleterious electrostatic interaction in silicon passivation stack between thin ALD Al_2O_3 and its a SiN_X:H capping layer: numerical and experimental evidences", Energy Procedia, **124**: 91-98, 2017.

[4] G. Fischer, E. Drahi, F. Lebreton, P. Bulkin, G. Poulain and E.V. Johnson, "nanotextured silicon surfaces using tailored voltage waveform plasmas: impact of ion bombardment energy on etching dynamics and passivation", *Proceedings of the 33rd European Photovoltaic Solar Energy Conference*, 2017.

[5] F. Lebreton, S.N. Abolmasov, F. Silva and P. Roca i Cabarrocas, "In situ photoluminescence study of plasma-induced damage at the a-Si:H/c-Si interface", *Applied Physics Letters*, **108**(5): 051603, 2016.

[6] A. Zauner, F. Lebreton, P. Saint-Cast, M. Hofmann, J.-Y. Letellier, E. Urrejola, Y. Marot, F. Gouhinec, C. Charpentier, J. Hong, F. Coeuret and S. Pouliquen, "PERC solar cells: comparison of Al precursors for rear-side surface passivation", *Proceedings of the 29th European Photovoltaic Solar Energy Conference*, 2014, pp. 1413-1416.

Patent pending

[1] F. Lebreton and A. Zauner, *Thermal drift - atomic layer deposition (TD-ALD) for very high passivation level with very thin ALD films*, November 2016.

Résumé

Ce travail de doctorat se focalise sur les propriétés passivantes octroyées par des couches minces d'oxyde d'aluminium déposées par *Atomic Layer Deposition* (ALD). Ces couches synthétisées à partir de trimethylaluminium et d'eau sont destinées aux cellules photovoltaïques en silicium ayant des températures de fabrication inférieures à 400 °C. La première étape de ce travail a été la caractérisation approfondie des propriétés physico-chimiques des couches d'Al_2O_3, en fonction de leur température de dépôt. Ainsi, les différentes caractéristiques ont été quantifiées : la vitesse de croissance et l'indice de réfraction par ellipsométrie spectroscopique, la masse volumique par réflexion des rayons-X, la stœchiométrie par spectroscopie de rétrodiffusion de Rutherford, la teneur en hydrogène par l'analyse du recul élastique et enfin la teneur en carbone grâce à l'analyse par réaction nucléaire. La teneur en hydrogène et la densité de la couche mince d'Al_2O_3 sont les deux paramètres les plus sensibles à la température de dépôt. En effet, plus cette dernière augmente, plus la quantité d'hydrogène diminue et plus la masse volumique de la couche mince augmente. La suite de ce travail vise à identifier les mécanismes de formation des charges électrostatiques négatives, que l'on retrouve dans l'oxyde d'aluminium. Pour ce faire, les effets de l'illumination post-dépôt (c'est-à-dire, le flux et l'énergie des photons), ainsi que la température du substrat ont été étudiés. Grâce à une quantification de la densité de charges par caractérisation d'oxyde de semi-conducteur par décharge corona, il a été montré qu'au moins 70 % de ce qu'on appelle généralement les « charges fixes » sont, en réalité, des charges piégées qui résulteraient de l'injection d'électrons du substrat de silicium dans l'oxyde d'aluminium. Par la suite, nous avons étudié l'influence des paramètres de dépôt de l'oxyde d'aluminium ainsi que l'impact des traitements post-dépôt sur le piégeage des charges et, a fortiori, sur les performances passivantes qui en résultent au sein d'un empilement Al_2O_3/a-SiN_X:H, déposé sur du silicium cristallin de type p. Les liens entre l'épaisseur de l'oxyde d'aluminium, la qualité et la durabilité de la passivation ont pu être établis. De ce fait, le meilleur compromis qui en est ressorti, s'est avéré se situer aux alentours de 60 cycles ALD (~6 nm) d'oxyde d'aluminium, permettant une durée de vie des porteurs de charges minoritaires allant jusqu'à 4500 µs.

La deuxième partie de ce travail doctoral consiste à étudier, et mettre en évidence, les mécanismes de dégradation de la passivation. La formation de cloques à l'interface c-Si/Al_2O_3 est le premier mécanisme de dégradation étudié. Grâce à la microscopie acoustique picoseconde colorée (APiC), la dégradation de l'interface Al_2O_3/c-Si a été confirmée lors de l'épaississement de l'oxyde d'aluminium. Cette dégradation a également été mise en évidence lors de la réduction de la température de dépôt, c'est-à-dire en augmentant la teneur en hydrogène au sein du film d'oxyde d'aluminium. Des mesures de spectroscopie de désorption thermique suggèrent que la déshydroxylation de l'oxyde d'aluminium donne de l'eau dans le volume du film, mais du dihydrogène à l'interface Al_2O_3/c-Si. L'activité catalytique des sites d'aluminium en coordination tétraédrique, particulièrement présents à cette interface, est proposée comme étant à l'origine de

la formation de ce dihydrogène et potentiellement responsable du cloquage observé à cette interface. Une dérive thermique pendant l'ALD (TD-ALD) a été utilisée pour résoudre ce problème de cloquage. Il a été montré que l'augmentation continue de la température du substrat, pendant le dépôt, favorise la libération de l'hydrogène à partir de l'interface c-Si/Al$_2$O$_3$. Ce procédé, particulièrement adapté aux réacteurs de dépôt de type ALD spatial, a été utilisé dans un réacteur temporel en utilisant le temps de thermalisation nécessaire au porte-substrat pour atteindre la température du réacteur de dépôt. Pour 60 cycles ALD, le TD-ALD a permis d'augmenter la durée de vie des porteurs de charges jusqu'à 5500 µs et de supprimer le cloquage qui était présent pour les plus fortes teneurs en hydrogène. Pour conclure ce travail doctoral, il a été mis en évidence, par simulation numérique, l'affaiblissement de la passivation par effet de champ résultant des charges positives dans la couche de protection en nitrure de silicium amorphe hydrogéné (a-SiN$_X$:H). Les propriétés de l'a-SiN$_X$:H ont été expérimentalement optimisées, grâce à une approche par plan d'expérience de type Box-Behnken. Ce plan d'expérience a rendu possible la modélisation des paramètres physiques, chimiques et électriques des couches de a-SiN$_X$:H en fonction des paramètres du dépôt chimique en phase vapeur assisté par plasma. Une nouvelle couche mince d'encapsulation d'a-SiN$_X$:H contenant 50 % de charges fixes positives en moins a permis d'obtenir une durée de vie des porteurs de charges de 8800 µs pour 60 cycles de TD-ALD, c'est-à-dire une vitesse de recombinaison de surface exceptionnellement basse de 0,8 cm.s^{-1}.

Titre : Passivation de la surface du silicium cristallin par l'oxyde d'aluminium synthétisé via *atomic layer deposition* pour la fabrication de cellules photovoltaïques à basse température.

Mots clés : Passivation ; Al$_2$O$_3$; ALD ; Photovoltaïque ; LIFE$_2$

Résumé : Cette thèse se focalise sur les propriétés passivantes octroyées par des couches minces d'Al$_2$O$_3$ déposées par *Atomic Layer Deposition* (ALD) à partir de TMA et H$_2$O pour les cellules photovoltaïques en silicium ayant des températures de fabrication inférieures à 400 °C. La première partie de ce travail de doctorat vise à identifier les mécanismes de formation des charges électrostatiques négatives présentes dans l'oxyde d'aluminium. Il a été constaté qu'au moins 70 % de ce qui est généralement appelé les « charges fixes » sont en fait des charges photo-injectées du c-Si dans l'Al$_2$O$_3$. Nous avons étudié l'influence des paramètres de dépôt de l'Al$_2$O$_3$ ainsi que l'impact des traitements post-dépôt sur le piégeage de ces charges au sein d'un empilement Al$_2$O$_3$/a-SiN$_X$:H déposé sur du silicium cristallin de type p. Les liens entre l'épaisseur de l'Al$_2$O$_3$, la qualité et la durabilité de la passivation ont pu être établis. Le meilleur compromis s'est avéré être aux alentours 60 cycles ALD (~6 nm), permettant d'atteindre une durée de vie des porteurs de charges minoritaires de 4500 µs. La deuxième partie de ce travail doctoral porte sur les mécanismes de dégradation de la passivation. Grâce à la microscopie acoustique colorée, la dégradation de l'interface Al$_2$O$_3$/c-Si lors de l'épaississement de l'Al$_2$O$_3$ mais également lors la réduction de sa température de dépôt, c'est-à-dire en augmentant sa teneur en hydrogène, a été confirmée. L'augmentation continue de la température du substrat pendant le dépôt ALD (TD-ALD) favorise la libération de l'hydrogène à partir de l'interface c-Si/Al$_2$O$_3$. Pour 60 cycles, le TD-ALD a permis d'augmenter la durée de vie des porteurs de charges jusqu'à 5500 µs. Enfin, l'affaiblissement de la passivation par effet de champ résultant des charges positives dans la couche de protection en a-SiN$_X$:H a été mis en évidence par simulation numérique. Une nouvelle couche mince d'a-SiN$_X$:H contenant 50 % de charges fixes positives en moins a permis d'obtenir une durée de vie des porteurs de charges de 8800 µs pour 60 cycles de TD-ALD, c'est-à-dire une vitesse de recombinaison de surface exceptionnelle basse de 0,8 cm.s^{-1}.

Title : Silicon surface passivation properties of aluminium oxide grown by atomic layer deposition for low temperature solar cells processes.

Keywords : Passivation ; Al$_2$O$_3$; ALD ; Photovoltaics ; LIFE$_2$

Abstract : This thesis focuses on the passivation properties provided by thin Al$_2$O$_3$ films grown by atomic layer deposition (ALD) from TMA and H$_2$O for silicon solar cells having process temperatures lower than 400 °C. The first part of this doctoral work aims at identifying the formation mechanisms of negative electrostatic charges in aluminium oxide. It was found that at least 70 % of what are generally named "fixed charges" are in fact trapped charges resulting from the injection of carriers from the silicon substrate into the aluminium oxide. Then, we studied the influence of Al$_2$O$_3$ deposition parameters and post-deposition treatments on charge trapping and resulting passivation performances within an Al$_2$O$_3$/a-SiN$_X$:H stack on p-type c-Si. The dependence of passivation performance (and stability) on Al$_2$O$_3$ thickness has been highlighted. Best compromise has been found to be around 60 ALD cycles (~6 nm), providing a lifetime up to 4500 µs. The second part of this PhD deals with the degradation mechanisms of passivation. Thanks to coloured picosecond acoustic microscopy, the Al$_2$O$_3$/c-Si adhesion has been confirmed to be reduced by Al$_2$O$_3$ thickening but also by the reduction of its deposition temperature, i.e. an increase of hydrogen content. A thermal drift during ALD (TD-ALD) has been used to solve this blistering issue. Gradual increase of the substrate temperature during the growth favours the release of hydrogen from the wafer/Al$_2$O$_3$ interface. For 60 ALD cycles, TD-ALD increased the lifetime up 5500 µs. Finally, the weakening of the electrostatic passivation arising from the positive charges in a-SiN$_X$:H capping layer has been underlined by finite element simulations. The a-SiN$_X$:H properties have been experimentally tuned thanks to a design of experiment approach. New a-SiN$_X$:H capping containing 50 % less positive fixed charges resulted in a lifetime of 8800 µs for 60 TD-ALD cycles, *i.e.* an outstanding surface recombination velocity of 0.8 cm.s^{-1}.